



2014

# Multidimensional Modeling of Pyrolysis Gas Transport Inside Orthotropic Charring Ablators

Haoyue Weng

*University of Kentucky*, kimomt@gmail.com

---

## Recommended Citation

Weng, Haoyue, "Multidimensional Modeling of Pyrolysis Gas Transport Inside Orthotropic Charring Ablators" (2014). *Theses and Dissertations--Mechanical Engineering*. Paper 50.  
[http://uknowledge.uky.edu/me\\_etds/50](http://uknowledge.uky.edu/me_etds/50)

This Doctoral Dissertation is brought to you for free and open access by the Mechanical Engineering at UKnowledge. It has been accepted for inclusion in Theses and Dissertations--Mechanical Engineering by an authorized administrator of UKnowledge. For more information, please contact [UKnowledge@lsv.uky.edu](mailto:UKnowledge@lsv.uky.edu).

**STUDENT AGREEMENT:**

I represent that my thesis or dissertation and abstract are my original work. Proper attribution has been given to all outside sources. I understand that I am solely responsible for obtaining any needed copyright permissions. I have obtained and attached hereto needed written permission statement(s) from the owner(s) of each third-party copyrighted matter to be included in my work, allowing electronic distribution (if such use is not permitted by the fair use doctrine).

I hereby grant to The University of Kentucky and its agents the irrevocable, non-exclusive, and royalty-free license to archive and make accessible my work in whole or in part in all forms of media, now or hereafter known. I agree that the document mentioned above may be made available immediately for worldwide access unless a preapproved embargo applies. I retain all other ownership rights to the copyright of my work. I also retain the right to use in future works (such as articles or books) all or part of my work. I understand that I am free to register the copyright to my work.

**REVIEW, APPROVAL AND ACCEPTANCE**

The document mentioned above has been reviewed and accepted by the student's advisor, on behalf of the advisory committee, and by the Director of Graduate Studies (DGS), on behalf of the program; we verify that this is the final, approved version of the student's dissertation including all changes required by the advisory committee. The undersigned agree to abide by the statements above.

Haoyue Weng, Student

Dr. Alexandre Martin, Major Professor

Dr. James M. McDonough, Director of Graduate Studies

---

Multidimensional modeling of pyrolysis gas transport inside orthotropic charring  
ablators

---

DISSERTATION

---

A dissertation submitted in partial  
fulfillment of the requirements for  
the degree of Doctor of Philosophy  
in the College of Engineering at the  
University of Kentucky

By  
Haoyue Weng  
Lexington, Kentucky

Director: Dr. Alexandre Martin, Professor of Mechanical Engineering  
Lexington, Kentucky 2014

Copyright© Haoyue Weng 2014

## ABSTRACT OF DISSERTATION

Multidimensional modeling of pyrolysis gas transport inside orthotropic charring  
ablators

During hypersonic atmospheric entry, spacecraft are exposed to enormous aerodynamic heat. To prevent the payload from overheating, charring ablative materials are favored to be applied as the heat shield at the exposing surface of the vehicle. Accurate modeling not only prevents mission failures, but also helps reduce cost. Existing models were mostly limited to one-dimensional and discrepancies were shown against measured experiments and flight-data. To help improve the models and analyze the charring ablation problems, a multidimensional material response module is developed, based on a finite volume method framework. The developed computer program is verified through a series of test-cases, and through code-to-code comparisons with a validated code. Several novel models are proposed, including a three-dimensional pyrolysis gas transport model and an orthotropic material model. The effects of these models are numerically studied and demonstrated to be significant.

KEYWORDS: atmospheric entry, thermal protection system, material response, numerical heat transfer

Author's signature: Haoyue Weng

Date: December 19, 2014

Multidimensional modeling of pyrolysis gas transport inside orthotropic charring  
ablators

By  
Haoyue Weng

Director of Dissertation: Alexandre Martin

Director of Graduate Studies: James M. McDonough

Date: December 19, 2014

Dedicated to my lovely wife, Dr. Wanjing Xiu.

Thank you for everything,  
especially for the moral support  
... and many attempts on cooking.

## ACKNOWLEDGMENTS

I would like to express my sincerest gratitude to Dr. Alexandre Martin for serving as my advisor. His guidance, patience, and humor have made my graduate study the most valuable experience that I could ever have. My accomplishment in this field would not have been possible without his extensive knowledge and novel ideas.

I would also like to thank Dr. James M. McDonough for his wealth of knowledge in computational sciences given to me through his lectures, and for serving as the co-chair in my doctoral advisory committee. I would like to extend my thanks to Dr. Thomas W. Lester, Dr. Kaveh A. Tagavi, Dr. Matthew J. Beck at University of Kentucky, as well as Mr. Michael Barnhardt at ERC Inc., for serving on my advisory committee with many advices and guides on my research.

Special thanks to the Elbert C. Ray eStudio in College of Engineering at University of Kentucky, for the writing assistance to this work. Additional thanks to the Associate Director of eStudio, Dr. Emily Dotson, for her professional dissertation planning and heart-warming encouragement through my dissertation writing.

Thanks also to Dr. Francesco Panerai at University of Kentucky for inspiring me on material modeling; Adam J. Amar at NASA Johnson Space Center for attentive reviews on my submitted papers; Tom van Eekelen at LMS-SAMTECH and Dr. Jean Lachaud at University of California, Santa Cruz, for providing theoretical ablative material data and comprehensive test-cases.

My thank is also extended to the colleagues in my lab, especially to Huaibao (Paul) for his initial guide in working with a supercomputer and for many useful discussions and collaborations we had, to Raghava for his encouragement during a conference, and to Rick, Zack, Ali, David, Tingting, Wenwei, and Weiyun for their countless support.

## TABLE OF CONTENTS

Acknowledgments . . . . .	iii
Table of Contents . . . . .	iv
List of Figures . . . . .	vi
List of Tables . . . . .	ix
Chapter 1 Introduction . . . . .	1
1.1 Background . . . . .	2
1.2 Extant work and research motivations . . . . .	7
Chapter 2 Computational Framework . . . . .	16
2.1 Finite volume method . . . . .	16
2.2 Parallel computing . . . . .	19
Chapter 3 Governing Equations . . . . .	21
Chapter 4 Boundary Conditions . . . . .	23
4.1 Wall BC . . . . .	23
4.2 Symmetry BC . . . . .	23
4.3 Outlet BC . . . . .	24
4.4 Aerodynamic heat BC . . . . .	24
4.5 Penetrated heat BC . . . . .	26
Chapter 5 Material Models . . . . .	28
5.1 Material properties models . . . . .	28
5.2 Solid decomposition model . . . . .	31
5.3 Pyrolysis gas model . . . . .	32
5.4 Pyrolysis gas transport model . . . . .	33
5.5 Mixture energy model . . . . .	35
Chapter 6 Model Verification . . . . .	36
6.1 Heat conduction . . . . .	36
6.2 Flow through a porous tube . . . . .	40
6.3 1D TACOT heating problem . . . . .	44
Chapter 7 Study of Pyrolysis Gas Flow Effects . . . . .	49
7.1 Motivation . . . . .	49
7.2 Applied models . . . . .	49
7.3 Cylinder sample test-cases . . . . .	50
7.4 Iso-Q sample test-cases . . . . .	60



7.5	Conclusions for pyrolysis gas effects study . . . . .	70
Chapter 8	Geometric Effects of an Arc-jet Sample . . . . .	71
8.1	Motivation . . . . .	71
8.2	Applied models . . . . .	72
8.3	Test-case descriptions . . . . .	72
8.4	Results and discussions . . . . .	76
8.5	Conclusions for geometric effects study . . . . .	108
Chapter 9	Effects of Orthotropic Material Properties . . . . .	110
9.1	Motivation . . . . .	110
9.2	Applied models . . . . .	110
9.3	Test-case descriptions . . . . .	110
9.4	Results and discussions . . . . .	113
9.5	Conclusions for orthotropic properties study . . . . .	121
Chapter 10	Conclusions . . . . .	122
10.1	Summary . . . . .	122
10.2	Original contributions . . . . .	122
10.3	Future work . . . . .	125
Appendices	. . . . .	128
A	Jacobian matrices in the governing equations . . . . .	128
B	Input deck of the material response module in KATS . . . . .	132
C	Derivation of conservation equations in porous media . . . . .	136
D	Material properties of TACOT . . . . .	140
Bibliography	. . . . .	149
Vita	. . . . .	167

## LIST OF FIGURES

1.1	MSL spacecraft entering the Martian atmosphere . . . . .	2
1.2	MSL aeroshell heat shield with PICA tiles . . . . .	4
1.3	NASA’s Stardust SRC after landing on the ground . . . . .	5
1.4	Micrograph of a virgin PICA surface . . . . .	5
1.5	Micrograph of a char PICA surface . . . . .	6
1.6	Illustration of charring ablative phenomena . . . . .	7
2.1	Illustration of an example of the domain decomposition method . . . . .	19
2.2	Illustration of example ghost cells in the domain decomposition method . . . . .	20
5.1	Illustration of IP and TTT directions regarding fiber orientation . . . . .	29
6.1	Analytical solution to the 1D heat conduction problem with heat flux specified on one side and adiabatic BC on the other side . . . . .	37
6.2	Solution errors to the heat equation in the temporal accuracy study . . . . .	39
6.3	Solution errors to the heat equation in the spatial accuracy study . . . . .	40
6.4	Illustration of the porous tube problem . . . . .	41
6.5	Mass flow rate within the porous tube . . . . .	43
6.6	Pressure and temperature profiles along the centerline of the porous tube . . . . .	43
6.7	Gas density and velocity profiles along the centerline of the porous tube . . . . .	44
6.8	Illustration of the 1D TACOT heating problem . . . . .	45
6.9	Temperature profiles for the 1D TACOT heating problem . . . . .	47
6.10	Overall solid density profiles for the 1D TACOT heating problem . . . . .	47
6.11	Zoomed-in temperature profiles for the 1D TACOT heating problem . . . . .	47
6.12	Zoomed-in solid density profiles for the 1D TACOT heating problem . . . . .	47
7.1	Computational geometry and boundary conditions for the cylinder sample cases in pyrolysis gas flow study . . . . .	51
7.2	Comparison between 3D cylinder and 1D model results . . . . .	52
7.3	Pressure contours of impermeable side wall cylinder . . . . .	53
7.4	Pressure contours of permeable side wall cylinder . . . . .	53
7.5	Gas mass transport of impermeable side wall cylinder . . . . .	55
7.6	Gas mass transport of permeable side wall cylinder . . . . .	55
7.7	Thermal response of impermeable side wall cylinder . . . . .	56
7.8	Thermal response of permeable side wall cylinder . . . . .	56
7.9	Pyrolysis gas blowing rate through surface of cylinder samples . . . . .	58
7.10	Residual $ \mathbf{R} $ contours for the cylinder case, using a permeable wall . . . . .	60
7.11	Inviscid flux $ \mathbf{G} $ for the cylinder case, using a permeable wall . . . . .	61
7.12	Computational geometries and boundary conditions for iso-Q case . . . . .	62
7.13	Heat flux and pressure distribution . . . . .	63
7.14	Heat flux and pressure boundary conditions ramping . . . . .	63

7.15	Pressure contours of impermeable side wall iso-Q sample . . . . .	64
7.16	Pressure contours of permeable side wall iso-Q sample . . . . .	64
7.17	Pressure contours with surface pressure distribution . . . . .	65
7.18	Gas mass transport of the impermeable side wall iso-Q sample . . . . .	65
7.19	Gas mass transport of the permeable side wall iso-Q sample . . . . .	66
7.20	Gas mass transport of pressure distribution iso-Q sample . . . . .	66
7.21	Pyrolysis gas blowing rate through surface of isoq samples . . . . .	67
8.1	Post-test photos of charring ablative articles with sample-holders . . . . .	72
8.2	Sample geometry and surface heat flux profile for samples <i>A</i> to <i>D</i> . . . . .	73
8.3	Computational grid for sample <i>C</i> , $(100 \times 20 + 150 \times 120) \times 2$ cells . . . . .	74
8.4	Geometry for samples <i>A</i> – to <i>D</i> – . . . . .	75
8.5	Temperature contours for sample <i>A</i> (Case 1.1), at various times . . . . .	77
8.6	Porosity contours for sample <i>A</i> (Case 1.1), at various times . . . . .	78
8.7	$ \dot{m} $ contours for sample <i>A</i> (Case 1.1), at various times . . . . .	79
8.8	Gas streamlines for sample <i>A</i> (Case 1.1), at various times . . . . .	80
8.9	Gas mass flow rate through the surface of iso-Q samples . . . . .	81
8.10	Temperature contours for sample <i>B</i> (Case 1.2), at various times . . . . .	83
8.11	Porosity contours for sample <i>B</i> (Case 1.2), at various times . . . . .	84
8.12	$ \dot{m} $ contours for sample <i>B</i> (Case 1.2), at various times . . . . .	85
8.13	Gas streamlines for sample <i>B</i> (Case 1.2), at various times . . . . .	86
8.14	Temperature contours for sample <i>C</i> (Case 1.3), at various times . . . . .	87
8.15	Porosity contours for sample <i>C</i> (Case 1.3), at various times . . . . .	88
8.16	$ \dot{m} $ contours for sample <i>C</i> (Case 1.3), at various times . . . . .	89
8.17	Gas streamlines for sample <i>C</i> (Case 1.3), at various times . . . . .	90
8.18	Temperature contours for sample <i>D</i> (Case 1.4), at various times . . . . .	91
8.19	Porosity contours for sample <i>D</i> (Case 1.4), at various times . . . . .	91
8.20	$ \dot{m} $ contours for sample <i>D</i> (Case 1.4), at various times . . . . .	92
8.21	Gas streamlines for sample <i>D</i> (Case 1.4), at various times . . . . .	92
8.22	Temperature contours for sample <i>A</i> – (Case 2.1), at various times . . . . .	94
8.23	Porosity contours for sample <i>A</i> – (Case 2.1), at various times . . . . .	94
8.24	$ \dot{m} $ contours for sample <i>A</i> – (Case 2.1), at various times . . . . .	95
8.25	Gas streamlines for sample <i>A</i> (Case 2.1), at various times . . . . .	95
8.26	Temperature contours for sample <i>B</i> – (Case 2.2), at various times . . . . .	97
8.27	Porosity contours for sample <i>B</i> – (Case 2.2), at various times . . . . .	98
8.28	$ \dot{m} $ contours for sample <i>B</i> – (Case 2.2), at various times . . . . .	99
8.29	Gas streamlines for sample <i>B</i> – (Case 2.2), at various times . . . . .	100
8.30	Temperature contours for sample <i>B</i> – (Case 2.3), at various times . . . . .	101
8.31	Porosity contours for sample <i>B</i> – (Case 2.3), at various times . . . . .	102
8.32	$ \dot{m} $ contours for sample <i>C</i> – (Case 2.3), at various times . . . . .	103
8.33	Gas streamlines for sample <i>C</i> – (Case 2.3), at various times . . . . .	104
8.34	Temperature contours for sample <i>D</i> – (Case 2.4), at various times . . . . .	105
8.35	Porosity contours for sample <i>D</i> – (Case 2.4), at various times . . . . .	105
8.36	$ \dot{m} $ contours for sample <i>D</i> – (Case 2.4), at various times . . . . .	106
8.37	Gas streamlines for sample <i>D</i> (Case 2.4), at various times . . . . .	106

8.38	Pyrolysis gas mass flow rate through surface at the stagnation point . . .	107
9.1	Geometry and thermocouples location of the iso-Q sample . . . . .	111
9.2	Illustration of boundary conditions and computational geometry . . . . .	111
9.3	Pressure and heat flux boundary condition . . . . .	112
9.4	Pyrolysis gas transport for Case 1 . . . . .	115
9.5	Pyrolysis gas transport for Case 2 . . . . .	115
9.6	Pyrolysis gas transport for Case 3 . . . . .	116
9.7	Pyrolysis gas transport for Case 4 . . . . .	116
9.8	Pyrolysis gas transport for Case 5 . . . . .	117
9.9	Pyrolysis gas transport for Case 6 . . . . .	117
9.10	Pyrolysis gas transport for Case 7 . . . . .	118
9.11	Temperature profiles at TC 1 . . . . .	119
9.12	Temperature profiles at TC 2 . . . . .	119
9.13	Temperature profiles at TC 3 . . . . .	120
9.14	Temperature profiles at TC 4 . . . . .	120
9.15	Temperature profiles at TC 5 . . . . .	120
9.16	Temperature profiles at TC 6 . . . . .	120
9.17	Temperature profiles at TC 7 . . . . .	120
9.18	Temperature profiles at TC 8 . . . . .	120
9.19	Temperature profiles at TC 9 . . . . .	120
9.20	Temperature profiles at TC 10 . . . . .	120

## LIST OF TABLES

6.1	Heat conduction problem parameters . . . . .	37
6.2	Grid parameters for temporal order of accuracy study . . . . .	38
6.3	Grid parameters for spatial order of accuracy study . . . . .	39
6.4	Flow through porous tube problem parameters . . . . .	42
6.5	Parameters for 1D TACOT heating problem . . . . .	45
6.6	Grid refinements and time step sizes for the convergence test . . . . .	46
6.7	Spatial orders of accuracy from the grid function convergence test . . . . .	46
7.1	Gas flow rate through the front and the side wall, for 3D cylinder cases . . . . .	58
7.2	Mass flow rate blowing from the front and the side wall, for iso-Q cases . . . . .	69
8.1	Geometric specifications for Case 1.1 to 1.4 . . . . .	72
8.2	Geometric specifications for Case 2.1 to 2.4 . . . . .	74
8.3	Initial and boundary conditions . . . . .	75
9.1	Coordinates of thermocouples in an iso-Q sample . . . . .	110

## Chapter 1 Introduction

With several space exploration missions announced in the past decade, the human presence is expanding fast beyond Earth. National Aeronautics and Space Administration (NASA) in United States has announced the plan for Orion Multi-Purpose Crew Vehicle (MPCV) in 2011, a manned spacecraft for missions to the Moon, Mars and asteroids. NASA also successfully launched three exploration rovers to Mars, two in 2004 and one in 2012. The unmanned spacecraft Hayabusa, launched by Japan Aerospace Exploration Agency (JAXA), landed on an asteroid and returned to Earth with samples in 2010. In these missions, Thermal Protection Systems (TPS) are essential to the atmospheric entry, for they protect the traveling vehicle from the severe heating during entry process. The material of choice for TPS is usually charring ablative, since it is effective and has light weight. Recent exploration missions have renewed the interest in modeling charring ablative materials, which initially started with the design of ballistic reentry weapon in the 1950s and the space race in the 1960s. Over the decades, computational material and thermal response programs have been important tools in the design and analysis of charring ablative TPS. However, most of the existing models were one-dimensional (1D) and developed in the 1960s. Due to the increasing challenge in future missions, there is a strong need to develop high-fidelity models for charring ablative TPS. This is important to ensure payload safety and reduce cost. In this dissertation, a versatile material response module that supports multidimensional models is developed, and the effects of pyrolysis gas transport within charring ablators are investigated.

## 1.1 Background

On August 6th, 2012, the Curiosity rover, carried by NASA's Mars Science Laboratory (MSL) spacecraft, landed successfully on the surface of Mars [1]. Thanks to the TPS that covered its blunt body, the spacecraft survived from the searing heat as it blazed through the Martian atmosphere. An artistic rendition of the entry is shown in Fig. 1.1. As a space capsule enters a planetary atmosphere at hypersonic speed, a

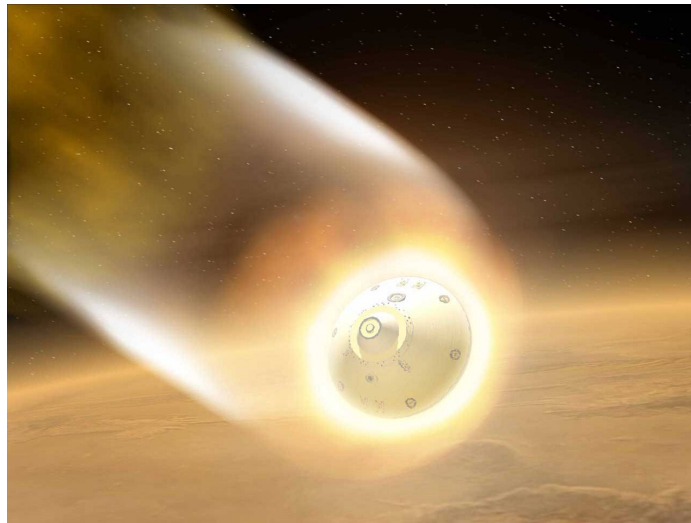


Figure 1.1: MSL spacecraft entering the Mars atmosphere (artist rendering) [2]

strong bow shock is formed in front of the forebody. Due to the friction, the vehicle decelerates rapidly, and a large amount of heat is generated and conveyed to the vehicle during the entry. This heating process is referred to as aerodynamic heating. TPS acts as a heat shield of the spacecraft, absorbs the excessive energy from aerodynamic heating and protects the payloads of the traveling vehicle. In general, TPS materials are categorized into two types: ablative and non-ablative. When heated, ablative materials undergo decomposition, vaporization, spallation, or other erosive processes that result in mass removal of the material. Ablative materials were applied on the TPS of NASA's Mercury, Gemini, and Apollo reentry capsules [3], as well as the recent Stardust sample return capsule [4,5] and the MSL spacecraft [6]. Non-ablative

materials experience little to no mass loss during the reentry process, and are often applied on lower orbit return vehicles. An example of non-ablative materials is the reusable ceramic tiles applied to the bottom of space shuttles. Non-ablative materials are usually reusable if none of the tiles are damaged. Ablative materials on the other hand, are usually expendable; they are also lighter and can sustain a much higher heat flux than non-ablative materials.

Ablative materials can be further classified into two subcategories: charring (or decomposing) and non-charring (or surface) ablators. When exposed to extreme heating, charring ablators undergo both surface erosion and in-depth decomposition; non-charring ablators erode, oxidize and sublimate only at or near the exposing surface. Examples of non-charring ablators are: metals, Teflon, graphite, and carbon-carbon [3]. Non-charring ablators usually have higher mechanical strength than charring ones. They are often applied to locations like stagnation point regions, nose cones, and drag flaps. For example, the material used on the leading edges of NASA's shuttle orbiters were non-charring ablators.

Charring ablators are typically applied on regions exposed to extreme heat flux, such as rocket nozzle linings and forebody surface of space shells. Some examples of charring ablators are: AVCOAT, carbon-phenolic, phenolic impregnated carbon ablator (PICA), PICA-X, etc. AVCOAT was the TPS material that used in Apollo missions, and it was also selected as the ablative material for the Orion MPCV. PICA is a modern TPS material that is more effective under high-peak-heating conditions [7], and has lower density than carbon-phenolic, which was used on Venus probes [8]. PICA was the TPS material for the MSL aeroshell that entered the Martian atmosphere [6], the heat shield of which is shown in Fig. 1.2. Another recent mission that used PICA was the Stardust sample return mission, which returned to Earth on January 15th, 2006. Entering the atmosphere at a velocity of 12.9 km/s, the Stardust sample return capsule (SRC) is the fastest man-made object that enters



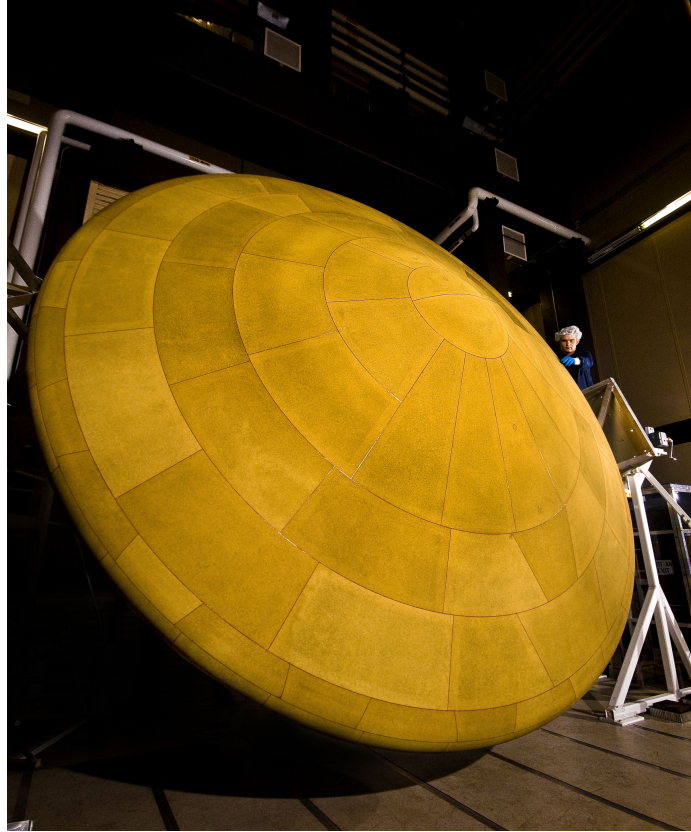


Figure 1.2: MSL aeroshell heat shield with PICA tiles (before mission) [9]

Earth atmosphere [5]. Figure 1.3 shows the photograph of the Stardust capsule after landed on the desert in Utah. Although the front surface was charred black, the shape of the aeroshell was well preserved.

Charring ablators consist of preform and resin materials. The preform material, such as carbon, silicon or quartz, is made in fiber form. The fibers are stacked by layers, forming a highly porous structure. This porous preform determines the structural strength of the ablator. Resin materials such as phenolic or nylon, are then impregnated into the preform. The charring ablative material in this state is referred as “virgin”. A scanning electron microscope (SEM) photography of a virgin charring ablative material is presented in Fig. 1.4. It is seen from the figure that the fibrous preform materials are randomly oriented and filled with flocculent resins.

The resin material decomposes when heated, losing mass and generating gas.



Figure 1.3: NASA's Stardust SRC after landing on the ground [10]

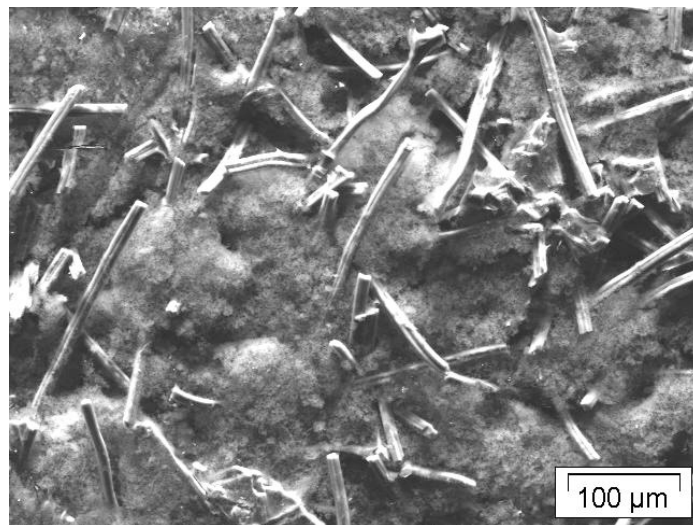


Figure 1.4: Micrograph of a virgin PICA surface [11]

This process is called pyrolysis, and the gas generated in the process is termed as pyrolysis gas. The resin materials not only decompose at the exposed material surface, but also from within, due to the temperature increase caused by the heat transfer. The generated pyrolysis gas builds up the inner pore pressure, which drives the gas to flow out of the material and into the reacting boundary layer, affecting surface

thermochemistry and momentum transport. When the resin is fully depleted, the material is charred and no more pyrolysis occurs.

The pyrolysis gas may consist of many species, depending on the resin formulation. As the gas flow through the material, these species react with each other and with the char and preform material. The effect of pyrolysis gas leaving residuals on the fiber surface is called “coking”. As depicted in Fig. 1.5: several fibers on the right half of the photo have added mass attached, even though the material is charred. In

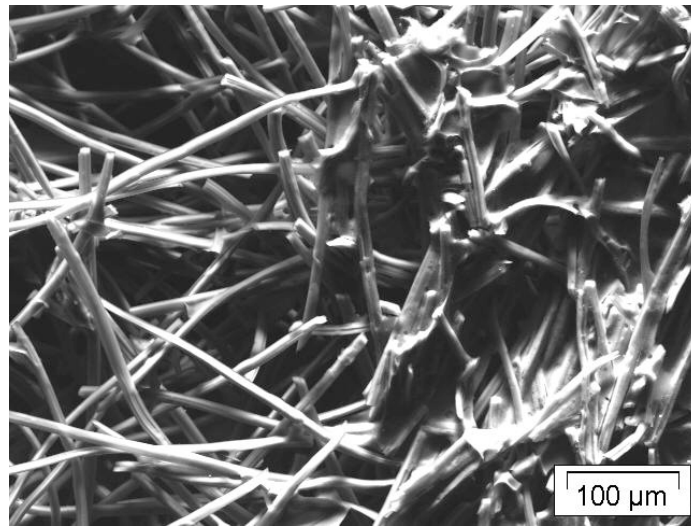


Figure 1.5: Micrograph of a char PICA surface [11]

addition to the coking effect, pyrolysis gas may also react with the char and remove mass through processes like oxidation, nitridation, etc. Moreover, when subjected to high thermal and mechanical stress, the char structure may break, and expel chunks of material from the surface. This effect is called spallation.

Compared to resins, preform materials barely react. Instead, they ablate (through oxidization, nitridation, sublimation, etc.) in a region near the surface. When preform fibers on the surface are depleted due to ablation, the ablators show surface recession. In addition, the preform may also lose mass from within the material, in which case oxygen penetrates inside the material and the material ablates from within [12].

The overall charring ablation process is illustrated in Fig. 1.6. In general, the

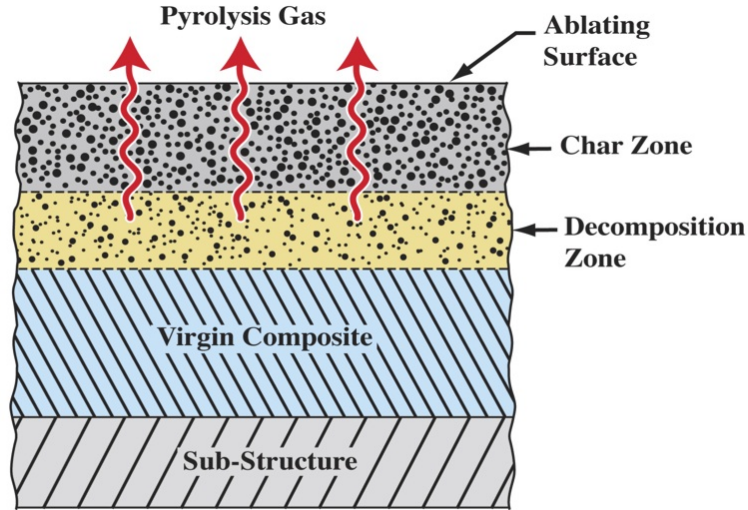


Figure 1.6: Illustration of charring ablative phenomena [3]

virgin and char zone have a constant solid density, while the pyrolysis (decomposition) zone has a changing density as the material decomposes. These zones except for the sub-structure are porous, allowing pyrolysis gas to flow within. The gas flow direction depends on the pressure gradient and the geometry of the material. The pyrolysis zone usually has a higher pressure than the pressure at the ablating surface, which leads to gas blowing out of the surface. However, the gas may also flow literally inside and exit through the sides, if they are permeable.

## 1.2 Extant work and research motivations

The earliest application of charring ablators can be traced back in the 1950s, when charring ablators were designed as heat shields for intercontinental ballistic missiles (ICBMs) [13], in order to survive the intense aerodynamic heating during the reentry process. Since then, ablative materials were found to be successful as the TPS for reentry capsules and rocket nozzles, which naturally stimulated research on the material. The development of charring ablators continued through a series of American human spaceflight missions: Project Mercury, Gemini, and Apollo. Aside from numerous experiments conducted in the period, computational modeling was found

useful in analyzing and predicting the behaviors of charring ablators, in terms of thermal and material response.

The most notable work in the 1950s and 1960s was the Charring Material Ablation (CMA) program. Developed by Aerotherm – one of NASA’s contractors in the period – CMA has served as a prototype of simulation and design tool for half a century. Moyer and Rindal [14] described the charring phenomena and the models used in CMA thoroughly. The 1D program CMA solved the energy balance by considering heat conduction and internal thermal decomposition (due to the generation of pyrolysis gas), as well as a simple mass conservation. The decomposition model in CMA was a three components model based on Arrhenius law. Note that the three components in this model were not chemical species; instead, the model was based on the fact that phenolic pyrolysis underwent a two stage decomposition during experimental observations [15]. Two out of the three components accounted for the decomposing resins and the last component represented the preform material. Since this model is based on observation rather than chemistry, it is often termed as a phenomenological model, and is still seen in most of the modern ablation programs. The pyrolysis gas species were assumed to be in chemical equilibrium and not reacting with char. Another major assumption was that the pyrolysis gas was assumed to leave the material surface as soon as it was generated from within, which inherently neglected the gas momentum balance. The ablation model in CMA used a node dropping algorithm. The idea of this technique is to move the computational nodes at the same speed with the recessing surface; the node that moves out the back wall is dropped and the node adjacent to the wall is resized. In terms of an equation discretization, CMA adopted an economical implicit finite difference formulation, which saved computation time but compromised accuracy.

Aside from the 1D work by Moyer and Rindal [14], it is worth noting that several multidimensional attempts were made during this period of time. Hurwicz et.

al. [16] emphasized multidimensional effects in ablation problems by comparing two-dimensional (2D) and three-dimensional (3D) results with 1D results on ablative wing leading edge problems. Differences found between multidimensional and 1D analysis were attributed to the effect of geometry, but the pyrolysis effects were not modeled. Another multidimensional attempt in the mid 1960s was made by Friedman and McFarland [17]. Their 2D-ABLATE program used a finite difference method to simulate the rocket engine thrust chamber ablation, which was verified through code-to-code comparison and experimental works. The surface recession and in-depth charring were modeled. Moreover, the thermal conductivity of the material was modeled as anisotropic with different values in axial and radial direction. The in-depth pyrolysis effects were modeled using mass flux, which was equivalent to gas mass balance; however the gas momentum was not solved. April, Pike and Valle [18–20] attacked the problem from another angle, by modeling the equilibrium, non-equilibrium, and frozen pyrolysis gas flow, in order to determine the gas composition and the energy transfer associated with the reacting pyrolysis gas flow. The model allowed the gas species to react among each other and with the char material, using finite rate chemistry data for a temperature range of 533–1925 K. However, the change in pyrolysis gas composition using non-equilibrium analysis was small, in the temperature range 533-1644 K [18].

Due to the shift in focus from human spaceflight to space shuttle missions in the 1980s, not much work on charring ablative materials was published in the 1980s and 1990s. However, a series of publications on ICBM by Blackwell and Hogan from Sandia National Laboratories is worth mentioning in that period of time, for they updated many numerical schemes used in CMA [21–24]. A control volume finite element method (CVFEM) was applied as the computational framework to replace the finite difference discretization in CMA. An exponential differencing was implemented to allow for a more accurate interpolation of temperature based properties. Moreover,

a 1D grid contracting scheme was proposed, in which the number of cells was fixed and the cell sizes were proportionally shrunk as the surface recessed. This new grid scheme suited CVFEM better than the grid-dropping scheme used in CMA, and was less complex. Amar adopted the CFVEM and grid contracting scheme in his master thesis, as well as in his publications in the following years [3, 25–27], in which models were verified with solution accuracy studies. A code-to-code comparison was performed against CMA where good agreements were shown; but more importantly, solution accuracy and efficiency was greatly enhanced. Amar’s recent work in NASA’s Johnson Space Center can be found in Ref. [28], where a 3D charring ablative solver was developed and verified.

Another body of works started in the mid 1990s was performed by researchers at the University of Tennessee at Knoxville. Their major focus was on modeling compressible flow within variable permeability media, which was directly applicable to pyrolysis flow within charring ablators. In Ref. [29], a modified mass conservation of gas was solved by replacing velocity terms with Darcy’s law, where material properties and temperature were assumed to be constants. Keyhani and Polehn [30] modeled 2D flows in anisotropic materials, where gas mass conservation was coupled with an energy equation. It was also reviewed by Amar [3] that, Keyhani and Polehn’s work showed significant different pore pressures using loosely and fully coupled solutions, but the temperatures were relatively close. The recent works performed by this group were on developing physical-based calibration methods that measures temperature, heat flux and thermophysical properties [31–33].

The ablation programs in NASA’s Ames research center in late 1990s were developed by Chen and Milos [34]. Based on the models in CMA, a 1D code was first developed and called the Fully Implicit Ablation and Thermal response program (FIAT). The major upgrade was to apply a fully implicit technique that stabilized the solution procedure and allowed a wider range of problems. It should be noted that

FIAT had been used for sizing calculations on many NASA space missions, including Stardust and Mars Pathfinder. The 1D assumption was based on the fact that the nose radius of a capsule shape reentry vehicle is relatively large when compared to the depth of charring. However, it might not be valid for slender hypersonic vehicles and arc-jet test models, where nose radius is comparable to the scale of charring. In addition, the heat transfer from sidewalls contributed to in-depth heating, which requires multidimensional consideration. Therefore, Chen and Milos developed a 2D code called the Two-dimensional Implicit Thermal response and Ablation program (TITAN) [35]. TITAN solved an energy balance as the governing equation with the three components decomposition model, while the pyrolysis gas effects were neglected. This program was integrated with a CFD solver to perform energy coupled fluid-solid simulations. Other coupling studies using TITAN can be found in Ref. [36,37]. A 3D ablation program was also developed in this group and called the Three-Dimensional Finite-volume alternating directional Implicit Ablation and Thermal response code (3dFIAT) [38]. Not only was the number of dimensions increased, but the numerical algorithm used in 3dFIAT was also different from TITAN. In the publication, 3dFIAT only solved for the energy equation, with additional terms accounting for pyrolysis energy-consumption and energy convected by pyrolysis; the gas mass and mass momentum equations were not solved. More recently, a multi-block moving grid system and an orthotropic thermal conductivity model were added in 3dFIAT [39]. The models were validated using arc jet experiments on PICA and the program predictions agreed well with thermocouple data. With these ablation programs, Chen and Milos simulated the Orion crew module and compared 3D results with 1D predictions at selected locations [40]. It was shown in the paper that multidimensional effects were insignificant, regarding surface recession, but under-predicted the bond line temperature at the shoulder region. An improved 1D model was proposed to take into account the variation of cross sectional area with depth from the surface.



Milos and Chen also improved the property model of PICA through validations [41]. The new PICA properties data, which was designed to be use with the model implemented in FIAT and TITAN, featured orthotropic and pressure dependent thermal conductivity models. For recent studies by this group, the non-equilibrium and the Darcy-Forcheimer effects of pyrolysis flow were investigated using FIAT [42], and the effect of a non-equilibrium gas surface interaction model was studied by loosely coupling a flow solver with TITAN [43].

In the early 2000s, the majority of research on modeling charring ablative materials in Japan was published by researchers at Tohoku University and the Japan Aerospace Exploration Agency (JAXA) [8, 44–46]. The 1D ablation program developed was called Super Charring Material Ablation (SCMA), which was based on Aerotherm’s CMA. The major improvement in SCMA was the modeling of pyrolysis gas motions by solving gas mass and momentum conservation. The momentum equation was proposed as a 1D Euler equation in porous scale with extra source terms, which accounted for frictional and inertial effects. The frictional source and inertial source were derived from Darcy’s law and Forcheimer’s law, respectively. SCMA showed satisfactory results on predicting the surface temperature and recession for two ground tests [47, 48] and the Pioneer-Venus probe flight case [47]. It was experimentally validated through a set of ablating samples in JAXA’s arc-heated wind tunnel [46]. The decomposition model was a curve-fit, four-stage expression which was based on thermogravimetry data for the resin, which was different from the two-stage model used in CMA. Gas pressure was measured within the ablative material and their 1D model predicted a much higher (one order of magnitude higher) pressure than the measured results. This discrepancy was attributed to the delamination, or the phenomenon of a huge chunk breaking from the material. They suggested that the delamination lead to pyrolysis gas leakage from the sidewalls of the sample, which brought down the gas pressure within. In a technical note earlier published by the

same group, gas permeability of an ablator was found to vary significantly, depending on the resin density and lamination angles of the cloth layers [44]. This work, as well as the observed side leaking effects facilitated the 2D development of their computer program, presented in Ref. [45], where SCMA was extended to 2D and named as SCMA2. Initially, the side wall boundary condition of SCMA2 was assumed to be an adiabatic wall, but 2D effects were still found: the centerline pressure was found to be one-third of that in 1D simulation. Later, SCMA2 was coupled with a non-equilibrium CFD solver [49] and the side wall heating effects were investigated [50,51]. However, due to the instability of the solution, the momentum equation was removed from the analysis. More recently, nitradation reactions on graphite surface in ICP wind tunnel were studied and also loosely coupled with SCMA2 [52, 53]. In terms of the ablation model, only heat conduction and shape change were modeled. The recent Hayabusa sample return mission encouraged further research works, including a prediction accuracy study [54] and a post flight analysis by loosely combining an axisymmetric non-equilibrium CFD solver, a radiative heat transfer analysis code, and an ablation thermal response code [55]. Another set of works conducted by Japanese researchers other than JAXA can be found in Ref. [56,57], where the unsteady effect of pyrolysis gas flow was modeled in 2D axisymmetric coordinates.

Recently, a set of high-fidelity study of ablative materials was performed by Lachaud et. al. [12, 58–70]. With several conservative assumptions removed, the state-of-art pyrolysis-ablation models were revisited. For instance, the oxidation of preform materials was studied and modeled from microscopic to macroscopic scales. The multi-scale models were based on experimental measurements, scanning electron microscope (SEM) observations and pore scale numerical simulations [58–64]. Due to the increasing complexity of the models, a computational toolbox was developed as a testbed for new pyrolysis and ablation models. This toolbox was based on OpenFOAM, an open source CFD software, which took care of the equation discretization

and numerical algorithms [12, 65, 68].

Concurrently, researchers in University of Kentucky went through a similar pattern: a toolbox called Kentucky Aerodynamic and Thermal-response System (KATS) was developed. KATS was also based on an open source CFD software, called freeCFD [71]. It handled the numerical algorithms, including equation discretization, domain decomposition, gradients calculation, parallelization, etc. A separate charring ablation module was developed based on this system [72, 73]. The program modeled decomposition of resins, unsteady pyrolysis gas transport in 3D and showed good agreement to a validated material response code [74]. Initial success was found for coupling the material response module with the CFD module [75], the parallel efficiency of which was studied by Zhang et. al. [76]. In addition, spallation was modeled by one-way coupling a finite rate chemistry code with the CFD module in KATS by Davuluri and Martin [77]. Pyrolysis gas chemistry models and volume averaged carbon oxidation models were developed by Martin et. al [70, 78–81].

Due to the increasing strength in computer powers and need for high-fidelity models in recent space exploration missions, it is possible and necessary to extend the heritage 1D ablation models to multidimensional. Although much multidimensional work has been carried out in the past decade, the pyrolysis gas transport were omitted in most of the developed material response codes. The few exceptions used simple assumptions on material properties, which were far from reality. Since pyrolysis gas blowing is crucial to the accurate modeling of boundary conditions, it is necessary to model the pyrolysis gas flow within a charring ablator. Therefore in this work, a multidimensional pyrolysis gas transport model is developed for orthotropic charring ablators; in addition, several effects due to the gas flow are found to be significant and presented in this study.

As the computational framework used in this work, KATS has two major modules: a fluid dynamic module and a material response module. The two modules were

developed individually at the University of Kentucky. The material response module was developed by the author, as is presented in the dissertation. There were several successful fluid/solid couplings between the two modules [75], but the discussion of the coupling is omitted in this work.

## Chapter 2 Computational Framework

The computational framework of KATS is introduced in this chapter. It includes a general formulation of the governing equation, a derivation of the equation discretization, the resultant discretized equation, and applied numerical schemes.

### 2.1 Finite volume method

The KATS is based on finite-volume method (FVM). For FVM in general, the governing equations can be written in the following conservation form:

$$\frac{\partial \mathbf{Q}}{\partial t} + \nabla \cdot (\mathbf{F} - \mathbf{F}_d) = \mathbf{S}, \quad (2.1)$$

where  $\mathbf{Q}$  is the vector of conservative variables,  $\mathbf{F}$  and  $\mathbf{F}_d$  are matrices of convective and diffusive fluxes, and  $\mathbf{S}$  is the vector of sources. Applying spatial integration over a control volume yields:

$$\frac{\partial}{\partial t} \int_V \mathbf{Q} dV + \int_V \nabla \cdot (\mathbf{F} - \mathbf{F}_d) dV = \int_V \mathbf{S} dV.$$

where divergence theorem is then applied:

$$\frac{\partial}{\partial t} \int_V \mathbf{Q} dV + \int_A (\mathbf{F} - \mathbf{F}_d) \cdot \mathbf{n} dA = \int_V \mathbf{S} dV. \quad (2.2)$$

Removing the integral sign by assuming the control volume is sufficiently small, Eq. (2.2) becomes:

$$\begin{aligned} \frac{\partial}{\partial t}(\mathbf{Q}V) + \sum_{\text{faces}} (\mathbf{F} - \mathbf{F}_d) \cdot \mathbf{n}A &= \mathbf{S}V, \\ \text{or, } \frac{\partial}{\partial t}(\mathbf{Q}V) &= - \sum_{\text{faces}} (\mathbf{F} - \mathbf{F}_d) \cdot \mathbf{n}A + \mathbf{S}V. \end{aligned} \quad (2.3)$$

The right hand side of Eq. (2.3) is designated as **RHS**, such that,

$$\mathbf{RHS} \equiv - \sum_{\text{faces}} (\mathbf{F} - \mathbf{F}_d) \cdot \mathbf{n}A + \mathbf{S}V. \quad (2.4)$$

Equation (2.3) can then be written as the following:

$$V \frac{\partial \mathbf{Q}}{\partial t} = \mathbf{RHS}, \quad (2.5)$$

where the control volume is assumed to be constant. To solve for primitive variables, chain rule is applied:

$$V \frac{\partial \mathbf{Q}}{\partial \mathbf{P}} \frac{\partial \mathbf{P}}{\partial t} = \mathbf{RHS}. \quad (2.6)$$

Using implicit backward Euler method, the temporal derivative is discretized as:

$$V \left. \frac{\partial \mathbf{Q}}{\partial \mathbf{P}} \right|_{(i,j,k)}^{(n)} \frac{\mathbf{P}_{(i,j,k)}^{(n+1)} - \mathbf{P}_{(i,j,k)}^{(n)}}{\Delta t} = \mathbf{RHS}_{(i,j,k)}^{(n+1)}, \quad (2.7)$$

where the superscript denotes the time step and the subscripts denote spatial indices. Since  $\mathbf{RHS}$  contains a summation of face fluxes, which are functions of  $\mathbf{P}_{(i,j,k)}$ ,  $\mathbf{P}_{(i-1,j,k)}$ ,  $\mathbf{P}_{(i+1,j,k)}$ ,  $\mathbf{P}_{(i,j-1,k)}$ ,  $\mathbf{P}_{(i,j+1,k)}$ ,  $\mathbf{P}_{(i,j,k-1)}$ , and  $\mathbf{P}_{(i,j,k+1)}$ , the right hand side of Eq. (2.7) can be approximated as:

$$\begin{aligned} \mathbf{RHS}_{(i,j,k)}^{(n+1)} &\approx \mathbf{RHS}_{(i,j,k)}^{(n)} + \left. \frac{\partial \mathbf{RHS}}{\partial \mathbf{P}} \right|_{(i,j,k)}^{(n)} \Delta \mathbf{P}_{(i,j,k)} \\ &+ \left. \frac{\partial \mathbf{RHS}}{\partial \mathbf{P}} \right|_{(i-1,j,k)}^{(n)} \Delta \mathbf{P}_{(i-1,j,k)} + \left. \frac{\partial \mathbf{RHS}}{\partial \mathbf{P}} \right|_{(i+1,j,k)}^{(n)} \Delta \mathbf{P}_{(i+1,j,k)} \\ &+ \left. \frac{\partial \mathbf{RHS}}{\partial \mathbf{P}} \right|_{(i,j-1,k)}^{(n)} \Delta \mathbf{P}_{(i,j-1,k)} + \left. \frac{\partial \mathbf{RHS}}{\partial \mathbf{P}} \right|_{(i,j+1,k)}^{(n)} \Delta \mathbf{P}_{(i,j+1,k)} \\ &+ \left. \frac{\partial \mathbf{RHS}}{\partial \mathbf{P}} \right|_{(i,j,k-1)}^{(n)} \Delta \mathbf{P}_{(i,j,k-1)} + \left. \frac{\partial \mathbf{RHS}}{\partial \mathbf{P}} \right|_{(i,j,k+1)}^{(n)} \Delta \mathbf{P}_{(i,j,k+1)}, \end{aligned} \quad (2.8)$$

where  $\Delta \mathbf{P} = \mathbf{P}^{(n+1)} - \mathbf{P}^{(n)}$ . Substitute Eq. (2.8) into Eq. (2.7) and combine  $\Delta \mathbf{P}_{(i,j,k)}$ s, while omitting the subscripts  $(i,j,k)$  and superscript  $(n)$ :

$$\begin{aligned} &\left[ \frac{V}{\Delta t} \frac{\partial \mathbf{Q}}{\partial \mathbf{P}} - \frac{\partial \mathbf{RHS}}{\partial \mathbf{P}} \right] \Delta \mathbf{P} - \left. \frac{\partial \mathbf{RHS}}{\partial \mathbf{P}} \right|_{(i-1,j,k)} \Delta \mathbf{P}_{(i-1,j,k)} \\ &- \left. \frac{\partial \mathbf{RHS}}{\partial \mathbf{P}} \right|_{(i+1,j,k)} \Delta \mathbf{P}_{(i+1,j,k)} - \dots - \left. \frac{\partial \mathbf{RHS}}{\partial \mathbf{P}} \right|_{(i,j,k+1)} \Delta \mathbf{P}_{(i,j,k+1)} = \mathbf{RHS}, \end{aligned} \quad (2.9)$$

where  $1 \leq i < i_{max}$ ,  $1 \leq j < j_{max}$ , and  $1 \leq k < k_{max}$ .

Applying Eq. (2.9) to all of the control volumes in the computational domain forms a large linear system:

$$\mathbf{M}\Delta\mathbf{P} = \mathbf{RHS} \quad (2.10)$$

where  $\mathbf{M}$  is a block band matrix. This linear system is solved at each time step via PETSc library [82].

### Jacobian Matrices

The first Jacobian matrix  $\frac{\partial\mathbf{Q}}{\partial\mathbf{P}}$  in Eq. (2.9) is calculated analytically. The complete matrix for charring ablation problems is given in Appendix A. The rest of the Jacobian matrices in Eq. (2.9), or  $\frac{\partial\mathbf{RHS}}{\partial\mathbf{P}}$  at different locations, are obtained numerically via forward difference:

$$\frac{\partial\mathbf{RHS}}{\partial\mathbf{P}} \approx \frac{\mathbf{RHS}(\mathbf{P} + \Delta\mathbf{P}) - \mathbf{RHS}(\mathbf{P})}{\Delta\mathbf{P}}, \quad (2.11)$$

where the perturbation  $\Delta\mathbf{P}$  is as small as the smallest positive floating-point number in double precision.

### Convective flux

The numerical scheme used to calculate the convective flux  $\mathbf{F}$  in the FVM formula is AUSM+-up (Advection Upstream Splitting Method) [83]. AUSM+-up is an upwind approach that capable of solving for all speed-regimes and multiphase flow. It features accurate shock capturing and contact discontinuities. Although the pyrolysis gas flow regime is subsonic (no shock within the material), there is a separation of flow along the pyrolysis front. Therefore, AUSM+-up is selected as the inviscid flux function (without using flux limiters) for solving the conservation equations in this study.

## 2.2 Parallel computing

The idea of parallel computing is to speed up the computational speed by dividing the problem into many subproblems, and distributing them to different processors, while solving them at the same time. In KATS, the computational domain is decomposed to  $np$  subdomains through ParMETIS [84], where  $np$  stands for number of processors. The domain is evenly divided, in the sense that the number of cells in each subdomains are equal, except for the last processor which takes the remainder of the division. Figure 2.1 illustrates how the domain is divided according to the number of processors. The large sparse linear system, represented by Eq. (2.9), is solved on each processor

**Computational domain ( $np = 4$ )**

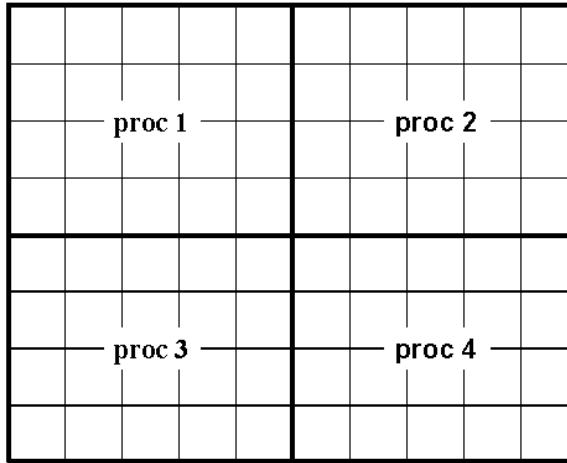


Figure 2.1: Illustration of an example of the domain decomposition method

for each subdomain. Boundary faces shared by two adjacent subdomains are named as partition faces in the KATS computer code. The partition faces are treated like a boundary: the information of ghost cells, as shown in Fig. 2.2, are exchanged at the partition face by the end of each time step. The exchanging of cell information is accomplished by Message Passing Interface (MPI).



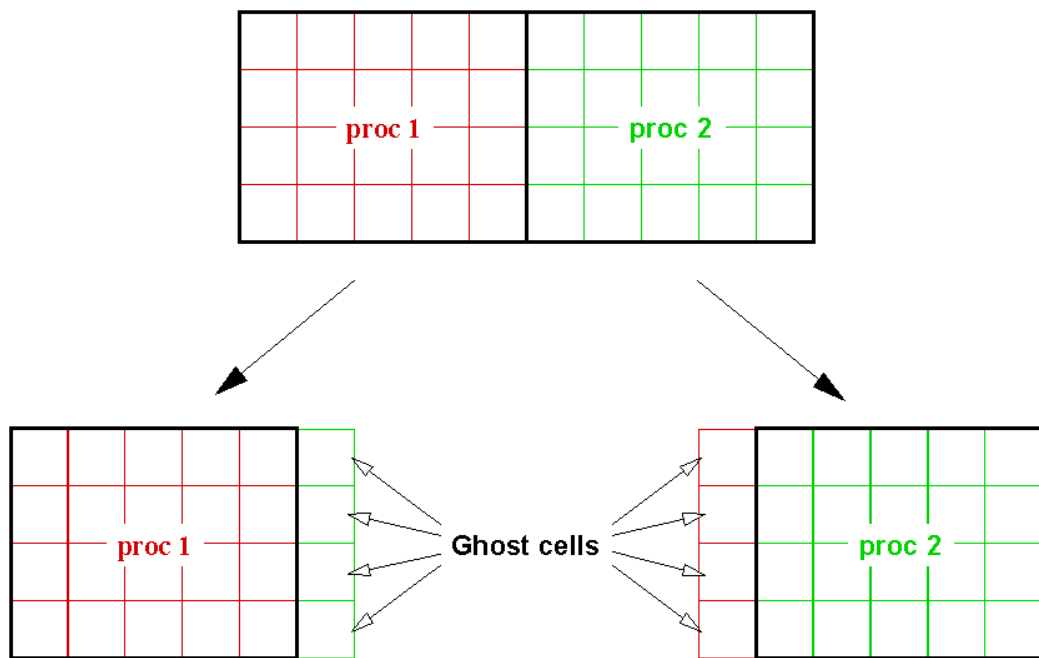


Figure 2.2: Illustration of example ghost cells in the domain decomposition method

## Chapter 3 Governing Equations

The governing equations of the material response module in KATS depend on the problem of concern. For instance, if a transient heat conduction is considered, only one energy equation will be solved in the system; but for a charring problem, the module might solve up to eight equations. The number of equations and models are controlled in the input deck of the computer program. An example of input deck is attached in the Appendix B.

In general, the governing equations consist of mass, momentum, and energy conservation. For charring ablation problems, the conservation equations are for pyrolysis gas mass, solid material mass, pyrolysis gas momentum and mixture energy. The derivations of these equations are given in Appendix C. The vectors and matrices in terms of Eq. (2.1), are presented as:

$$\frac{\partial \mathbf{Q}}{\partial t} + \nabla \cdot (\mathbf{F} - \mathbf{F}_d) = \mathbf{S}, \quad (2.1 \text{ revisited})$$

$$\mathbf{Q} = \begin{pmatrix} \phi \rho_{g_1} \\ \vdots \\ \phi \rho_{g_{ngs}} \\ \rho_{s_1} \\ \vdots \\ \rho_{s_{nss}} \\ \phi \rho_g u \\ \phi \rho_g v \\ \phi \rho_g w \\ \phi E_g + E_s \end{pmatrix}, \quad \mathbf{P} = \begin{pmatrix} p_1 \\ \vdots \\ p_{ngs} \\ \rho_{s_1} \\ \vdots \\ \rho_{s_{nss}} \\ u \\ v \\ w \\ T \end{pmatrix}, \quad \mathbf{S} = \begin{pmatrix} \omega_{g_1} \\ \vdots \\ \omega_{g_{ngs}} \\ \omega_{s_1} \\ \vdots \\ \omega_{s_{nss}} \\ D_x \\ D_y \\ D_z \\ S_D \end{pmatrix}, \quad (3.1)$$

$$\mathbf{F} = \begin{pmatrix} \phi\rho_{g_1}u & \phi\rho_{g_1}v & \phi\rho_{g_1}w \\ \vdots & \vdots & \vdots \\ \phi\rho_{g_{ngs}}u & \phi\rho_{g_{ngs}}v & \phi\rho_{g_{ngs}}w \\ 0 & 0 & 0 \\ \vdots & \vdots & \vdots \\ 0 & 0 & 0 \\ \phi\rho_g u^2 + p & \phi\rho_g uv & \phi\rho_g uw \\ \phi\rho_g uv & \phi\rho_g v^2 + p & \phi\rho_g vw \\ \phi\rho_g uw & \phi\rho_g vw & \phi\rho_g w^2 + p \\ \phi\rho_g uH & \phi\rho_g vH & \phi\rho_g wH \end{pmatrix}, \quad \mathbf{F}_d = \begin{pmatrix} \vdots & \vdots & \vdots \\ \mathbf{0} & & \\ \vdots & \vdots & \vdots \\ F_{cond,x} & F_{cond,y} & F_{cond,z} \end{pmatrix}, \quad (3.2)$$

where  $ngs$  is number of gas species,  $nss$  is number of solid species,  $\phi$  is porosity,  $\omega_s$  are reaction rates of the species,  $D_s$  are source terms that accounts for diffusive effects of porous structure in the momentum equation,  $S_D$  is diffusive source in the energy equation, and  $\mathbf{F}_{cond} = (F_{cond,x}, F_{cond,y}, F_{cond,z})$  represents conductive heat flux. The  $D_s$  and  $S_D$  are related with gas transport models, which is discussed in Section 5.4. The formulation of  $\mathbf{F}_{cond}$  is based on mixture energy models, as described in Section 5.5.

## Chapter 4 Boundary Conditions

As part of the input, the boundary condition (BC) type is required to be specified in KATS. For the material response module, three types are most frequently used: wall, symmetry, and outlet. Each type will be discussed in the following sections. In addition to these common types, two special thermal boundary conditions are introduced in the last two sections.

### 4.1 Wall BC

The wall BC in KATS assumes non-diffusion of species (zero mass flux) at the boundary. It offers two kinds of velocity condition: slip BC and no-slip BC. Slip BC is for inviscid flow and non-slip BC is for viscous flow. In either case, the normal gas velocity is zero due to the impermeable wall. The tangential velocity is assigned to be zero for non-slip BC. For slip BC, it is calculated to satisfy zero gradient at the wall. In terms of thermal condition, wall BC can be chosen from one of the two options: fixed temperature or fixed heat flux. The fixed temperature and fixed heat flux BCs correspond to Dirichlet and Neumann conditions, respectively. For ablation problems, wall BC is often assigned on the interface between charring ablator and non-reacting substructure.

### 4.2 Symmetry BC

For symmetry BC, every primitive variable has zero gradient at the boundary. Therefore, symmetry BC is a Neumann type. It is usually assigned to planes of symmetry.

### 4.3 Outlet BC

The outlet BC in the material response module of KATS is programmed to handle the exposing (usually heated) surface of charring ablators. Note that it is different from the concept of outlet/exit/non-reflecting BC in CFD, which assumes the flow leaving this boundary is not affecting the interior domain. For the outlet BC in this work, gas species are allowed to travel across the boundary. In addition, flow velocity, species densities, and static pressure can be specified at the boundary. Finally, either temperature or heat flux has to be specified on the boundary.

### 4.4 Aerodynamic heat BC

The aerodynamic BC is a special thermal BC that calculates the penetrated heat flux for the outlet BC. The modeled fluxes can be applied together or individually, including aerodynamic heat flux, radiation heat flux, energy flux due to ablation and pyrolysis gas blowing, as respectively given by:

$$\dot{q}_{pen}'' = \dot{q}_{ah}'' - \epsilon\sigma(T^4 - T_\infty^4) - \dot{m}_s''h_w - \dot{m}_g''h_w \quad (4.1)$$

where  $h_w$  is the gas enthalpy at the wall, and is obtained by a three-variable interpolation in a surface thermochemistry table. The interpolation requires pressure, pyrolysis gas blowing rate, and wall temperature as inputs. The details of the interpolation procedure can be found in Appendix C of Ref. [3].

The aerodynamic heat flux  $\dot{q}_{ah}''$  in Eq. (4.1) is given by:

$$\dot{q}_{ah}'' = (\rho_e u_e C_{h_0}) \left( \frac{C_h}{C_{h_0}} \right) (h_r - h_w), \quad (4.2)$$

where  $\rho_e u_e C_{h_0}$  is the heat transfer coefficient,  $\rho_e$  is the gas density obtained at the boundary layer edge,  $u_e$  is the boundary layer edge velocity,  $C_{h_0}$  is the uncorrected Stanton number,  $C_h/C_{h_0}$  is the correction factor to the Stanton number, and  $h_r$  is the recovery enthalpy. Here,  $\rho_e u_e C_{h_0}$ ,  $u_e$ , and  $h_r$  are input parameters for the

aerodynamic heat flux BC. In addition, the pressure  $p$  at the boundary is also required, since it is one of the inputs for the interpolation of  $h_w$ . Note that, for 2D or 3D geometry, the surface pressure  $p$  and the heat transfer coefficient  $\rho_e u_e C_{h_0}$  could be nonuniform in space and time. The nonuniform profiles are usually obtained via CFD simulations. The Stanton number correction factor is the product of a hot wall and a blowing corrections:

$$\frac{C_h}{C_{h_0}} = \Omega_{hw} \Omega_{blw}. \quad (4.3)$$

These two corrections are discussed in the following subsections.

### Hot wall correction

The hot wall correction has two expressions, depending on whether the surrounding flow is laminar or turbulent. If the flow is laminar, the correction factor is given by Cohen and Reshotko [85]:

$$\Omega_{hw} = \left( \frac{\rho_{hw} \mu_{hw}}{\rho_{cw} \mu_{cw}} \right)^{0.1}, \quad (4.4)$$

where the subscript  $hw$  and  $cw$  are for properties obtained at hot wall and cold wall conditions, respectively. The hot wall condition refers to the heated surface calculated in the material response solver. The cold wall condition is the wall condition assumed in the precede CFD simulation.

For turbulent flow, the correction factor is based on Eckert and Drake [86]

$$\Omega_{hw} = \left( \frac{\mu_{hw}^*}{\mu_{cw}^*} \right)^{0.2} \left( \frac{\rho_{hw}^*}{\rho_{cw}^*} \right)^{0.8}, \quad (4.5)$$

where the properties with superscript  $*$  are interpolated by the following reference enthalpies:

$$h_{hw}^* = 0.5(h_e + h_{hw}) + 0.11ru_e^2, \quad (4.6)$$

$$h_{cw}^* = 0.5(h_e + h_{cw}) + 0.11ru_e^2, \quad (4.7)$$

where the boundary layer edge enthalpy is:

$$h_e = h_r - r \frac{u_e^2}{2}, \quad (4.8)$$

and the recovery factor is given by:

$$r = \text{Pr}_{hw}^{1/3}. \quad (4.9)$$

### Blowing correction

The blowing correction is based on an empirical study by Kays and Crawford [87]:

$$\Omega_{blw} = \frac{\Phi}{e^\Phi - 1}, \quad (4.10)$$

where

$$\Phi = 2\lambda \frac{\dot{m}''}{\rho_e u_e C_{h0}}, \quad (4.11)$$

The blowing reduction parameter  $\lambda$  is 0.5 for laminar flow and 0.4 for turbulent.

### 4.5 Penetrated heat BC

As opposed to the aerodynamic heating BC, the penetrated heat BC models the effective heat that directly applied to the material, rather than the heat transmitted from the flow field. Therefore, the surface energy balance, or Eq. (4.2) is not solved [88]; instead, the value of  $\dot{q}_{ah}''$  in Eq. (4.2) is explicitly given. This type of BC is preferred for parametric problems with specific focus on the models other than the ones come with the aerodynamic heating BC. With this approach, there is no need to take into account the surface phenomena, such as re-radiation (Stefan-Boltzmann law) and surface catalysis, since the given heat flux is the end result of these phenomena. For the same reason, the boundary layer corrections (hot wall and blowing corrections) mentioned in Section 4.4 are unnecessary.

The value of the penetrated heat flux can be specifically chosen so that no near-surface ablation occurs, since the modeling of near-surface ablation requires the use of complex surface models, whether it is finite-rate chemistry [89] or aerothermodynamic equilibrium tables [90]. The chosen heat flux is usually significantly lower than the ones reported in CFD analysis, due to the fact that the boundary layer corrections (which result in heat flux reduction) are not applied.



## Chapter 5 Material Models

### 5.1 Material properties models

Charring ablative material consists of virgin, decomposition (pyrolysis) and char zone, as was shown in Fig. 1.6. The virgin and char properties are obtained through experimental measurements. The properties in the decomposition zone are modeled by interpolation between virgin and char properties. The interpolation is characterized by degree of char  $\beta$ , which is a function of local solid density:

$$\beta = \frac{\rho_v - \rho_s}{\rho_v - \rho_c}. \quad (5.1)$$

The solid properties including porosity  $\phi$ , permeability  $K$ , and radiation emissivity  $\epsilon$ , are interpolated using  $\beta$ :

$$\phi = (1 - \beta)\phi_v + \beta\phi_c, \quad (5.2)$$

$$K = (1 - \beta)K_v + \beta K_c. \quad (5.3)$$

For the thermal properties of the pyrolyzing material, including heat capacity  $c_{p,s}$ , thermal conductivity  $k_s$ , and solid enthalpy  $h_s$ , they are interpolated as:

$$c_{p,s}(T) = \frac{(1 - \beta)\rho_v}{\rho_s}c_{p,v}(T) + \frac{\beta\rho_c}{\rho_s}c_{p,c}(T), \quad (5.4)$$

$$k_s(T) = \frac{(1 - \beta)\rho_v}{\rho_s}k_v(T) + \frac{\beta\rho_c}{\rho_s}k_c(T), \quad (5.5)$$

$$h_s(T) = \frac{(1 - \beta)\rho_v}{\rho_s}h_v(T) + \frac{\beta\rho_c}{\rho_s}h_c(T). \quad (5.6)$$

### Orthotropic material model

Charring ablative materials often possess different transport properties in different directions of concern [91]. This anisotropic behavior is due to the orientation of fibers in microscopic scale [92]. For instance, carbon preforms are manufactured by laying

carbon fibers on top of each other. This process forms layers of carbon fibers, as illustrated in Fig. 5.1, in which two major directions are identified: in-plane (IP) and through-the-thickness (TTT) directions. This kind of anisotropic is termed as

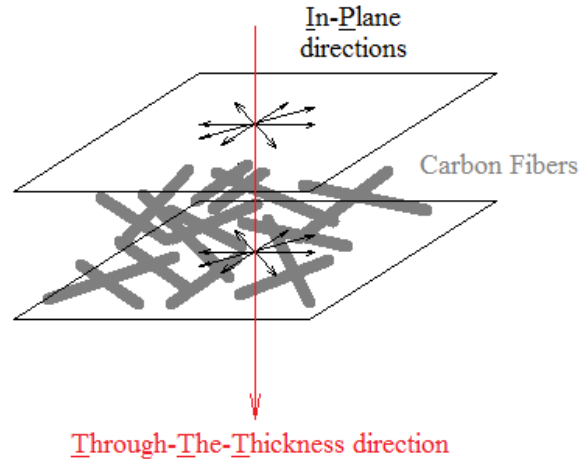


Figure 5.1: Illustration of IP and TTT directions regarding fiber orientation

transverse isotropic. Transverse isotropic material is a subset of orthotropic material. The latter has different properties along each of the three orthogonal axes, while the former has a plane of isotropy and a perpendicular axis as shown in Fig. 5.1. Therefore, transverse isotropic systems are sometimes referred as orthotropic, since the former can be described with the orthotropic system by assuming two orthogonal axes having the same IP value. Note that the orthotropic axes might not necessarily align with the Cartesian axes, and there might be one to three rotation angles between the orthotropic axes and the original axes. Assuming the rotation angles (counterclockwise using right hand rule) are  $\alpha$ ,  $\beta$ , and  $\gamma$  for rotation axes  $x$ ,  $y$ , and  $z$ , respectively, the rotation matrices are:

$$\mathbf{R}_x(\alpha) = \begin{pmatrix} 1 & 0 & 0 \\ 0 & \cos \alpha & -\sin \alpha \\ 0 & \sin \alpha & \cos \alpha \end{pmatrix}, \quad (5.7)$$

$$\mathbf{R}_y(\beta) = \begin{pmatrix} \cos \beta & 0 & \sin \beta \\ 0 & 1 & 0 \\ -\sin \beta & 0 & \cos \beta \end{pmatrix}, \quad (5.8)$$

$$\mathbf{R}_z(\gamma) = \begin{pmatrix} \cos \gamma & -\sin \gamma & 0 \\ \sin \gamma & \cos \gamma & 0 \\ 0 & 0 & 1 \end{pmatrix}. \quad (5.9)$$

Then the overall rotation matrix is obtained by the product of all of the individual rotation matrices:

$$\mathbf{R} = \mathbf{R}_z(\gamma)\mathbf{R}_y(\beta)\mathbf{R}_x(\alpha). \quad (5.10)$$

Note that the order of matrices in the multiplication is determined by the inverse order of rotation in the geometry of concern. For example, if an orthotropic direction is obtained by counterclockwise rotating  $\alpha$  degrees around  $x$ -axis first and then rotating  $\gamma$  degrees around  $z$ -axis, the overall rotation matrix is calculated by:

$$\mathbf{R} = \mathbf{R}_z(\gamma)\mathbf{R}_x(\alpha) = \begin{pmatrix} \cos \gamma & -\sin \gamma & 0 \\ \sin \gamma & \cos \gamma & 0 \\ 0 & 0 & 1 \end{pmatrix} \begin{pmatrix} 1 & 0 & 0 \\ 0 & \cos \alpha & -\sin \alpha \\ 0 & \sin \alpha & \cos \alpha \end{pmatrix}. \quad (5.11)$$

For the material response module in KATS, two material properties are assumed to be orthotropic: the permeability  $K$  and the thermal conductivity  $k_s$ . The effective matrices of both properties are thus given by the product of the overall rotation matrix multiplied by a diagonal matrix of orthotropic properties:

$$\mathbf{K} \equiv \begin{pmatrix} K_{xx} & K_{xy} & K_{xz} \\ K_{yx} & K_{yy} & K_{yz} \\ K_{zx} & K_{zy} & K_{zz} \end{pmatrix} = \mathbf{R} \begin{pmatrix} K_{xx} & & \\ & K_{yy} & \\ & & K_{zz} \end{pmatrix}, \quad (5.12)$$

and

$$\mathbf{k}_s \equiv \begin{pmatrix} k_{xx} & k_{xy} & k_{xz} \\ k_{yx} & k_{yy} & k_{yz} \\ k_{zx} & k_{zy} & k_{zz} \end{pmatrix} = \mathbf{R} \begin{pmatrix} k_{xx} & & \\ & k_{yy} & \\ & & k_{zz} \end{pmatrix}. \quad (5.13)$$

For transverse isotropic properties model, the TTT value is assigned to one of the diagonal element in the orthotropic matrix, and IP value is assigned to the other two elements.

## 5.2 Solid decomposition model

The solid material is modeled with  $nss$  components, each with a volume fraction of  $\Gamma_i$ . The total solid density is computed by the sum of all components:

$$\rho_{st} = \sum_{i=1}^{nss} \Gamma_i \rho_{s_i}. \quad (5.14)$$

The decomposition rate of each solid component is modeled with a modified Arrhenius equation:

$$\frac{\partial \rho_{s_i}}{\partial t} = \omega_{s_i} = -\rho_{s_{i,v}} \left( \frac{\rho_{s_i} - \rho_{s_{i,c}}}{\rho_{s_{i,v}}} \right)^{\psi_i} A_i e^{-E_i/(RT)}, \quad T > T_{reac,i}. \quad (5.15)$$

The density of each solid component has a virgin density of  $\rho_{s_{i,v}}$ , which gradually decreases to a minimum char density,  $\rho_{s_{i,c}}$ . Equation (5.15) ensures zero decomposition rate when the material is charred (resin depleted). The parameter  $\psi_i$  on the right hand side of the equation provides additional control to the model: for example, if  $\psi_i = 0$ , the density control to the reaction rate is turned off.

The most widely used resin decomposition model is the phenomenological three-components (or two-stage) model, which was based on experimental observations of phenolic decomposition by Goldstein [15] and used in Moyer and Rindal's CMA program [14]. In this model, the overall solid density is defined as:

$$\rho_{st} = \Gamma(\rho_{s_A} + \rho_{s_B}) + (1 - \Gamma)\rho_{s_C}, \quad (5.16)$$

where  $(\rho_{s_A} + \rho_{s_B})$  represents the resin density, and  $\rho_{s_C}$  is the density of the preform material and pyrolysis residuals. The reason to divide resin density to two parts is due to the experimentally observed two-stage decomposition process of phenolic resin. Therefore, three virtual components are identified and the number of solid species is three, or  $n_{ss} = 3$ . In this model, the volume fraction  $\Gamma$  is usually taken to be 1/2. Therefore, the  $\Gamma_i$ s in Eq. (5.14) are all 1/2 for the solid components A, B and C.

### 5.3 Pyrolysis gas model

KATS can model multiple gas species by solving mass conservations for each species. The overall gas density is calculated by:

$$\rho_g = \sum_{i=1}^{ngs} \rho_{g_i}, \quad (5.17)$$

where  $\rho_{g_i}$  is the  $i$ th species density. For each species, an ideal gas law is assumed:

$$p_i = \rho_{g_i} \frac{R_u}{M_i} T, \quad (5.18)$$

where  $R_u$  is the universal gas constant, and  $M_i$  is the molecular weight of species  $i$ .

### Chemical equilibrium model

For this model, the pyrolysis gas species are assumed to be at chemical equilibrium. Therefore, only one gas conservation is solved, giving  $ngs = 1$  and  $\rho_g = \rho_{g_1}$ . The gas properties are obtained via equilibrium table, as a function of temperature and pressure. The pyrolysis gas generation rate balances with the solid decomposition rates:

$$\omega_g = - \sum_{i=1}^{n_{ss}} \Gamma_i \omega_{s_i}. \quad (5.19)$$

## 5.4 Pyrolysis gas transport model

Heritage solvers [14, 23, 26, 34, 93] modeled pyrolysis gas transport using Darcy's law [94].:

$$\nabla p = -\phi \frac{\mu}{K} \mathbf{V}. \quad (5.20)$$

Darcy's law is a 1D steady state correlation for incompressible flow. However, pyrolysis gas inside charring ablator might not always be at steady state and they are compressible. Therefore, the original Darcy's law might not be appropriate for the application of charring ablation modeling. As alternatives, several options are listed in the following subsections.

### Unsteady Darcy's law for compressible flow

This model was initially inspired by an unsteady 1D formulation presented by Ahn et. al. [8]. In this work, the formulation is extended to 3D (isotropic) as:

$$\frac{\partial(\phi \rho_g u)}{\partial t} + \frac{\partial \phi(\rho_g u^2 + p)}{\partial x} + \frac{\partial \phi(\rho_g uv)}{\partial y} + \frac{\partial \phi(\rho_g uw)}{\partial z} = -\phi \frac{\mu}{K} u, \quad (5.21a)$$

$$\frac{\partial(\phi \rho_g v)}{\partial t} + \frac{\partial \phi(\rho_g uv)}{\partial x} + \frac{\partial \phi(\rho_g v^2 + p)}{\partial y} + \frac{\partial \phi(\rho_g vw)}{\partial z} = -\phi \frac{\mu}{K} v, \quad (5.21b)$$

$$\frac{\partial(\phi \rho_g w)}{\partial t} + \frac{\partial \phi(\rho_g uw + p)}{\partial x} + \frac{\partial \phi(\rho_g vw)}{\partial y} + \frac{\partial \phi(\rho_g w^2 + p)}{\partial z} = -\phi \frac{\mu}{K} w. \quad (5.21c)$$

A simple verification to the model can be performed by assuming steady state and incompressible (divergence free), where Eqs. (5.21) should fall back to Darcy's law (Eq. (5.20)). However, the equations become:

$$\nabla(\phi p) = -\phi \frac{\mu}{K} \mathbf{V}, \quad (5.22)$$

which is different from the Darcy's law by a factor of  $\phi$ . Therefore, a modified version is adopted:

$$\frac{\partial(\phi\rho_g u)}{\partial t} + \frac{\partial(\phi\rho_g u^2 + p)}{\partial x} + \frac{\partial(\phi\rho_g uv)}{\partial y} + \frac{\partial(\phi\rho_g uw)}{\partial z} = -\phi\frac{\mu}{K}u, \quad (5.23a)$$

$$\frac{\partial(\phi\rho_g v)}{\partial t} + \frac{\partial(\phi\rho_g uv)}{\partial x} + \frac{\partial(\phi\rho_g v^2 + p)}{\partial y} + \frac{\partial(\phi\rho_g vw)}{\partial z} = -\phi\frac{\mu}{K}v, \quad (5.23b)$$

$$\frac{\partial(\phi\rho_g w)}{\partial t} + \frac{\partial(\phi\rho_g uw + p)}{\partial x} + \frac{\partial(\phi\rho_g vw)}{\partial y} + \frac{\partial(\phi\rho_g w^2 + p)}{\partial z} = -\phi\frac{\mu}{K}w. \quad (5.23c)$$

Note that Eq. (5.23) is an isotropic formulation, where orthotropic properties model was not applied. For the orthotropic model, the following equation is solved for  $\mathbf{D} \equiv (D_x, D_y, D_z)$  using Gauss elimination method:

$$\mathbf{K}\mathbf{D} = -\phi\mu\mathbf{V}, \quad (5.24)$$

where  $\mathbf{K}$  is the orthotropic matrix given by Eq. (5.12). The solution  $\mathbf{D}$  is then applied to the governing equation as a source term, as shown in Eq. (3.1).

### Darcy-Forcheimer's law

Forcheimer's law accounts for high speed effects in porous media, which introduces an inertial term to the conventional Darcy's law. The classical form of Forcheimer's law can be found in Douglas et. al. [95]:

$$\phi\frac{\mu}{K}\mathbf{V} + b\phi^2\rho|\mathbf{V}|\mathbf{V} + \nabla p = 0, \quad (5.25)$$

where the parameter  $b$  is material dependent. An investigation on the Forcheimer effect applicable to charring ablators can be found by Martin and Boyd [93], where the value  $b$  ( $\beta$  in the reference) was given for several materials. In this study, the Darcy-Forcheimer's law is modeled by solving the following system for  $\mathbf{D}$ :

$$\mathbf{K}(\mathbf{D} + b\phi^2\rho|\mathbf{V}|\mathbf{V}) = -\phi\mu\mathbf{V}, \quad (5.26)$$

where  $\mathbf{D}$  is again the source terms in Eq. (3.1).

## Diffusive effects in energy equation

The diffusive effect of porous media is modeled as a source term in the energy equation, which is given as:

$$S_D = \begin{pmatrix} D_x \\ D_y \\ D_z \end{pmatrix} \begin{pmatrix} u & v & w \end{pmatrix} = D_x u + D_y v + D_z w, \quad (5.27)$$

where  $\mathbf{D} \equiv (D_x, D_y, D_z)$  is obtained via the models presented in the previous subsections.

## 5.5 Mixture energy model

In this work, the pyrolysis gas is assumed to be in thermal equilibrium with the solid material, yielding  $T = T_g = T_s$  and one mixture energy equation to solve. The thermal equilibrium assumption is usually reasonable for charring ablation problems [96]. The conductive heat flux,  $\mathbf{F}_{cond}$  (the last element of diffusive flux in Eq. (3.2)), is the product of the orthotropic thermal conductivity matrix and temperature gradient:

$$\mathbf{F}_{cond} = \mathbf{k}_s \begin{pmatrix} \partial T / \partial x \\ \partial T / \partial y \\ \partial T / \partial z \end{pmatrix}, \quad (5.28)$$

where the matrix of  $\mathbf{k}_s$  is given by Eq. (5.13).



## Chapter 6 Model Verification

### 6.1 Heat conduction

The first model verification is performed for the transient heat conduction. Heat conduction is a fundamental physical phenomenon in charring ablation problems. The governing equation to the problem is the heat equation, whose solution can be found analytically. Using this problem, the order of accuracy of the solver is verified on uniform grids, by performing a grid convergence study.

#### Problem statement and equations

Consider a constant-property, uniform-density planar slab with a constant heat flux applied on the front face and adiabatic on the back face. The governing equation describing the problem is the heat equation with constant properties:

$$\rho c_p \frac{\partial T}{\partial t} = k \frac{\partial^2 T}{\partial x^2}, \quad x \in [0, L], \quad (6.1)$$

with boundary conditions:

$$\begin{aligned} -k \frac{\partial T}{\partial x} &= \dot{q}'', \quad \text{at } x = 0, \\ -k \frac{\partial T}{\partial x} &= 0, \quad \text{at } x = L, \end{aligned}$$

and initial conditions:

$$T(x, t = 0) = T_0.$$

The exact analytical solution to the problem can be found in Arpaci [97] or Beck et al. [98], which is given as,

$$\frac{T(x, t) - T_0}{\dot{q}'' L / k} = \frac{\alpha t}{L^2} + \frac{1}{3} - \frac{x}{L} + \frac{1}{2} \left( \frac{x}{L} \right)^2 - \frac{2}{\pi^2} \sum_{n=1}^{\infty} \frac{1}{n^2} \exp \left( -n^2 \pi^2 \frac{\alpha t}{L^2} \right) \cos \left( n \pi \frac{x}{L} \right), \quad (6.2)$$

where  $\alpha$  is the thermal diffusivity  $\alpha = k/(\rho c_p)$ , which is a constant. Since Eq. (6.2) has an infinite summation, an extra C++ program is written to evaluate the solution, where a small truncation error is introduced. The truncation error can be controlled from input, which by default is assigned to one order of magnitude smaller than the tolerance in KATS.

The parameters that characterize the problem are summarized in Table 6.1. The

Table 6.1: Heat conduction problem parameters

	$\rho$	$c_p$	$k$	$L$	$\dot{q}''$	$T_0$
Values	8000 kg/m <sup>2</sup>	500 J/kg K	10 W/m K	0.01 m	$7.5 \times 10^5$ W/m <sup>2</sup>	300 K

analytical solution to Eq. (6.2) is presented in Fig. 6.1, for  $t = 4$  s, 8 s, 12 s, 16 s, 20 s, and 40 s.

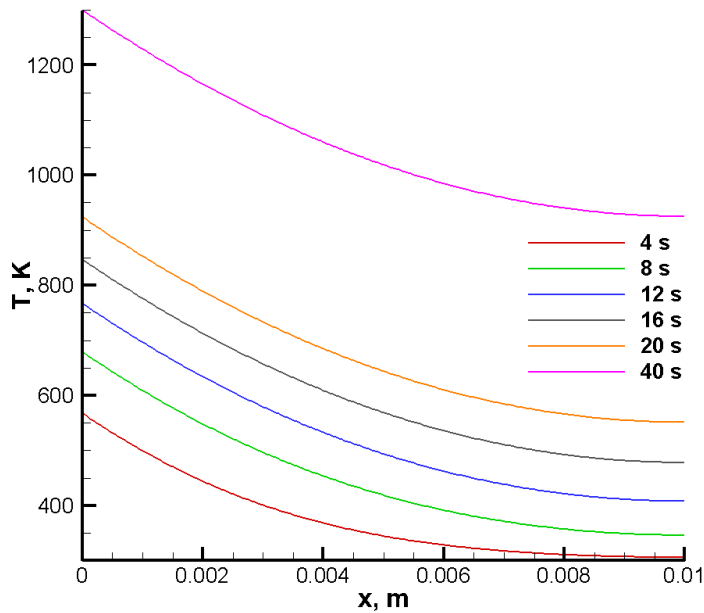


Figure 6.1: Analytical solution to the 1D heat conduction problem with heat flux specified on one side and adiabatic BC on the other side

### Grid convergence study

The solution accuracy consists of two parts: the temporal accuracy and the spatial accuracy. In order to evaluate both parts, the general error formulation is first

considered:

$$e_{\Delta t, \Delta x} = a\Delta t^{q_1} + b\Delta x^{q_2}, \quad a, b \equiv \text{const.} \neq 0 \quad (6.3)$$

where  $e_{\Delta t, \Delta x}$  is the solution error for time step size  $\Delta t$  and cell size  $\Delta x$ ;  $q_1$  and  $q_2$  are orders of accuracy in time and space, respectively.

To obtain the temporal accuracy, a highly refined mesh such that  $\Delta x \ll \Delta t$ , is considered. The second term on the right hand side of Eq. (6.3) is therefore negligible. Equation (6.3) then becomes:

$$e_{\Delta t, \Delta x} = a\Delta t^{q_1}. \quad (6.4)$$

If the time step size is halved, Eq. (6.4) is changed to:

$$e_{\Delta t/2, \Delta x} = a \left( \frac{\Delta t}{2} \right)^{q_1}. \quad (6.5)$$

Dividing Eq. (6.5) by (6.4), the order of temporal accuracy is revealed to be:

$$\begin{aligned} \frac{e_{\Delta t, \Delta x}}{e_{\Delta t/2, \Delta x}} &= \frac{a\Delta t^{q_1}}{a(\Delta t/2)^{q_1}} = 2^{q_1}, \\ \Rightarrow q_1 &= \log_2 \left( \frac{e_{\Delta t, \Delta x}}{e_{\Delta t/2, \Delta x}} \right). \end{aligned} \quad (6.6)$$

For the heat conduction problem given by Table 6.1, five grids are chosen for the temporal accuracy study, as presented in Table 6.2. The solution errors of each grid

Table 6.2: Grid parameters for temporal order of accuracy study

Grid	$\Delta t$ , s	$\Delta x$ , m	# of time steps	# of grid cells
extra coarse	$4 \times 10^{-2}$	$2.5 \times 10^{-6}$	1000	4000
coarse	$2 \times 10^{-2}$	$2.5 \times 10^{-6}$	2000	4000
medium	$1 \times 10^{-2}$	$2.5 \times 10^{-6}$	4000	4000
fine	$5 \times 10^{-3}$	$2.5 \times 10^{-6}$	8000	4000
extra fine	$2.5 \times 10^{-3}$	$2.5 \times 10^{-6}$	16000	4000

are presented in Fig. 6.2. It is clear from the figure that as the total number of time steps increases, the errors of the solution decrease linearly. The solution slope is as

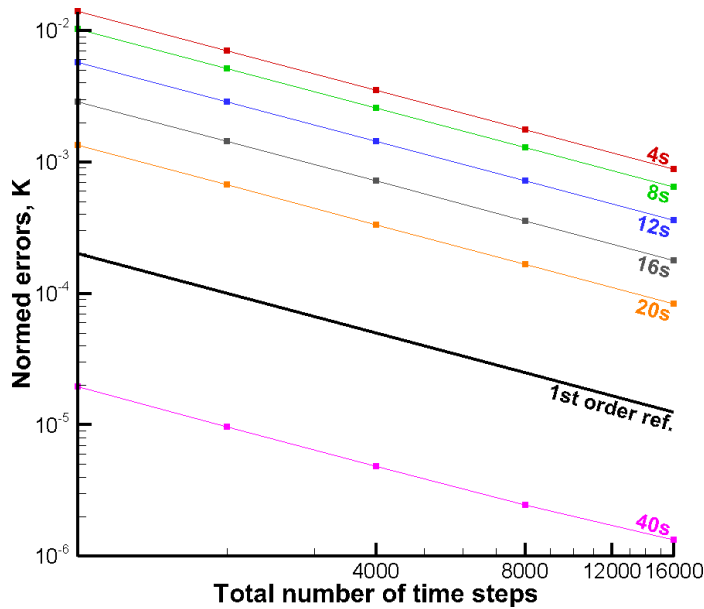


Figure 6.2: Solution (temperature) errors to the heat equation in the temporal accuracy study: errors have the same slope as the 1st order reference

same as the first order reference, which is given by  $e_{\Delta t, \Delta x} = 2e_{\Delta t/2, \Delta x}$ . The first order temporal accuracy is therefore confirmed and is considered verified.

For the spatial accuracy, another set of grids is selected as presented in Table 6.3. Note that from coarse grid to medium and from medium to fine, the numbers of grid

Table 6.3: Grid parameters for spatial order of accuracy study

Grid	$\Delta t$ , s	$\Delta x$ , m	# of time steps	# of grid cells
coarse	$4 \times 10^{-2}$	$5 \times 10^{-5}$	1000	200
medium	$1 \times 10^{-2}$	$2.5 \times 10^{-5}$	4000	400
fine	$2.5 \times 10^{-3}$	$1.25 \times 10^{-5}$	8000	800

cells are doubled, while the numbers of time steps are quadrupled. This ramping is necessary to verify the spatial order of accuracy. Recalling Eq. (6.3),

$$\begin{aligned}
 e_{\Delta t, \Delta x} &= a\Delta t^{q_1} + b\Delta x^{q_2}, & (6.3 \text{ revisited}) \\
 \Rightarrow e_{\Delta t/4, \Delta x/2} &= a\left(\frac{\Delta t}{4}\right)^{q_1} + b\left(\frac{\Delta x}{2}\right)^{q_2}.
 \end{aligned}$$

Since  $q_1$  has been verified to be one (1), it is possible to show

$$\frac{e_{\Delta t, \Delta x}}{e_{\Delta t/4, \Delta x/2}} = \frac{a\Delta t + b\Delta x^{q_2}}{a\left(\frac{\Delta t}{4}\right) + b\left(\frac{\Delta x}{2}\right)^{q_2}}. \quad (6.7)$$

If the solution has second order spatial accuracy, or  $q_2 = 2$ , Eq. (6.7) becomes:

$$\frac{e_{\Delta t, \Delta x}}{e_{\Delta t/4, \Delta x/2}} = \frac{a\Delta t + b\Delta x^2}{a\left(\frac{\Delta t}{4}\right) + b\left(\frac{\Delta x}{2}\right)^2} = \frac{a\Delta t + b\Delta x^2}{\frac{1}{4}(a\Delta t + b\Delta x^2)} = 4. \quad (6.8)$$

Figure 6.3 displays the solution errors against a second order reference that satisfies Eq. (6.8). The slopes selected in the figure confirm that the solution is second order accurate in space.

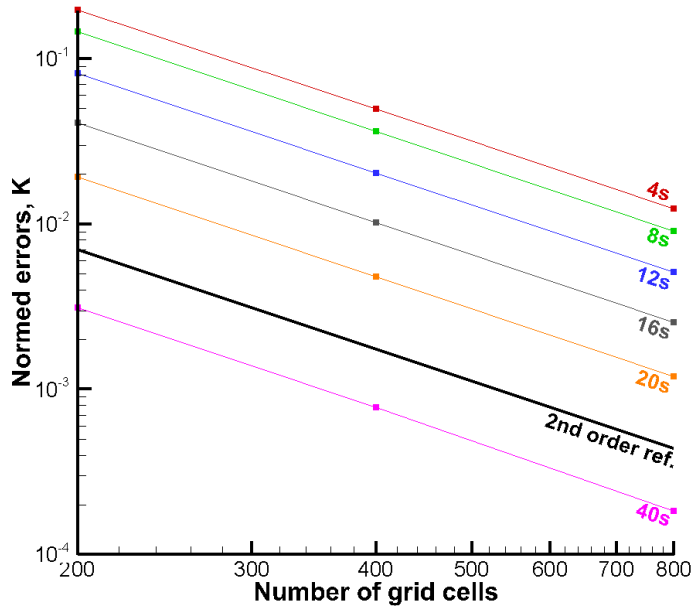


Figure 6.3: Solution (temperature) errors to the heat equation in the spatial accuracy study: errors have the same slope as the 2nd order reference

## 6.2 Flow through a porous tube

With the heat conduction model verified, the second model problem is intended to verify the mass and energy conservation of gas, in addition to the porous media flow model in the momentum equation. The geometry of concern is a 3D tube, which demonstrates the ability of solving on 3D meshes.

## Problem statement and equations

Consider a finite-long porous cylindrical tube that is subjected to constant static pressures at the two ends. The pressure difference drives air to flow through the porous tube. The porous material is assumed to be non-reactive, permeable at the two ends, but impermeable through the side wall of the tube. Figure 6.4 illustrates the problem setup, where  $L = 0.01$  m,  $R = L/4$ .

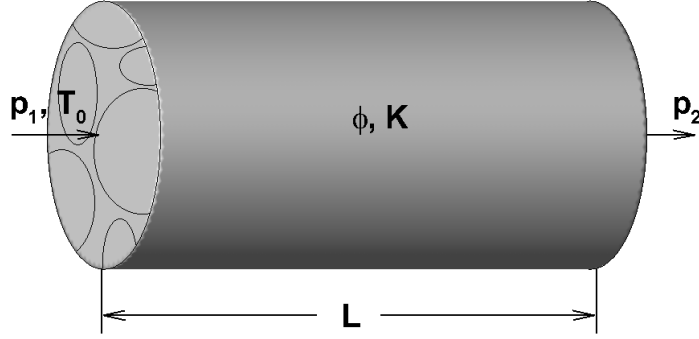


Figure 6.4: Illustration of the porous tube problem (air flow is driven by the pressure difference on two ends)

The governing equations for the given problem are:

$$\frac{\partial(\phi\rho_g)}{\partial t} + \frac{\partial(\phi\rho_g u)}{\partial x} + \frac{\partial(\phi\rho_g v)}{\partial y} + \frac{\partial(\phi\rho_g w)}{\partial z} = 0, \quad (6.9a)$$

$$\frac{\partial(\rho_g u)}{\partial t} + \frac{\partial p}{\partial x} = -\mu \frac{\phi}{K} u, \quad (6.9b)$$

$$\frac{\partial(\rho_g v)}{\partial t} + \frac{\partial p}{\partial y} = -\mu \frac{\phi}{K} v, \quad (6.9c)$$

$$\frac{\partial(\rho_g w)}{\partial t} + \frac{\partial p}{\partial z} = -\mu \frac{\phi}{K} w, \quad (6.9d)$$

$$\frac{\partial(\phi\rho_g E_g)}{\partial t} + \frac{\partial(\phi\rho_g u H)}{\partial x} + \frac{\partial(\phi\rho_g v H)}{\partial y} + \frac{\partial(\phi\rho_g w H)}{\partial z} = 0, \quad (6.9e)$$

with boundary conditions:

$$p = p_1, \quad T = T_0, \quad \text{at } x = 0,$$

$$p = p_2, \quad \text{at } x = L,$$

$$\frac{\partial u}{\partial r} = 0, \quad u_r = 0, \quad \text{at } r^2 \equiv y^2 + z^2 = R^2,$$

and initial conditions:

$$T = T_0, \quad p = p_2, \quad (u, v, w) = (0, 0, 0) \quad \text{at } t = 0.$$

Here, Eqs. (6.9a) and (6.9e) are mass and energy conservations in porous structure, respectively. Eqs. (6.9b) to (6.9d) are unsteady formulations of Darcy’s law. The solution to the governing equations is expected to reproduce Darcy’s law when steady state is reached. Table 6.4 lists the parameters that characterize this problem.

Table 6.4: Flow through porous tube problem parameters

$p_1$	$p_2$	$\phi$	$K$	$\mu$	$T_0$
101750 Pa	101050 Pa	0.8	$1.6 \times 10^{-11} \text{ m}^2$	$1.85052 \times 10^{-5} \text{ kg/m s}$	300 K

## Results and discussions

In order to verify the solution with Darcy’s law, the steady state of the solution has to be confirmed first. When steady state is reached, Eq. (6.9a) yields:

$$\frac{\partial(\phi\rho u)}{\partial x} = 0,$$

$$\text{or, } \phi\rho u \equiv \text{const.}$$

Therefore, an easy way to verify the steady state is to check if the mass flow rate is uniform over the computational domain. Figure 6.5 shows the mass flow rate over porosity (since porosity is constant in this case) at 5000 time steps. As is seen from the figure, the mass flow rate is constant everywhere within the tube. Therefore, the solution to the porous media equations of KATS is considered to be steady state.

The centerline temperature and pressure profiles obtained by KATS are presented in Fig. 6.6. As expected, the pressure is linearly ramping down from inlet to outlet, and the temperature is uniform. In addition, the gas density and  $x$ -component of the velocity are plotted, as shown in Fig. 6.7. Since the fluid is compressible, the density also decreases linearly with the pressure due to the ideal gas law. The velocity, on the

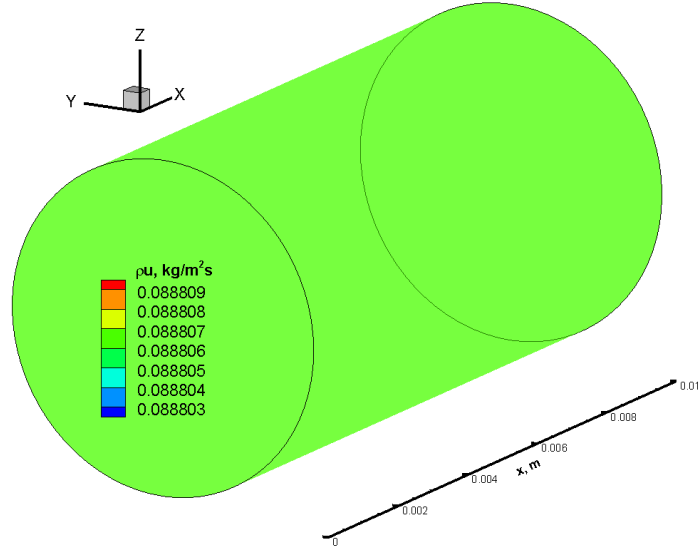


Figure 6.5: Mass flow rate within the porous tube (constant indicates steady state)

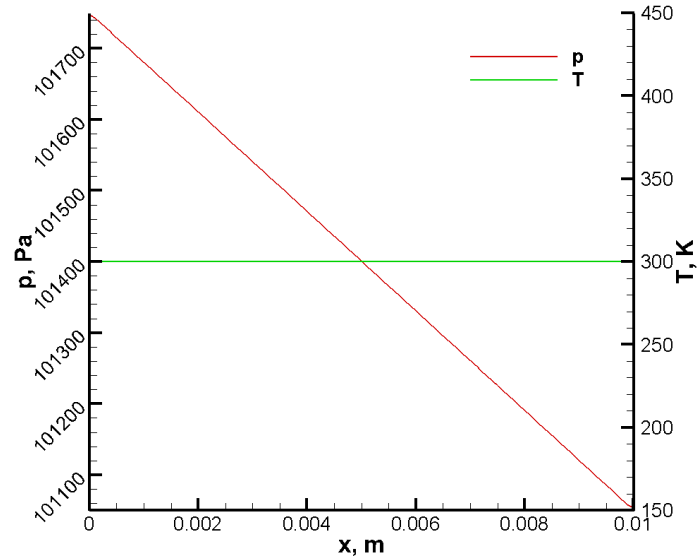


Figure 6.6: Pressure and temperature profiles along the centerline of the porous tube

other hand, constantly accelerates so as to preserve the mass balance. The differences between the two ends, however, are not significant.

Performing a volume average for the velocity gives:  $u_{avg} = 7.56543 \times 10^{-2} \text{ m/s}$ . The result is compared with Darcy's law:

$$\phi u = \frac{-K}{\mu} \frac{p_2 - p_1}{L}. \quad (6.10)$$

Substitute the parameters in Table 6.4 into Eq. (6.10), and the averaged flow velocity



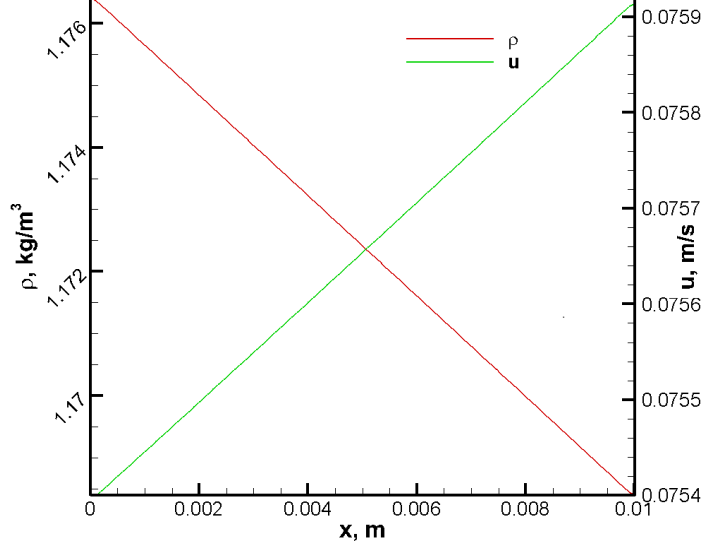


Figure 6.7: Gas density and velocity profiles along the centerline of the porous tube: gas density is linearly decreasing and velocity is linearly increasing, resulting a constant mass flow rate

is acquired:

$$u = \frac{-K p_2 - p_1}{\phi \mu L},$$

$$u = \frac{-1.6 \times 10^{-11}}{(0.8)(1.85052 \times 10^{-5})} \frac{101050 - 101750}{0.01},$$

$$u = 7.56541 \times 10^{-2} \text{ m/s.}$$

Note that the numerical solution is in good agreement with the analytical one, with an error percentage of merely:

$$|e_u| = \left| \frac{7.56543 - 7.56541}{7.56541} \right| \times 100\% = 0.00026\%.$$

### 6.3 1D TACOT heating problem

This test-case is intended to verify the resin decomposition model using the ablative material TACOT. TACOT, or Theoretical Ablative Composite for Open Testing [99], is a low-density artificial material based on PICA [7]. The thermodynamic properties of TACOT are given in Appendix D. The charring process of TACOT is modeled

with the phenomenological three-component decomposition model introduced in Section 5.2. The model yields three solid mass balance equations describing the carbon matrix, and the conversion of resin to pyrolysis gas and char. Use of this model results in a total of eight equations to solve, which are given by Eqs. (3.1) and (3.2) with  $n_{gs} = 1$  and  $n_{ss} = 3$ .

### Problem statement

The 1D problem considered here is a 0.05 m long TACOT sample, with one side maintained at a constant temperature of 1644 K for 60 s. The other wall is set to be adiabatic. The initial temperature of the material is assumed to be 298 K. The initial pore pressure is assumed to be identical to the free stream pressure (10132.5 Pa). Figure 6.8 illustrates the problem setup, with parameters given in Table 6.5.

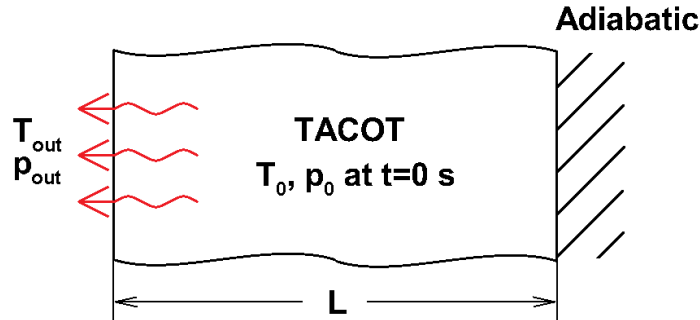


Figure 6.8: Illustration of the 1D TACOT heating problem: a  $L = 0.01$  m long TACOT sample with pressure and temperature maintained at one end and impermeable adiabatic wall at the other end

Table 6.5: Parameters for 1D TACOT heating problem

	$T_{out}$	$p_{out}$	$T_o$	$p_0$	$L$
Values	1644 K	10132.5 Pa	298 K	10132.5 Pa	0.01 m

### Grid function convergence test

In order to verify the solution is converging to the exact solution of the governing equations, a grid function convergence test is performed for this problem. Since KATS

is a cell centered solver, the number of grid cells is tripled for each level of refinement in order to maintain the locations of cell centers unchanged. The grids and the time step sizes for the test are presented in Table 6.6. Assuming the solutions of variable  $X$

Table 6.6: Grid refinements and time step sizes for the convergence test

Refinement	Number of grid cells	Time step size	Number of time steps
coarse	100	0.009	2000
finer	300	0.003	6000
finest	900	0.001	18000

obtained at coarse, finer, and finest mesh are respectively  $X_{coarse}$ ,  $X_{finer}$ , and  $X_{finest}$ , the spatial order of accuracy can thus be calculated as:

$$order = \log_3 \frac{\|X_{coarse} - X_{finer}\|_2}{\|X_{finer} - X_{finest}\|_2}. \quad (6.11)$$

Table 6.7: Spatial orders of accuracy from the grid function convergence test

Variable	$T$	$p$	$\rho_{s_1}$	$\rho_{s_2}$	$\rho_{s_3}$	$w$
Order	1.850157	2.281906	1.846132	1.93456	–	2.575495

The calculated orders of accuracy for each primitive variable in the charring problem are presented in Table 6.7. Note that, the order for  $\rho_{s_3}$  is not available because  $\rho_{s_3}$  is the solid density of the non-reacting component, which is a constant. The orders of accuracy for variables  $T$ ,  $p$ ,  $\rho_{s_1}$  and  $\rho_{s_2}$  are quite close to the expected order of accuracy, two (2). The last variable  $w$ , however, has a much higher order of accuracy than the desired value. This is because the velocity component for this problem is almost zero in the region below the charring front; at the evaluated time,  $t = 18$  s, the values of  $w$  are at the order of solution tolerance for  $0.011 < z < 0.05$  m. Therefore, the calculated norms of  $w$  might not be able to reflect the exact spatial accuracy. The  $p$  accuracy is also slightly above the desired order, since the pressure is closely related to the velocity through the modified Darcy’s law. In all, based on the results in Table 6.7, the grid shows satisfactory convergence to the exact solution of the system.

## Results and discussions

This problem is further verified through a code-to-code comparison with a validated material response code, MOPAR [74]. Figures 6.9 and 6.10 respectively show the temperature and solid density profiles at  $t = 20$  s, 40 s, and 60 s. The KATS results

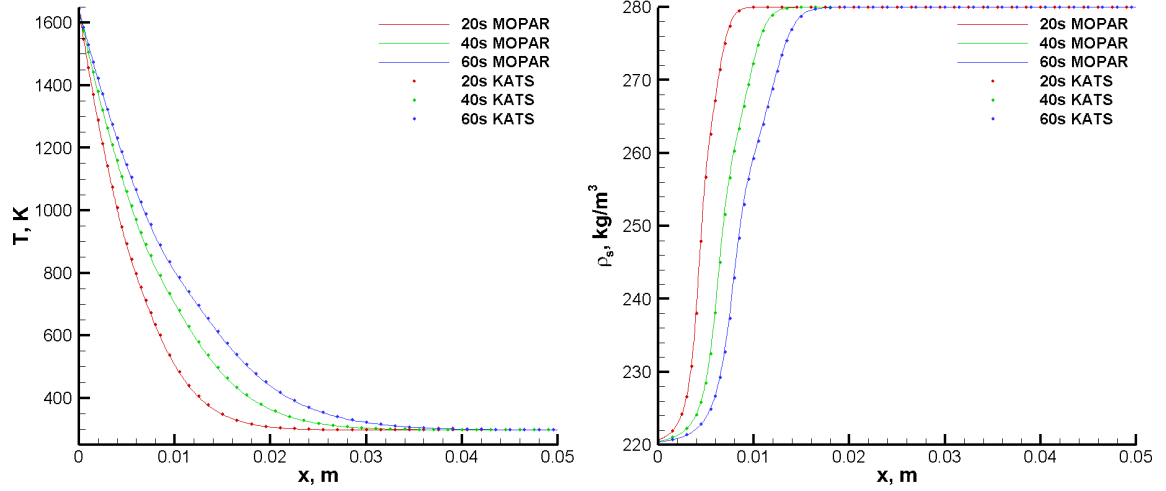


Figure 6.9: Temperature profiles for the 1D TACOT heating problem

Figure 6.10: Overall solid density profiles for the 1D TACOT heating problem

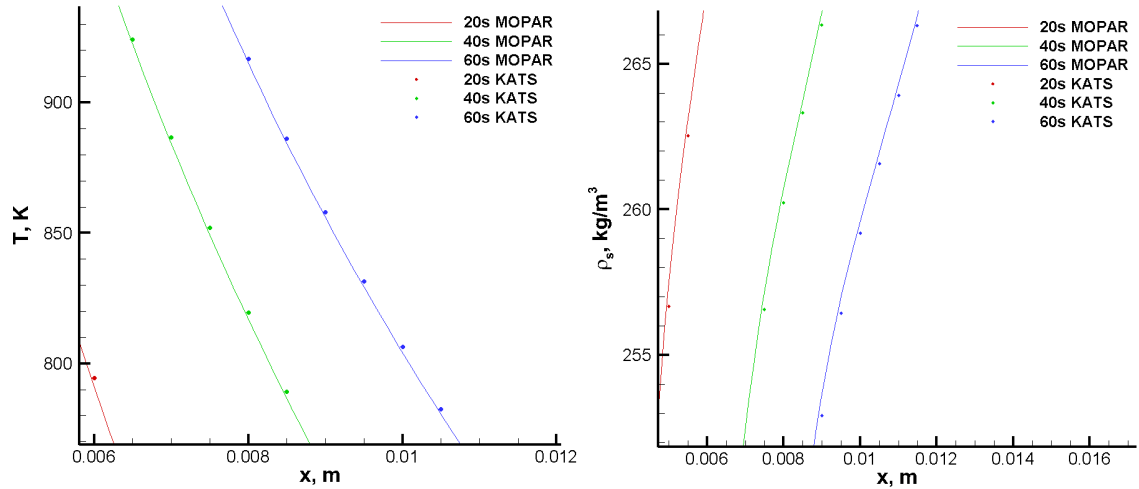


Figure 6.11: Zoomed-in temperature profiles for the 1D TACOT heating problem

Figure 6.12: Zoomed-in solid density profiles for the 1D TACOT heating problem

are plotted using symbols while the MOPAR results are plotted using solid lines.

It is seen from these figures that, the KATS results are in good agreement with the MOPAR results in general. But Figs. 6.11 and 6.12 show that the predicted temperatures are slightly greater than those predicted by MOPAR, and the solid densities slightly under-predict the MOPAR densities. The tiny discrepancy is likely due to the difference in the gas enthalpy calculation: MOPAR numerically integrates heat capacity to get the enthalpy, where as KATS interpolates the enthalpy values directly from the gas equilibrium table.

# Chapter 7 Study of Pyrolysis Gas Flow Effects

## 7.1 Motivation

Resin materials in a charring ablator decompose when heated, generating pyrolysis gas. As the pyrolysis gas flows within the ablator, it might affect the material thermal response. Moreover, the pyrolysis gas surface blowing rate is part of the surface energy balance, which is closely related to the thermal boundary condition. Therefore, it is important to model the pyrolysis gas flow in an ablation program. On one hand, existing works with pyrolysis gas flow models were mostly seen in 1D, where steady state Darcy's law was applied [26,34,93]. But pyrolysis gas flow could be highly time dependent, especially near the decomposition zone. In addition, the flow direction is very sensitive to the geometry, and 1D assumption might not be able to catch the geometric effects. On the other hand, multidimensional research works mainly focused on the coupling of fluid and solid, where ablation programs only modeled the heat transfer and the solid decomposition, without considering the pyrolysis gas momentum conservations [35,38,50]. Therefore in this chapter, the effect of pyrolysis gas flow is studied through a series of 3D test-cases.

## 7.2 Applied models

The governing equations for this study are given in Eqs. (2.1), (3.1), and (3.2), where  $n_{gs} = 1$  and  $n_{ss} = 3$ . The pyrolysis gas model for this problem assumes chemical equilibrium, as discussed in Section 5.3. The decomposition of the solid material is modeled with the phenomenological three components model discussed in Section 5.2. The pyrolysis gas momentum equations are given by Eqs. (5.23) in Section 5.4. The considered material in this study is isotropic TACOT [99].

### 7.3 Cylinder sample test-cases

The study begins with two test-cases using the same geometry: a cylindrical material sample. The front surface of the cylinder is assumed to be permeable, and is exposed to an uniform heat flux and an uniform pressure. The side surface, however, is where the two cases vary: the side is impermeable in the first case, but it is permeable in the second case. The first case is expected to represent the 1D model, since the pyrolysis gas can only be expelled through the front surface. The second case steps a little further by allowing the pyrolysis gas to exit through the permeable side, which introduces minimal 3D effects. Note that, the two cases are theoretical problems that are designed to discover differences between the 1D and 3D frameworks; they are not based on any specific experiments.

Since the cylinder geometry is axisymmetric, a 4-degree slice of the cylinder is chosen as the computational geometry, as shown in Fig. 7.1. The boundary conditions are also demonstrated in Fig. 7.1. The applied surface heat flux  $q_w$  in the figure is removed after 40 seconds. The pore pressure and temperature of the material are initialized with 10132.5 Pa and 298 K, respectively.

#### 3D impermeable side cylinder case and 1D model

To demonstrate that the impermeable side cylinder case is same as the 1D model, a 1D simulation is first run using the same conditions as described earlier. The in-depth results of the 1D simulation and the 3D cylinder case are presented by lines and symbols respectively in Fig. 7.2. The results of the 3D cylinder case are taken along the centerline. It can be seen from Fig. 7.2 that, the 3D cylinder case (with impermeable wall) has almost the same solutions as obtained with the 1D model.

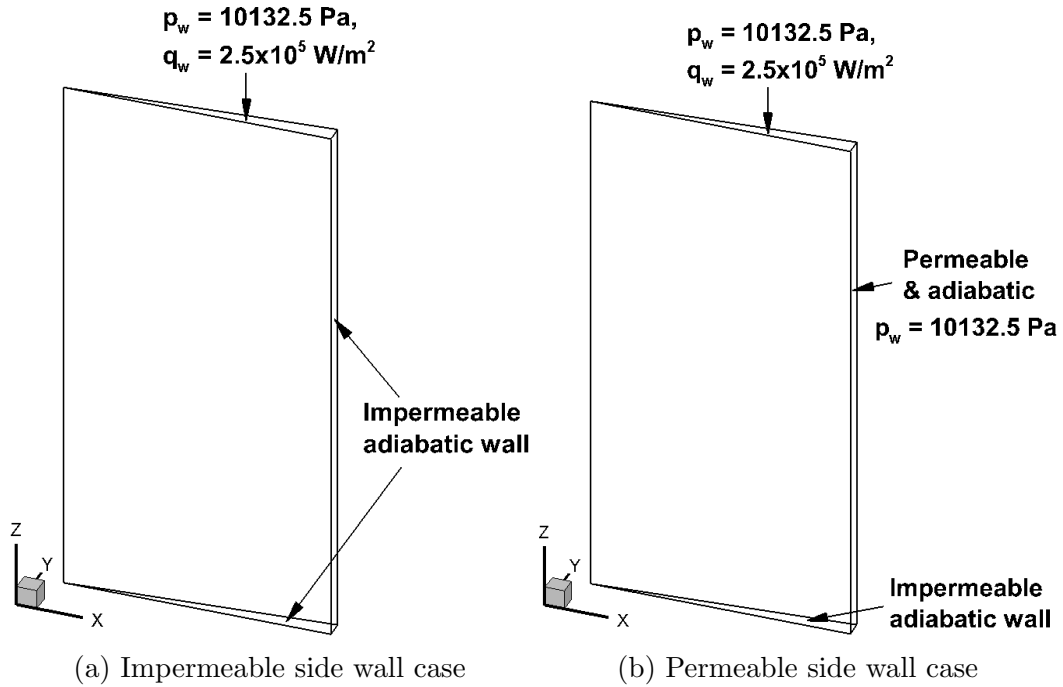


Figure 7.1: Computational geometry and boundary conditions for the cylinder sample cases in pyrolysis gas flow study

### Pressure contour plots of 3D cylinder cases

Figure 7.3 shows the pressure contour plots for the impermeable side case at 20, 40 and 60 seconds. As expected, the contour lines are uniform and paralleled to the  $x$ -axis, which matches the 1D assumption. In addition, the pressure is increasingly higher inside the material than on the surface. This is because the pyrolysis gas generated within the sample cannot escape, and are thus trapped inside the material, since the side wall is impermeable. Therefore, the inner pressure builds up, and the gas mass accumulates within the sample.

The pressure distribution for the permeable side case, however, is very different, as is shown in Fig. 7.4. The pressure contour lines are not paralleled to each other; instead, they form a high-pressure region inside the cylinder sample. This region corresponds to the decomposition zone, in where pyrolysis gas is formed. This can be explained by the fact that the generated gas may leave the sample immediately from



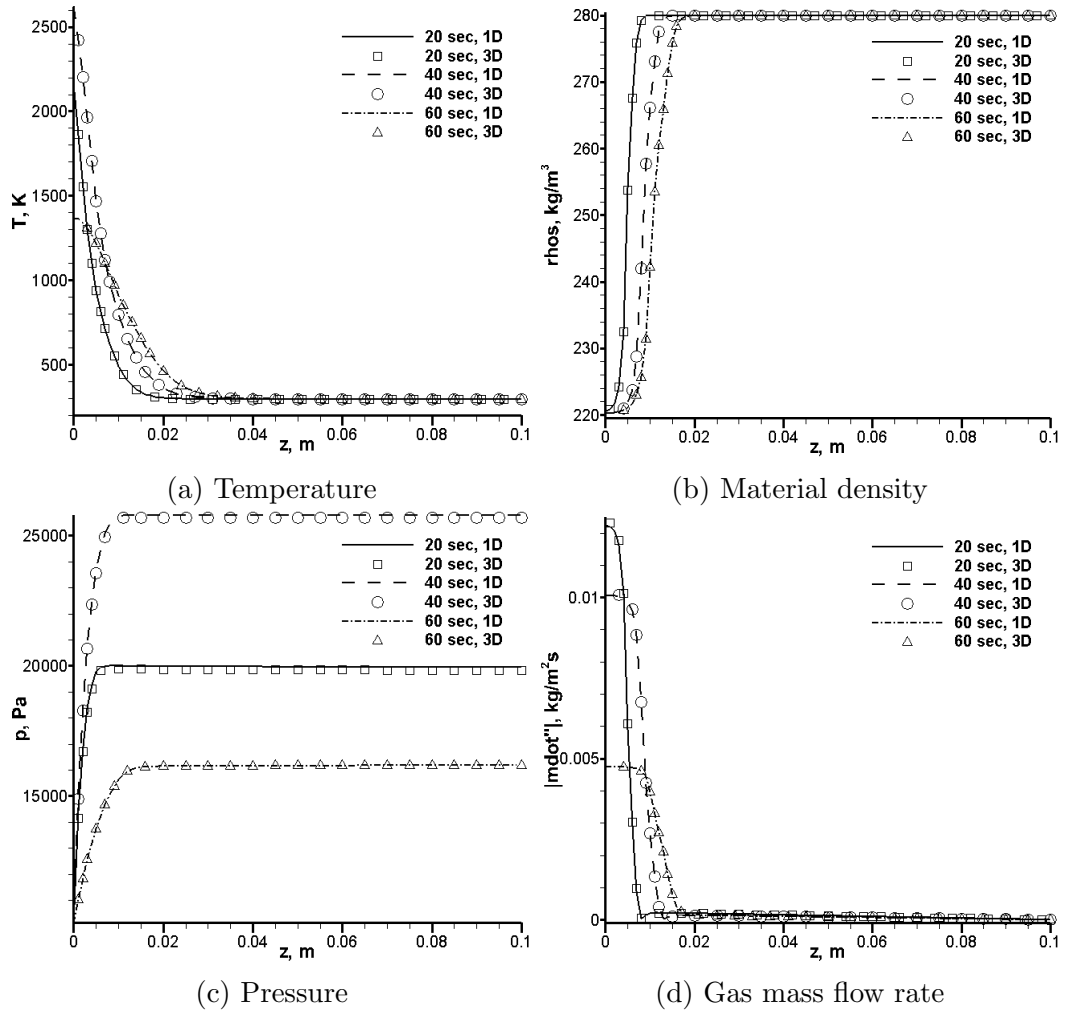


Figure 7.2: Comparison between 3D cylinder and 1D model results

all open sides, thus preventing the pressure build-up and the gas mass accumulation.

Note that the pressure behavior is valid for light-weight, highly-porous charring ablative materials, such as PICA and TACOT; it might not be fully extensible to high density and low permeability ablators such as the legacy carbon-phenolic [100]. This is because the dense ablators with low permeability (and porosity) might not be able to facilitate the gas transport to the extent seen in this study, and the pore pressure might build up (due to close pores) even if the side is permeable; therefore the difference between the 1D and 3D models might not be as significant as in this case. But for low-density ablators such as TACOT selected in this study, the 3D

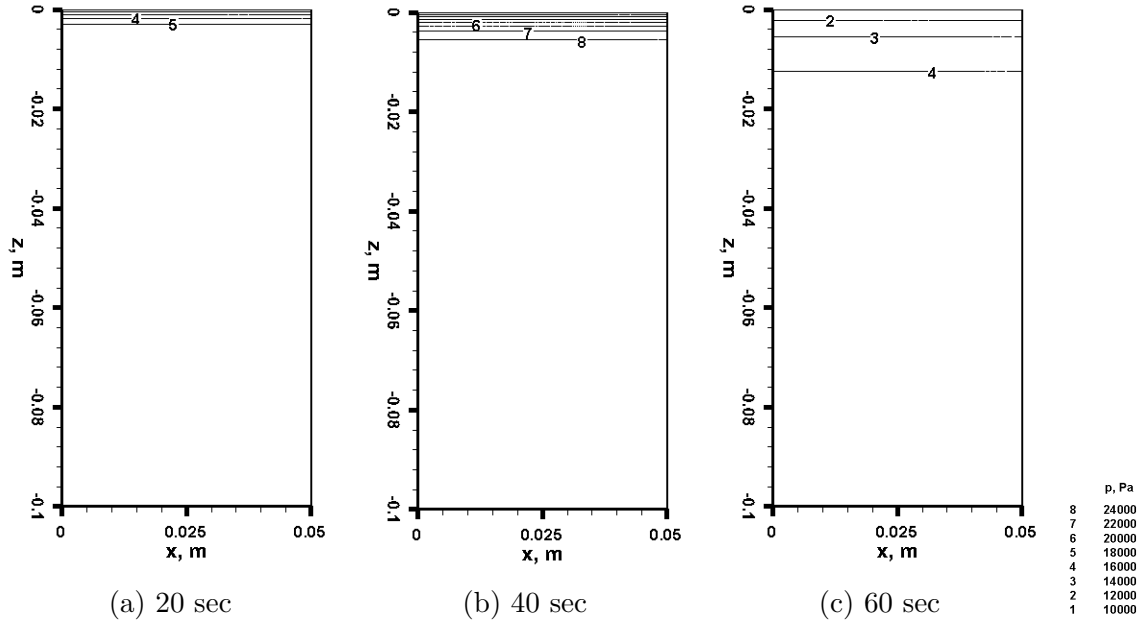


Figure 7.3: Pressure contours of impermeable side wall cylinder

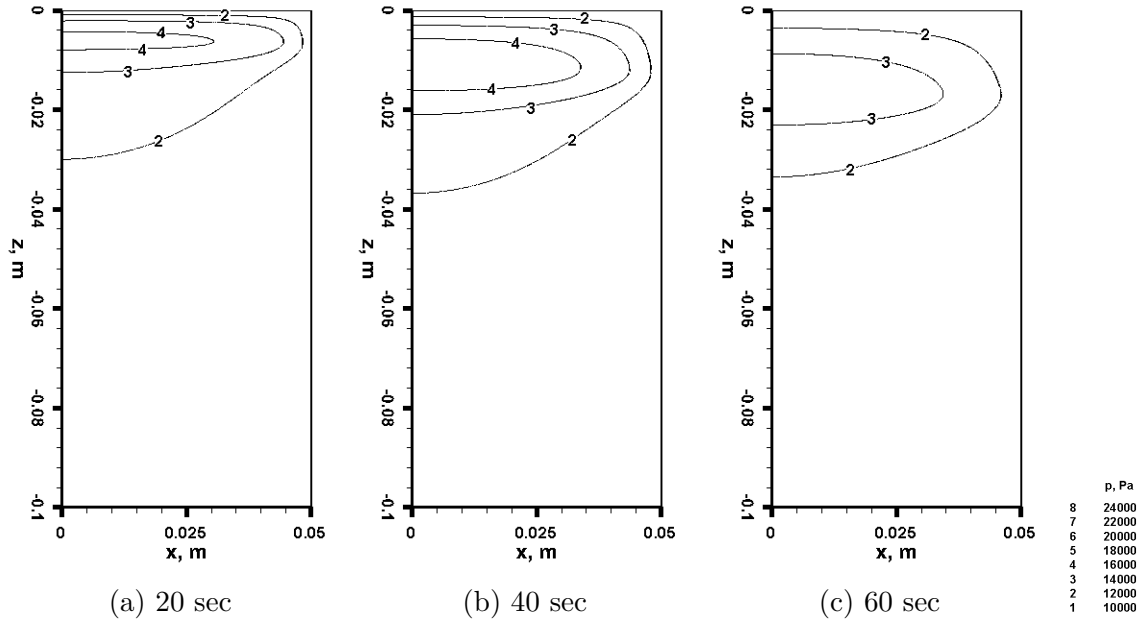


Figure 7.4: Pressure contours of permeable side wall cylinder

(permeable side cylinder) pressure distributions are in sharp contradiction with the 1D distributions.

## Pyrolysis gas flow patterns of 3D cylinder cases

The pyrolysis gas flow behavior is demonstrated by streamlines and local gas momentum contours. The local gas momentum is represented by  $|\dot{m}''| = \phi \rho_g \sqrt{u^2 + v^2 + w^2}$ , which has the same unit as the momentum. The gas flow results for the impermeable side cylinder case are shown in Fig. 7.5. The streamlines are all straight and parallel, pointing upwards. This indicates the pyrolysis gas only travels vertically, and blows through the front surface, which is same as the 1D model. Note that, the equation set used to represent the pyrolysis gas momentum is analogous to the Euler equation, for which the wall boundary condition is slip. This is a sound assumption for porous media, since the non-slip condition occurs at the surface of the pores, not at the surface of test-piece. As a result, the simulation of the impermeable side wall case should be, and is, exactly the same as a 1D case.

For the permeable side wall case, as shown in Fig. 7.6, the gas flows separate at the decomposition zone (high pressure region), traveling both to top and bottom. The top part of the flow blows through the front surface, while the bottom part curves and eventually exists through the open side wall. The gas momentums of the two flow directions are not equal, as indicated by the contours of Fig. 7.6: the gas mass transport towards the front (upward) is clearly less than towards the side (downward first then rightward). This suggests the majority of gas leaves from the side surface, instead of the front.

## Thermal response of 3D cylinder cases

The thermal responses of the two cylinder cases are presented by Fig. 7.7 and Fig. 7.8. When comparing the two figures, the material temperatures in the permeable side wall case are higher than those in the impermeable side wall case. In other words, the in-depth heating is enhanced with the open side wall assumption. This phenomenon was not expected originally, since the thermal boundary conditions were identical for the

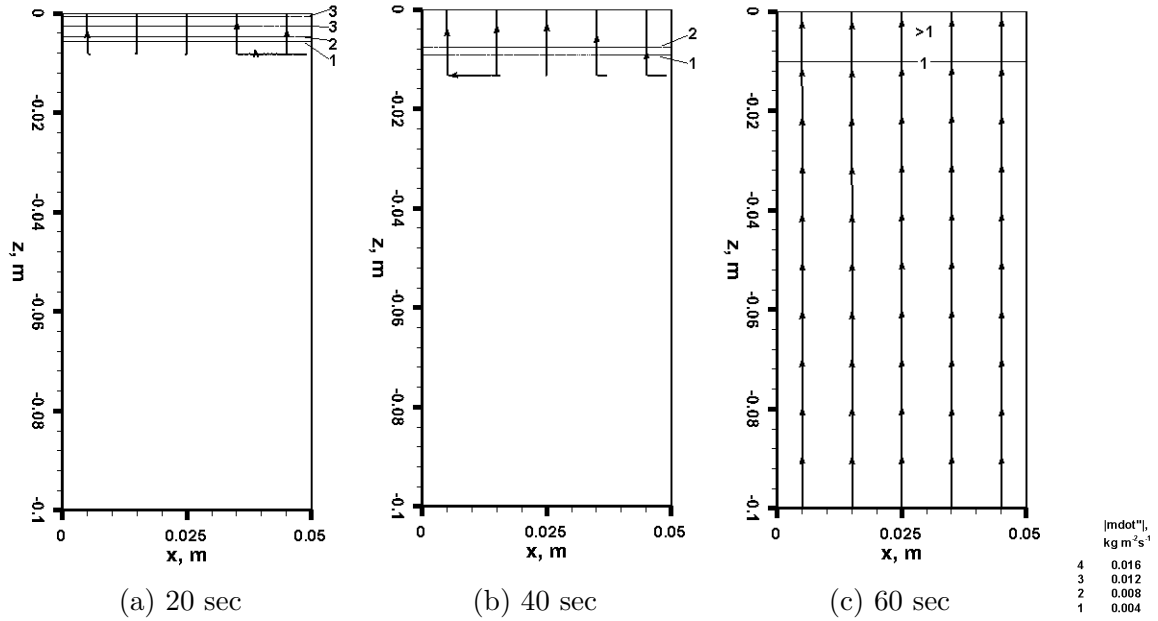


Figure 7.5: Gas mass transport of impermeable side wall cylinder

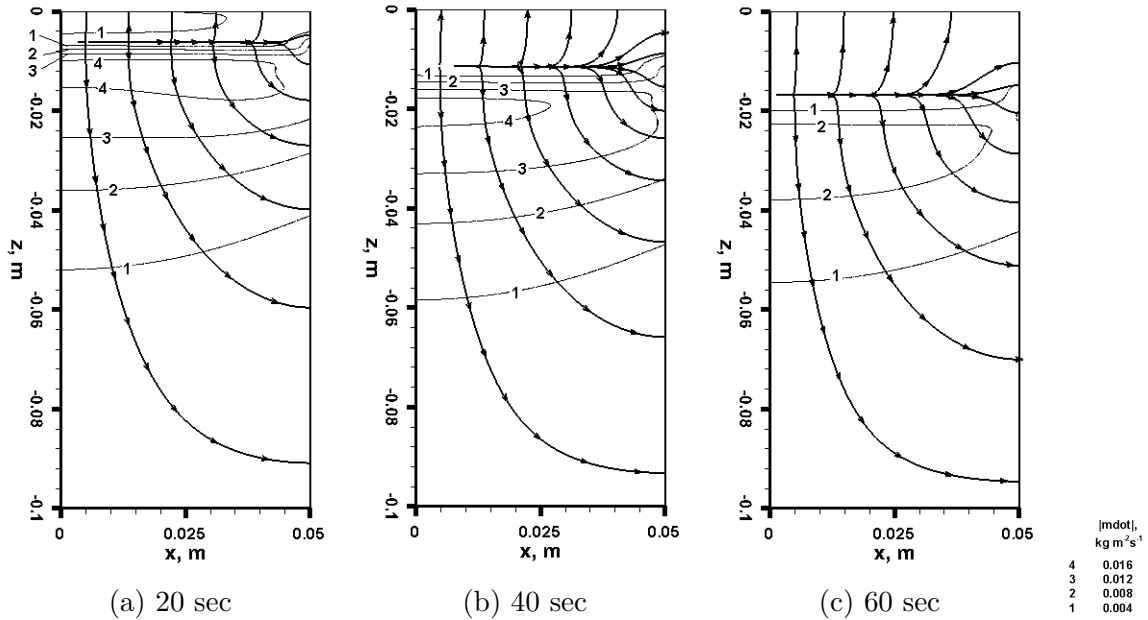


Figure 7.6: Gas mass transport of permeable side wall cylinder

two simulations. A possible explanation is that, as the hot pyrolysis gas travels within the porous structure, the material is further heated due to the thermal equilibrium assumption. The region right below the decomposition zone has the highest mass transport, as was shown in Fig. 7.6; therefore, the material in this region was heated

most due to the hot pyrolysis gas flow. Moreover, the non-uniform temperature contours (*e.g.* Fig. 7.8c) are the results of the non-uniform gas flow directions and momentum contours (Fig. 7.6c).

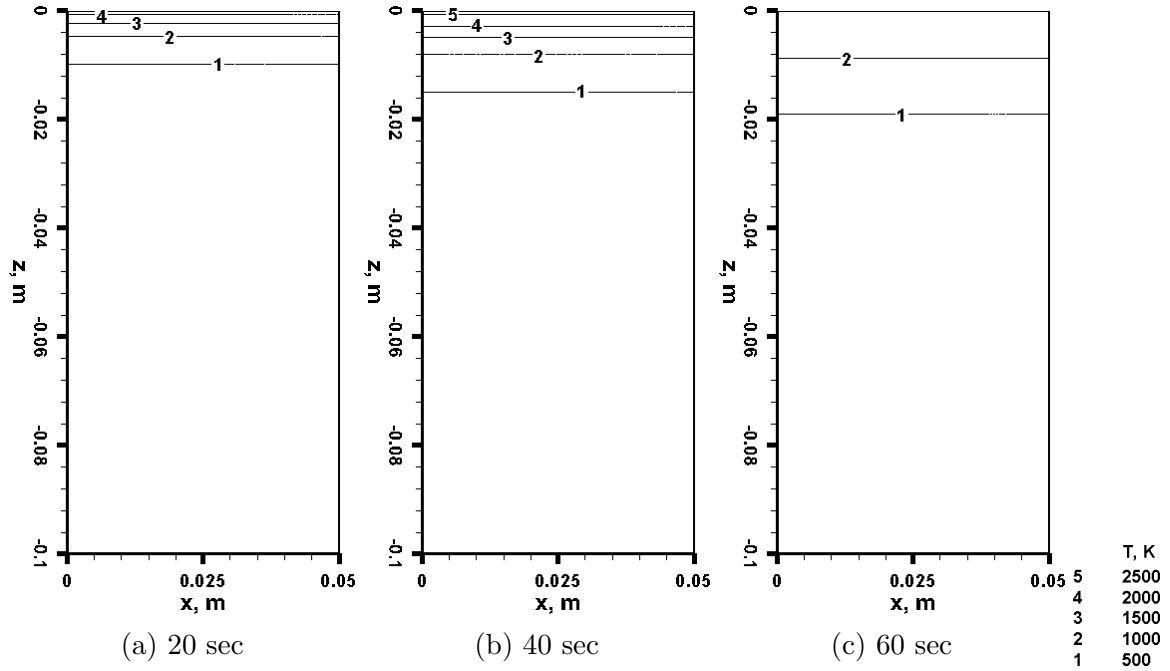


Figure 7.7: Thermal response of impermeable side wall cylinder

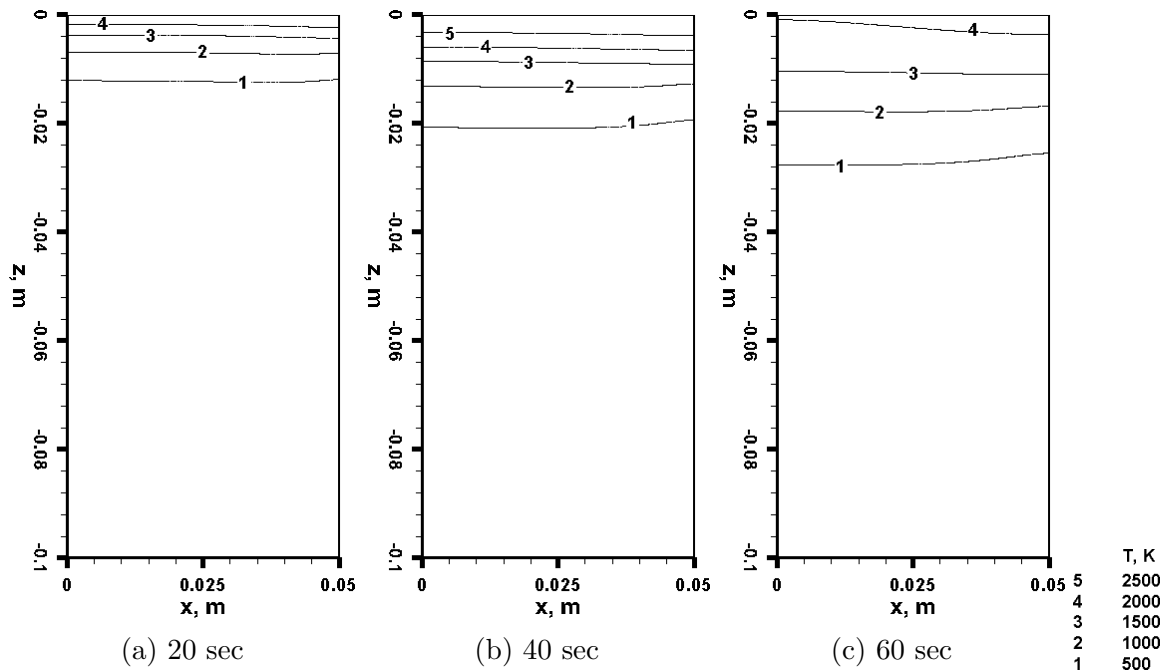


Figure 7.8: Thermal response of permeable side wall cylinder

In the impermeable side wall cylinder case, the pyrolysis gas can only travel upward and exit through the front surface. Therefore, the inner solid material did not experience the extra heating due to the pyrolysis gas; instead, extra energy was carried away with the gas, as it travels upward.

As a brief summary, multi-dimensional pyrolysis gas transport was shown to affect the thermal response of the cylindrical charring ablators considered in this subsection. Use of the 1D model would lead to an under prediction of the in-depth temperatures. This observation is quite important, since ultimately, the inner temperature is most crucial to the design of TPS.

### **Surface gas blowing rates of 3D cylinder cases**

Figure 7.9 shows the surface gas blowing rate the two cylinder cases. The arc length is defined as  $L = \sqrt{x^2 + y^2 + z^2}$ , *i.e.*  $L = 0$  represents the center of the sample at the surface, and  $L = 0.05$  m the top corner of the cylinder.

In Fig. 7.9a, 1D results are also plotted using circles, to again demonstrate the equivalence between the 1D case and the 3D impermeable wall cylinder case. The surface gas blowing rates are uniform curves that are only observed on the front surface. For the permeable wall case, however, the highest gas blowing rate locates at a few centimeters below the corner of the sample, as shown in Fig. 7.9b. The gas blowing rate through the front surface is considerably less significant than through the side wall, which is very different from the 1D assumption.

Table 7.1 shows the gas blowing rate for the 1D and the 3D model, by presenting the integrated mass flow rates for the two cylinder cases. The integrations were performed on the front and side wall surface of each cylindrical slice presented in Fig. 7.1. Since the angle of the cylinder slice is 4 degrees, the blowing rate for the whole cylinder sample will simply be 90 times the current values in the table; the percentage however, will not change. For the permeable side case, the integrated

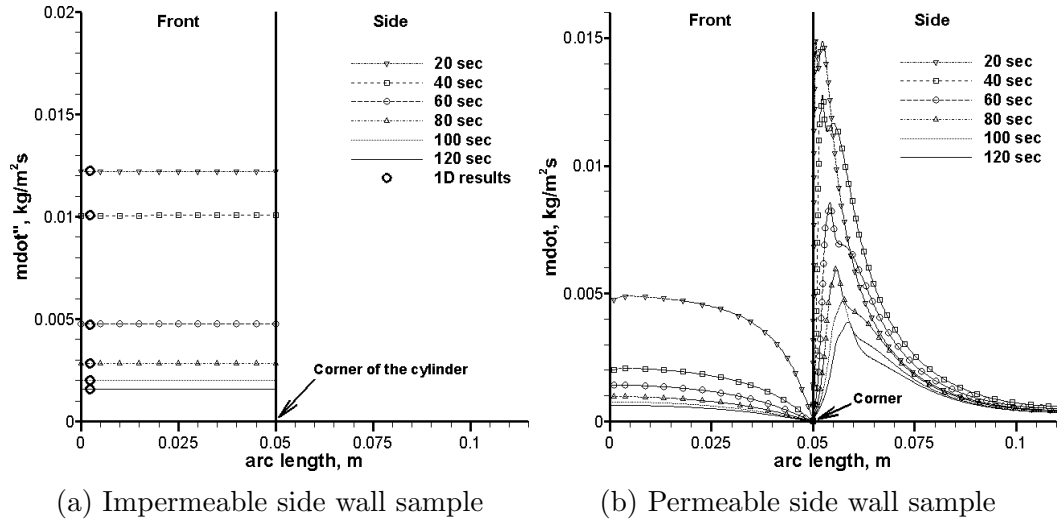


Figure 7.9: Pyrolysis gas blowing rate through surface of cylinder samples

Table 7.1: Gas flow rate through the front and the side wall, for 3D cylinder cases

Case Time, s	Impermeable side		Permeable side	
	Front, kg/s		Front, kg/s	side wall, kg/s
20	$1.07 \times 10^{-6}$ (100%)		$2.96 \times 10^{-7}$ (16%)	$1.60 \times 10^{-6}$ (84%)
40	$8.78 \times 10^{-7}$ (100%)		$1.10 \times 10^{-7}$ (7%)	$1.49 \times 10^{-6}$ (93%)
60	$4.14 \times 10^{-7}$ (100%)		$6.97 \times 10^{-8}$ (7%)	$9.88 \times 10^{-7}$ (93%)
80	$2.46 \times 10^{-7}$ (100%)		$4.59 \times 10^{-8}$ (6%)	$6.89 \times 10^{-7}$ (94%)
100	$1.75 \times 10^{-7}$ (100%)		$3.52 \times 10^{-8}$ (6%)	$5.48 \times 10^{-7}$ (94%)
120	$1.37 \times 10^{-7}$ (100%)		$2.89 \times 10^{-8}$ (6%)	$4.64 \times 10^{-7}$ (94%)

mass flow rate through the side wall is significantly higher than through the front surface, while for the impermeable side case, zero flow rate is seen on the side and the entire pyrolysis gas flow is blown through the front surface. Comparing only the mass flow rates that blow through the front surface, the impermeable side sample has a greater blowing rate than the permeable side one. This is due to the built-up pressure in the impermeable side case, which leads to a larger pressure gradient and thus more front surface blowing.

Hirata et. al. [56] also performed similar simulations, but the pyrolysis gas blowing results were reported to be higher on the front surface than on the side, which is in contrast with the results in this study. The discrepancy might come from the difference in the material models: Hirata et. al. [56] used a constant permeability

for the entire material; in the present study however, the permeability is modeled by interpolation of virgin and char permeability. Note that the material permeability is directly related to the gas flow behavior through the gas momentum equations, therefore it is necessary to properly take into account the permeability model. Other possible sources that might lead to the different conclusions are different boundary conditions and different heating time.

### Effect of the unsteady porous gas momentum equation

As discussed in Section 7.2, the pyrolysis gas momentum equations in this study are given by Eqs. (5.23), which is a time dependent version of Darcy's law. The pyrolysis gas momentum equations are given by Eqs. (5.23) in Section 5.4.

Since most material response codes use the steady state version, it is therefore important to quantify the effect of using the modified equations. Consider the gas momentum equation in  $x$ -direction for instance, Eq. (5.23a) can be rearranged as:

$$\frac{\partial(\phi\rho u)}{\partial t} + \frac{\partial(\phi\rho u^2)}{\partial x} + \frac{\partial(\phi\rho uv)}{\partial y} + \frac{\partial(\phi\rho uw)}{\partial z} = -\frac{\partial p}{\partial x} - \phi\frac{\mu}{K}u \quad (7.1)$$

The right hand side of Eq. (7.1) is defined as the residual in  $x$ -direction:

$$R_x = -\frac{\partial p}{\partial x} - \phi\frac{\mu}{K}u. \quad (7.2)$$

Similarly, the  $y$ - and  $z$ -direction residuals are defined as:

$$R_y = -\frac{\partial p}{\partial y} - \phi\frac{\mu}{K}v, \quad (7.3)$$

$$R_z = -\frac{\partial p}{\partial z} - \phi\frac{\mu}{K}w. \quad (7.4)$$

Therefore, if the steady state Darcy's law is satisfied, the residual  $\mathbf{R} = (R_x, R_y, R_z)$  should be close to zero. The modulus of  $\mathbf{R}$  is plotted in Fig. 7.10, which shows that  $|\mathbf{R}| \gg 0$  in most part of the domain, especially near the boundaries with high blowing rates. Therefore, it can be concluded that a time-dependent Darcian



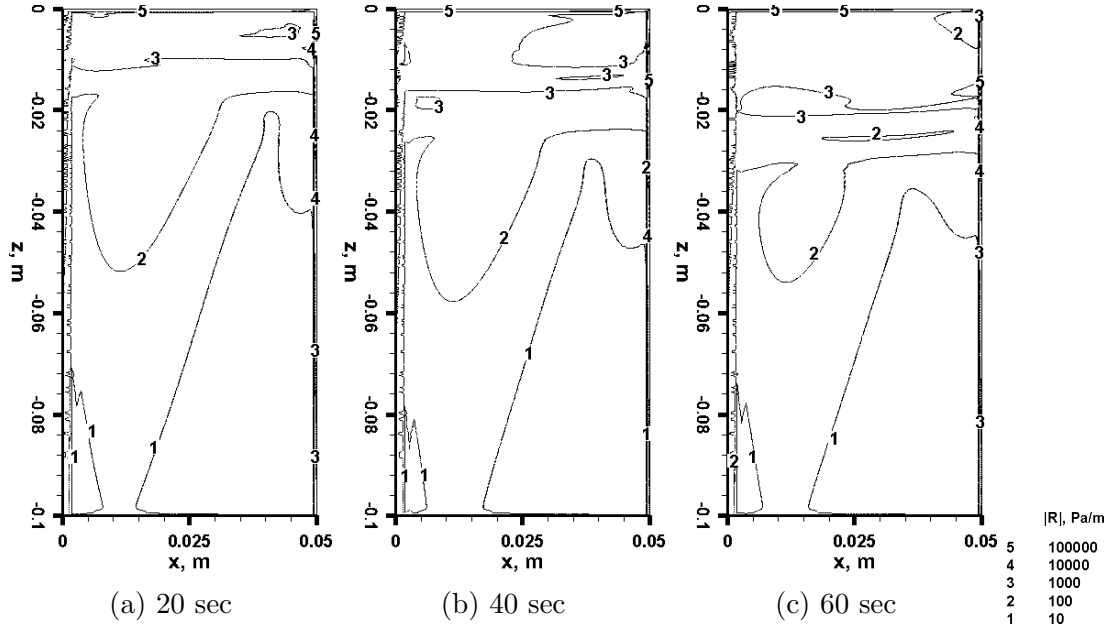


Figure 7.10: Residual  $|\mathbf{R}|$  contours for the cylinder case, using a permeable wall

formulation is necessary for small charring sample simulations.

In order to identify which term is contributing the most to the residual  $\mathbf{R}$ , the modulus of the inviscid flux  $\mathbf{G}$  is plotted in Fig. 7.11. The flux  $\mathbf{G}$  is defined by its directional components  $(G_x, G_y, G_z)$ , where, for instance,  $G_x$  is the time independent terms of the left hand side of Eq. (7.1):

$$G_x = \frac{\partial(\phi\rho u^2)}{\partial x} + \frac{\partial(\phi\rho uv)}{\partial y} + \frac{\partial(\phi\rho uw)}{\partial z} \quad (7.5)$$

In this case, the value is extremely small when compared to  $|\mathbf{R}|$ , which implies that the time derivative in Eq. (7.1) is the main contributor to  $\mathbf{R}$ .

#### 7.4 Iso-Q sample test-cases

For the iso-Q geometry, three test-cases are considered. Figure 7.12 illustrates a sketch of all iso-Q test-cases presented in this study. The first two are similar to the two cylinder test-cases presented in the previous section: one has impermeable side wall and the other has permeable side wall, while the rest of the conditions are identical. The surface heat flux is non-uniform along the iso-Q geometry, and is applied for 40

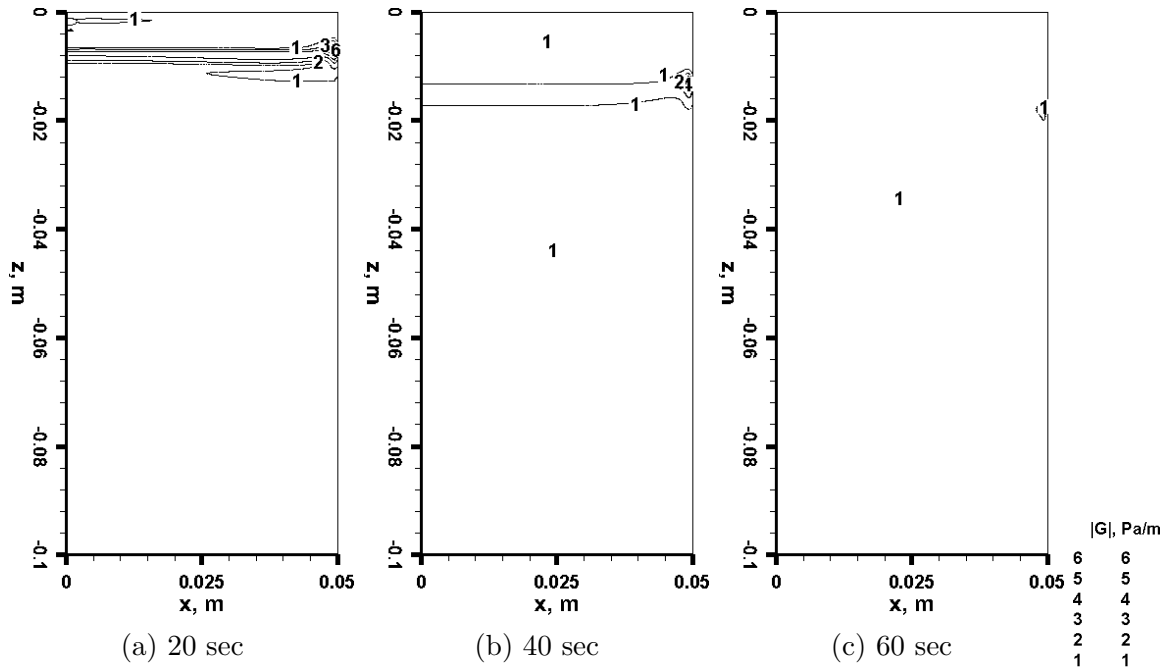


Figure 7.11: Inviscid flux  $|\mathbf{G}|$  for the cylinder case, using a permeable wall

seconds. The heat flux distribution is presented in Fig. 7.13, which is obtained from a CFD simulation [101]. Note that the heat flux applied on the surface of the material is the penetrated heat flux discussed in Section 4.5, which removes the necessity of modeling surface models, such as re-radiation, surface catalysis, and boundary layer corrections. The pressure boundary condition along the surface, however, is uniform for the first two cases. In the last case, the effect of non-uniform pressure boundary condition is explored. The last case uses the permeable wall iso-Q sample as test-piece and applies a pressure distribution shown in Fig. 7.13, in addition to the heat flux distribution. A 20-second linear ramping is used on the pressure distribution, in order to prevent the atmospheric gas from being pulled out immediately through the sample, which causes numerical problems. The ramping profiles for both heat flux and pressure boundary condition are presented in Fig. 7.14.

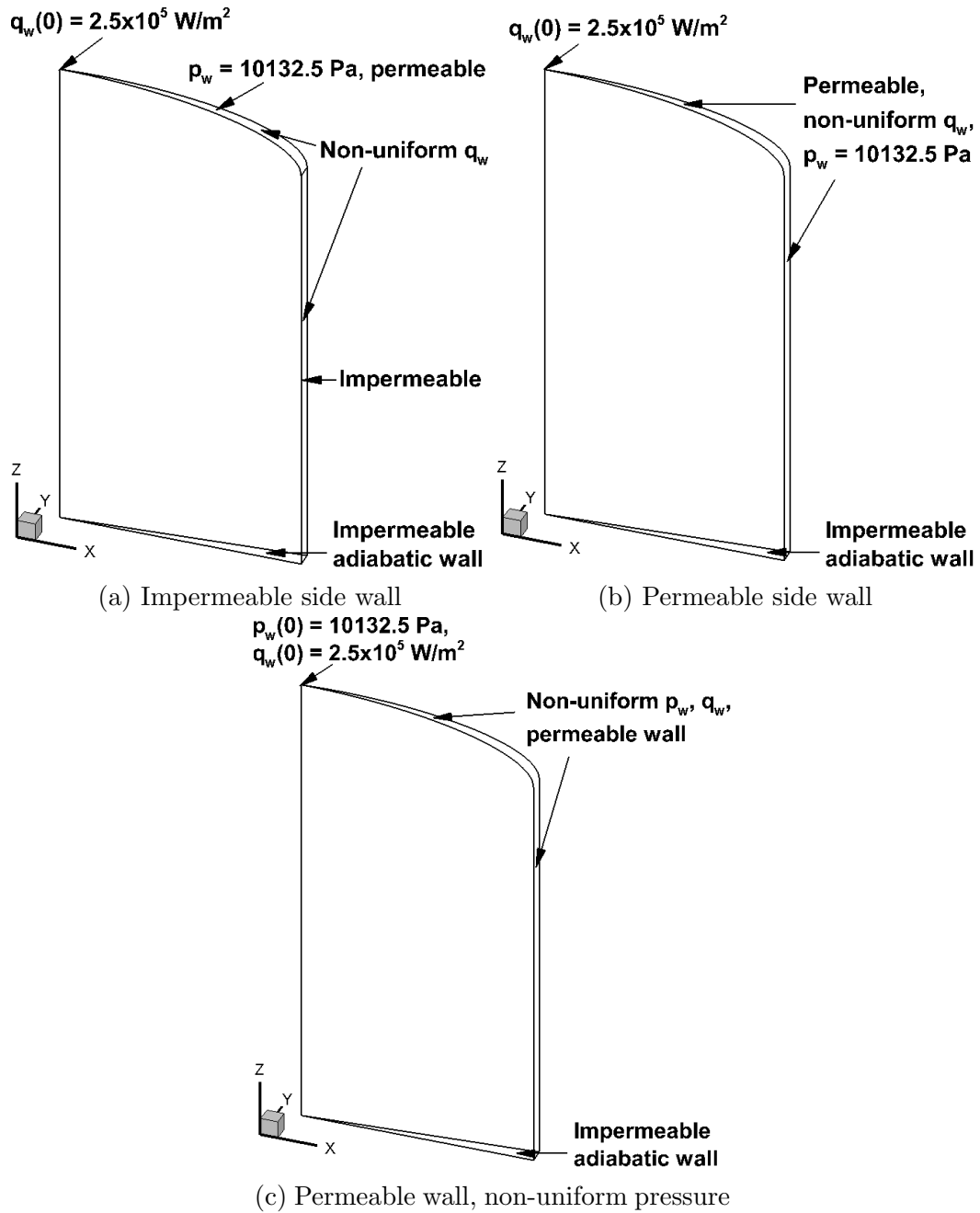


Figure 7.12: Computational geometries and boundary conditions for iso-Q case

### Pressure contour plots for iso-Q samples

In Fig. 7.15, 7.16, and 7.17, pressure contour plots of the three iso-Q test-cases are presented. It is seen from Fig. 7.15 that, the impermeable side wall results in a pressure build-up inside the material, as was the case with the cylinder sample.

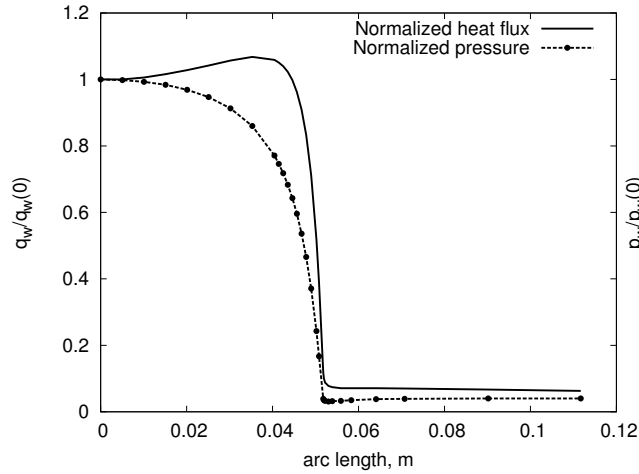


Figure 7.13: Heat flux and pressure distribution [101]

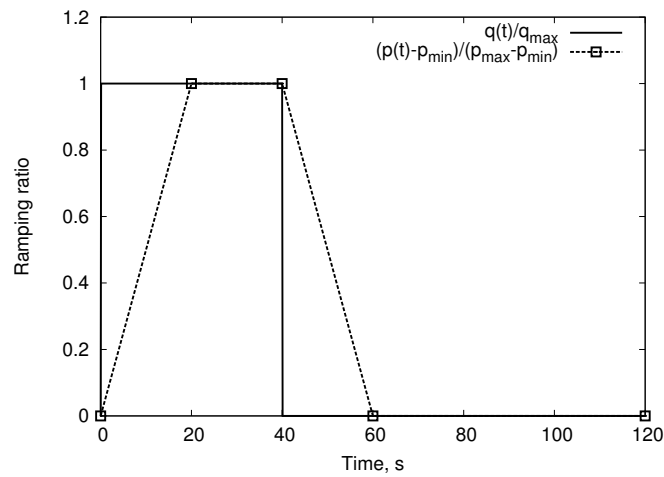


Figure 7.14: Heat flux and pressure boundary conditions ramping

When the side wall is permeable, the inner pressure does not build up and the contour values are less than in the first case, as shown in Fig. 7.16. In the third case with non-uniform surface pressure, the in-depth pressure is even less than the second case. This is due to the pressure gradient applied by the non-uniform pressure profile, which drives the generated gas to flow through the side faster than in the second case.

### Pyrolysis gas flow patterns for iso-Q samples

Figure 7.18 shows the gas flow pattern for the impermeable side sample. It is clear to see that a huge amount of gas blows through the outer corner of the iso-Q geometry.

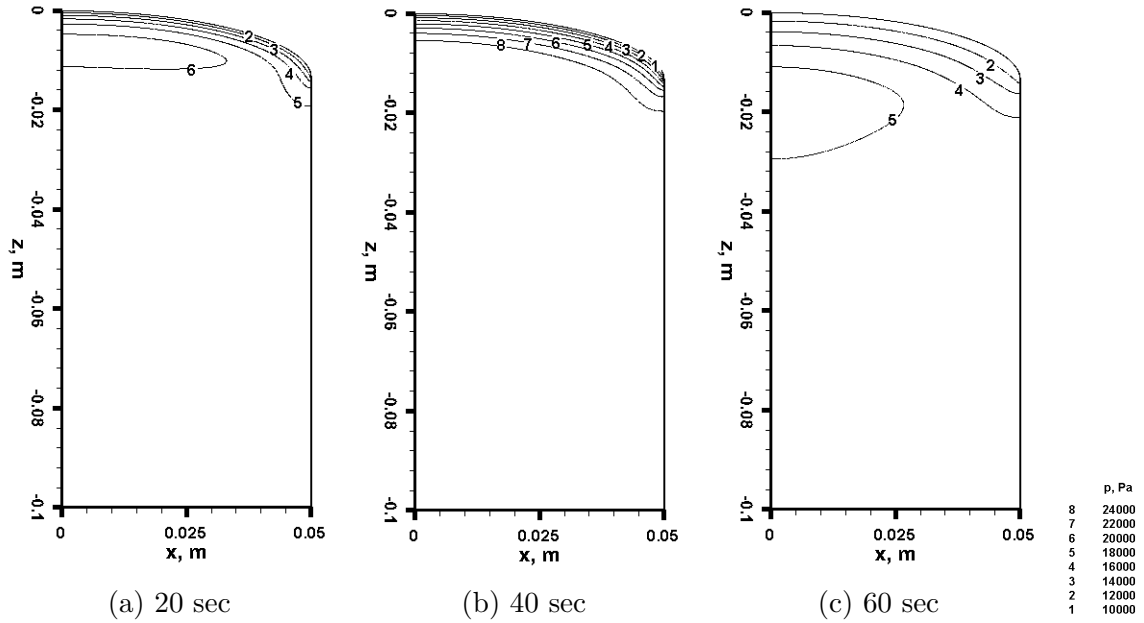


Figure 7.15: Pressure contours of impermeable side wall iso-Q sample

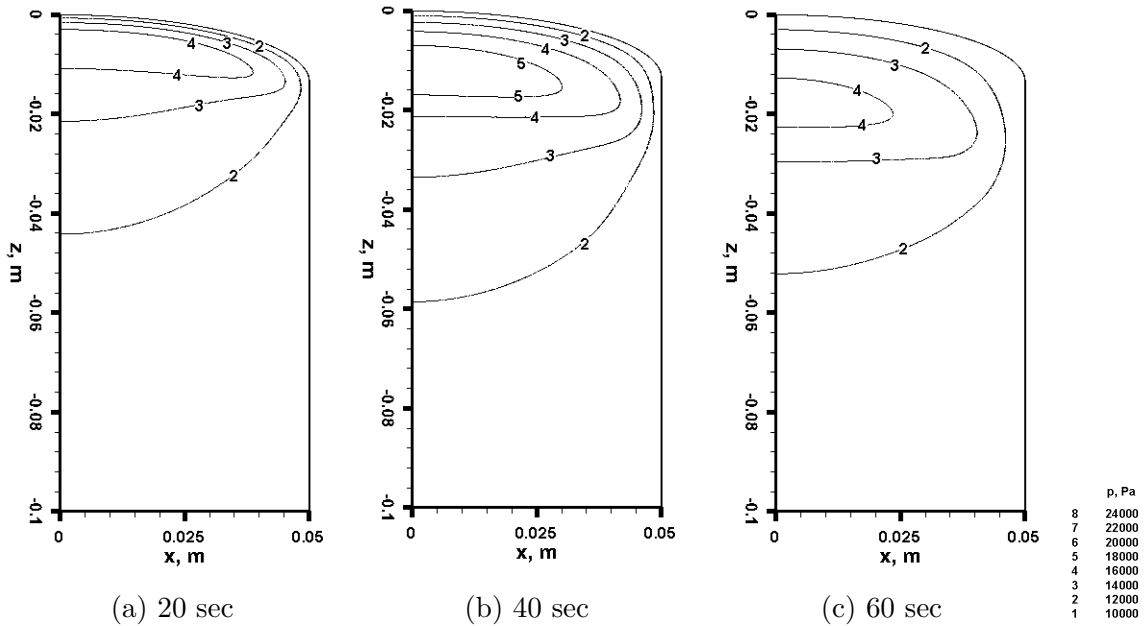


Figure 7.16: Pressure contours of permeable side wall iso-Q sample

Despite the fact that this geometry is very close to the impermeable wall cylinder case, the pyrolysis gas flow patterns are very different. This suggests that, a small change in test-sample geometry may lead to a very different gas flow behavior, and that 3D modeling of pyrolysis gas is of great influence. For the permeable side wall

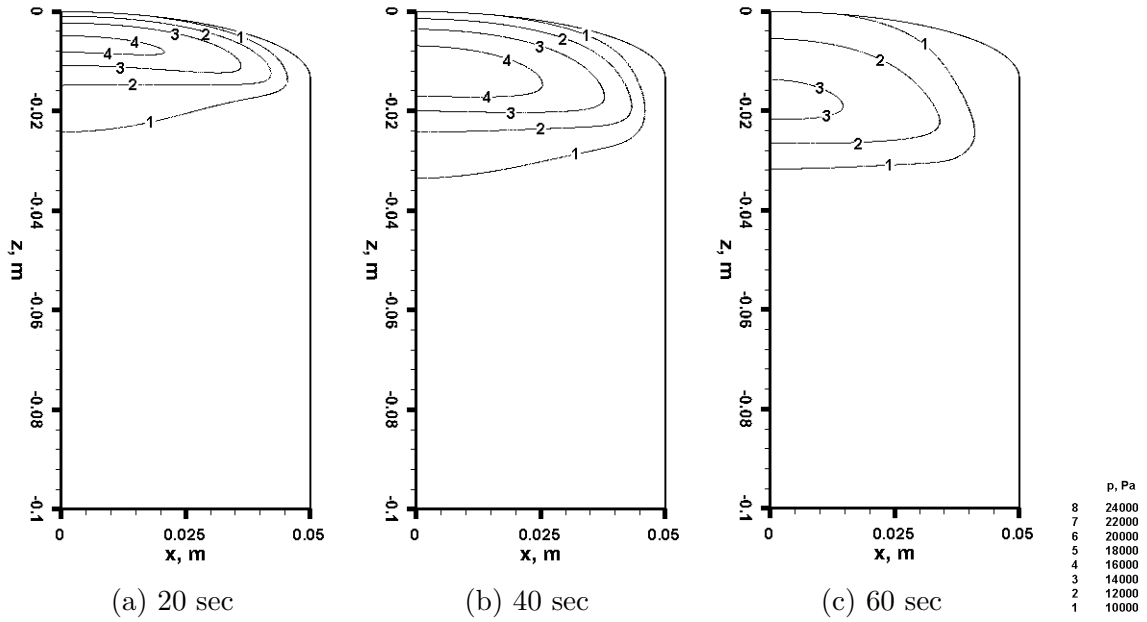


Figure 7.17: Pressure contours with surface pressure distribution

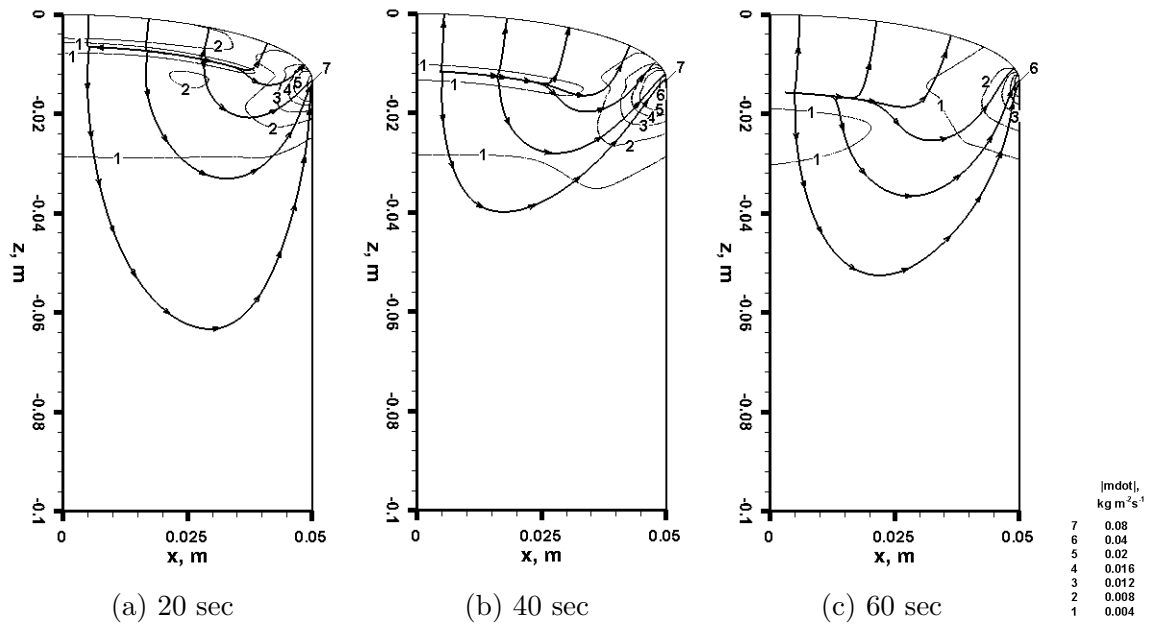


Figure 7.18: Gas mass transport of the impermeable side wall iso-Q sample

case, as is shown in Fig. 7.19, a strong momentum transport layer takes place right below the charring front. This transport shows similar behavior to the permeable side cylinder case: the pyrolysis gas goes inside of the material and rounds toward the sides. When surface pressure distribution is added, the pyrolysis gas behavior

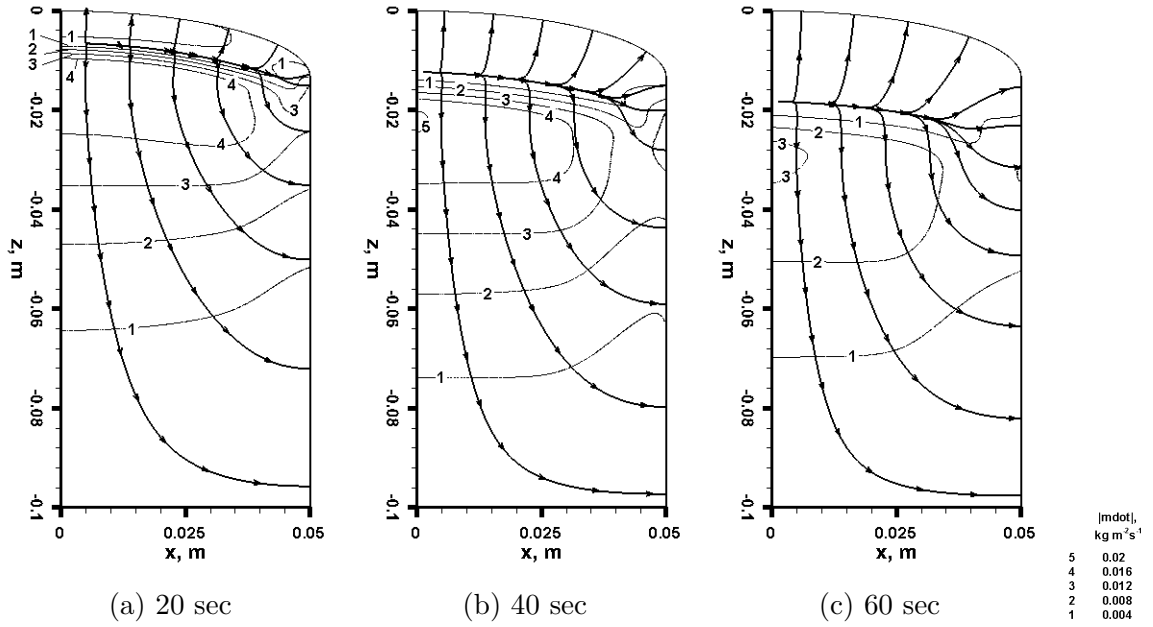


Figure 7.19: Gas mass transport of the permeable side wall iso-Q sample

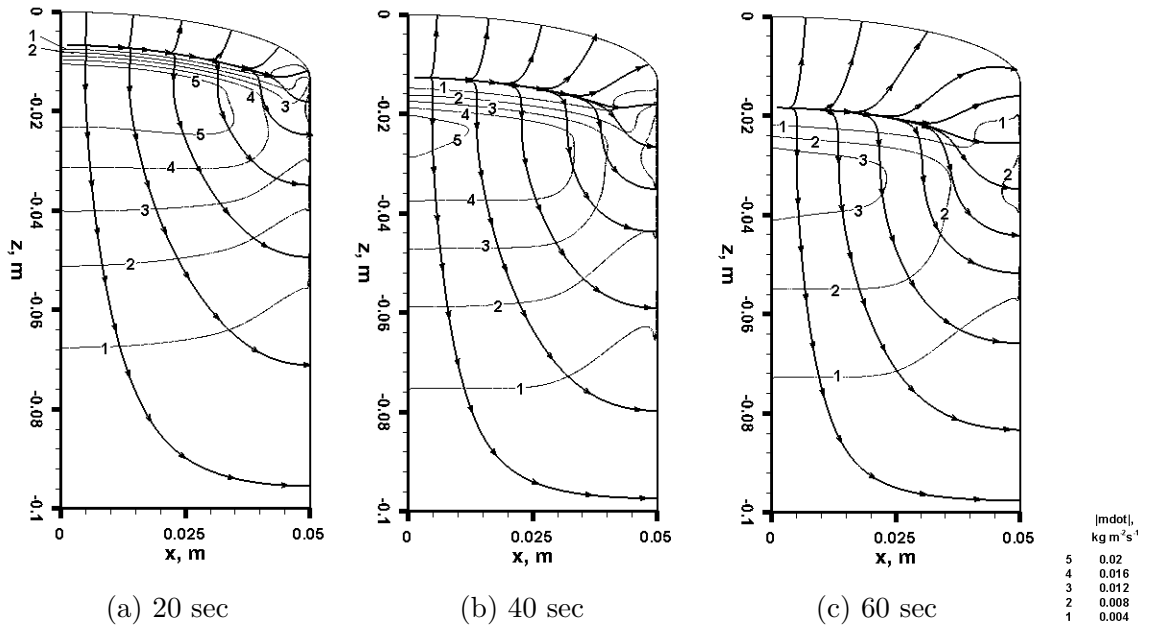


Figure 7.20: Gas mass transport of pressure distribution iso-Q sample

within the material does not deviate much from the second case.

## Surface gas blowing rates of iso-Q test-cases

The profiles of surface gas blowing rate are presented in Fig. 7.21 for all three iso-Q test-cases. The first iso-Q case is a small extension from the impermeable cylinder

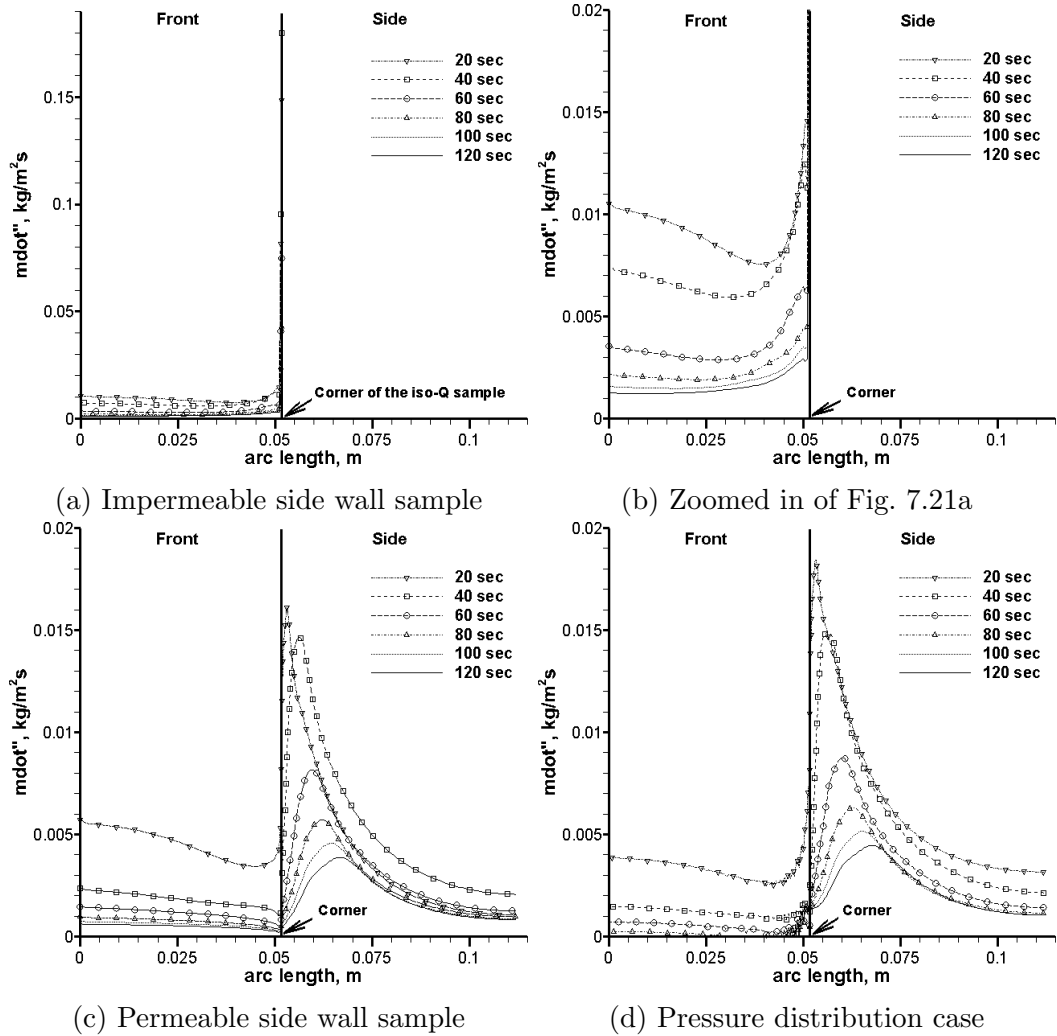


Figure 7.21: Pyrolysis gas blowing rate through surface of isoq samples

case, that only the front surface geometry is changed. However, the surface blowing rate profiles, as shown in Fig. 7.21a, are very different from the impermeable cylinder case: the blowing rate starts from a relative flat value at the front, and as it approaches the end of the iso-Q front, the blowing rate jumps tremendously, indicating a huge amount of gas exits through the corner. The highest blowing rate in Fig. 7.21a located at the corner of the iso-Q sample, and is about an order of magnitude higher than



the blowing rate at the front surface, where as the impermeable cylinder case (1D) only predicted an uniform gas blowing through the front.

For the permeable side case, as shown in Fig. 7.21c, the highest gas blowing rate takes place on the sides, not front. The pyrolysis blowing peak is located right below the shoulder region, and the blowing rate quickly tails down as the side wall reaches the bottom. The blowing rates through the front surface are about half of the values in the first case (impermeable iso-Q).

When non-uniform surface pressure is applied, as depicted in Fig. 7.21d, small differences are observed if compared with Fig. 7.21c: 1) the front surface blowing rate is reduced; 2) the blowing rate peak value on the side is increased; 3) negative blowing (sucking) rate is found on the front surface, long after the heat is removed. These behaviors are the results of applied pressure distribution: due to the pressure gradient enforced by the boundary condition which drives the flow from the front to the side, the gas mass transport to the front is attenuated and the transport to the side is enhanced. When the heat is removed, the generation of pyrolysis gas gradually diminishes, thus making it possible to pull gas inside through the front surface.

Taking a surface integral of  $\dot{m}''$  over the iso-Q slice surface, yields the mass flow rates at the front and side surface. The values of integration are presented in Table 7.2. As expected, all of the gases flow through the front, in the impermeable side wall iso-Q case. For the permeable side case, more than 70% of the gas mass blows through the side; this percentage increases to more than 90% at 40 seconds. When non-uniform pressure distribution is applied, the percentage of the front surface blowing rate is further reduced. At 100 seconds and 120 seconds, the front surface intakes gas from the surrounding flow. Comparing the mass flow rates at the front, the impermeable case blows the most, due to the pressure build-up.

Table 7.2: Mass flow rate blowing from the front and the side wall, for iso-Q cases

Case Time, s	Impermeable side, kg/s	Permeable side, kg/s		Non-uniform pressure, kg/s	
	Front	Front	side wall	Front	side wall
20	$1.30 \times 10^{-6}$ (100%)	$4.17 \times 10^{-7}$ (21%)	$1.57 \times 10^{-6}$ (79%)	$3.45 \times 10^{-7}$ (13%)	$2.33 \times 10^{-6}$ (87%)
40	$1.22 \times 10^{-6}$ (100%)	$1.61 \times 10^{-7}$ (8%)	$1.84 \times 10^{-6}$ (92%)	$1.15 \times 10^{-7}$ (6%)	$1.90 \times 10^{-6}$ (94%)
60	$5.85 \times 10^{-7}$ (100%)	$9.77 \times 10^{-8}$ (8%)	$1.09 \times 10^{-6}$ (92%)	$4.92 \times 10^{-8}$ (4%)	$1.20 \times 10^{-6}$ (96%)
80	$3.78 \times 10^{-7}$ (100%)	$6.53 \times 10^{-8}$ (8%)	$7.94 \times 10^{-7}$ (92%)	$1.28 \times 10^{-8}$ (1%)	$9.16 \times 10^{-7}$ (99%)
100	$2.89 \times 10^{-7}$ (100%)	$5.08 \times 10^{-8}$ (7%)	$6.62 \times 10^{-7}$ (93%)	$-5.85 \times 10^{-9}$ (-1%)	$7.94 \times 10^{-7}$ (101%)
120	$2.40 \times 10^{-7}$ (100%)	$4.23 \times 10^{-8}$ (7%)	$5.87 \times 10^{-7}$ (93%)	$-1.81 \times 10^{-8}$ (-3%)	$7.31 \times 10^{-7}$ (103%)

## 7.5 Conclusions for pyrolysis gas effects study

The pyrolysis gas transport within a small charring ablative material sample was numerically studied by performing a series of simulations on a cylinder and an iso-Q model. As expected, the gas mass fluxes at the surface were significantly different between the 1D and the 3D models: instead of blowing through the front surface, the majority of the gas flew through the side wall. For the iso-Q model, even if the wall was impermeable, most of the gas left the sample through the surface corner. The geometric effect played an important role in the pyrolysis gas transport.

The thermal response of the sample was found affected due to the pyrolysis gas transport. This was explained by the fact that, the generated gas carries a great amount of enthalpy, which further heated the material in the direction of gas flow.

The effect of a non-uniform surface pressure distribution (based on aerodynamics) was also investigated. It was concluded that the surface pressure distribution enhanced the side wall blowing.

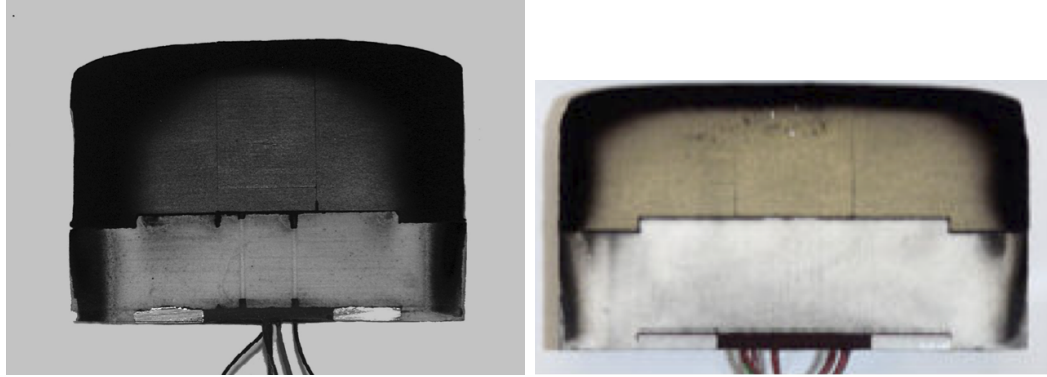
The results of this study suggest that the boundary layer effects might be different from currently assumed, and these effects would be more significant for smaller samples in arc-jet facilities. Moreover, samples with impermeable side wall might not be able to correctly reproduce the interactions between the pyrolysis gas and the solid matrix inside the ablative materials.

As a conclusion, the results of this study have shown 1) contradictory blowing results when compared with the 1D model, 2) the importance of modeling pyrolysis gas flow using time-dependent equations, 3) the effect of non-uniform surface pressure distribution, and 4) the capability of solving multi-dimensional gas transport using the material response module in KATS.

## Chapter 8 Geometric Effects of an Arc-jet Sample

### 8.1 Motivation

The primary approach to test the performance of charring ablative material is to use an arc-jet facility [102]. Arc-jet experiments are performed by passing a gas through an electric arc that energizes the flow. The gas is then accelerated through a nozzle before reaching the material sample mounted in test chamber. The sample shape for these tests is typically flat-faced with rounded corners. One sample geometry in particular, the iso-Q geometry, is increasingly being used for arc-jet experiments. The intent of this geometry is to produce nearly uniform heat flux along its front surface, which should allow the use of a 1D assumption when modeling the experiments [101]. In a validation work conducted by Covington et. al. [103], a series of arc-jet experiments were performed on PICA samples, with three different diameters: 2.54 cm, 5.08 cm, and 10.16 cm. Analyzed using 1D material response code FIAT [34], 2.54 cm and 5.08 cm results showed the best agreement when using an assumption of no pyrolysis gas blowing. The 10.16 cm results, however, were found to have better agreement when pyrolysis gas blowing was considered. These results suggest that the diameter of the sample greatly affects the pattern of gas transport within the interior of the sample. Inspired by this paper, the effect of iso-Q sample geometry is studied in this chapter. In addition, sample-holders used to fix the sample materials in the test chamber, as illustrated in Fig. 8.1, are also investigated to explore their significances to the sample performance.



(a) Covington et. al. [103]

(b) Agrawal et. al. [104]

Figure 8.1: Post-test photos of charring ablative articles with sample-holders

## 8.2 Applied models

The governing equations and applied models used in this study are exactly the same as the ones used in the previous study, which were given in Section 7.2.

## 8.3 Test-case descriptions

In this study, two sets of TACOT iso-Q samples are modeled. The first set of samples aims at studying the effect of sample diameter and thickness, by performing simulations on four different geometries. The specifications of these samples are given in Table 8.1.

Table 8.1: Geometric specifications for Case 1.1 to 1.4

Case #	Sample	$d$ , cm	$h$ , cm
1.1	<i>A</i>	2.5	6
1.2	<i>B</i>	5	6
1.3	<i>C</i>	10	6
1.4	<i>D</i>	10	3

The front surface of all four samples has the same iso-Q curvature, described in Ref. [101]. The surface curvature of each test-case is geometrically scaled with the sample diameter, as depicted in Fig. 8.2a. Using a hypersonic aerothermo-dynamic

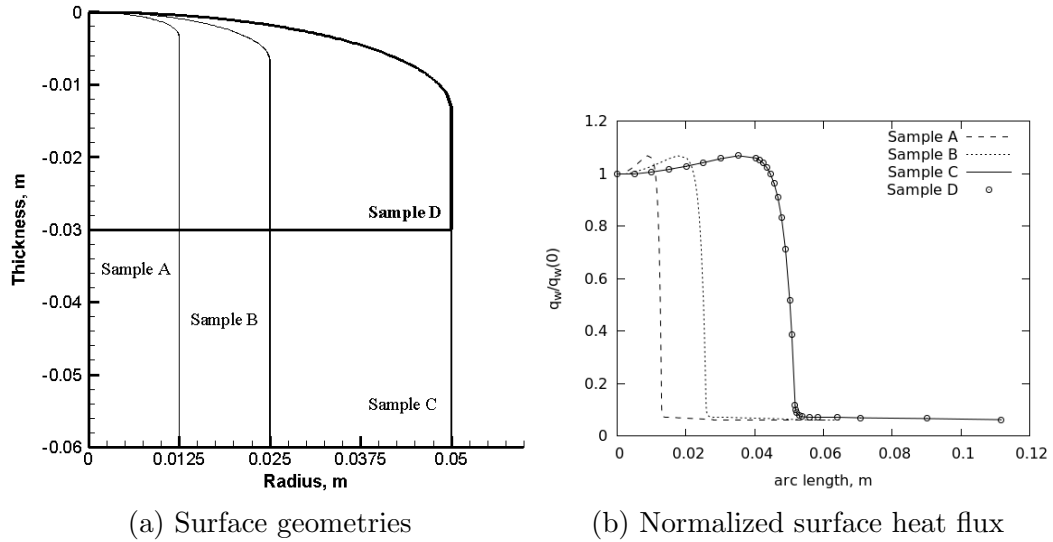


Figure 8.2: Sample geometry and surface heat flux profile for samples *A* to *D*

CFD solver [76] over the geometry of sample *C*, a nominal surface heat flux profile was obtained, which was scaled in proportion to the sample diameters, resulting in the profiles shown in Fig. 8.2. The axisymmetry of the iso- $Q$  geometry allowed the computational domain to be limited to a 4 degree slice around the vertical axis, reducing computational cost. The computational mesh used for simulations of sample *C* is shown in Fig. 8.3. Although the problem is 2D axisymmetric, the KATS code solves the problem entirely in 3D using axisymmetric boundary conditions.

In addition to the cases presented in Table 8.1, a second set of simulations were also conducted. In this set, the geometry of samples *A* to *D* were further modified to represent the effects of mounting the samples on impermeable sample-holders. Geometrically, these modifications take one of two different forms. For samples with small diameters, the exterior surface of the sample is cut away to allow the holder to sheath the exterior of the sample. For larger samples, the back face of the sample is modified as shown in Fig. 8.1 to allow the sample to be fixed onto the holder. Therefore, the geometries were modified as presented in Fig. 8.4. The geometric specifications of these modified samples are presented in Table 8.2. For the larger-style sample-holders, an adiabatic assumption is usually made [103,104]. Specifically,

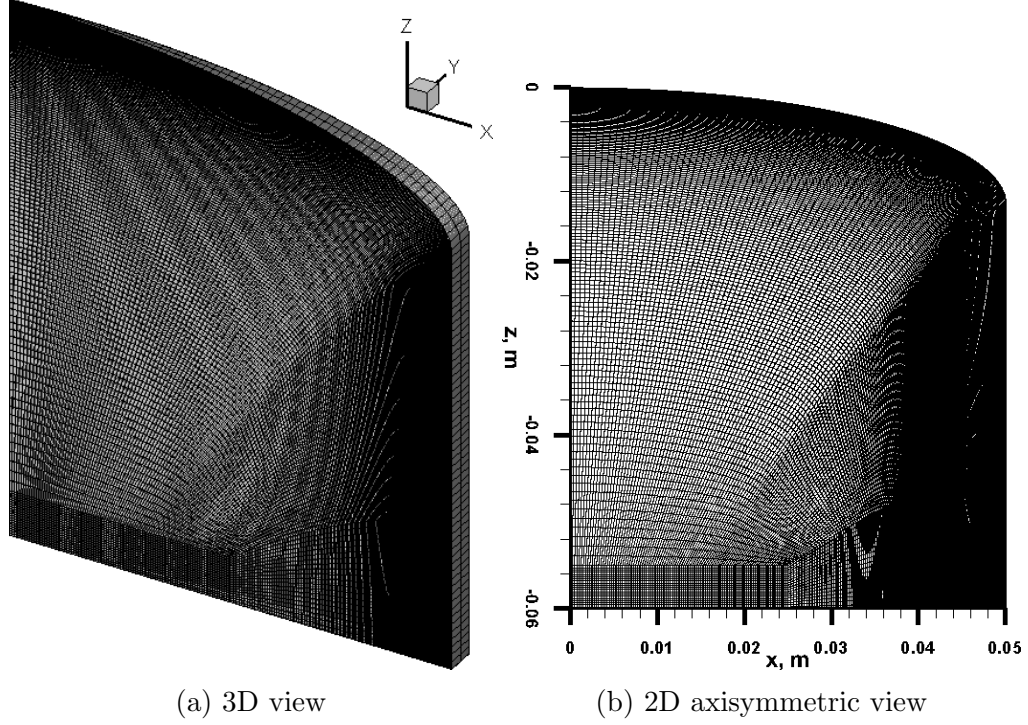


Figure 8.3: Computational grid for sample *C*,  $(100 \times 20 + 150 \times 120) \times 2$  cells

Table 8.2: Geometric specifications for Case 2.1 to 2.4

Case #	Sample	$d$ , cm	$h$ , cm	Sample-holder location $(x_1, z_1)$ to $(x_2, z_2)$ , cm
2.1	<i>A</i> –	2.5	6	(0.75,-6) to (1.25,-4)
2.2	<i>B</i> –	5	6	(1.5,-6) to (2.5,-4)
2.3	<i>C</i> –	10	6	(0,-6) to (3,-5.5)
2.4	<i>D</i> –	10	3	(0,-3) to (3.5,-2.5)

in Ref. [103], alumina enhanced thermal barrier (AETB) was used as the supporting material for the largest diameter sample, and graphite adaptors were used for smaller samples. Since graphite has a very high thermal conductivity, the thermal behavior of the smaller sample-holder is expected to be very similar to the one without the sample-holder. Therefore, the investigation of graphite sample-holders is omitted; the sample-holder materials in this study are all assumed to be impermeable and adiabatic. It is to be noted that some experiments on pyrolyzing ablators have used water cooled sample-holders [105, 106].

The initial and boundary conditions of the two sets of simulations were identical,

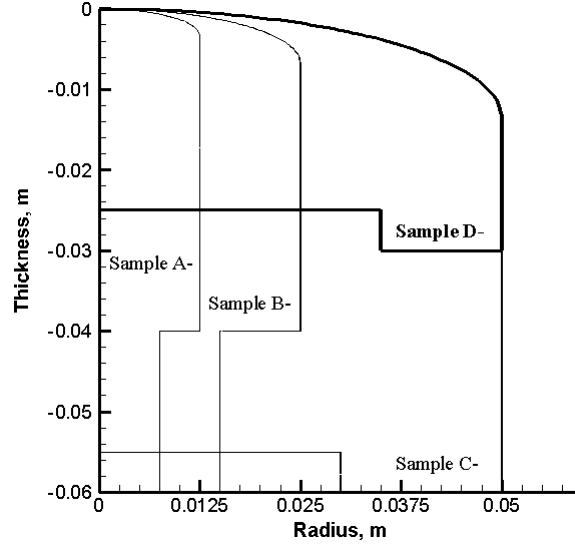


Figure 8.4: Geometry for samples A– to D–

and were adopted from the arc-jet experiments of Ref. [103]. These conditions are summarized in Table 8.3. Note that, along the iso-Q sample surface, the pressure

Table 8.3: Initial and boundary conditions

Initial conditions			Boundary conditions	
$p$ , atm	$T$ , K	$\phi$	$p$ , atm	$q_w(0)$ , W/m <sup>2</sup>
0.65	298	0.8	0.65	10 <sup>6</sup>

boundary condition is uniform, as opposed to the heat flux boundary condition, which follows the curves shown in Fig. 8.2b. The effect of a non-uniform pressure boundary condition was previously discussed in Chapter 7. In general, the front surface pressure profile is relatively flat, but drops quickly around the shoulder of the sample. This enhances the side wall pyrolysis gas blowing as it creates a pressure gradient between the front surface and the sides. In order to minimize the parameters varied for this study, and isolate the pyrolysis gas transport caused by the geometry, and not the outside pressure gradient, the pressure distribution on the surface of the sample was uniform for all test-cases.

The geometry of the sample was fixed and was therefore not changing with time: surface recession (surface ablation) was not taken into account. The heat flux applied



at the surface was a penetrated heat flux, as discussed in Section 4.5. It is to be noted that when changing the diameter of samples, the stagnation heat flux and the heat flux profile will also change if the free stream conditions remain the same. In order to limit the parametric variables to a minimum and attempt to only look at the effects of the geometry, all heat flux boundary conditions were set to be identical. For each case, the heat flux was applied constantly from  $t = 0$  to 20 s, then linearly ramped down to zero over the next 0.1 seconds. The thermal boundary condition became adiabatic from  $t = 20.1$  to 30 s when the simulation was stopped. Again, these heat flux values were all based on the penetrated heat BC discussed in Section 4.5, which reduces the complexity of the problem by removing models that are themselves prone to uncertainties.

#### 8.4 Results and discussions

For each test-case, the transient results are presented in three contour plots, one streamline plot, and one surface line plot. The contour plots show the distributions of temperature, porosity and  $|m|$ , which correspond to thermal response, material response, and the scale of local gas momentum, respectively. The streamline plot is an indication of the gas transport direction, and the line plot shows the gas blowing rate along the surface. For samples  $A$  to  $D$ , a grid independence study was performed and is presented for each mesh. It is to be noted that for identical geometry and boundary conditions, the results may vary significantly depending on mesh. Therefore, grid independence is vitally important in material response simulations. Here, a grid independence study was not conducted on samples  $A-$  to  $D-$  as these meshes are subsets of the meshes used for sample  $A$  to  $D$ . For samples  $A$  to  $D$ , the grid independence study results are presented within the discussion of the results from each sample.

## First set: effect of sample diameter and thickness

### Case 1.1

As the first test-case, the 0.0125 m radius iso-Q sample *A* is considered. Figure 8.5 shows the evolution of temperature within the sample from  $t = 5$  to  $t = 30$  s. It can be

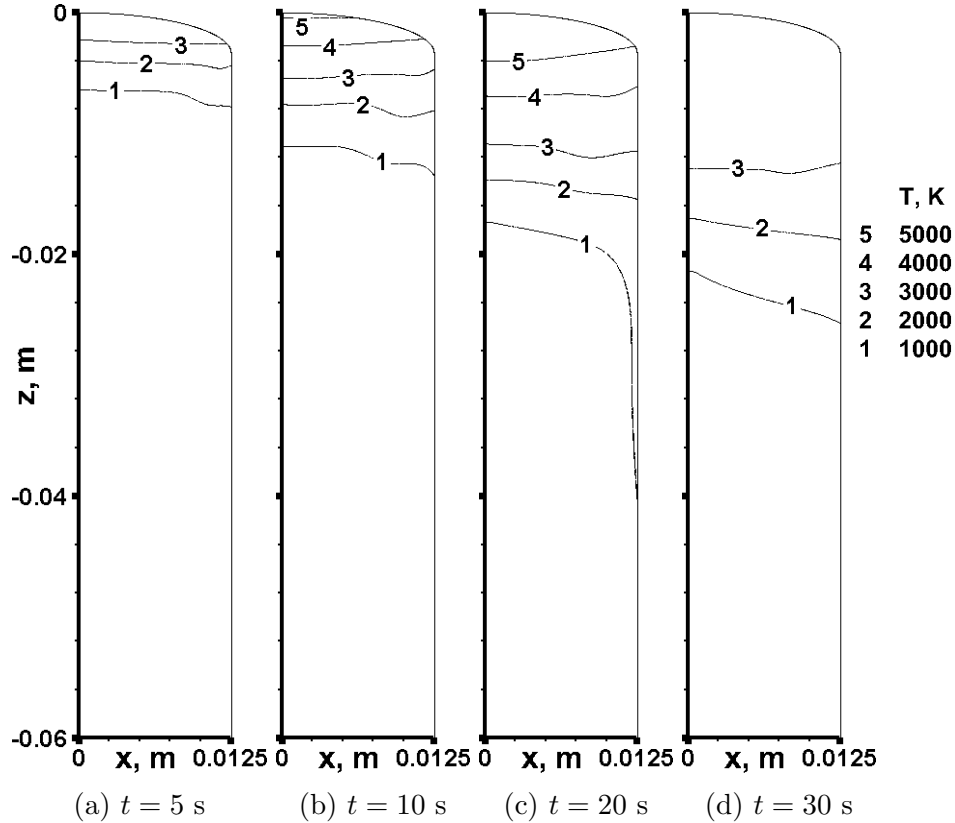


Figure 8.5: Temperature contours for sample *A* (Case 1.1), at various times

seen that at  $t = 5$  s, the temperature contour lines are almost paralleled to each other, reflecting the intended behavior of the iso-Q sample geometry. This is true except near the side face, where there is a small but noticeable inflection in temperature (most noticeable through contour line 1) due to the non-uniform heat flux applied on the surface. The heat flux at the sample shoulder, as shown in Fig. 8.2, is noticeably higher than the stagnation heat flux. Similarly at  $t = 10$  s, the inflection is observed on contour 2. At  $t = 20$  and 30 s, it is also noticeable on contour 3.

Figure 8.6 depicts the corresponding porosity contours for sample *A*. Note that

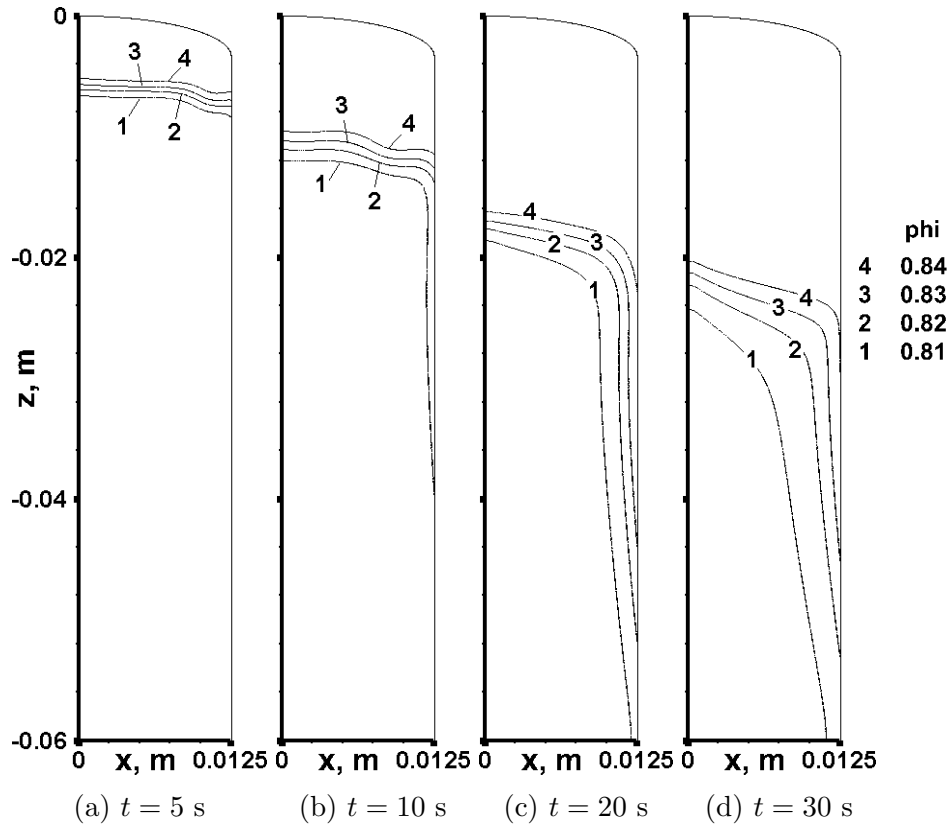


Figure 8.6: Porosity contours for sample *A* (Case 1.1), at various times

TACOT has a virgin porosity of 0.8 and a char porosity of 0.85. Since the material porosity is modeled as a linear function of degree of char, as alluded in Eq. (5.3), the porosity plots reflect the pyrolysis and char zone. It is seen from Fig. 8.6 that the material above contour line 4 is charred and the region between contour line 1 and 4 is the pyrolysis zone. At  $t = 5$  and 10 s, there are inflections in the porosity near the side wall, which is similar to the inflections observed in temperature. This is expected because the charring process is directly linked to the heat penetration. At  $t = 20$  and 30 s, the inflection in the porosity due to the shoulder heat flux disappears, but the heat flux from the side wall forms vertical pyrolysis zone near the side wall.

Figure 8.7 and 8.8 show the pyrolysis gas transport behavior within sample *A*. The divergence of streamlines in Fig. 8.8 indicates the location of the charring front, where material decomposes and generates pyrolysis gases. Mapping the streamlines onto Fig. 8.7, it can be seen that the greatest amount of gas transport takes place

slightly below the charring front and its direction is downward. Also a fast-moving region is identified near the shoulder region of the sample, where pyrolysis gases are expelled out of the material through the side wall.

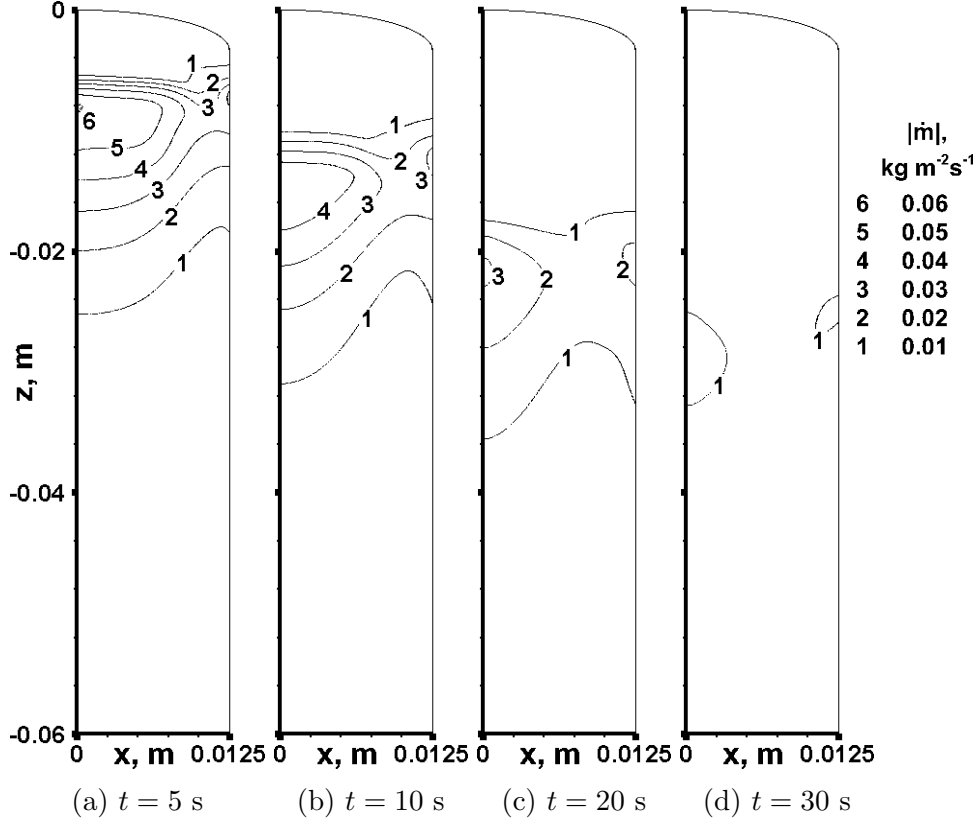
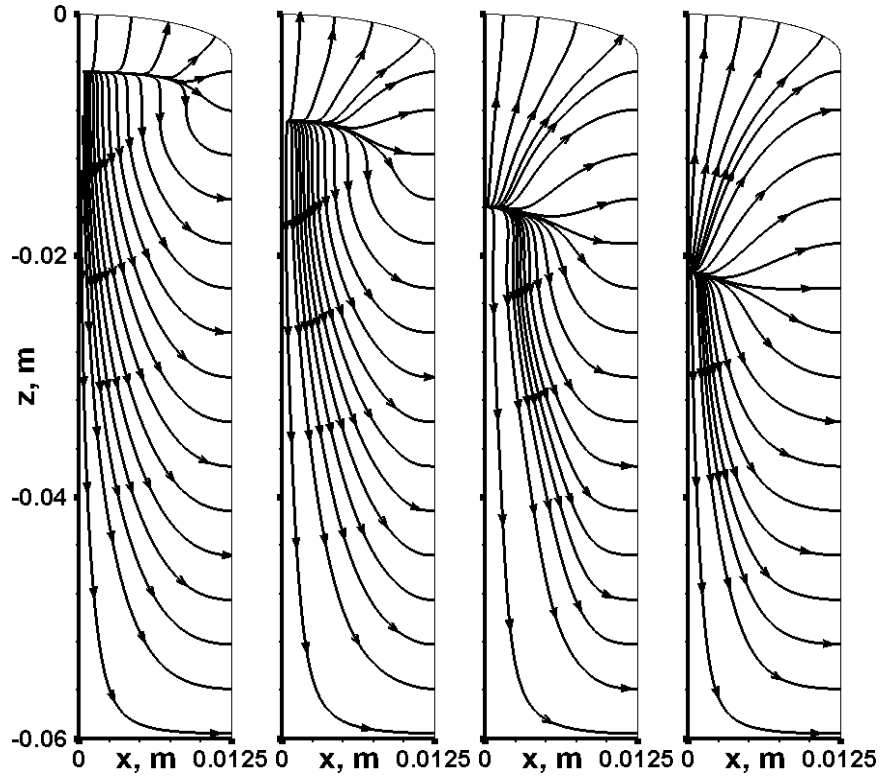


Figure 8.7:  $|\dot{m}|$  contours for sample *A* (Case 1.1), at various times

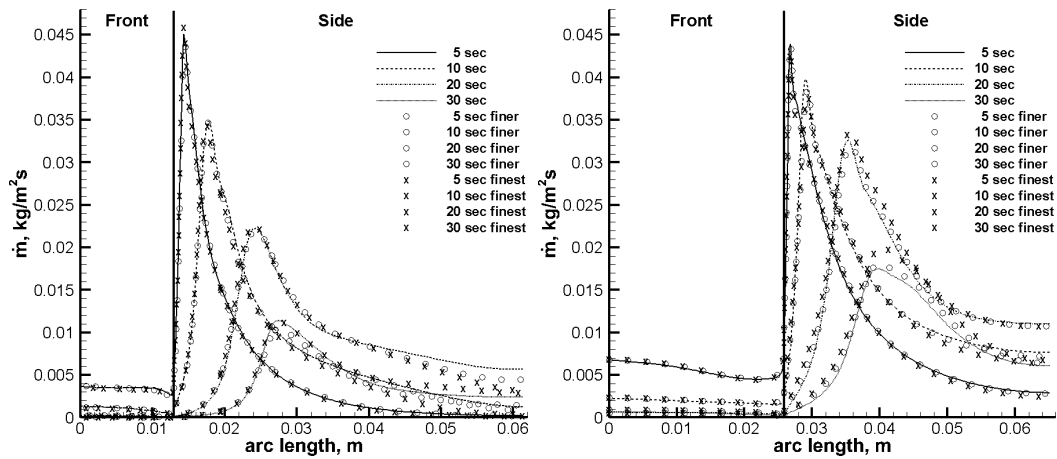
Figure 8.9a shows the normal blowing rate along the sample surface, using three different refinements of mesh. The results obtained on the evaluated mesh are presented in lines, while the results on the finer and finest mesh are depicted by circles and crosses, respectively. Compared with the evaluated mesh, the grid spacing on the finer mesh is halved and it is only one-third on the finest mesh. It is seen from Fig. 8.9a that the lines and symbols coincide except for the portion corresponding to the lower half of the side wall, when  $t > 5$  s. The discrepancies are due to the less-refined mesh in the region, since in most of the time, the lower part of sample *A* barely reacts and the phenomena are less complicated than the upper part where pyrolysis and charring take place. Apart from the bottom region, the rest of the mesh



(a)  $t = 5$  s      (b)  $t = 10$  s      (c)  $t = 20$  s      (d)  $t = 30$  s

Figure 8.8: Gas streamlines for sample A (Case 1.1), at various times

is well refined, and the contour plots are very comparable. Note that the surface gas blowing rate is one of the most grid-sensitive results, since it contains five primitive variables in the formulation.



(a) Sample A on 3 refined-levels

(b) Sample B on 3 refined-levels

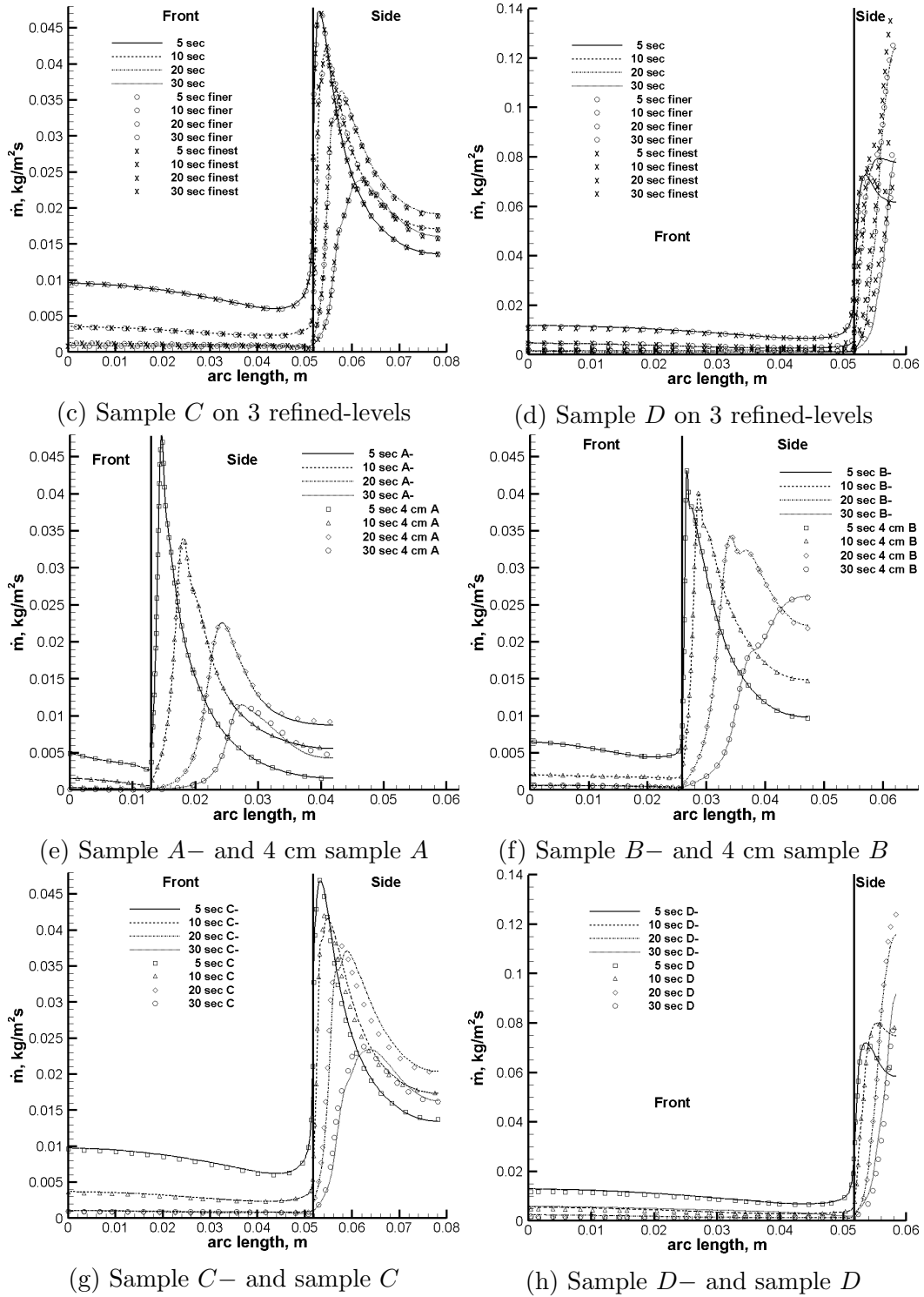


Figure 8.9: Gas mass flow rate through the surface of iso-*Q* samples

In Fig. 8.9a, it is seen that the location of maximum blowing is located on the side wall during the entire simulation time. As time proceeds, the peak blowing loca-

tion shifts downwards and the magnitude decreases. Front surface blowing however, remains at a relatively low level. These results are very different from the usual 1D model, where pyrolysis gases are assumed to blow through the front surface only. A detailed comparison and discussion between the 1D and 3D model was presented in Chapter 7.

### Case 1.2

The time evolution of temperature within sample *B* are shown in Fig. 8.10. The results are qualitatively very close to sample *A* in that the contour lines are largely parallel to each other, except for the perturbations near the side boundary, which is likely due to the directional side wall heating.

The evolution of porosity shown in sample *B* (Fig. 8.11) displays similar behavior to that of sample *A*. Also similar to sample *A* is the pyrolysis gas mass transport, shown in Fig. 8.12 and 8.13. These results also indicate the existence of two large mass transport regions: the highest located right below the charring front, moving downward and the other is below the shoulder, near the side wall, moving outward.

Figure 8.9b presents the normal gas blowing rate along the surface of iso-Q sample *B*. The results on the finer and finest mesh are also presented. However, unlike for sample *A*, for sample *B* the finer mesh was only 1.5 times refined and the finest mesh was 2 times refined to the evaluated mesh, so as to reduce the computational cost. It is clear to see from Fig. 8.9b that the results on different meshes are almost the same, except for the peak blowing point at  $t = 30$  s, which due to a large time step size and/or the less-refined mesh on the side near the lower portion of sample *B*. This suggests that the evaluated mesh is mostly grid-independent. Comparing Fig. 8.9b with sample *A* shows small but observable differences: the mass blowing rate from the front surface is increased; the peak value of side wall blowing drops at  $t = 5$  s, but is increased at  $t = 10, 20,$  and  $30$  s; and the mass blowing near the bottom of the

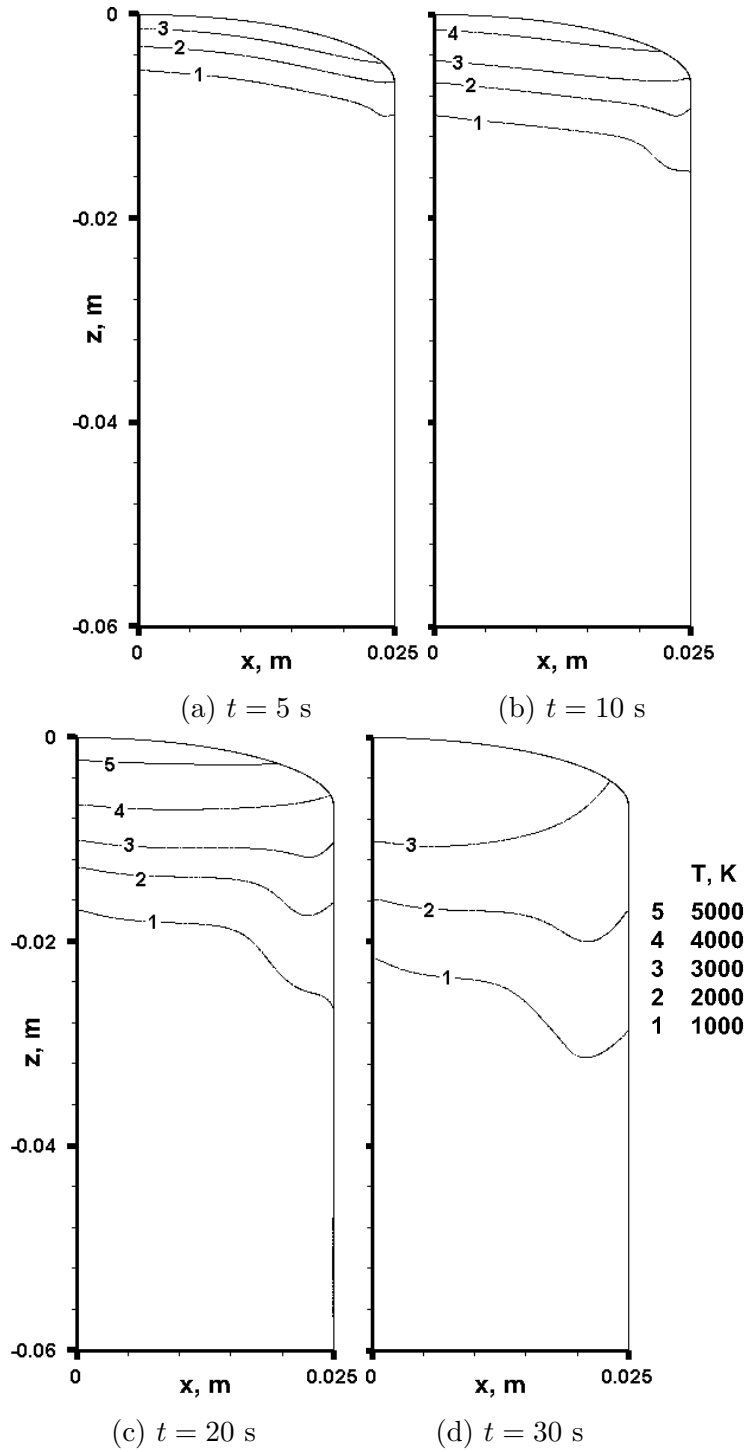


Figure 8.10: Temperature contours for sample *B* (Case 1.2), at various times

side wall rises. These results indicate that by changing the sample diameter, the gas blowing behavior is also changed on both the front and the side surface.



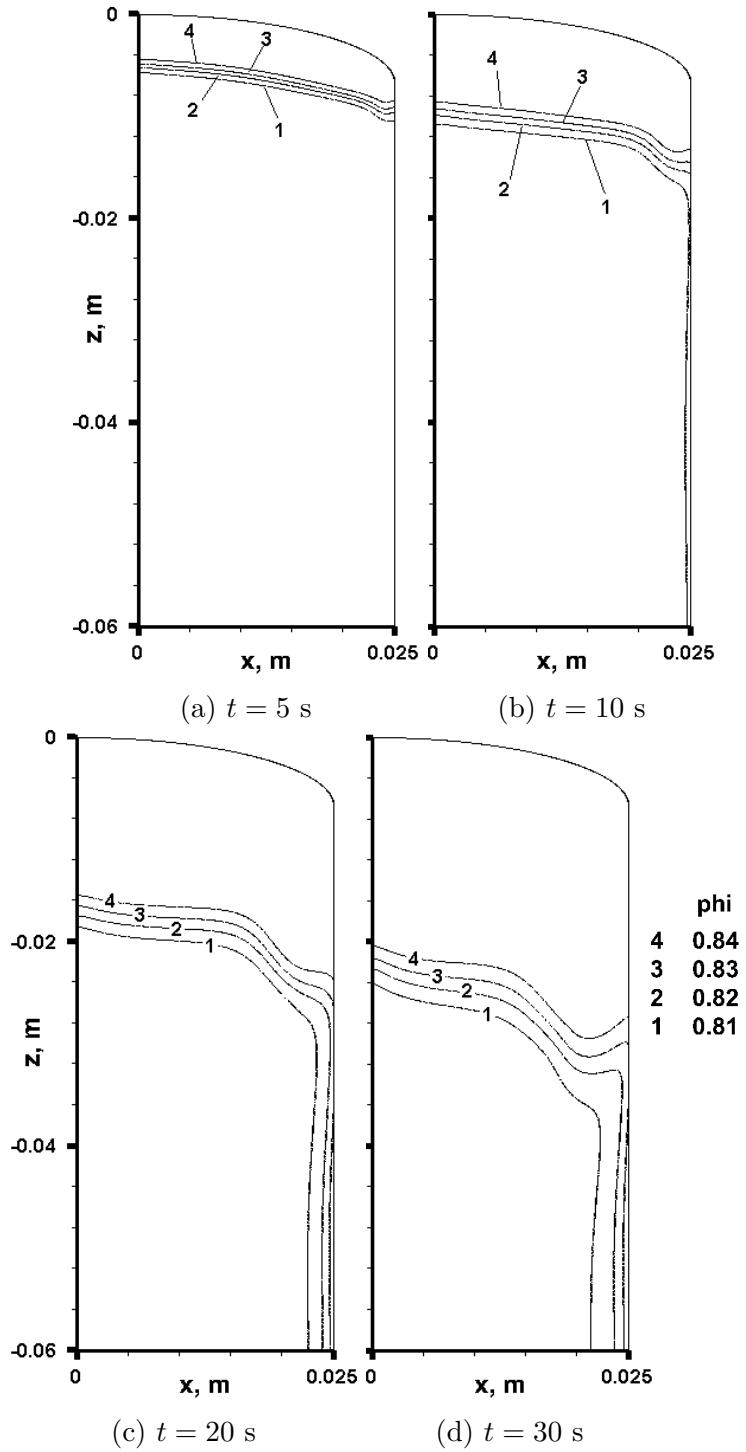


Figure 8.11: Porosity contours for sample *B* (Case 1.2), at various times

### Case 1.3

Iso-Q sample *C* in Case 1.3 has a diameter twice that of sample *B*. Its thermal response to the applied heat flux is displayed in Fig. 8.14.

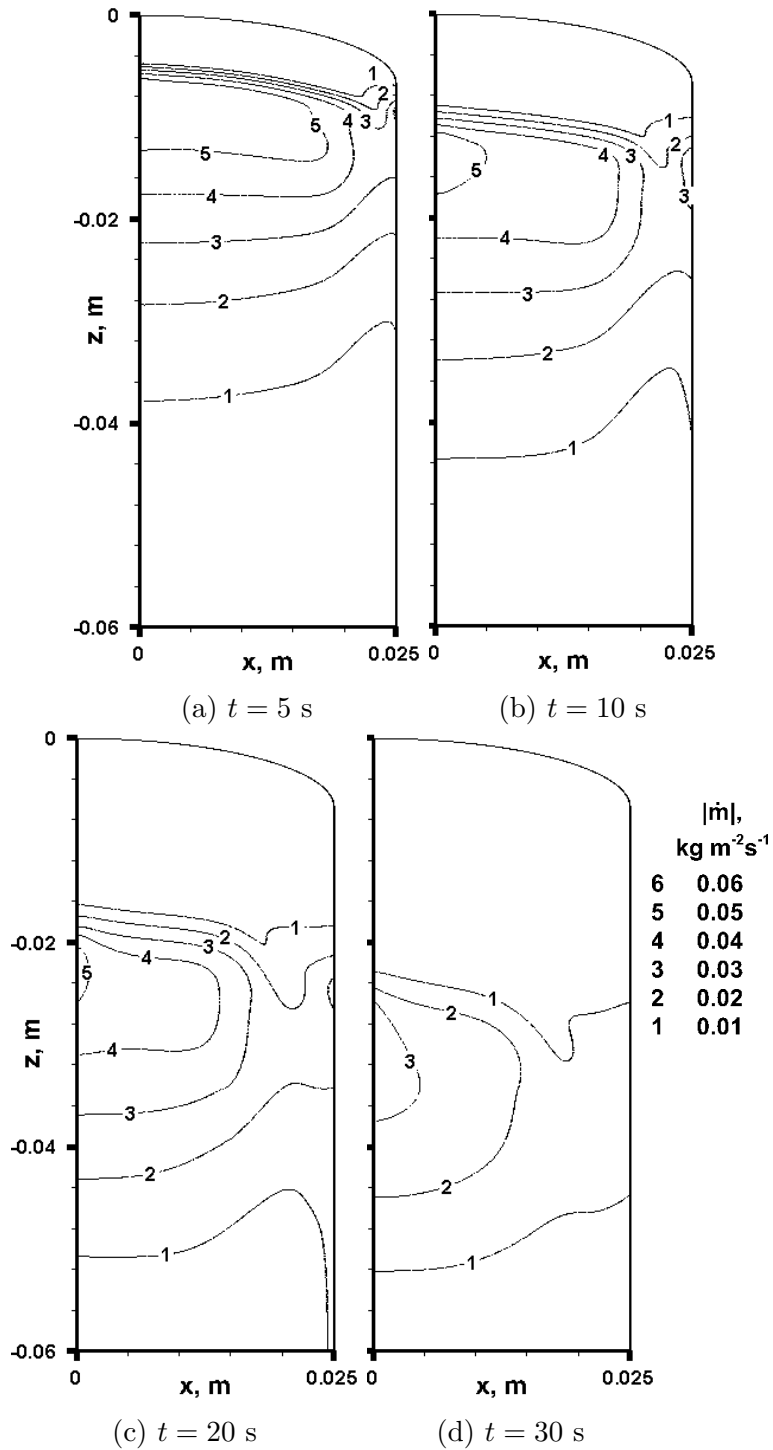


Figure 8.12:  $|\dot{m}|$  contours for sample *B* (Case 1.2), at various times

For sample *C*, the temperature contours mostly remain parallel to the front surface curvature throughout the length of the simulation. The small perturbations noticed in Figs. 8.14c and 8.14d are due to the geometry and heating from the side wall.

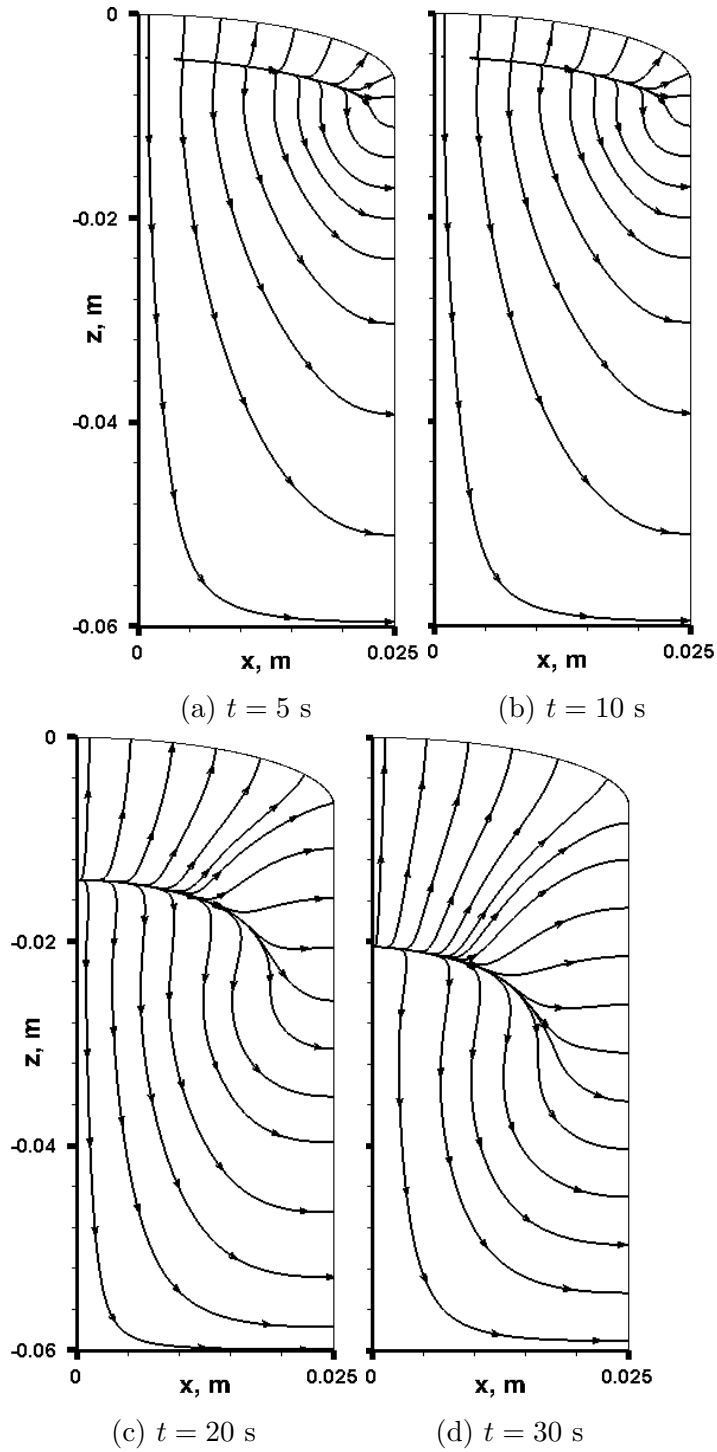


Figure 8.13: Gas streamlines for sample  $B$  (Case 1.2), at various times

Porosity, as depicted in Fig. 8.15, shows similar time evolution to that of temperature, although with much more localized gradients. Thus, for this sample diameter, the iso-Q geometry behaves as intended and closely approximates 1D behavior.

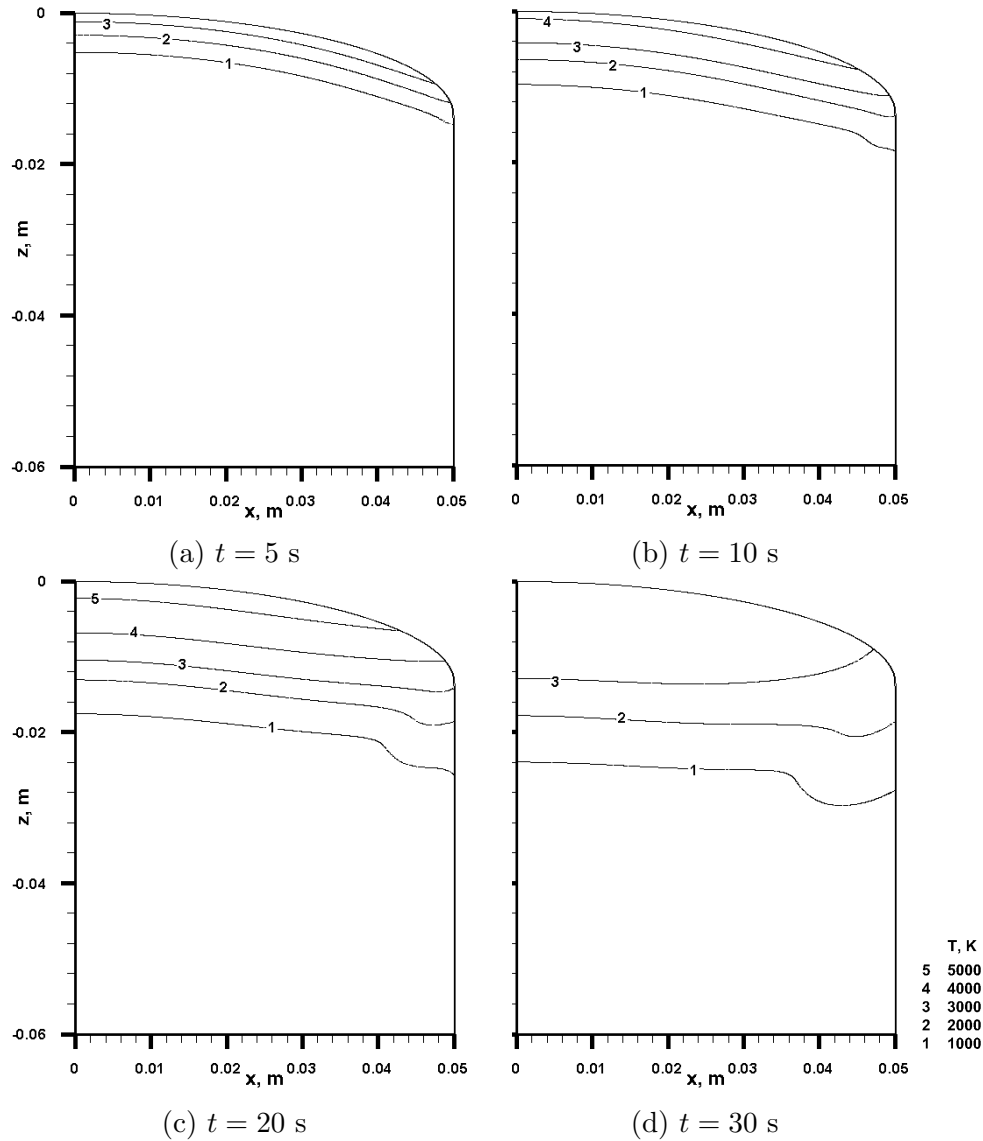


Figure 8.14: Temperature contours for sample *C* (Case 1.3), at various times

Gas mass transport for sample *C* is presented in Figs. 8.16 and 8.17 for magnitude and direction, respectively. It can be observed from Fig. 8.16a that the largest mass transport region is located between the center and the side wall. Over time, as shown in Fig. 8.16b, the location of greatest mass flux migrates towards the center of the sample. As with the other samples, the direction of pyrolysis gas motion is away from the char front, downwards and outwards.

Figure 8.9c shows pyrolysis gas blowing through the surface of sample *C*. The evaluated mesh, whose results are plotted in lines, was again refined to 1.5 times and

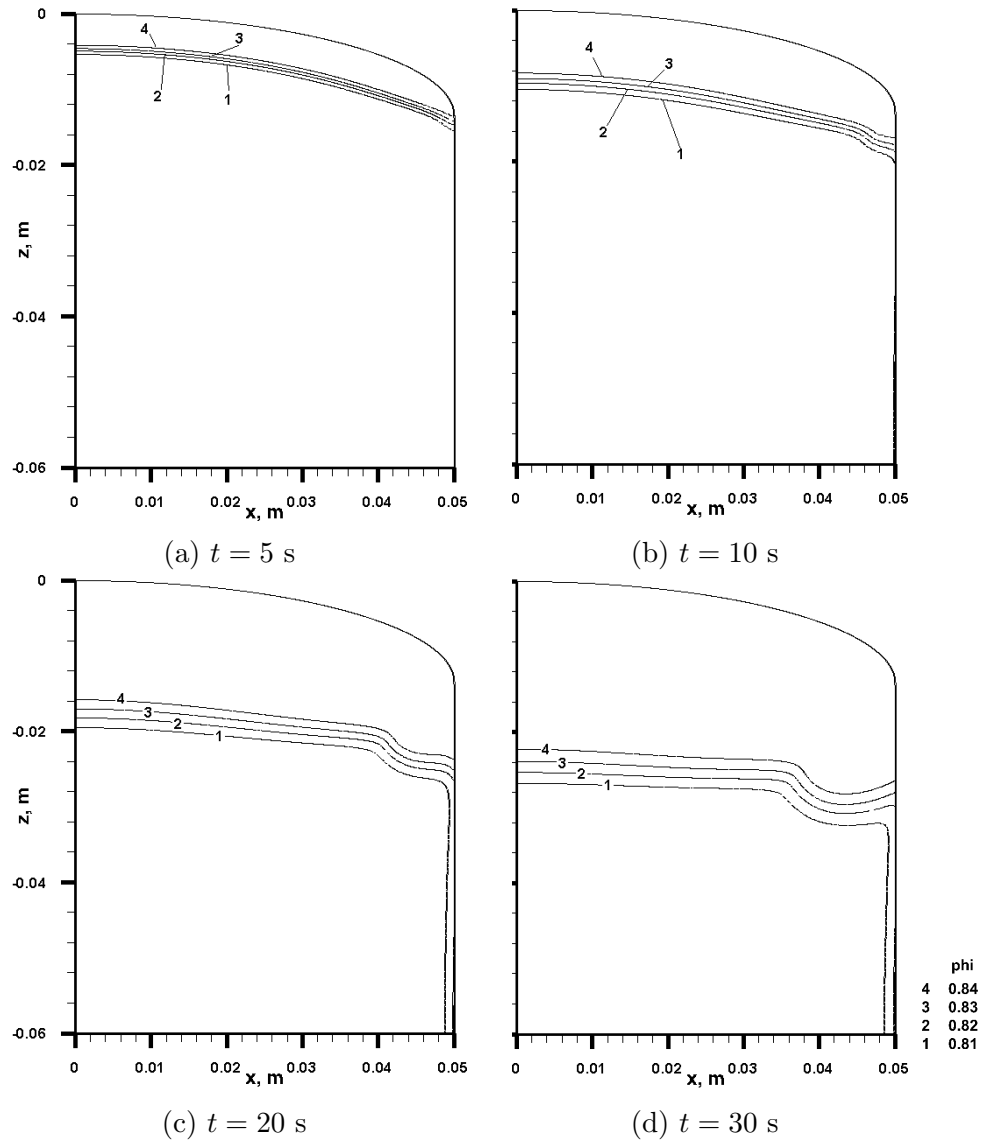


Figure 8.15: Porosity contours for sample  $C$  (Case 1.3), at various times

2 times, corresponding to the finer mesh and finest mesh in the figure. It is seen from these results that they are very close to each other, which indicates a well-refined mesh and a grid-independent solution. As is seen in Fig. 8.9c, although the blowing rate through the front surface is still less than through the side wall, it is much greater than in previous cases. Also, the blowing rate at the lowest bottom of the side wall is increased. This suggests that the larger the sample diameter, the greater the blowing rate through the front surface, and closer to the 1D assumption.

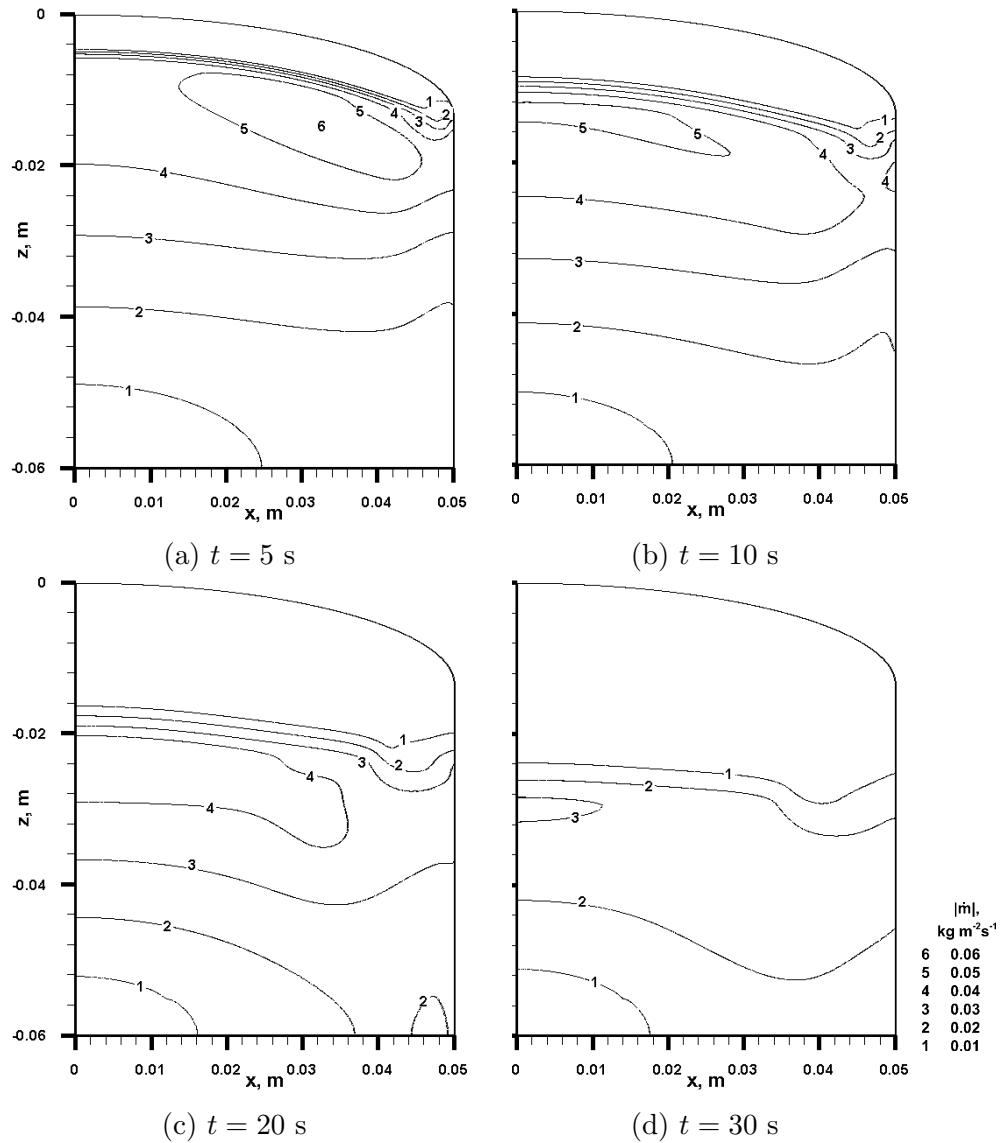


Figure 8.16:  $|\dot{m}|$  contours for sample  $C$  (Case 1.3), at various times

### Case 1.4

It is seen from Figs. 8.18 and 8.19 that, the side wall heating effect is suppressed for sample  $D$ , which has identical diameter to sample  $C$ , but reduced thickness. From the  $t = 5$  s and 10 s results, both temperature and porosity contour lines are parallel to the front surface curvature, indicating little side wall heating effects. Even at  $t = 20$  s and 30 s, the side wall heating effects on the material and thermal response are not significant, whereas for the longer samples, they noticeably increased.

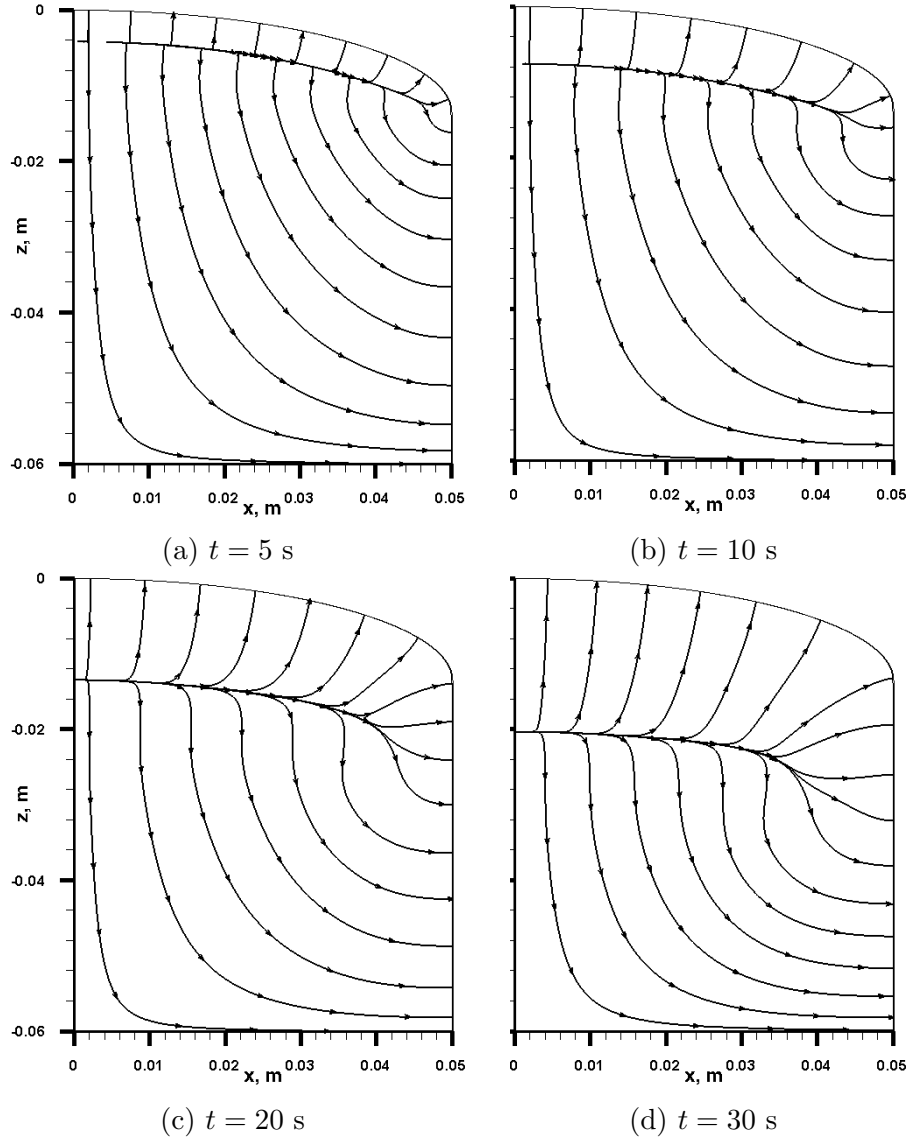


Figure 8.17: Gas streamlines for sample *C* (Case 1.3), at various times

The motion of pyrolysis gases within the sample is also greatly changed when compared to sample *C*. Figures 8.20 and 8.21 present the gas mass transport magnitude and direction, respectively. As is seen from these two figures, the greatest mass flux is located at the lower corner of the sample and is noticeably higher than observed in the other samples. This is explained by the fact that the back wall is assumed to be impermeable and the length of the side wall is limited. Therefore, the pyrolysis gas flowing downwards accumulates the mass flow rate at the lower corner of the sample, resulting in a much larger mass flow rate at this location.

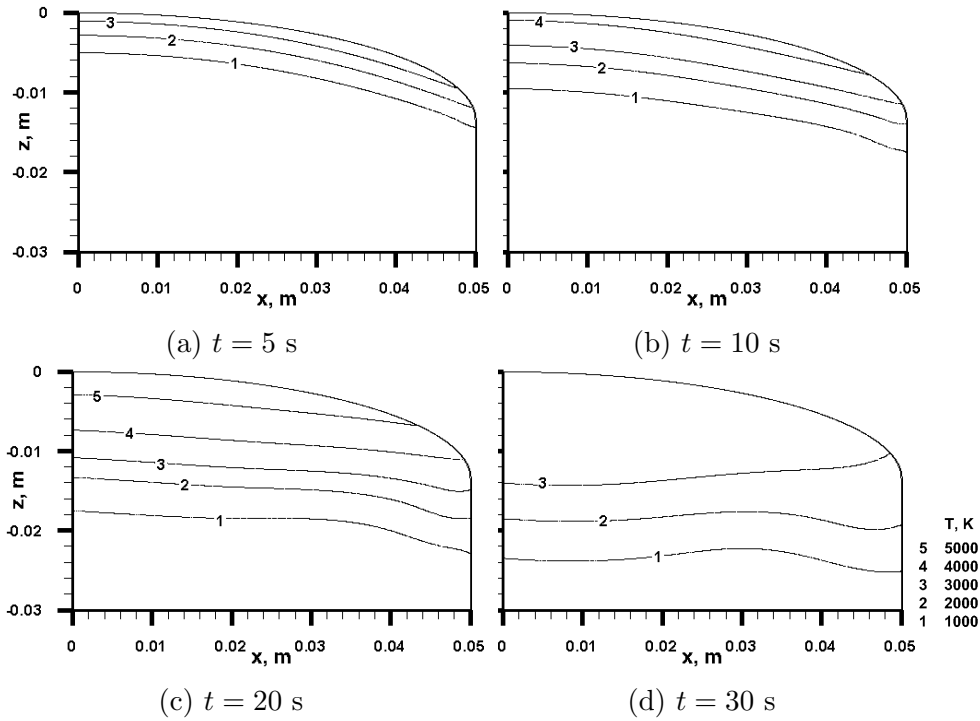


Figure 8.18: Temperature contours for sample  $D$  (Case 1.4), at various times

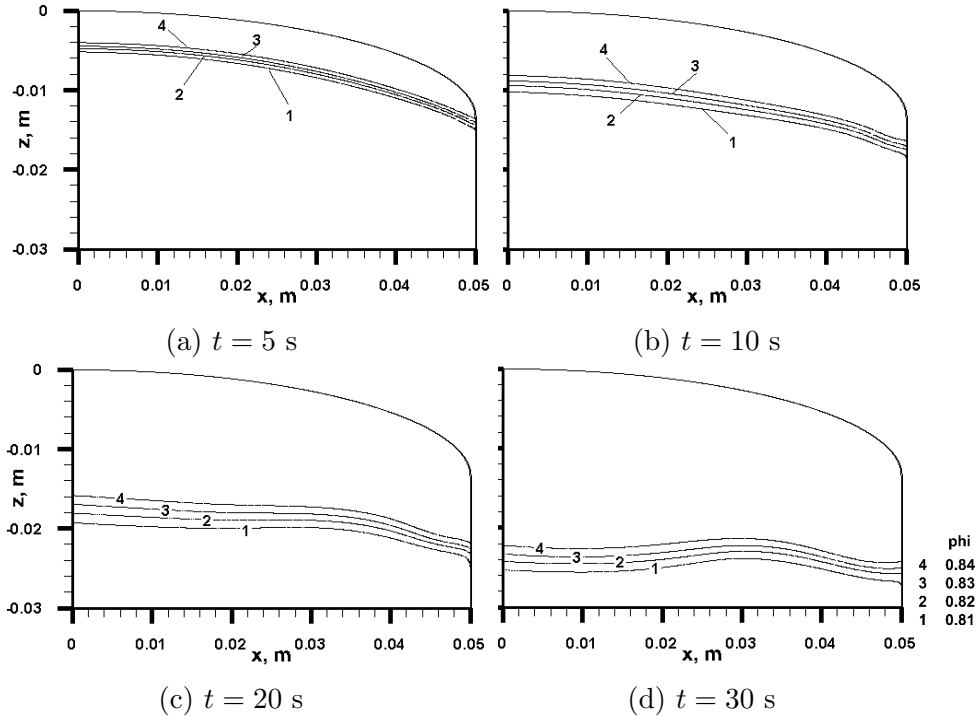


Figure 8.19: Porosity contours for sample  $D$  (Case 1.4), at various times

The pyrolysis gas blowing rates are presented in Fig. 8.9d, along with results obtained using 1.5 times and 2 times refined meshes. It can be seen from the figure



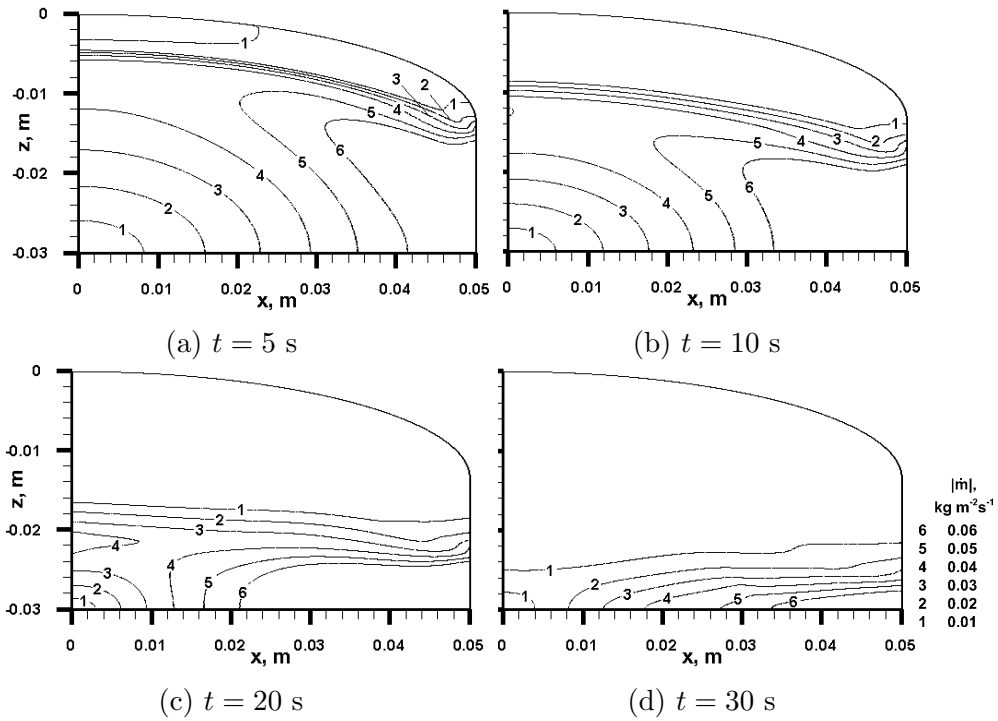


Figure 8.20:  $|\dot{m}|$  contours for sample  $D$  (Case 1.4), at various times

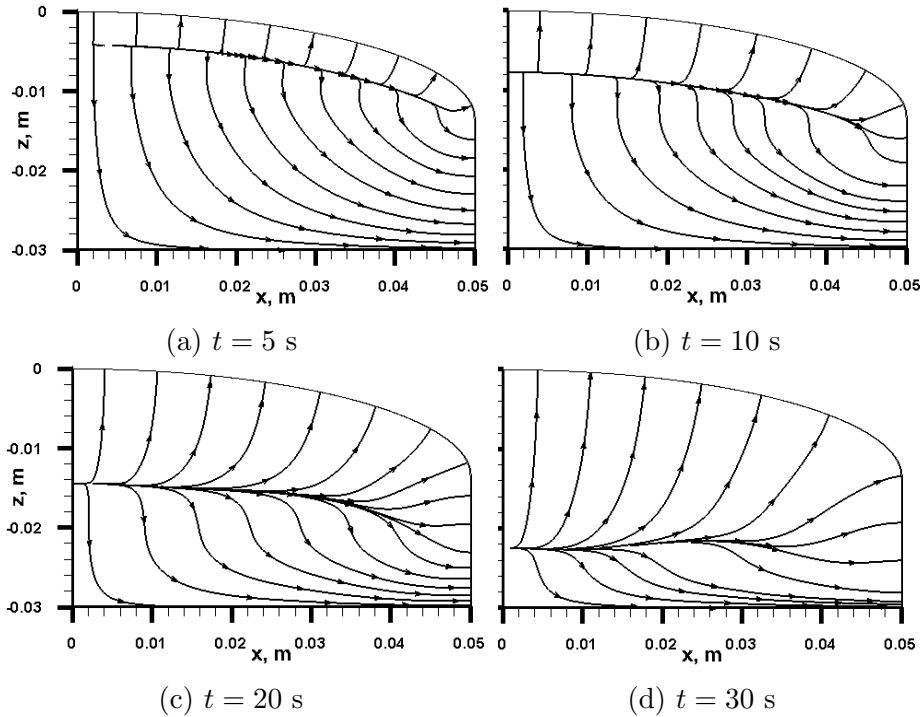


Figure 8.21: Gas streamlines for sample  $D$  (Case 1.4), at various times

that the greatest discrepancy locates near the lower corner of sample  $D$ , where a strong blowing occurs. The differences between each gas blowing curves are within

5 percent of the evaluated result, indicating the solutions are close to the converged solution, though they are not fully grid-independent at the corner of the sample.

For all meshes in Fig. 8.9d, the blowing rate through the front surface is further increased when compared to the previous samples. This is due to the back-wall of sample *D* being very close to the decomposition/pyrolysis zone, which builds up the pressure near the wall and drives more gas towards the front surface. But the magnitude of this increase in front surface blowing is small, compared to the increase in mass flux out the sides of the samples. The maximum value of gas blowing rate is located at the lower corner, and shows non-monotonic behavior in time, unlike for the previous samples. In all, the reduction of sample thickness alters the blowing pattern on both the front and side surface; however, the influence on the side is more significant than on the front surface.

## **Second set: effect of sample holders**

### **Case 2.1**

Temperature distributions within sample *A-* at various times are presented in Fig. 8.22. Despite minor differences compared to sample *A* (Fig. 8.5), the distributions are strikingly similar. Figure 8.23 shows that this similarity extends to the porosity. In both cases the greatest differences are observed late in the run, at  $t = 30$  s. At this point in time, the extent of heating and charring along the centerline in sample *A-* is greater than in sample *A*, thus leading to a flatter temperature and porosity contours within sample *A-* compared to sample *A*.

The magnitude of mass flux in sample *A-*, as depicted in Fig. 8.24, also has a similar pattern to that of sample *A*. However, as shown in Fig. 8.25, the impermeability of the sample holder walls causes the pyrolysis gas flow to be largely confined to the portion of the sample not encased within the sample holder. A small portion of the gas flows into the region enclosed by the sample holder, but reverses its direction

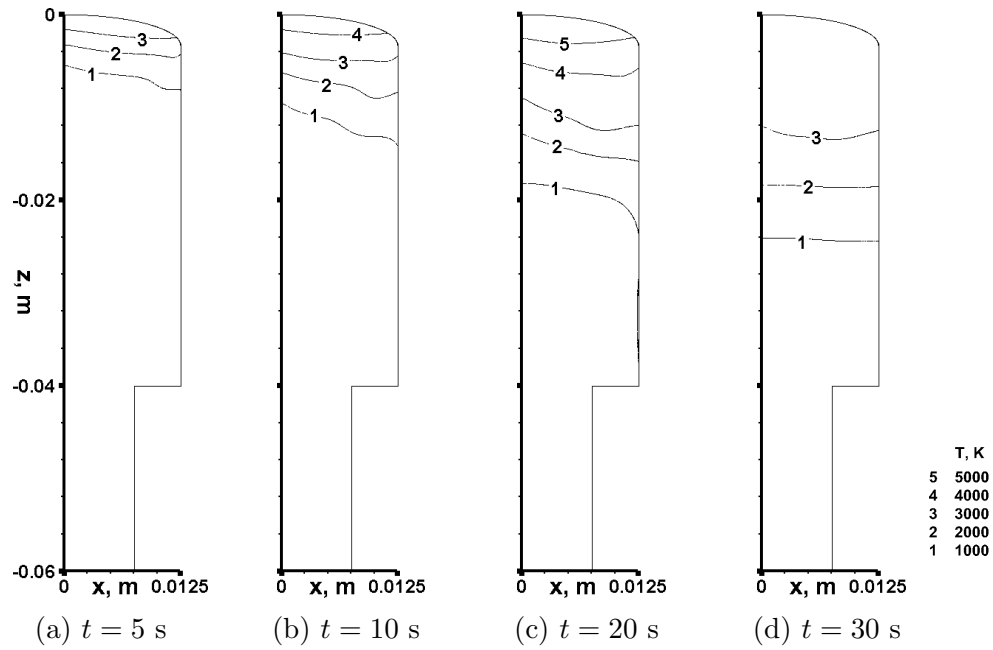


Figure 8.22: Temperature contours for sample A- (Case 2.1), at various times

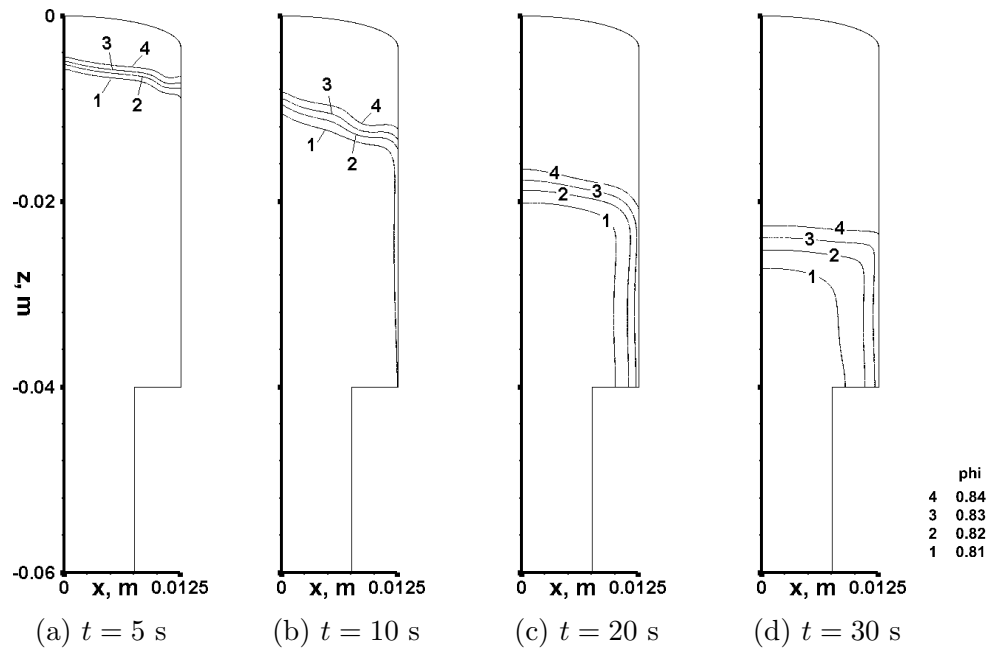


Figure 8.23: Porosity contours for sample A- (Case 2.1), at various times

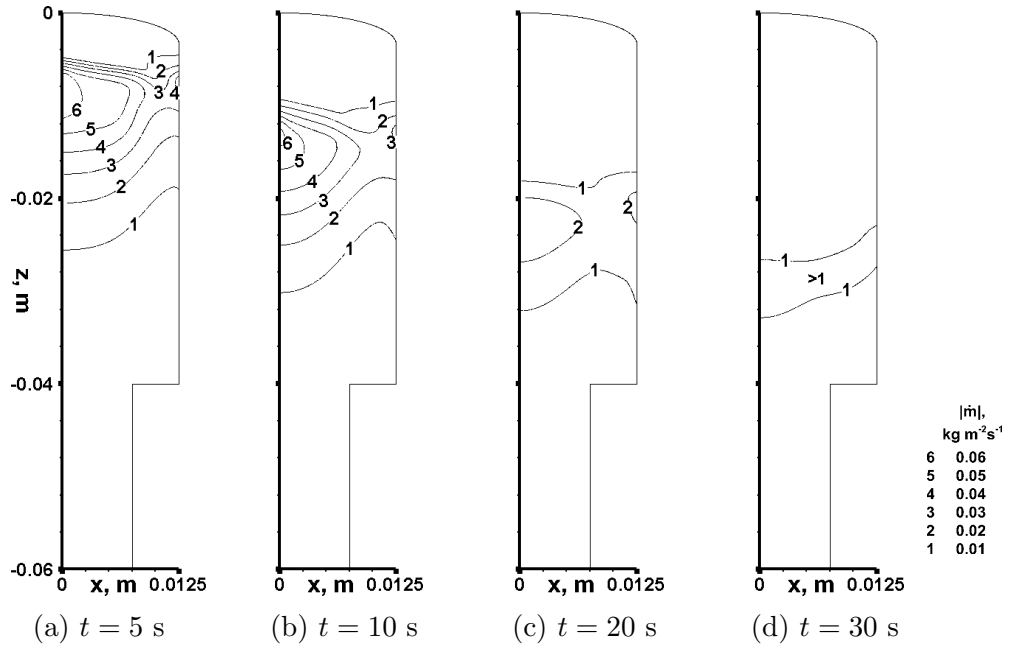


Figure 8.24:  $|\dot{m}|$  contours for sample A— (Case 2.1), at various times

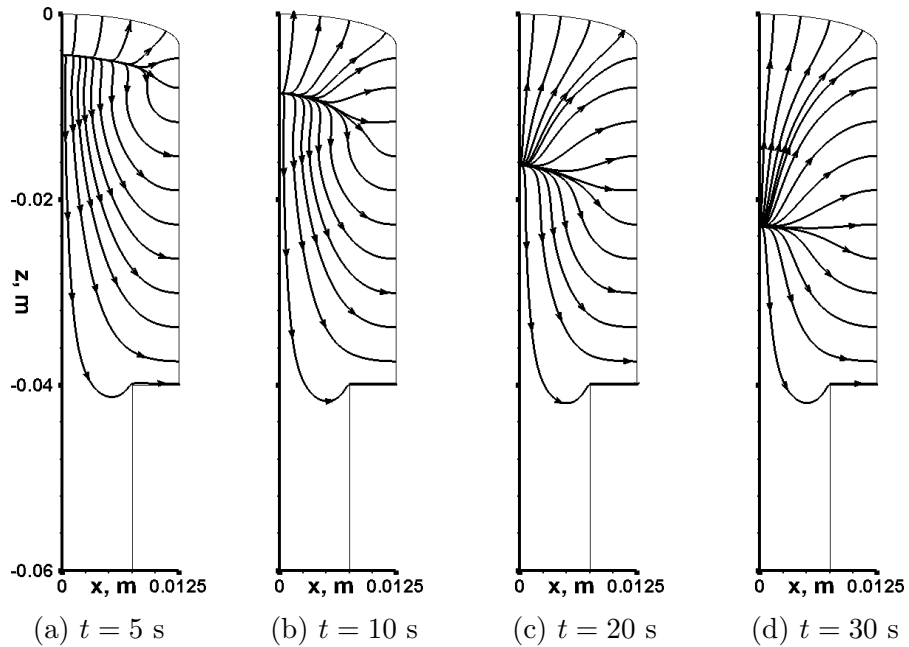


Figure 8.25: Gas streamlines for sample A (Case 2.1), at various times

and exits out through the lower corner on the side of the sample.

As illustrated by comparing Fig. 8.9e and 8.9a, despite the gas flow being confined to a smaller region of the sample when a holder is present, the overall surface gas blowing performance is quite similar. To illustrate the effect of the sample holder further, an additional simulation was conducted for the same geometry as sample *A* but with length of only 0.04 m, which corresponds to the length of sample *A* that protrudes from the holder. The resulting mass flow rate through the surface are shown as symbols in Fig. 8.9e. As expected, the results are almost identical to the surface gas blowing rate for sample *A*. This suggests that, especially where the surface blowing is concerned, this type of sample holder essentially shortend the effective length of the material sample.

## Case 2.2

The temperature and porosity distributions within sample *B*, as shown in Figs. 8.26 and 8.27, are basically unchanged when compared to the same results for sample *B* (Figs. 8.10 and 8.11). Only slight differences are evident near the sample holder.

The pyrolysis gas transport magnitude and direction are shown in Figs. 8.28 and 8.29, respectively. As with sample *B*, the location of greatest  $|\dot{m}|$  is located below the charring front. It is seen from the streamline plot presented by Fig. 8.29, the pyrolysis gas flows into the region enclosed by the holder of sample *B* and it reverses direction and exits out the side of the sample. Note that this behavior was also seen for sample *A* (Fig. 8.25).

Another simulation was performed using a shorter (4 cm) version of sample *B*. The results of surface mass flux are presented in Fig. 8.9f, using symbols. The surface blowing rate distributions are again almost identical, lending further support to the hypothesis that this type of sample holder produces similar behavior to that of a shorter sample.

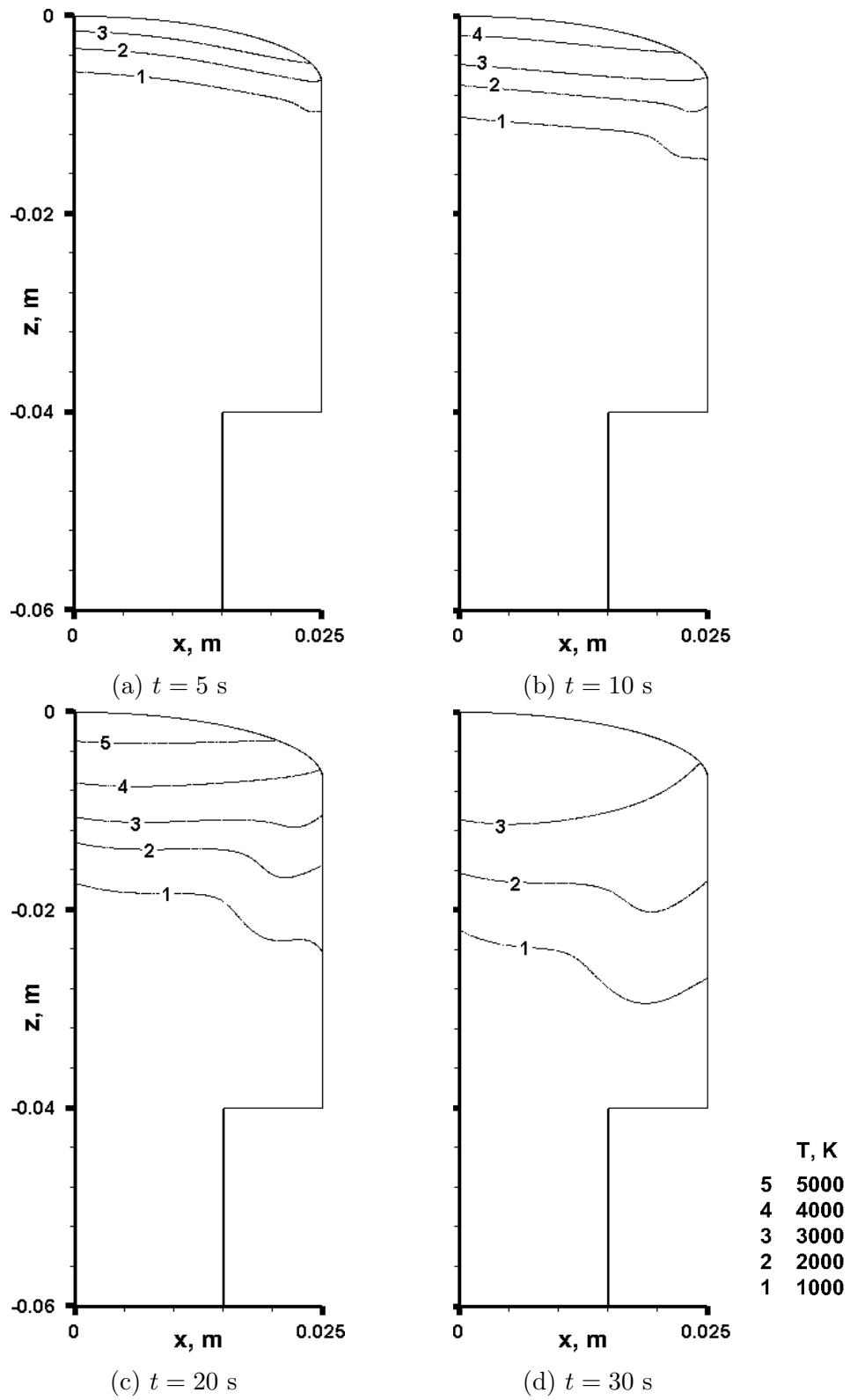


Figure 8.26: Temperature contours for sample  $B-$  (Case 2.2), at various times

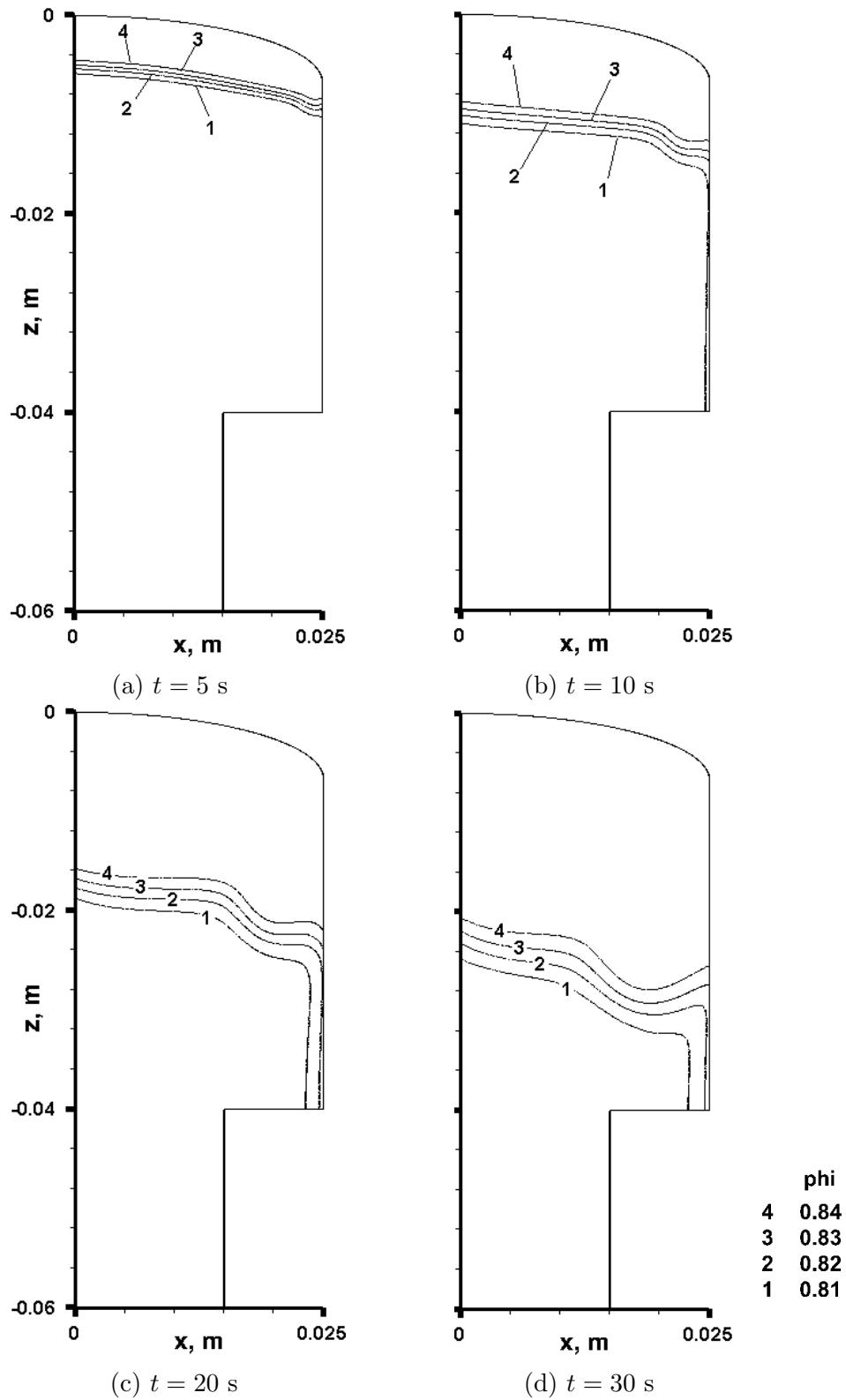


Figure 8.27: Porosity contours for sample  $B-$  (Case 2.2), at various times

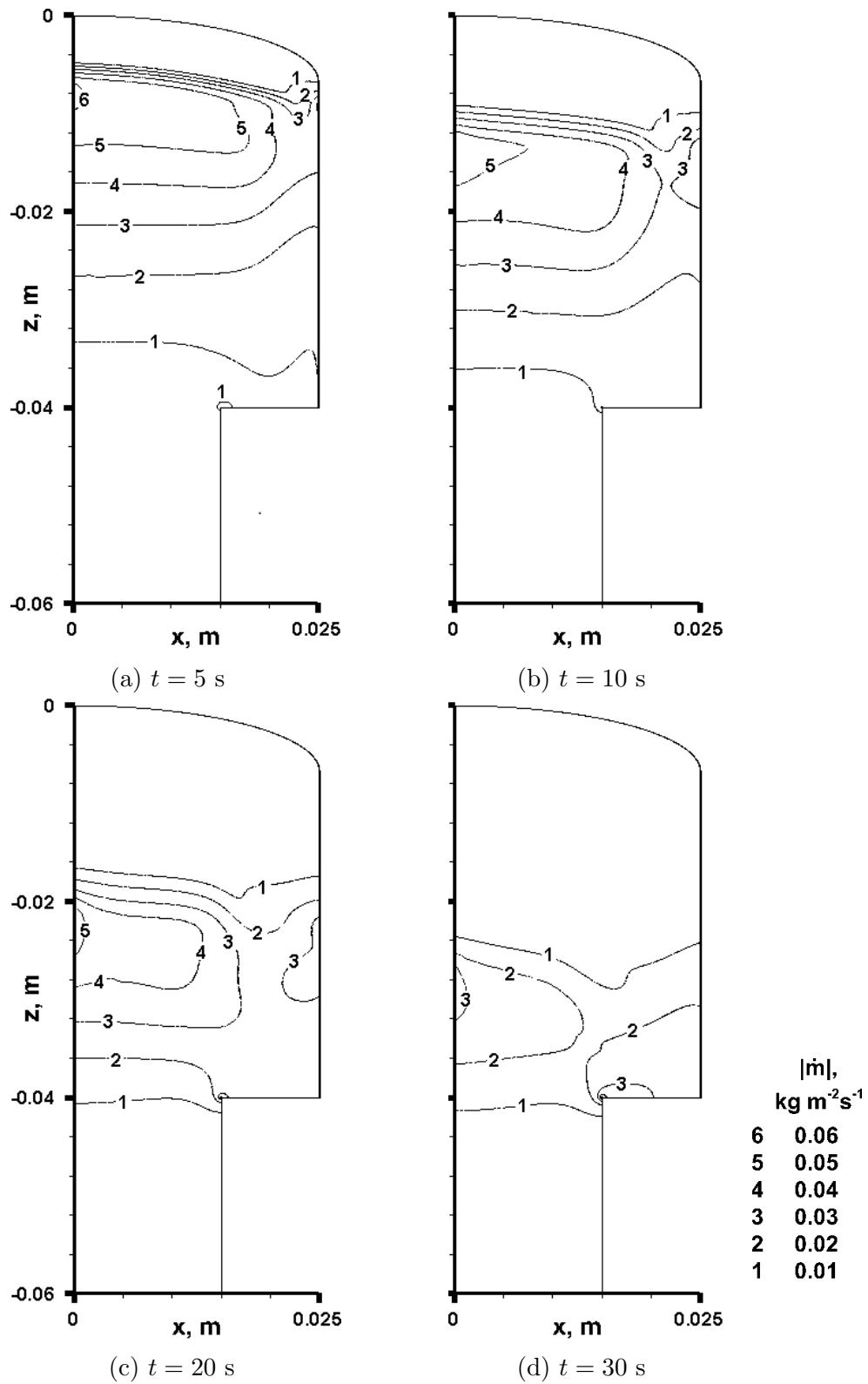


Figure 8.28:  $|\dot{m}|$  contours for sample  $B-$  (Case 2.2), at various times



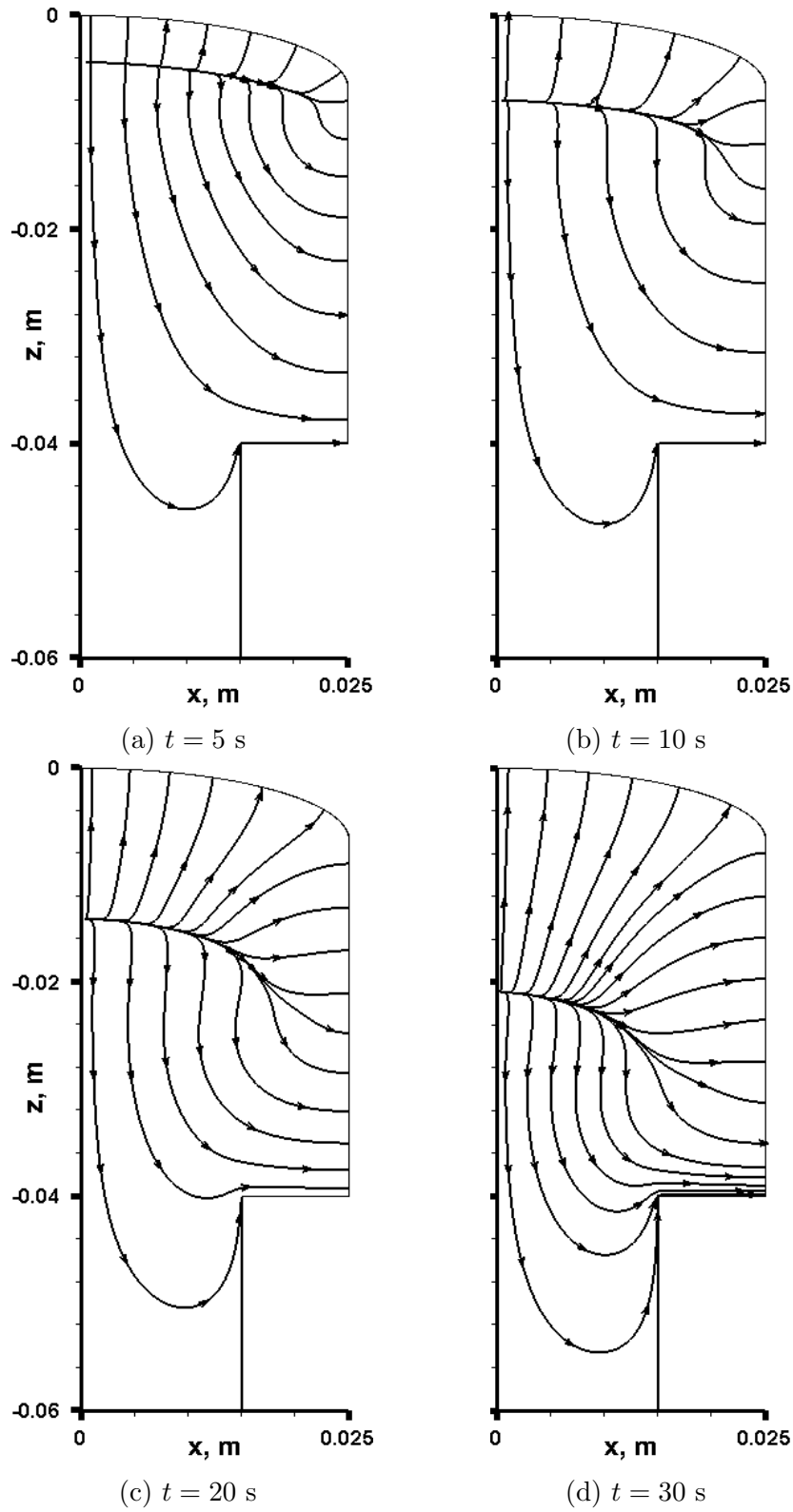


Figure 8.29: Gas streamlines for sample  $B-$  (Case 2.2), at various times

### Case 2.3

For Case 2.3, which simulates a sample holder mounted to the back face, the thermal and material response shown in Figs. 8.30 and 8.31 are found to be virtually identical to the sample without holder (Figs. 8.14 and 8.15).

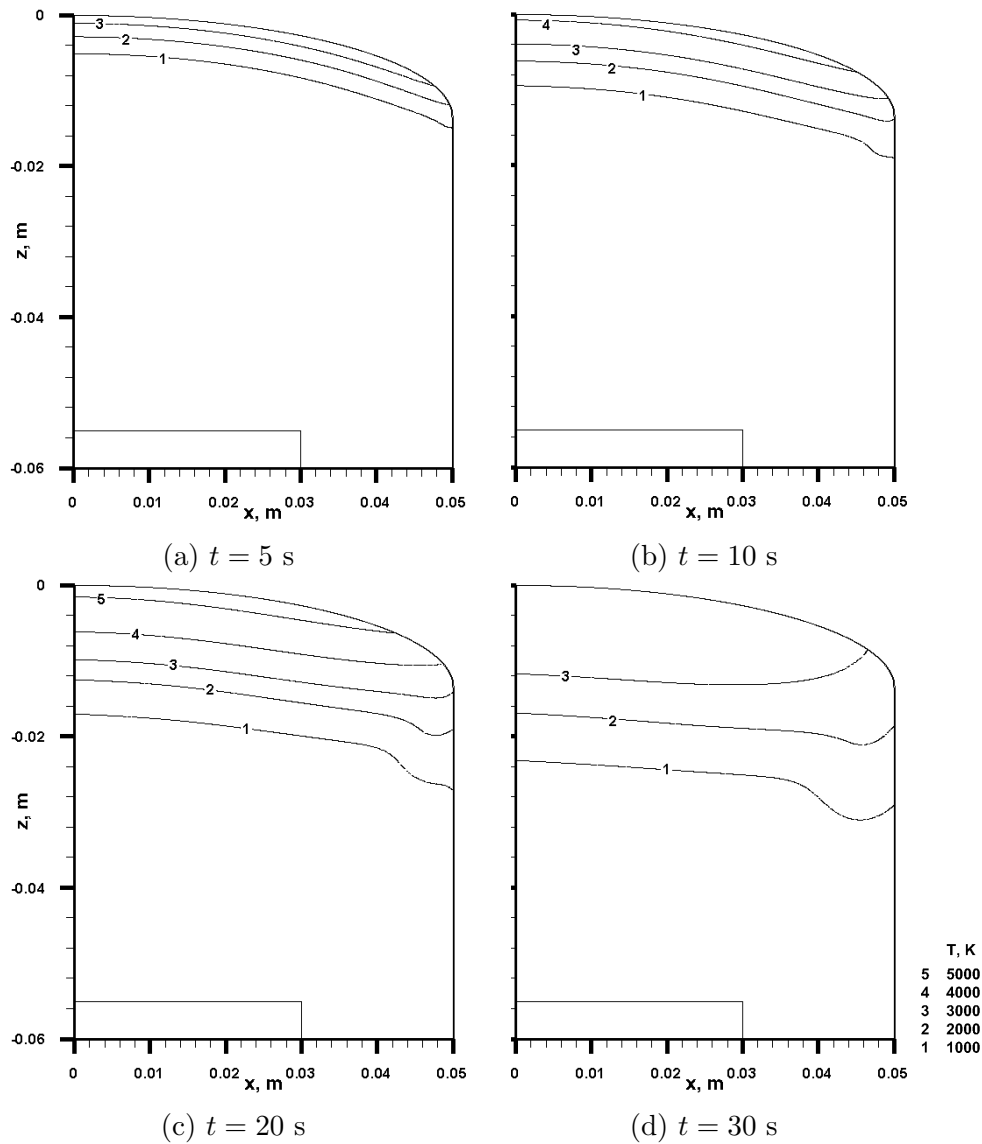


Figure 8.30: Temperature contours for sample  $B-$  (Case 2.3), at various times

Furthermore, the pyrolysis gas mass transport for sample  $C-$ , as shown in Figs. 8.32 and 8.33, shows that without the confinement effects produced by the holder enclosing the sample, the presence of the holder results in a small acceleration and deviation

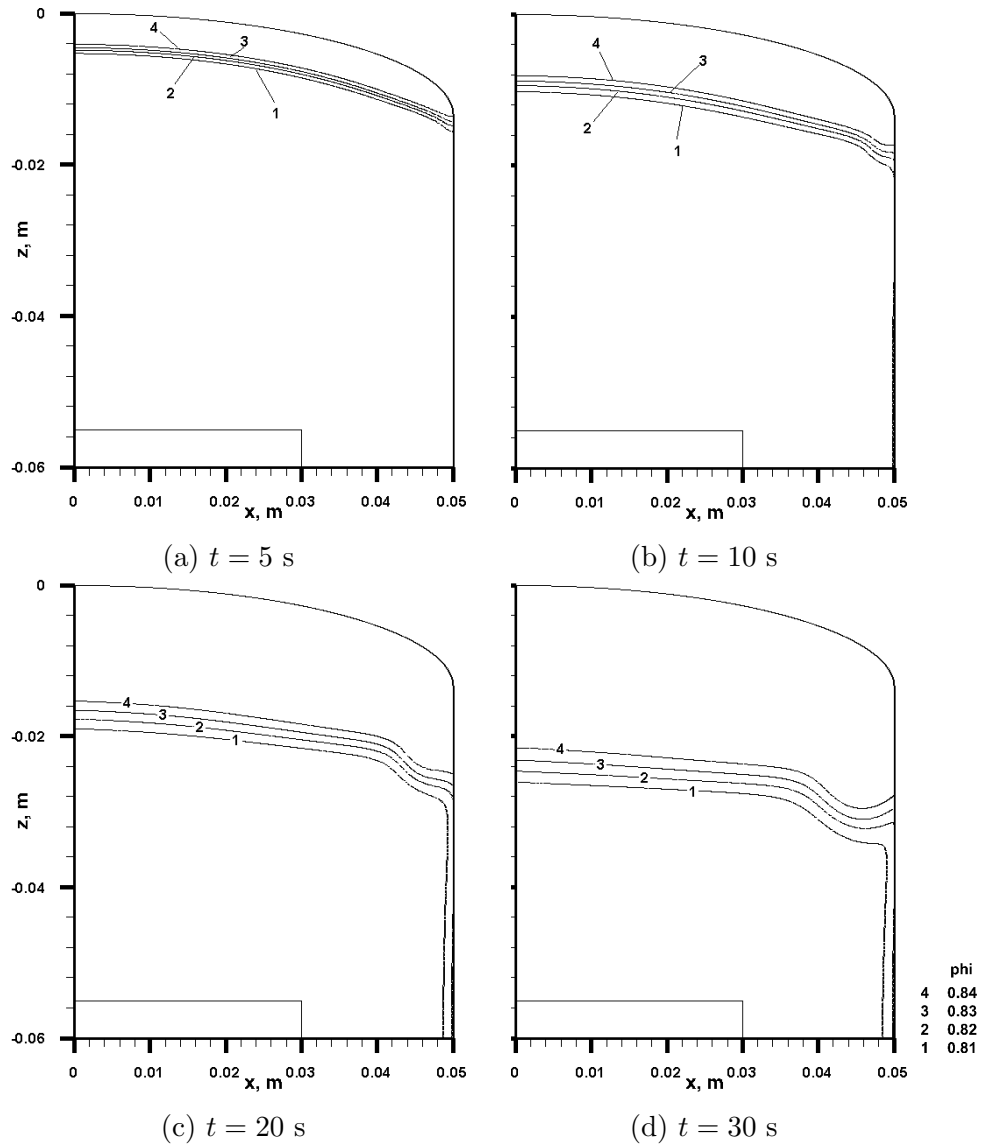


Figure 8.31: Porosity contours for sample *B-* (Case 2.3), at various times

in mass flux direction close to the holder. As a result, the pyrolysis gas transport results for sample *C-* are mostly similar to those for sample *C* (Figs. 8.16 and 8.17).

This similarity is also reflected in the mass flux out of the surface, as shown in Fig. 8.9g, where sample *C* profiles are also presented on the same figure using symbols. It is clear to see from the figure that the two solutions are almost identical, except for the small differences on the side wall when  $t \geq 10$  s. Thus it appears that the distortions due to mounting a sample are minimized when mounting the sample using

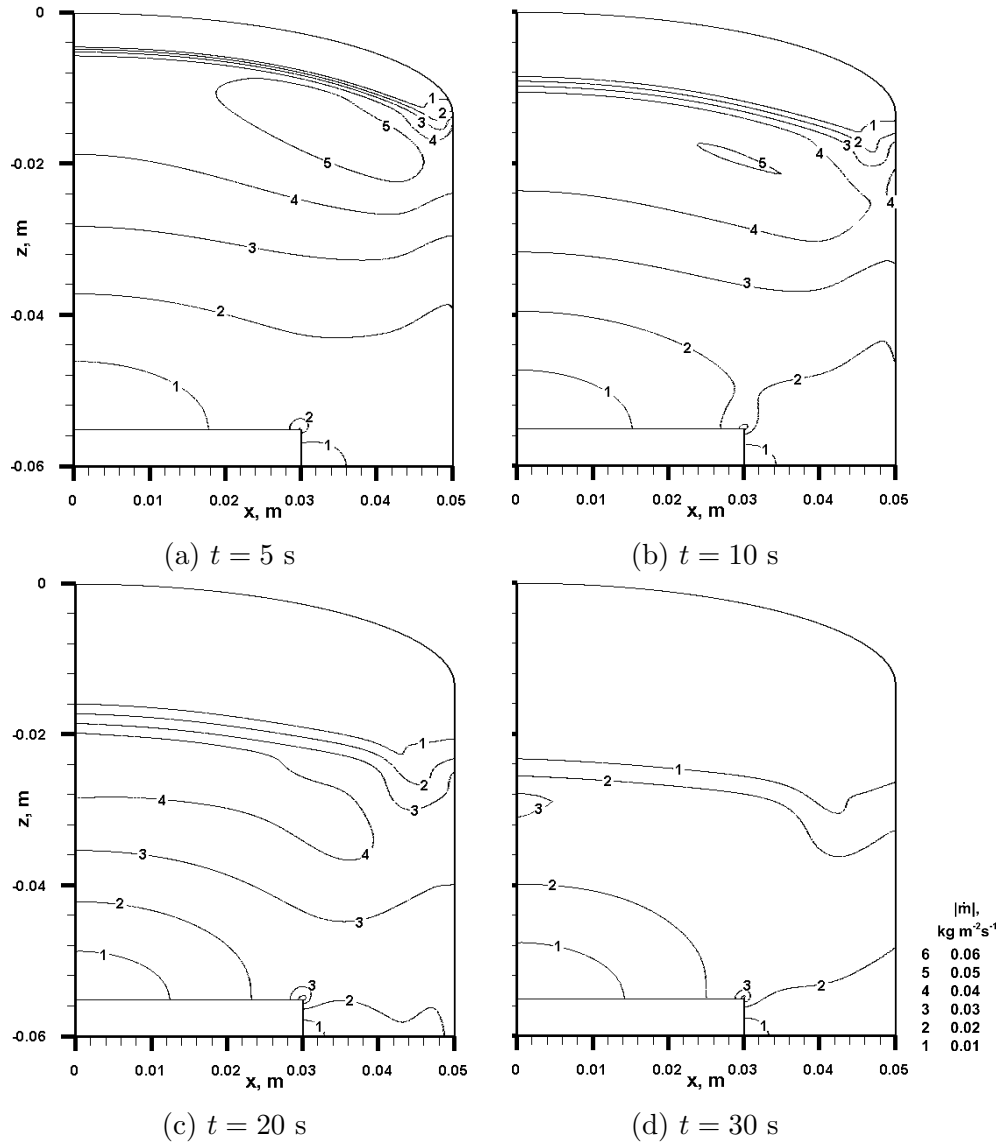


Figure 8.32:  $|\dot{m}|$  contours for sample  $C-$  (Case 2.3), at various times

its back face.

### Case 2.4

This observation is preserved for sample  $D-$  for which the sample holder is considerably closer to the charring front. The temperature and porosity distributions for this sample, Figs. 8.34 and 8.35 respectively, are comparable to those found for sample  $D$ .

As with sample  $C-$ , the differences in pyrolysis gas mass transport within sample

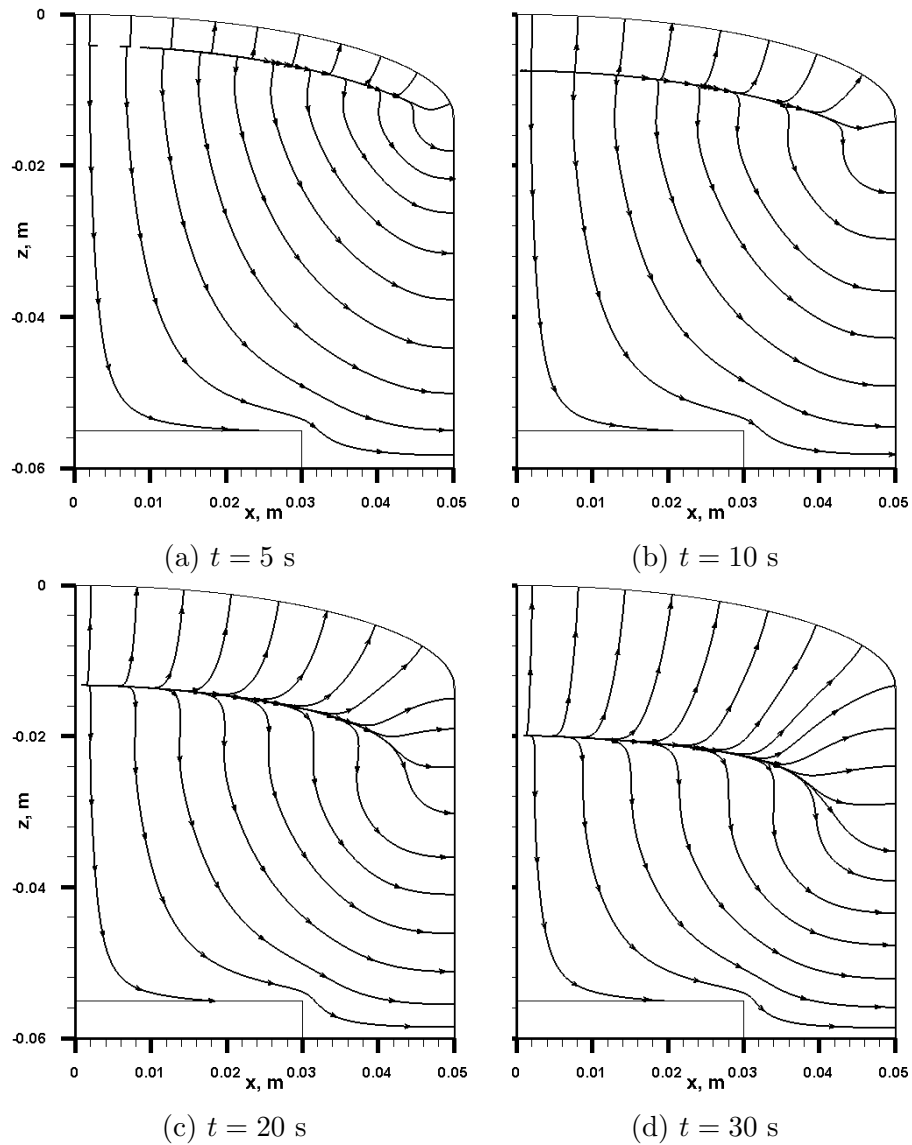


Figure 8.33: Gas streamlines for sample  $C-$  (Case 2.3), at various times

$D-$  are confined to the region near the sample, as depicted in Figs. 8.36 and 8.37. However, due to the proximity of the char front to the sample holder for this case, these effects are amplified. Thus, as illustrated by comparison of the mass flux out of the surface for sample  $D-$ , shown as lines in Fig. 8.9h and that of sample  $D$ , shown as symbols, differences are only evident when  $t \geq 30$  s. These differences are created when the char front is within close proximity to the sample holder, resulting in a slight increase in mass flux out the side of the sample.

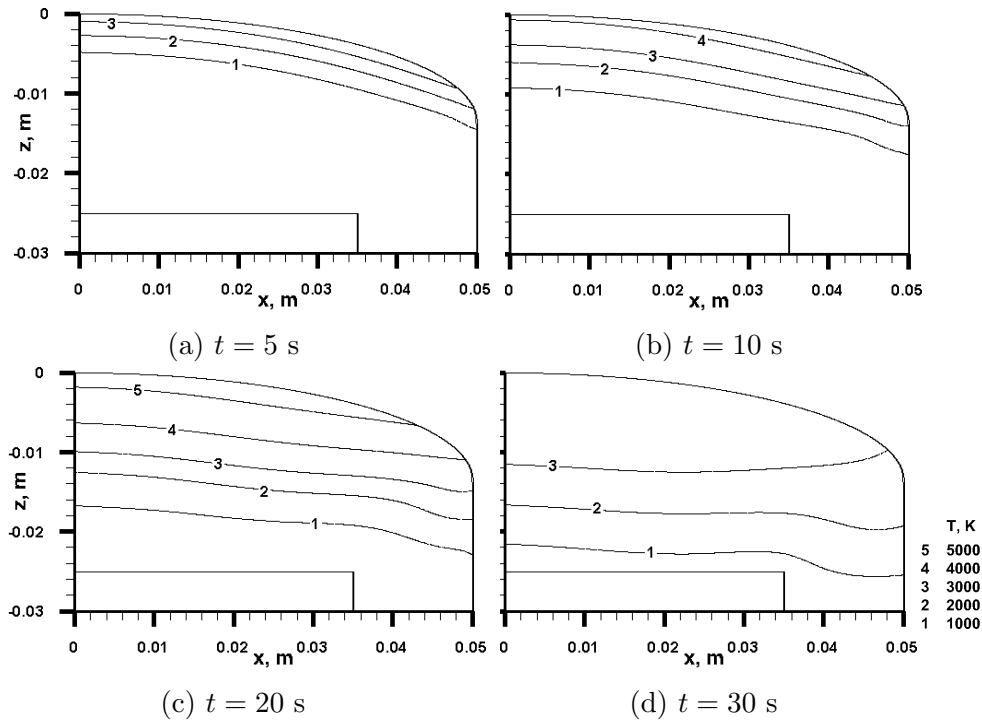


Figure 8.34: Temperature contours for sample  $D-$  (Case 2.4), at various times

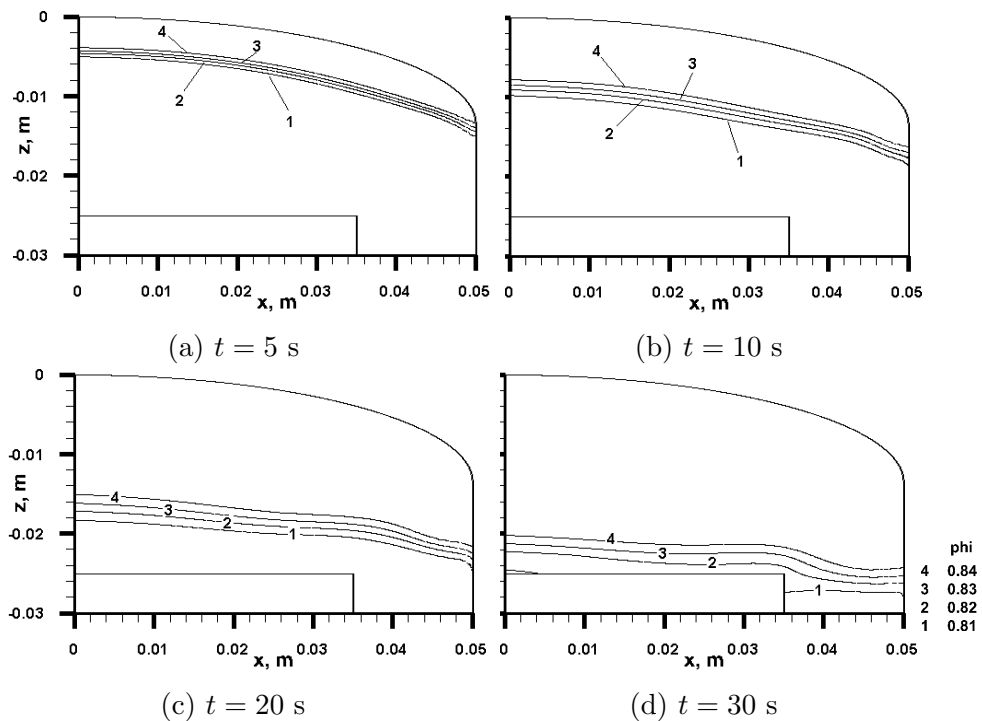


Figure 8.35: Porosity contours for sample  $D-$  (Case 2.4), at various times

### Comparison of mass flow rate at the stagnation point

As noted in the motivation, experiments such as those conducted in arc-jet facilities are often used to validate and develop 1D models later used for TPS design. Therefore,

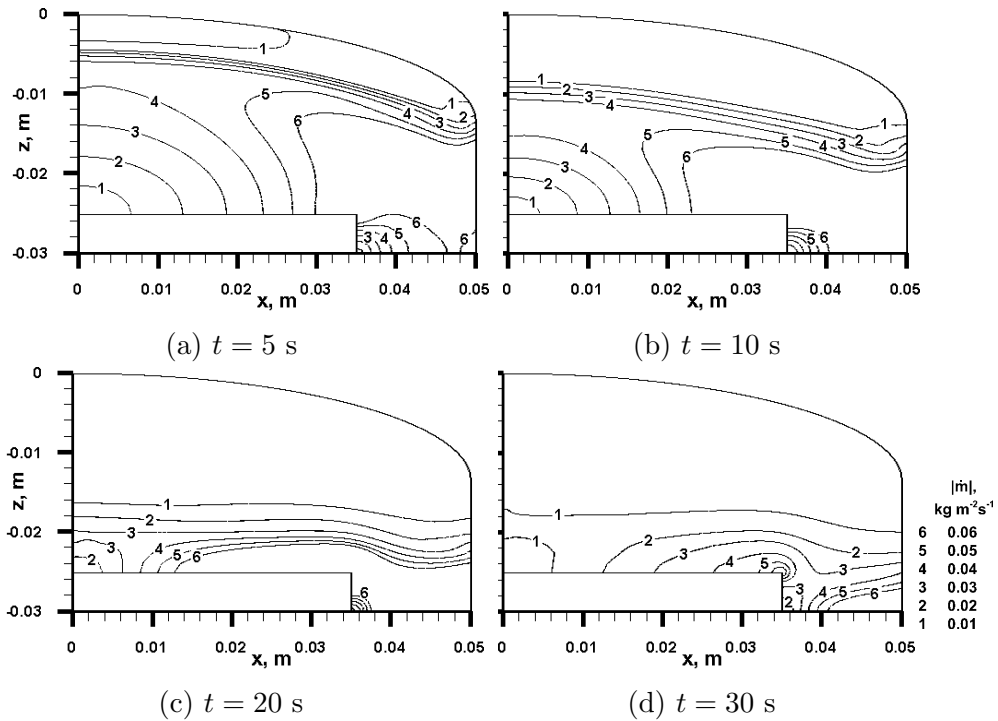


Figure 8.36:  $|\dot{m}|$  contours for sample  $D-$  (Case 2.4), at various times

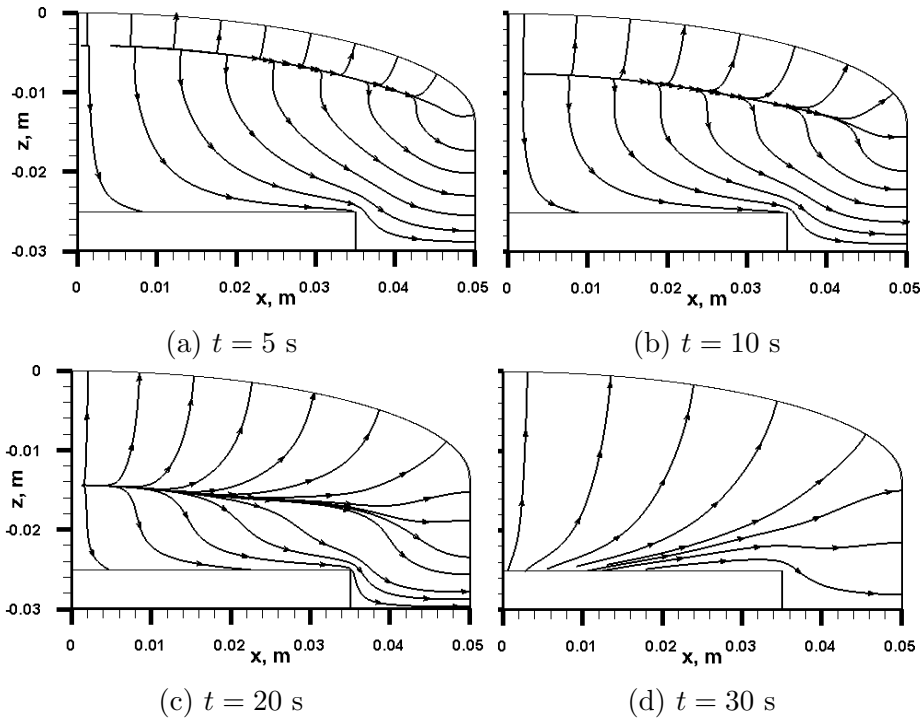


Figure 8.37: Gas streamlines for sample  $D$  (Case 2.4), at various times

an important consideration is how the effects of sample geometry and experimental configuration impact the 1D approximation. In Fig. 8.38, the pyrolysis gas mass

flux out of each sample at its stagnation point is compared to that predicted by a 1D model using the same conditions [74]. There are significant differences evident

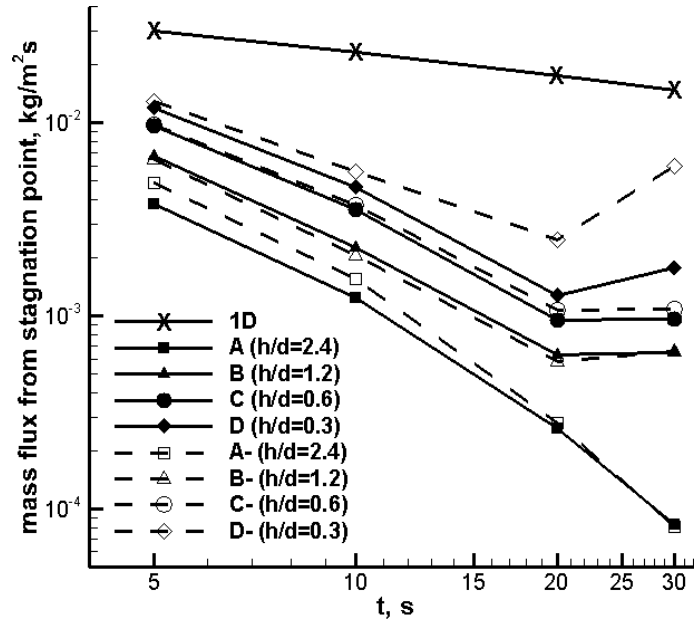


Figure 8.38: Pyrolysis gas mass flow rate through surface at the stagnation point

between the blowing rate predicted by the 1D model and that predicted by the 3D simulations, with as much as an order of magnitude difference in  $|\dot{m}|$  between the 1D and 3D cases and faster decay in blowing rate for the 3D simulations. Regardless, the samples with the smallest thickness to diameter ratio do show the greatest agreement with the 1D model, as expected. However, it is also evident that as the char front approaches the back face there is an increase, rather than decrease, of pyrolysis gas mass flux out of the front surface. Only the samples with the highest  $h/d$  ratio do not show this behavior. Furthermore, the mass flux out of the front face can be further modified when the sample holder is included in the simulation. For the largest sample with the smallest  $h/d$  ratio, the effect of the sample holder is significant. This is in contrast to the earlier observations of  $|\dot{m}|$  which were dominated by the sidewall mass flux. As diameter decreases and  $h/d$  ratio increases, the effect of the sample holder on mass flux out the front surface becomes negligible, except for the smallest diameter sample with the largest  $h/d$  ratio. For this sample, the effect of the sample holder is



only evident at the beginning of the simulation.

## 8.5 Conclusions for geometric effects study

In order to investigate the influence of sample geometry, a series of 3D material response simulations were performed under conditions that are likely to be encountered in arc-jet experiments. For these simulations, four iso-Q TACOT samples with different diameters and thicknesses were examined; the effect of sample holder was also investigated for each of the four samples. A CFD simulation was performed for the flow field around one iso-Q geometry to acquire heat flux on the surface; the heat flux on the other geometries were scaled proportionally according to the diameter of the sample.

In contrast to the the widely-used 1D assumption, the majority of the pyrolysis gas mass transfer was through the side wall of the material sample, regardless of the sample diameter and thickness.

For a light-weight ablator such as the TACOT material, sample thickness-to-diameter ratio is crucial to the thermal and material response of a given test specimen: the smaller the diameter, the greater the effect caused by side wall heating and the less the front surface blowing. Sample thickness mainly influences the side wall blowing distribution: if sample thickness is much greater than the charring depth, the side wall blowing pattern is a single peak distribution that highly skewed toward the shoulder corner of the sample; if sample thickness is short enough to be comparable with charring depth, a strong gas blowing will take place at the lower corner of the sample side wall. These conclusions are likely extensible to other low-density, highly-porous ablators but likely not applicable to low porosity carbon-phenolic ablators [48], or to ablators that are encapsulated in a supporting structure, such as AVCOAT [107], used on Apollo vehicles or the Orion MPCV. For ablators with low virgin permeability and very high char permeability, such as SIRCA [108], the gas blowing pattern is expected

to be similar, although the pyrolysis gas transport in the virgin material is expected to diminish greatly.

Impermeable sample holders, if sheathed outside of the material, altered the material, thermal, and blowing responses slightly. The altered behaviors were very similar to the sample thickness being shortened by the length of the sample holder. Sample holders located inside of the material did not change much of the material and thermal responses, except for high diameter-to-thickness samples for which the blowing rate was enhanced at stagnation point. As a conclusion, the results of this study have 1) questioned the 1D surface blowing model for small test models, 2) shown qualitative relation between the sample diameter and the strength of side wall heating effects, 3) investigated the effects of the sample holder to the sample response, 4) provided a 3D numerical perspective of charring process in arc-jet tests. Keeping in mind that the actual experimental conditions may vary, these results may be used as qualitative guidelines for choosing model geometries in future arc-jet experiments.

## Chapter 9 Effects of Orthotropic Material Properties

### 9.1 Motivation

Charring ablative materials usually have transverse isotropic (a subset of orthotropic) properties due to fiber orientations, as was discussed in Section 5.1. Therefore in this chapter, the effects of orthotropic material properties are numerically investigated using an arc-jet sample. The comparisons of models are presented by showing pyrolysis gas streamlines and time series of temperature at selected virtual thermocouples.

### 9.2 Applied models

The material models and the governing equations are same as discussed in Chapter 7, except that the material properties are assumed to be transverse isotropic.

### 9.3 Test-case descriptions

In this study, a total of seven cases is performed using TACOT material [99]. The sample geometry used in each case is the iso-Q shape as was used in previous studies.

Figure 9.1 illustrates the iso-Q sample geometry mesh as well as the location of virtual thermocouples. The location of the thermocouples are listed in Table 9.1.

Table 9.1: Coordinates of thermocouples in an iso-Q sample

TC#	Coordinate, m	TC#	Coordinate, m
1	$(0, 0, -3.81 \times 10^{-3})$	6	$(0, 0, -2.286 \times 10^{-2})$
2	$(0, 0, -7.62 \times 10^{-3})$	7	$(2.54 \times 10^{-2}, 0, -2.286 \times 10^{-2})$
3	$(0, 0, -1.143 \times 10^{-2})$	8	$(3.81 \times 10^{-2}, 0, -2.286 \times 10^{-2})$
4	$(0, 0, -1.524 \times 10^{-2})$	9	$(4.445 \times 10^{-2}, 0, -2.286 \times 10^{-2})$
5	$(0, 0, -3.048 \times 10^{-2})$	10	$(4.445 \times 10^{-2}, 0, -3.048 \times 10^{-2})$

Since the objective of this test is to solely investigate the orthotropic material model, the boundary conditions and initial settings of each case are set to be identi-

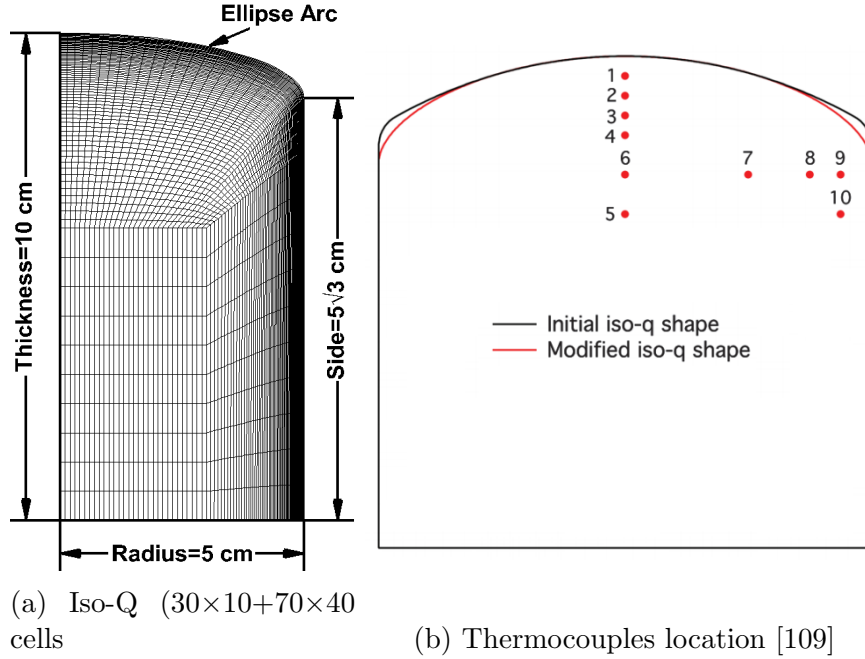


Figure 9.1: Geometry and thermocouples location of the iso-Q sample [101]

cal. Figure 9.2 shows the boundary conditions applied. The heat flux and pressure

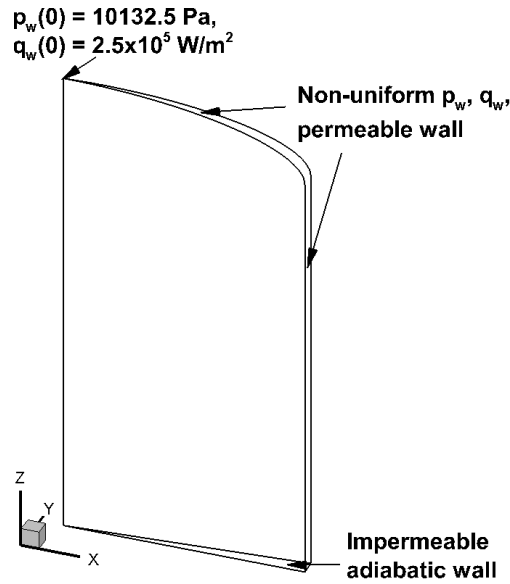


Figure 9.2: Illustration of boundary conditions and computational geometry

on the surface are non-uniform, the profiles of which are given in Fig. 9.3a, where the arc length is defined as  $L = \sqrt{x^2 + y^2 + z^2}$ , *i.e.*  $L = 0$  represents the center of the sample at the surface; the corner of the iso-Q sample is located at where

$L = \sqrt{0.05^2 + 0.0133975^2} = 0.0517638$  m. The thermal boundary condition applied along the surface is the explicit penetrated heat to the material, as was discussed in Section 4.5. The stagnation value of the penetrated heat flux is shown in Fig. 9.2 as  $q_w(0)$ .

The ramping profiles for the heat flux and the pressure boundary conditions are identical, as illustrated in Fig. 9.3b. Initially ( $t = 0$  s), the pressure and temperature are assumed to be uniform within the material and along the surface. Then from  $t = 0.1$  to 40 s, the heat flux and pressure distributions given in Fig. 9.3a are applied constantly on the boundary. Over the next 0.1 seconds, the heat flux boundary condition is linearly ramped down to zero and the pressure is ramped down to the initial value. The boundary stays adiabatic and is subjected to uniform pressure from  $t = 40.1$  to 60 s, which is the end of the simulation.

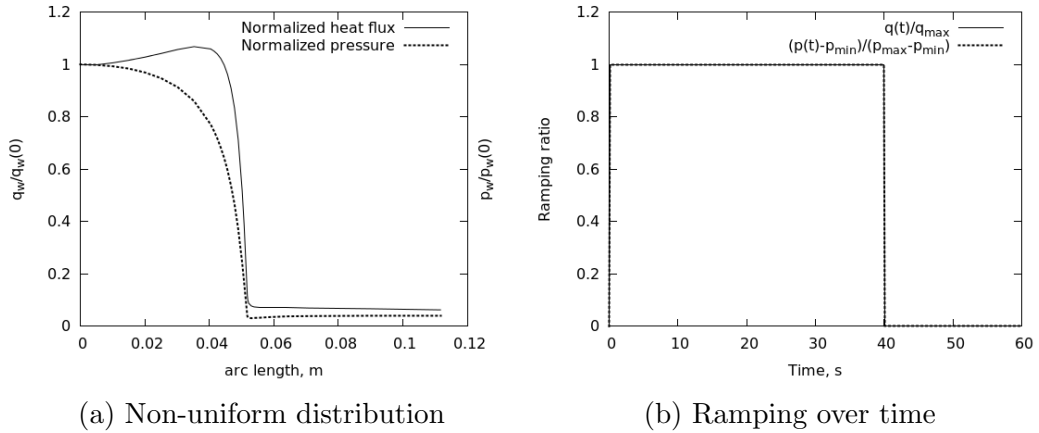


Figure 9.3: Pressure and heat flux boundary condition

The specific material model setups for each test-case are described in the following.

- First case: the control test-case, in which material properties are all assumed to be isotropic. In the rest of the cases, the in-plane (IP) orientation and the through-the-thickness (TTT) direction are corresponding to  $x$ - $y$  plane and  $z$ -direction, respectively.

- Second case: the permeability in IP direction is assumed to be twice as large as in TTT direction; the thermal conductivity is isotropic.
- Third case: the permeability in IP direction is assumed to be three times as in TTT direction; the thermal conductivity is isotropic.
- Fourth case: the permeability in IP direction is assumed to be half of the value in TTT direction; the thermal conductivity is isotropic.
- Fifth case: the permeability is isotropic but the thermal conductivity in IP direction is assumed to be two times as in TTT direction.
- Sixth case: both the permeability and the thermal conductivity in IP direction is assumed to be two times as in TTT direction.
- Seventh case: both the permeability and the thermal conductivity in IP direction is assumed to be half of the value in TTT direction.

The reason to pick  $K_{IP}/K_{TTT} = 2$  for the second case, and  $K_{IP}/K_{TTT} = 3$  for the third case is because  $K_{IP}/K_{TTT} = 2.62$  for virgin PICA, based on an experimental estimation [91]. For the thermal conductivity, the ratio of  $k_{IP}/k_{TTT} = 2$  is based on the values reported in Ref. [109]. In the fourth case and the seventh case, the orthotropic ratios are inverted in order to investigate the sample performance when the material is rotated by 90 degrees.

## 9.4 Results and discussions

### Pyrolysis gas transport

The numerical results of pyrolysis gas transport are presented in Figs. 9.4 to 9.10, for case 1 to case 7, respectively. In these plots, the contour  $|\dot{m}''|$  represented the local momentum of pyrolysis gas, which is given as  $|\dot{m}''| = \phi\rho_g\sqrt{u^2 + v^2 + w^2}$ . It can

be seen from Figs. 9.4 to 9.6 that, when permeability was greater in IP direction, the streamlines leaned towards the horizontal IP direction, especially in the char layer. The gas momentum (flow rate) was also increased at about 0.005 m below the shoulder point. In the fourth case (Fig. 9.7), the permeability was smaller in the IP direction and the streamlines leaned towards the TTT direction. These effects were due to the fact that the pyrolysis gas would travel more easily in the direction with higher permeability.

Comparing the first case (Fig. 9.4) with the fifth case (Fig. 9.8), it can be seen that the streamline patterns were very similar, if not identical. This is because the change in thermal conductivity had little influence on the gas flow direction. When comparing Fig. 9.4a with Fig. 9.8a, it can be observed that the gas momentum right below the decomposition zone was slightly enhanced. This was probably caused by the greater thermal conductivity in the IP direction, which enhanced the side wall heating; more heating leads to higher centerline temperature and more pyrolysis gas generation (thus, greater gas momentum).

When both orthotropic models were used, the thermal response followed a trend similar to a combination of each model. As expected, the streamlines in Fig. 9.9 are very close to the ones in Fig. 9.5, in which they had the same permeability matrix. This was due to the fact that the pyrolysis gas flow pattern is dominated by the permeability orientation, and the thermal conductivity is insignificant to the gas flow. For the same reason, the streamline patterns of the fourth case (Fig. 9.7) and the seventh case (Fig. 9.10) are quite close. The difference in the gas momentum contours was due to the same analysis between the first case (Fig. 9.4) and the fifth case (Fig. 9.8), described in the previous paragraph.

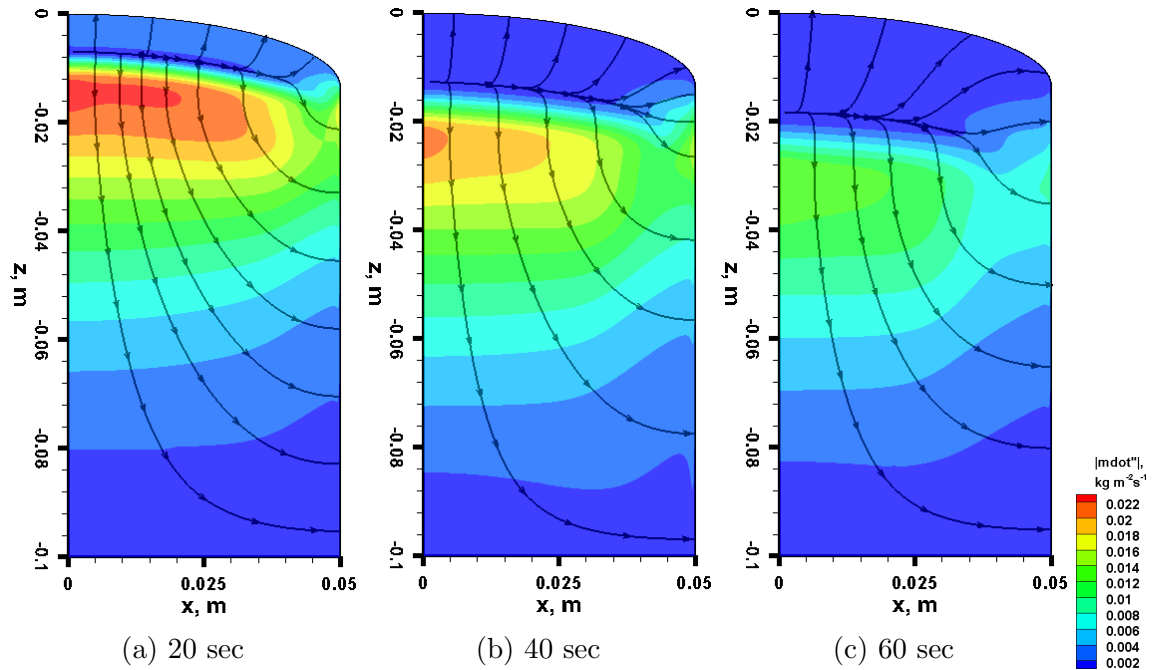


Figure 9.4: Pyrolysis gas transport for Case 1, isotropic permeability

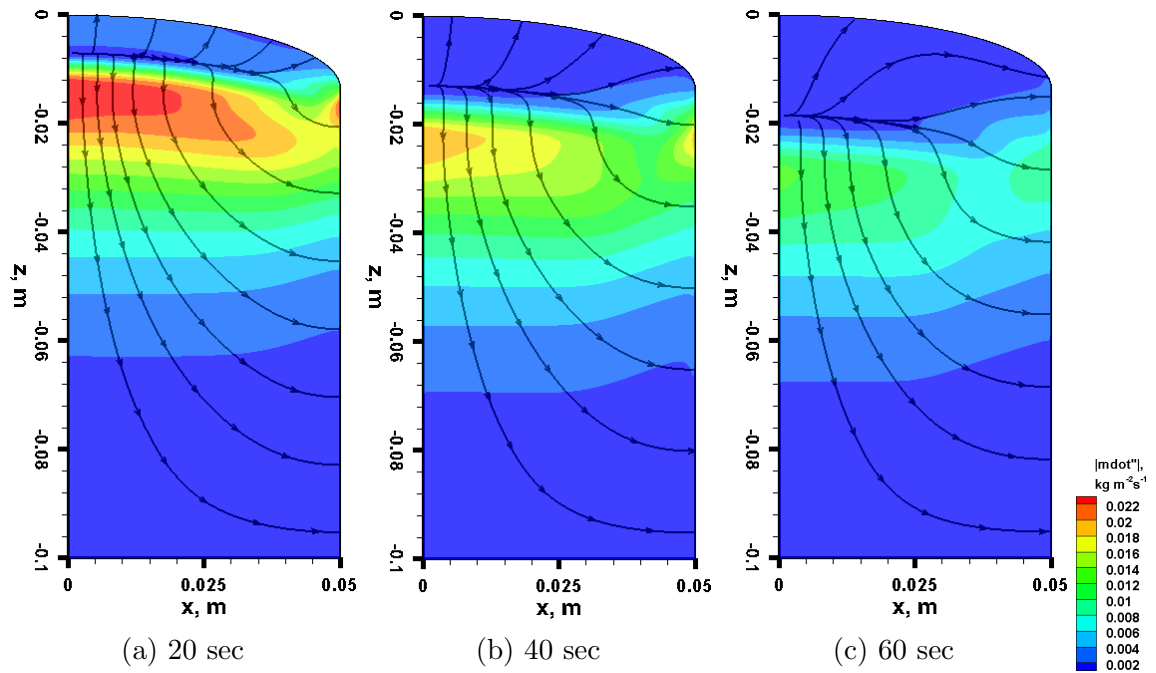


Figure 9.5: Pyrolysis gas transport for Case 2, orthotropic permeability:  $K_{IP}/K_{TTT} = 2$

### Thermocouple results analysis

The temperature time-series on 10 thermocouples are presented in Figs. 9.11 to 9.20. The results of the first case in which isotropic properties are used, are plotted using



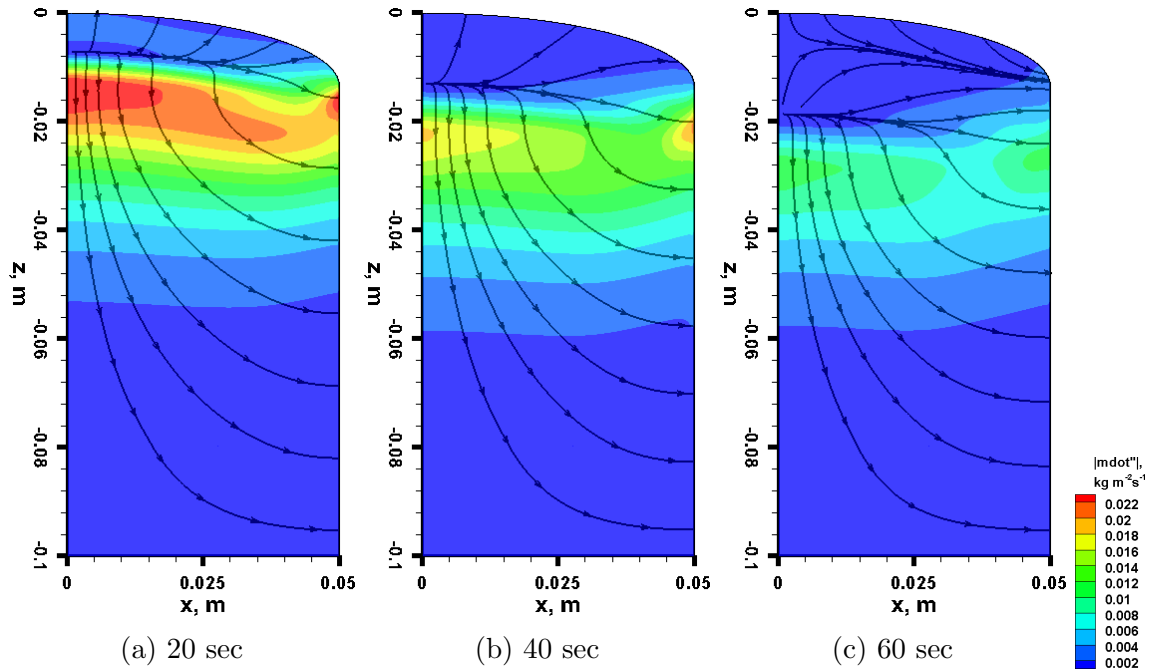


Figure 9.6: Pyrolysis gas transport for Case 3, orthotropic permeability:  $K_{IP}/K_{TTT} = 3$

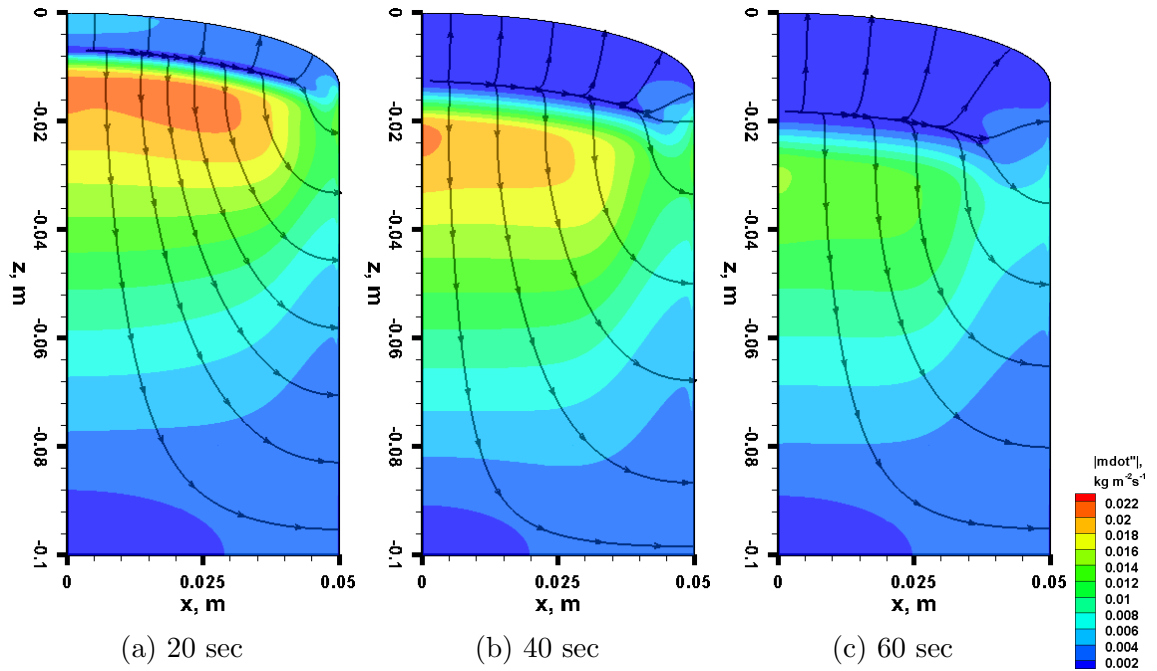


Figure 9.7: Pyrolysis gas transport for Case 4, orthotropic permeability:  $K_{IP}/K_{TTT} = 0.5$

a solid line, while results of the other cases are dotted with symbols. As shown in Fig. 9.1b, the first six thermocouples are located along the centerline of the iso- $Q$

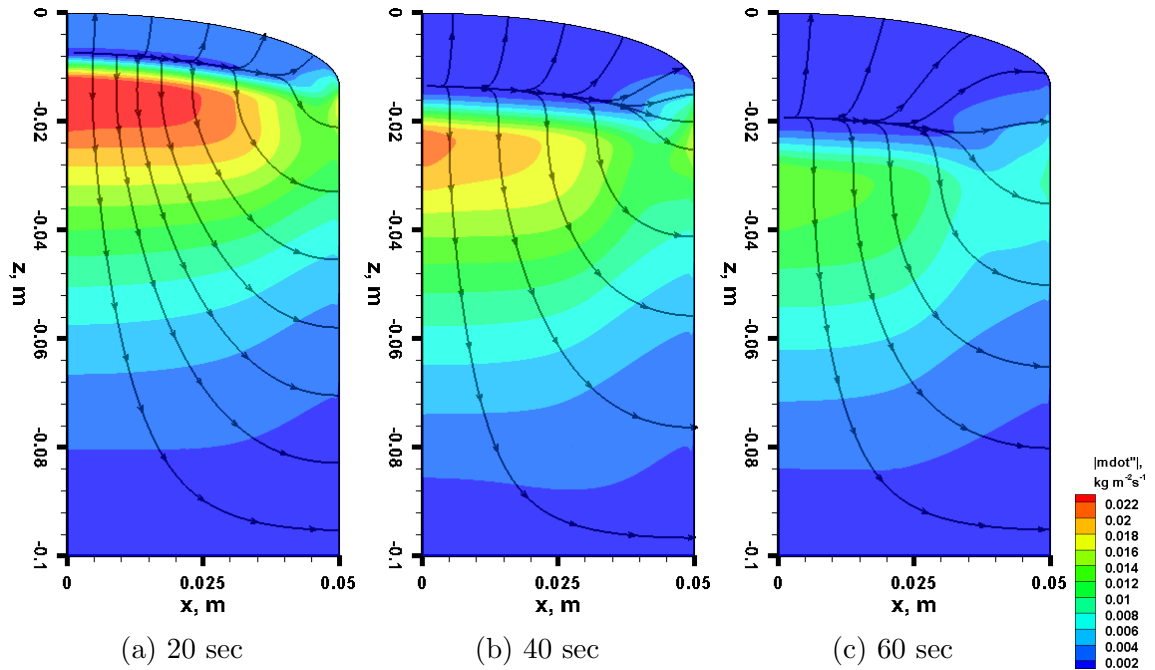


Figure 9.8: Pyrolysis gas transport for Case 5, orthotropic thermal conductivity:  $k_{IP}/k_{TTT} = 2$

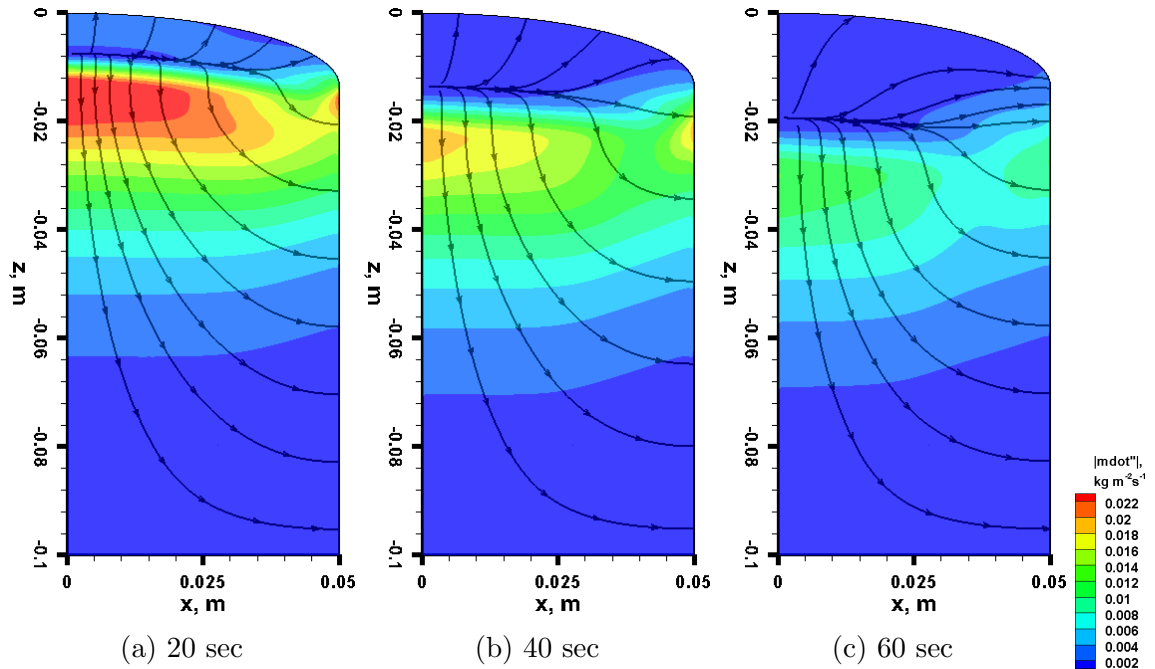


Figure 9.9: Pyrolysis gas transport for Case 6, orthotropic permeability and thermal conductivity:  $K_{IP}/K_{TTT} = k_{IP}/k_{TTT} = 2$

sample. The temperature profiles on these thermocouple locations confirmed the importance of side wall heating effect: when IP thermal conductivity was greater,

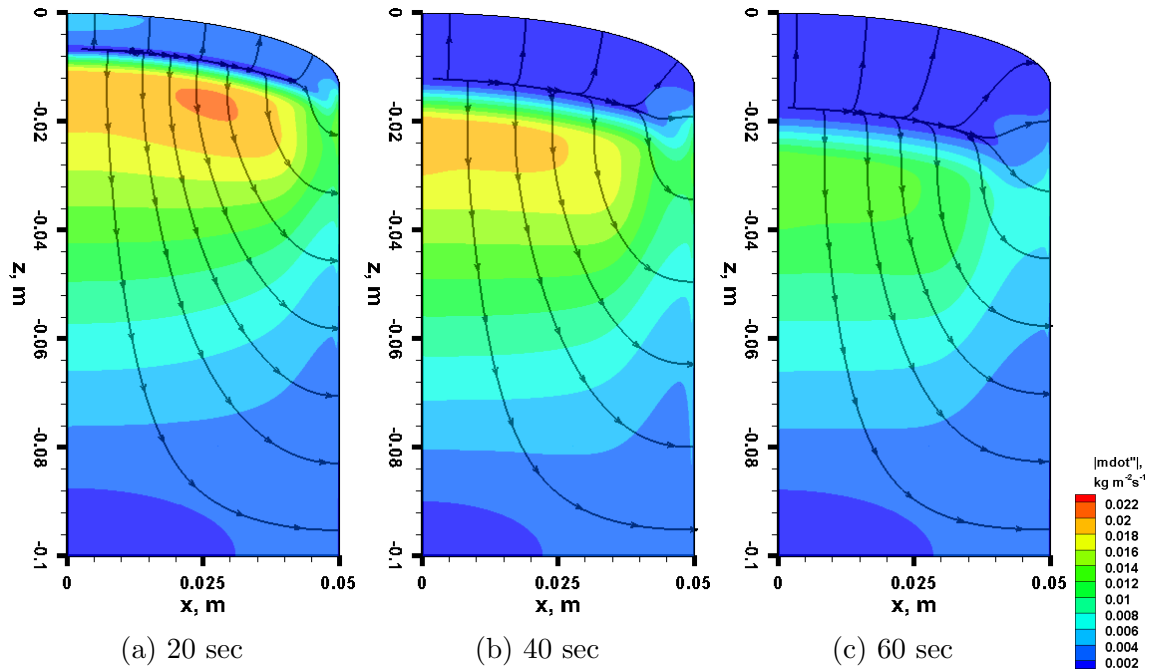


Figure 9.10: Pyrolysis gas transport for Case 7, orthotropic permeability and thermal conductivity:  $K_{IP}/K_{TTT} = k_{IP}/k_{TTT} = 0.5$

the temperatures at thermocouple 1 to 6 were higher than the isotropic case; when  $k_{IP}$  was smaller, these temperatures were lower. This observation confirmed that the horizontal heat transfer is very important to the centerline thermal response.

For the material permeability, it can be seen from Fig. 9.11 to 9.16 that, the orthotropic models also altered the temperature profiles: when  $K_{IP}$  is greater, the centerline temperature is slightly greater than the value with the isotropic model, and vice versa. To explain the connection between the permeability models and the temperatures, consider the pyrolysis gas flow pattern in any of the figure from Fig. 9.4 to Fig. 9.10: a majority of the gas traveled downward first, then leaned towards the right, and eventually exited through the side wall. When  $K_{IP}$  was increased, the horizontal gas movement was enhanced, thus more gas was pulled to flow downward. The pulled gas was generated in the decomposition zone, which was hotter than the material below, therefore, the hot gas further heated up the material along the centerline, and more gas led to more heating. However, this temperature increment

was small when compared to the temperature increment caused by the increased IP thermal conductivity.

The temperature profiles for thermocouples 8 to 10, which located near the side wall of the material, are presented in Figs 9.18 to 9.20. When the IP permeabilities ( $K_{IP}$ ) were doubled and tripled (depicted as the green and purple stars, respectively), the temperatures were lower than in the isotropic case (the red solid lines). When  $K_{IP}$  is halved, as depicted by the blue open squares in the figures, the behavior is just the opposite. Note that this behavior is just the opposite to the behaviors for thermocouples 1 to 6. The reason of the opposite behavior is because the pyrolysis gas flowed towards the shoulder region were from inside of the material, which was cooler than the heated side wall. Therefore, when  $K_{IP}$  was increased, the horizontal gas transport was enhanced, and the temperatures at thermocouples 8 to 10 are decreased due to the cooling effect.

The thermocouple 7 is located in between the centerline and the side wall of the material. The temperature profiles for this thermocouple is presented in Fig. 9.17, which were neither similar to the ones at the centerline nor to the ones near the side wall. Since the results in Fig. 9.17 were very close to each other, the orthotropic behaviors at thermocouple 7 cannot be categorized into any of the analyses above. The thermal response at this location was appeared to behave under the influences of both analyses.

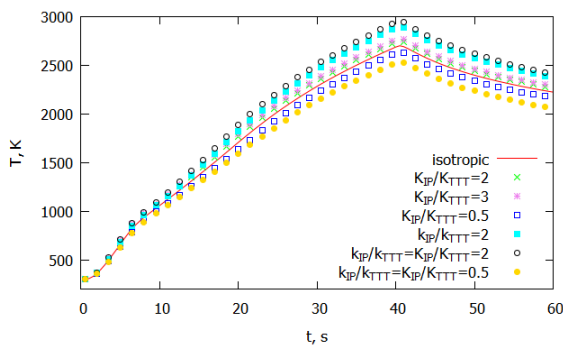


Figure 9.11: T profiles at TC 1

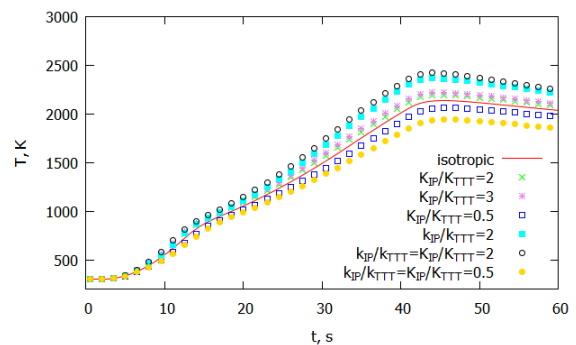


Figure 9.12: T profiles at TC 2

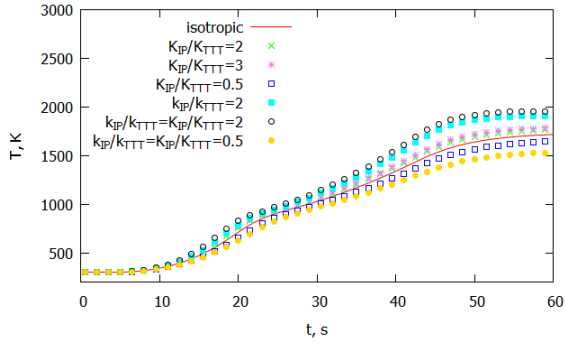


Figure 9.13: T profiles at TC 3

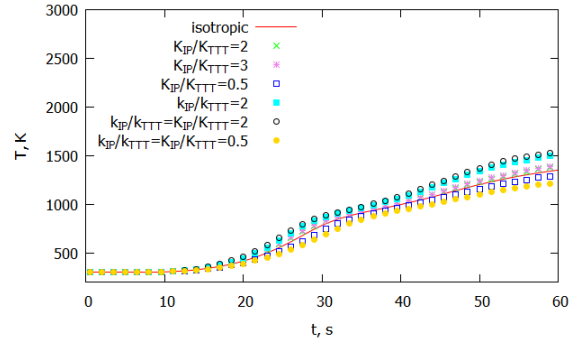


Figure 9.14: T profiles at TC 4

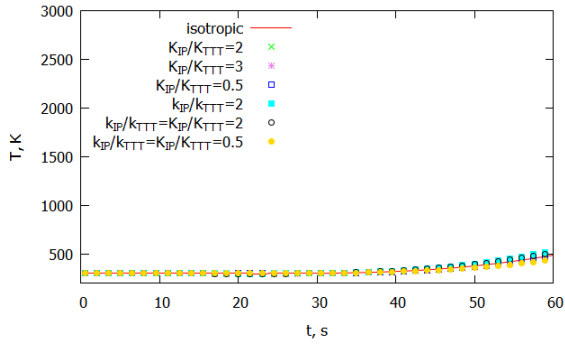


Figure 9.15: T profiles at TC 5

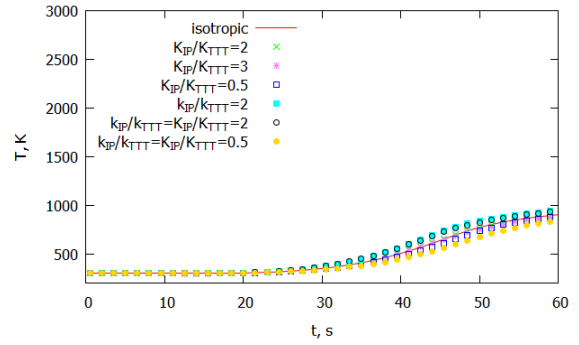


Figure 9.16: T profiles at TC 6

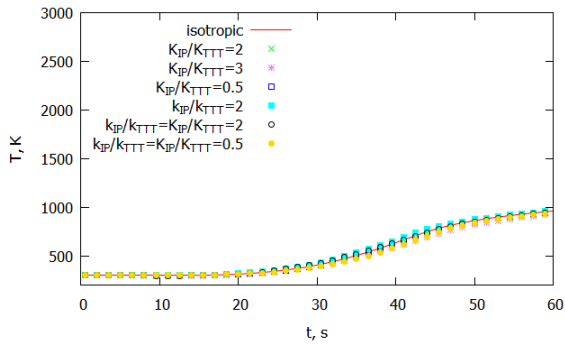


Figure 9.17: T profiles at TC 7

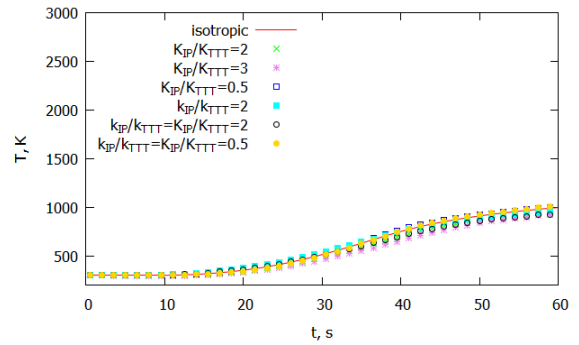


Figure 9.18: T profiles at TC 8

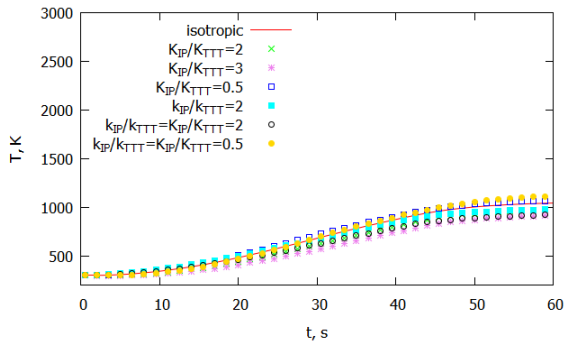


Figure 9.19: T profiles at TC 9

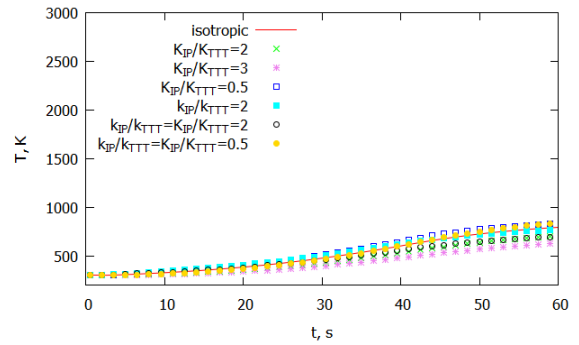


Figure 9.20: T profiles at TC 10

## 9.5 Conclusions for orthotropic properties study

An orthotropic material properties model was numerically studied by performing a series of 3D simulations on the iso-Q sample. As expected, the orthotropic model affected the inner thermal response and the pyrolysis gas flow pattern noticeably.

In particular, the orthotropic permeability enhanced the pyrolysis gas flow in the direction that had higher permeability. Moreover, the orthotropic permeability also altered the thermal response slightly, either heating or cooling the material, depending the location and the flow direction. The temperature changes were explained to be due to the enthalpy carried by the pyrolysis gas, as it traveled within the porous material. Using this information, the gas flow within the material and the blowing direction can be manipulated by altering the orientation angle of the material to obtain the desired thermal or blowing performance.

The orthotropic thermal conductivity greatly affected the thermal response within the iso-Q sample, as expected. However, its influence to the gas flow pattern was small. It is also worthwhile to mention that the experiment with high IP thermal conductivity demonstrated the significance of the side wall heating effect.

The conclusions in this study are likely extendible to highly porous, highly permeable, orthotropic charring materials such as PICA and SIRCA, where the effects of pyrolysis gas transport are noticeable. But for dense materials with low permeability, the gas effects and permeability models are expected to be insignificant; the importance of conductivity models however, is expected to remain significant.

As a summary of this study, 1) a comprehensive orthotropic material properties model was implemented, 2) the significances of the properties models were shown, 3) the effects of pyrolysis gas transport within orthotropic materials were demonstrated and analyzed.

## Chapter 10 Conclusions

### 10.1 Summary

The development of a multidimensional thermal and material response module was presented. The module is based on a FVM computational system with first order accuracy in time and second order accuracy in space. The major application of this solver is to analysis and predict the behavior of charring ablative materials.

In this work, a thorough literature review regarding the history of charring ablation modeling was first presented (Chapter 1), which focused on multidimensional and pyrolysis gas transport models. The computational framework (Chapter 2) and governing equations (Chapter 3) were presented next, followed by material models (Chapter 5). The material charring models were verified using analytical solutions and through a code-to-code comparison, in which promising results were shown (Chapter 6). Moreover, several multidimensional effects were investigated through the series of parametric studies presented in Chapter 7, 8, and 9. The outcomes of these studies and the original contributions of this work are emphasized in the following section.

### 10.2 Original contributions

A list of original contributions to the field of charring ablation modeling and numerical heat transfer is outlined in this section.

1. **A multidimensional pyrolysis gas transport model using time dependent equations and orthotropic, density-based permeability model. (Chapter 5)** Most of the existing multidimensional works did not model the pyrolysis gas transport within charring ablators [35, 37, 38, 45]. In this work, the multidimensional gas transport was modeled with a set of time-dependent

momentum equations based on Darcy's law. The permeability was assumed to be orthotropic, and was modeled by interpolation between virgin and char value, based on degree of char (Eq. (5.1)). This model is important, since the permeability of charring ablative materials may vary by two to three times depending on the orientation, and even as much as three order of magnitudes between virgin and char [92].

- 2. A study of pyrolysis gas transport performed to find the difference between a 3D model and the conventional 1D model. (Chapter 7)** For small charring ablative samples in ground-test facilities such as arc-jet and ICP torches, the conventional 1D assumption breaks. By solving the momentum equations proposed in the previous contribution, the pyrolysis gas was found to blow majorly through the side walls of a test article, as opposed to the 1D assumption where gas only blows through the front surface. Correct modeling of gas blowing is important since the blowing rate is directly related to the accurate modeling of thermal boundary conditions and reacting boundary layers. Moreover, the 3D gas transport behavior was also found to affect the thermal response of the sample. This was explained by the enthalpy carried by the pyrolysis gas: as the generated hot gas flows within the material, the material is further heated in the flow direction. This further strengthens the importance of the 3D gas transport model proposed in this work.

It was also found in this study that, the non-uniform pressure boundary condition introduced by multidimensional modeling actually encourages the side blowing effect, since the stagnation pressure at the material front is usually higher than the pressure on the sides.

- 3. A study of geometric effects of iso-Q test sample aiming to find the relation between sample performance and sample diameter, thick-**



**ness, holder geometry. (Chapter 8)** It was found in this study that, the iso-Q sample thickness-to-diameter ratio is crucial to the thermal and material response. In general, the smaller the diameter, the greater heat penetration from the side and the less blowing through the front surface. Moreover, the sample thickness is found to mainly affect the side wall blowing distribution: if the sample thickness is much greater than the charring depth, the side wall blowing pattern is a single peak distribution that highly skewed toward the shoulder corner of the sample; if the sample thickness is short enough to be comparable with charring depth, a strong gas blowing will take place at the lower corner of the sample side wall. These conclusions are likely extensible to other low density, highly porous ablative articles used in ground-test facilities. For ablators with low virgin permeability and very high char permeability such as SIRCA [108], the gas blowing pattern is expected to be similar, although the pyrolysis gas transport in the virgin material is expected to diminish greatly.

The sample holders, if sheathed outside of the material, altered the material's thermal and blowing response slightly. The altered behaviors were very similar to the sample thickness being shortened by the length of the sample holder. Sample holders located inside of the material did not change much of the ablator performance, except at the stagnation point for high diameter-to-thickness ratio samples. Keeping in mind that the actual experimental conditions may vary, these results may be used as qualitative guidelines for choosing model geometries in future arc-jet experiments.

4. **A study of orthotropic material properties performed to find the significance of the orthotropic model on iso-Q sample performance. (Chapter 9)** The orthotropic material properties essentially altered the material thermal and blowing performance in the direction of isotropy. In particular, the orthotropic thermal conductivity greatly influenced the sample thermal re-

sponse, since the heat transfer to the material came from both the front and the side; thus, the directional properties resulted in different temperature profiles from using isotropic properties. However, the effect of orthotropic thermal conductivity to the pyrolysis gas flow pattern was negligible. The orthotropic permeability enhanced the pyrolysis gas flow in the direction with higher permeability. In addition, the permeability model also slightly altered the thermal response in the direction of the flow. Using these information, the gas flow within the material and the blowing direction can be manipulated by altering the orientation angle of the material, to obtain the desired thermal or blowing performance.

These conclusions are likely extendible to highly porous, highly permeable, orthotropic charring materials such as PICA and SIRCA, in which the effects of pyrolysis gas transport are noticeable. For dense materials with low permeability, the effects of gas flow and orthotropic permeability are expected to be insignificant, while the effect of orthotropic thermal conductivity should remain significant.

### 10.3 Future work

This work provided a tool box with basic models for charring materials, yet several phenomena in the charring ablation process were not modeled. The following models are partially implemented or considered to be implemented in the future:

1. **3D moving mesh and ablation models.** Ablation is an endothermic process, which is very important for charring ablation problems with surface recessions. The obstacle preventing the implementation of ablation models is 3D moving mesh, which was not an option in the current KATS and not trivial. Once this obstacle is overcome, the ablation models will be implemented to investi-

gate the effects of ablation in conjunction with material decomposition and its significance to the existing conclusions.

2. **Volume-averaged carbon oxidation model.** Ablation has two limited regime: diffusion limited and reaction limited. The volume-averaged carbon oxidation model is for reaction limited ablation, for which oxygen are diffused inside the material and carbon fibers are oxidized from within. Since the model is volume-averaged, it fits well with the finite volume method used in KATS.
3. **Chemical non-equilibrium pyrolysis gas model with multiple gas species and reactions among them.** The chemical non-equilibrium model is necessary for a high fidelity material response program. With this model, not only the overall blowing rate, but also the blowing rate of individual species can be obtained, which enable a more accurate analysis of boundary layer flow and a stronger coupling with a CFD solver.
4. **Thermal non-equilibrium between the pyrolysis gas and the material.** Thermal equilibrium is usually assumed for the heat transfer between the pyrolysis gas and the solid material, since it is valid for a large range of Nusselt number. Charring ablation problems with Nusselt number beyond the equilibrium range (though rare) may require a thermal non-equilibrium model. In addition, the heat transfer between the inner pyrolysis gas and the solid matrix will be modeled, which allows controlled modeling of the heat transfer due to the pyrolysis gas transport discussed in this thesis. Finally, it is also interesting to investigate the difference between the thermal equilibrium and non-equilibrium models, and find out how much they vary.
5. **Spallation and delamination models due to thermal and mechanical stresses.** Spallation is part of the ablation phenomena, yet few literatures have modeled it or looked into its effect. This phenomenon requires information from

both the material and the flow field. Delamination is the phenomenon that the material forms cracks within the material, and some cracks may be observed from outside. The delamination is due to thermal and mechanical stresses. Coupled with a stress solver, the delamination effects can be modeled on top of the existing material response solver.

## Appendix A

### Jacobian matrices in the governing equations

The Jacobian matrices in Eq. (2.9) are presented in this appendix. The Jacobian matrix  $\frac{\partial \mathbf{Q}}{\partial \mathbf{P}}$  consists of derivatives of conservative variables over primitive variables.

The two conservative and primitive vectors are revisited as:

$$\mathbf{Q} = \begin{pmatrix} \phi \rho_{g1} \\ \vdots \\ \phi \rho_{gngs} \\ \rho_{s1} \\ \vdots \\ \rho_{snss} \\ \phi \rho_g u \\ \phi \rho_g v \\ \phi \rho_g w \\ \phi E_g + E_s \end{pmatrix}, \quad \mathbf{P} = \begin{pmatrix} p_1 \\ \vdots \\ p_{ngs} \\ \rho_{s1} \\ \vdots \\ \rho_{snss} \\ u \\ v \\ w \\ T \end{pmatrix}, \quad (3.1 \text{ revisited})$$

where

$$\rho_g = \rho_{g_1} + \rho_{g_2} + \cdots + \rho_{g_{ngs}},$$

$$p = p_1 + p_2 + \cdots + p_{ngs},$$

$$\rho_s = \Gamma_1 \rho_{s_1} + \Gamma_2 \rho_{s_2} + \cdots + \Gamma_{nss} \rho_{s_{nss}},$$

$$E_g = \rho_g h + \frac{1}{2} \rho_g (u^2 + v^2 + w^2) - p,$$

$$E_s = \rho_s c_{p,s} T = \rho_s h_s.$$

The Jacobian matrix  $\frac{\partial \mathbf{Q}}{\partial \mathbf{P}}$  is thus calculated as Eq. (1), which is given in the next page.

$$\frac{\partial \mathbf{Q}}{\partial \mathbf{P}} = \begin{pmatrix} \phi \frac{\partial \rho_{g1}}{\partial p_1} & 0 & \dots & 0 & \frac{\partial \phi}{\partial \rho_{s1}} \rho_{g1} & \frac{\partial \phi}{\partial \rho_{s2}} \rho_{g1} & \dots & \frac{\partial \phi}{\partial \rho_{s_{n,ss}}} \rho_{g1} & 0 & 0 & 0 & \phi \frac{\partial \rho_{g1}}{\partial T} \\ 0 & \phi \frac{\partial \rho_{g1}}{\partial p_2} & \dots & 0 & \frac{\partial \phi}{\partial \rho_{s1}} \rho_{g2} & \frac{\partial \phi}{\partial \rho_{s2}} \rho_{g2} & \dots & \frac{\partial \phi}{\partial \rho_{s_{n,ss}}} \rho_{g2} & 0 & 0 & 0 & \phi \frac{\partial \rho_{g2}}{\partial T} \\ \vdots & \vdots & \ddots & \vdots & \vdots & \vdots & \ddots & \vdots & \vdots & \vdots & \vdots & \vdots \\ 0 & 0 & \dots & \phi \frac{\partial \rho_{g_{n,gs}}}{\partial p_{n,gs}} & \frac{\partial \phi}{\partial \rho_{s1}} \rho_{g_{n,gs}} & \frac{\partial \phi}{\partial \rho_{s2}} \rho_{g_{n,gs}} & \dots & \frac{\partial \phi}{\partial \rho_{s_{n,ss}}} \rho_{g_{n,gs}} & 0 & 0 & 0 & \phi \frac{\partial \rho_{g_{n,gs}}}{\partial T} \\ 0 & 0 & \dots & 0 & 1 & 0 & \dots & 0 & 0 & 0 & 0 & 0 \\ 0 & 0 & \dots & 0 & 0 & 1 & \dots & 0 & 0 & 0 & 0 & 0 \\ \vdots & \vdots & \ddots & \vdots & \vdots & \vdots & \ddots & \vdots & \vdots & \vdots & \vdots & \vdots \\ 0 & 0 & \dots & 0 & 0 & 0 & \dots & 1 & 0 & 0 & 0 & 0 \\ \frac{\partial \rho_g}{\partial p_1} \phi u & \frac{\partial \rho_g}{\partial p_2} \phi u & \dots & \frac{\partial \rho_g}{\partial p_{n,gs}} \phi u & \frac{\partial \phi}{\partial \rho_{s1}} \rho u & \frac{\partial \phi}{\partial \rho_{s2}} \rho u & \dots & \frac{\partial \phi}{\partial \rho_{s_{n,ss}}} \rho u & \phi \rho_g & 0 & 0 & \phi u \frac{\partial \rho_g}{\partial T} \\ \frac{\partial \rho_g}{\partial p_1} \phi v & \frac{\partial \rho_g}{\partial p_2} \phi v & \dots & \frac{\partial \rho_g}{\partial p_{n,gs}} \phi v & \frac{\partial \phi}{\partial \rho_{s1}} \rho v & \frac{\partial \phi}{\partial \rho_{s2}} \rho v & \dots & \frac{\partial \phi}{\partial \rho_{s_{n,ss}}} \rho v & 0 & \phi \rho_g & 0 & \phi v \frac{\partial \rho_g}{\partial T} \\ \frac{\partial \rho_g}{\partial p_1} \phi w & \frac{\partial \rho_g}{\partial p_2} \phi w & \dots & \frac{\partial \rho_g}{\partial p_{n,gs}} \phi w & \frac{\partial \phi}{\partial \rho_{s1}} \rho w & \frac{\partial \phi}{\partial \rho_{s2}} \rho w & \dots & \frac{\partial \phi}{\partial \rho_{s_{n,ss}}} \rho w & 0 & 0 & \phi \rho_g & \phi w \frac{\partial \rho_g}{\partial T} \\ \frac{\partial E}{\partial p_1} & \frac{\partial E}{\partial p_2} & \dots & \frac{\partial E}{\partial p_{n,gs}} & \frac{\partial E}{\partial \rho_{s1}} & \frac{\partial E}{\partial \rho_{s2}} & \dots & \frac{\partial E}{\partial \rho_{s_{n,ss}}} & \phi \rho_g u & \phi \rho_g v & \phi \rho_g w & \frac{\partial E}{\partial T} \end{pmatrix}. \quad (1)$$

The derivatives in the Jacobian matrix are given as:

$$\begin{aligned}
\frac{\partial \rho_{g_i}}{\partial p_i} &= \frac{\partial(p_i/(R_i T))}{\partial p_i} = R_i T = \frac{\rho_{g_i}}{p_i}, \quad i = 1, 2, \dots, ngs \\
\frac{\partial \rho_{g_i}}{\partial T} &= \frac{\partial(p_i/(R_i T))}{\partial T} = \frac{p_i}{R_i} \left(-\frac{1}{T^2}\right) = -\frac{\rho_{g_i}}{T}, \quad i = 1, 2, \dots, ngs \\
\frac{\partial \phi}{\partial \rho_{s_i}} &= \frac{\partial \phi}{\partial \rho_s} \frac{\partial \rho_s}{\partial \rho_{s_i}} = \frac{\partial \beta(\phi_c - \phi_v)}{\partial \rho_s} \Gamma_i = \frac{\phi_c - \phi_v}{\rho_c - \rho_v} \Gamma_i, \quad i = 1, 2, \dots, nss \\
\frac{\partial E_s}{\partial T} &= \rho_s c_{p,s} \\
\frac{\partial E_s}{\partial \rho_{s_i}} &= (h_s + \rho_s \frac{\partial h_s}{\partial \rho_s}) \Gamma_i, \quad i = 1, 2, \dots, nss \\
\frac{\partial h_s}{\partial \rho_s} &= (h_v - h_c) \frac{\partial \tau}{\partial \rho_s} = -(h_v - h_c) \frac{\rho_c \rho_v}{(\rho_v - \rho_c)} \left(-\frac{1}{\rho_s^2}\right) = (h_v - h_c) \frac{\rho_c \rho_v}{(\rho_v - \rho_c) \rho_s^2} \\
\frac{\partial E_g}{\partial p_i} &= \left( h_g + \frac{1}{2}(u^2 + v^2 + w^2) \right) \frac{\partial \rho_g}{\partial p_i} - 1, \quad i = 1, 2, \dots, ngs \\
\frac{\partial E_g}{\partial T} &= \left( h_g + \frac{1}{2}(u^2 + v^2 + w^2) \right) \frac{\partial \rho_g}{\partial T} + \rho_g c_{p,g}, \quad i = 1, 2, \dots, ngs
\end{aligned}$$

The rest of the derivatives in Eq. (2.9) are obtained numerically, using Eq. (2.11) in Section 2.1.



## Appendix B

### Input deck of the material response module in KATS

A sample input deck of KATS is presented in this appendix. The input deck is the one that used to solve the theoretical charring problem given in Section 6.3.

```
reference {Mach=1.;p=0;T=0.;}
time marching {
    step size=1e-2;
    number of steps = 6000;
    update frequency = 1000;
}
grid_1 {
    file=grid/3D200.cgns;
    transform_1 (
        function=scale;
        anchor=[0.,0.,0.];
        factor=[5,5,5];
    );
    dimension=3;
    equations=heat conduction;
    heat conduction (
        // Debug info
```

```

debug cell index = [0,2,200,202];
debug face index = [3];
//debug mode = 0;

// Number of ...
number of gas species = 1;
number of solid species = 3;
number of dimensions = 3;
number of energy equations = 1;

// Problem type
problem type = charring ablative;

// Momentum equation type
momentum equations = Darcys law;

convective flux = AUSM+up;
order = second;
relative tolerance = 1e-8;
absolute tolerance = 1e-9;
maximum iterations = 1000;
);
write output (
    format=tecplot;
    volume variables=[T,p,rhos,hg];
    surface variables=[T,pi,rhos,hg,mu,mdot,qdot];
    volume plot frequency = 1000;

```

```

        surface plot frequency = 1000;
        restart frequency = 2000;
        moment center = [0.,0.,0.];
        load frequency = 10;
        include bcs=[4];
//        sampling file = tcpoints.txt;
//        sampling variables = [T];
//        sampling frequency = 10;
    );
    material (
        fluid file = material/fluid.mat;
        solid file = material/solid.mat;
    );
    IC_1 (T=298; p=10132.5; rhos=[60,180,320]);
    BC_1 (type=wall);
    BC_3 (type=symmetry);
    BC_2 (type=outlet;
        p = 10132.5;
        T = 1644;
    );
}

```

Most of the inputs are self-explanatory, except for the material section, which is defined in separate files. The input deck only provides the directories of the material files. In each material file, the material model is first specified. For instance, the solid material file (material/solid.mat) for this case defines the decomposition model as phenomenological first; then the virgin and char properties are specified, such that:

```
decomposition model = phenomenological;
```

```

virgin{
    density = 280;
    porosity = 0.8;
    permeability = 1.6E-11;
    tuotorsity = 1.2;
    volume fraction = 0.5;
    thermal properties table = svrgn.txt;
}

char{
    density = 220;
    porosity = 0.85;
    permeability = 2.0E-11;
    tuotorsity = 1.1;
    volume fraction = 0.5;
    thermal properties table = schar.txt;
}

reaction file = r3cmp.txt;

```

Similarly, the fluid material file (material/fluid.mat) for this case specifies the single species model (or using an equilibrium table) in the first line:

```

gas model = eq table; // single species model
gas species = [gpyro]; // linked to gpyro.txt

```

The properties of the species are given by a file named “gpyro.txt” in the material directory, as indicated by the file name inside the brackets. For gas materials with multiple species, the names of all species have to be specified in the brackets, separated by comma.

## Appendix C

### Derivation of conservation equations in porous media

The derivation of conservation equations presented here is 2D, and is easily extensible to 3D. Consider a 2D porous control volume, as illustrated in Fig. C.1. The size of the volume is  $\Delta x$  by  $\Delta y$ ; the volume is therefore  $V = \Delta x \Delta y$ . The volume of the gas portion is given as  $V_g = \phi V$ , where  $\phi$  is porosity.

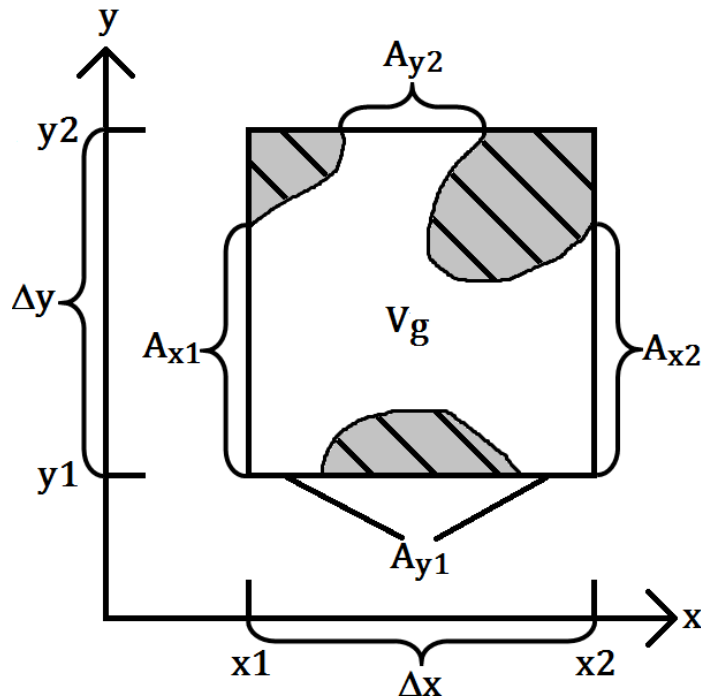


Figure C.1: Sketch of a 2D control volume for derivation of conservation equations

The mass conservation in a control volume can be expressed as: the mass change in a time interval  $\Delta t$  equals to the net mass flow through the boundaries + the mass change by internal sources. This conservation idea can be represented by the following

equation:

$$(V_g \rho_g)^{(n+1)} - (V_g \rho_g)^{(n)} = (\rho_g u A)_{x1} \Delta t - (\rho_g u A)_{x2} \Delta t + (\rho_g v A)_{y1} \Delta t - (\rho_g v A)_{y2} \Delta t + \omega_g V \Delta t, \quad (2)$$

where the superscript  $(n)$  represents the time marching level, that  $t^{(n+1)} = t^{(n)} + \Delta t$ . Assuming  $A_{x1} = \phi_{x1} \Delta y$ ,  $A_{x2} = \phi_{x2} \Delta y$ ,  $A_{y1} = \phi_{y1} \Delta x$ ,  $A_{y2} = \phi_{y2} \Delta x$ , and replacing  $V_g$  with  $\phi V$ , Eq. (2) becomes:

$$V [(\phi \rho_g)^{(n+1)} - (\phi \rho_g)^{(n)}] = \Delta y \Delta t [(\phi \rho_g u)_{x1} - (\phi \rho_g u)_{x2}] + \Delta x \Delta t [(\phi \rho_g v)_{y1} - (\phi \rho_g v)_{y2}] + \omega_g V \Delta t. \quad (3)$$

Divided Eq. (3) by  $\Delta x \Delta y \Delta t$ , the following equation is obtained:

$$\frac{(\phi \rho_g)^{(n+1)} - (\phi \rho_g)^{(n)}}{\Delta t} = \frac{(\phi \rho_g u)_{x1} - (\phi \rho_g u)_{x2}}{\Delta x} + \frac{(\phi \rho_g v)_{y1} - (\phi \rho_g v)_{y2}}{\Delta y} + \omega_g. \quad (4)$$

Assuming the volume size and the time step size are infinitesimal, or  $\Delta x, \Delta y, \Delta t \rightarrow 0$ , Eq. (4) can be written into the differential form as following:

$$\begin{aligned} \lim_{\Delta t \rightarrow 0} \frac{(\phi \rho_g)^{(n+1)} - (\phi \rho_g)^{(n)}}{\Delta t} &= - \lim_{\Delta x \rightarrow 0} \frac{(\phi \rho_g u)_{x2} - (\phi \rho_g u)_{x1}}{\Delta x} \\ &- \lim_{\Delta y \rightarrow 0} \frac{(\phi \rho_g v)_{y2} - (\phi \rho_g v)_{y1}}{\Delta y} + \omega_g \\ \Rightarrow \frac{\partial(\phi \rho_g)}{\partial t} &= - \frac{\partial(\phi \rho_g u)}{\partial x} - \frac{\partial(\phi \rho_g v)}{\partial y} + \omega_g \\ \Rightarrow \frac{\partial(\phi \rho_g)}{\partial t} + \frac{\partial(\phi \rho_g u)}{\partial x} + \frac{\partial(\phi \rho_g v)}{\partial y} &= \omega_g \end{aligned} \quad (5)$$

For the momentum conservation, similar analysis is applied. The conservation law can be expressed as: the momentum change in a time interval  $\Delta t$  equals to the net momentum flow through the boundaries + the net momentum change due to the pressure on the boundary + the diffusive effects of the porous media. The  $x$ -direction conservation law can be written as:

$$(V_g \rho_g u)^{(n+1)} - (V_g \rho_g u)^{(n)} = (\rho_g u^2 A)_{x1} \Delta t - (\rho_g u^2 A)_{x2} \Delta t + (\rho_g uv A)_{y1} \Delta t - (\rho_g uv A)_{y2} \Delta t + p_{x1} \Delta y \Delta t - p_{x2} \Delta y \Delta t + D_x V \Delta t. \quad (6)$$

Divided by  $\Delta x \Delta y \Delta t$ , the following is obtained:

$$\begin{aligned} \frac{(\phi \rho_g u)^{(n+1)} - (\phi \rho_g u)^{(n)}}{\Delta t} &= \frac{(\phi \rho_g u^2)_{x1} - (\phi \rho_g u^2)_{x2}}{\Delta x} + \frac{(\phi \rho_g uv)_{y1} - (\phi \rho_g uv)_{y2}}{\Delta y} \\ &+ \frac{p_{x1} - p_{x2}}{\Delta x} + D_x. \end{aligned} \quad (7)$$

Taking limits that  $\Delta x, \Delta y, \Delta t \rightarrow 0$ , the Eq. (7) yields:

$$\frac{\partial(\phi \rho_g u)}{\partial t} + \frac{\partial(\phi \rho_g u^2 + p)}{\partial x} + \frac{\partial(\phi \rho_g uv)}{\partial y} = D_x. \quad (8)$$

Similarly, the energy balance can be described as: the overall energy change in a time interval  $\Delta t$  equals to the net enthalpy flux through the boundaries + the conductive heat transfer + the energy change due to other diffusive effects. Therefore, the equation for the energy conservation can be written as:

$$\begin{aligned} (V_g E_g + V E_s)^{(n+1)} - (V_g E_g + V E_s)^{(n)} &= S_D V \Delta t \\ + (\rho_g u H A)_{x1} \Delta t - (\rho_g u H A)_{x2} \Delta t + (\rho_g v H A)_{y1} \Delta t - (\rho_g v H A)_{y2} \Delta t \\ - F_{cond,x}|_{x1} \Delta y \Delta t + F_{cond,x}|_{x2} \Delta y \Delta t - F_{cond,y}|_{y1} \Delta y \Delta t + F_{cond,y}|_{y2} \Delta y \Delta t, \end{aligned} \quad (9)$$

where  $E_s = \rho_s c_{p,s} T$  and the solid density here is the effective density (solid mass over the whole volume), therefore  $E_s$  is multiplied with the whole control volume rather than the solid volume. Divide Eq. (9) by  $\Delta x \Delta y \Delta t$ , then the following is obtained:

$$\begin{aligned} \frac{(\phi E_g + E_s)^{(n+1)} - (\phi E_g + E_s)^{(n)}}{\Delta t} &= S_D \\ + \frac{(\phi \rho_g u H)_{x1} - (\phi \rho_g u H)_{x2}}{\Delta x} + \frac{(\phi \rho_g v H)_{y1} - (\phi \rho_g v H)_{y2}}{\Delta y} \\ - \frac{F_{cond,x}|_{x1} - F_{cond,x}|_{x2}}{\Delta x} - \frac{F_{cond,y}|_{y1} - F_{cond,y}|_{y2}}{\Delta y}. \end{aligned} \quad (10)$$

Taking limit for  $\Delta x, \Delta y$ , and  $\Delta t$ , the following differential equation is obtained:

$$\frac{\partial(\phi E_g + E_s)}{\partial t} + \frac{\partial(\phi \rho_g u H)}{\partial x} + \frac{\partial(\phi \rho_g v H)}{\partial y} - \frac{\partial F_{cond,x}}{\partial x} - \frac{\partial F_{cond,y}}{\partial y} = S_D. \quad (11)$$

In summary, the conservation equations of mass, momentum, and energy were derived in 2D and given by Eqs. (5), (8), (11), respectively. Based on these equations,

the conservation equations in 3D can be extended as:

$$\frac{\partial(\phi\rho_g)}{\partial t} + \frac{\partial(\phi\rho_g u)}{\partial x} + \frac{\partial(\phi\rho_g v)}{\partial y} + \frac{\partial(\phi\rho_g w)}{\partial z} = \omega_g, \quad (12a)$$

$$\frac{\partial(\phi\rho_g u)}{\partial t} + \frac{\partial(\phi\rho_g u^2 + p)}{\partial x} + \frac{\partial(\phi\rho_g uv)}{\partial y} + \frac{\partial(\phi\rho_g uw)}{\partial z} = D_x, \quad (12b)$$

$$\frac{\partial(\phi\rho_g v)}{\partial t} + \frac{\partial(\phi\rho_g uv)}{\partial x} + \frac{\partial(\phi\rho_g v^2 + p)}{\partial y} + \frac{\partial(\phi\rho_g vw)}{\partial z} = D_y, \quad (12c)$$

$$\frac{\partial(\phi\rho_g w)}{\partial t} + \frac{\partial(\phi\rho_g uw)}{\partial x} + \frac{\partial(\phi\rho_g vw)}{\partial y} + \frac{\partial(\phi\rho_g w^2 + p)}{\partial z} = D_z, \quad (12d)$$

$$\begin{aligned} \frac{\partial(\phi E_g + E_s)}{\partial t} + \frac{\partial(\phi\rho_g uH)}{\partial x} + \frac{\partial(\phi\rho_g vH)}{\partial y} + \frac{\partial(\phi\rho_g wH)}{\partial z} \\ - \frac{\partial F_{cond,x}}{\partial x} - \frac{\partial F_{cond,y}}{\partial y} - \frac{\partial F_{cond,z}}{\partial z} = S_D. \end{aligned} \quad (12e)$$

The solid mass conservation equation is quite trivial:

$$\frac{\partial\rho_{s_i}}{\partial t} = \omega_{s_i}, \quad i = 1, \dots, n_{ss}. \quad (13)$$

Note that, Eqs. (12) and (13) are equivalent to the governing equations presented by Eqs. (3.1) and (3.2), except the gas mass conservation was extended to multiple species. The conservation equations in porous media are thus derived.



## Appendix D

### Material properties of TACOT

The material used in this document is TACOT 3.0, which can be found in Ref. [110]. The thermal properties of the virgin and char material are given in Table D.1 and Table D.2, respectively.

Table D.1: TACOT virgin thermal properties

T (K)	cp (J/kg/K)	k (W/m/K)	h(J/kg)
2.556E+02	8.792E+02	3.975E-01	-8.967E+05
2.980E+02	9.839E+02	4.025E-01	-8.57E+05
4.444E+02	1.298E+03	4.162E-01	-6.901E+05
5.556E+02	1.465E+03	4.530E-01	-5.365E+05
6.444E+02	1.570E+03	4.698E-01	-4.016E+05
8.333E+02	1.717E+03	4.860E-01	-9.124E+04
1.111E+03	1.863E+03	5.234E-01	4.059E+05
1.389E+03	1.934E+03	5.601E-01	9.334E+05
1.667E+03	1.980E+03	6.978E-01	1.477E+06
1.944E+03	1.989E+03	8.723E-01	2.028E+06
2.222E+03	2.001E+03	1.109E+00	2.583E+06
2.778E+03	2.010E+03	1.751E+00	3.697E+06
3.333E+03	2.010E+03	2.779E+00	4.813E+06

The pyrolysis gas model assumes chemical equilibrium. The equilibrium gas properties at 1 atm is given in Table. D.3.

Table D.2: TACOT char thermal properties

T (K)	$c_p$ (J/kg/K)	k (W/m/K)	h(J/kg)
2.556E+02	7.327E+02	3.975E-01	-3.216E+04
2.980E+02	7.829E+02	4.025E-01	0.000E+00
4.444E+02	1.093E+03	4.162E-01	1.373E+05
5.556E+02	1.319E+03	4.530E-01	2.713E+05
6.444E+02	1.432E+03	4.698E-01	3.936E+05
8.333E+02	1.675E+03	4.860E-01	6.870E+05
1.111E+03	1.842E+03	5.234E-01	1.175E+06
1.389E+03	1.968E+03	5.601E-01	1.705E+06
1.667E+03	2.052E+03	6.050E-01	2.263E+06
1.944E+03	2.093E+03	7.290E-01	2.839E+06
2.222E+03	2.110E+03	9.221E-01	3.422E+06
2.778E+03	2.135E+03	1.458E+00	4.602E+06
3.333E+03	2.152E+03	2.318E+00	5.793E+06

Table D.3: TACOT pyrolysis gas properties at 1 atm

$T$ (K)	$\gamma$	$Mw$ (kg/mol)	$c_p$ (J/kg/K)	$h_g$ (J/kg)	$\mu$ (Pa s)
2.000E+02	1.3334E+00	2.1996E-02	1.5119E+03	-7.2465E+06	8.6881E-06
2.250E+02	1.3271E+00	2.1996E-02	1.5336E+03	-7.2084E+06	9.6663E-06
2.500E+02	1.3199E+00	2.1996E-02	1.5597E+03	-7.1698E+06	1.0645E-05
2.750E+02	1.3114E+00	2.1996E-02	1.5921E+03	-7.1304E+06	1.1615E-05
3.000E+02	1.3018E+00	2.1996E-02	1.6308E+03	-7.0901E+06	1.2572E-05
3.250E+02	1.2914E+00	2.1996E-02	1.6755E+03	-7.0488E+06	1.3514E-05
3.500E+02	1.2807E+00	2.1995E-02	1.7259E+03	-7.0063E+06	1.4438E-05
3.750E+02	1.2697E+00	2.1994E-02	1.7826E+03	-6.9625E+06	1.5344E-05
4.000E+02	1.2587E+00	2.1992E-02	1.8467E+03	-6.9171E+06	1.6232E-05
4.250E+02	1.2475E+00	2.1988E-02	1.9205E+03	-6.8700E+06	1.7102E-05
4.500E+02	1.2362E+00	2.1981E-02	2.0075E+03	-6.8210E+06	1.7955E-05
4.750E+02	1.2248E+00	2.1968E-02	2.1124E+03	-6.7695E+06	1.8792E-05
5.000E+02	1.2133E+00	2.1948E-02	2.2411E+03	-6.7152E+06	1.9615E-05

Continued on next page

$T$ (K)	$\gamma$	$Mw$ (kg/mol)	$c_p$ (J/kg/K)	$h_g$ (J/kg)	$\mu$ (Pa s)
5.250E+02	1.2018E+00	2.1917E-02	2.4018E+03	-6.6572E+06	2.0424E-05
5.500E+02	1.1902E+00	2.1870E-02	2.6053E+03	-6.5947E+06	2.1221E-05
5.750E+02	1.1786E+00	2.1804E-02	2.8670E+03	-6.5265E+06	2.2007E-05
6.000E+02	1.1670E+00	2.1712E-02	3.2102E+03	-6.4507E+06	2.2785E-05
6.250E+02	1.1554E+00	2.1587E-02	3.6707E+03	-6.3650E+06	2.3556E-05
6.500E+02	1.1440E+00	2.1418E-02	4.3012E+03	-6.2657E+06	2.4323E-05
6.750E+02	1.1333E+00	2.1191E-02	5.1709E+03	-6.1479E+06	2.5089E-05
7.000E+02	1.1242E+00	2.0890E-02	6.3506E+03	-6.0046E+06	2.5861E-05
7.250E+02	1.1174E+00	2.0495E-02	7.8823E+03	-5.8274E+06	2.6644E-05
7.500E+02	1.1131E+00	1.9990E-02	9.7476E+03	-5.6077E+06	2.7443E-05
7.750E+02	1.1113E+00	1.9369E-02	1.1854E+04	-5.3380E+06	2.8261E-05
8.000E+02	1.1116E+00	1.8644E-02	1.4029E+04	-5.0144E+06	2.9092E-05
8.250E+02	1.1136E+00	1.7840E-02	1.6010E+04	-4.6382E+06	2.9930E-05
8.500E+02	1.1171E+00	1.7004E-02	1.7437E+04	-4.2185E+06	3.0761E-05
8.750E+02	1.1219E+00	1.6190E-02	1.7887E+04	-3.7745E+06	3.1571E-05
9.000E+02	1.1283E+00	1.5457E-02	1.7009E+04	-3.3353E+06	3.2349E-05
9.250E+02	1.1364E+00	1.4855E-02	1.4765E+04	-2.9356E+06	3.3086E-05
9.500E+02	1.1473E+00	1.4410E-02	1.1647E+04	-2.6045E+06	3.3780E-05
9.750E+02	1.1620E+00	1.4119E-02	8.5576E+03	-2.3529E+06	3.4435E-05
1.000E+03	1.1804E+00	1.3947E-02	6.2218E+03	-2.1701E+06	3.5060E-05
1.025E+03	1.1992E+00	1.3854E-02	4.7840E+03	-2.0342E+06	3.5663E-05
1.050E+03	1.2138E+00	1.3804E-02	4.0135E+03	-1.9254E+06	3.6250E-05
1.075E+03	1.2220E+00	1.3778E-02	3.6439E+03	-1.8303E+06	3.6828E-05
1.100E+03	1.2240E+00	1.3763E-02	3.5092E+03	-1.7412E+06	3.7398E-05
1.125E+03	1.2202E+00	1.3752E-02	3.5606E+03	-1.6533E+06	3.7965E-05

Continued on next page

$T$ (K)	$\gamma$	$Mw$ (kg/mol)	$c_p$ (J/kg/K)	$h_g$ (J/kg)	$\mu$ (Pa s)
1.150E+03	1.2087E+00	1.3737E-02	3.9007E+03	-1.5609E+06	3.8536E-05
1.175E+03	1.1899E+00	1.3706E-02	4.8067E+03	-1.4535E+06	3.9133E-05
1.200E+03	1.1737E+00	1.3639E-02	6.2352E+03	-1.3159E+06	3.9793E-05
1.225E+03	1.1662E+00	1.3531E-02	7.4468E+03	-1.1438E+06	4.0528E-05
1.250E+03	1.1638E+00	1.3399E-02	8.1396E+03	-9.4797E+05	4.1314E-05
1.275E+03	1.1633E+00	1.3256E-02	8.4790E+03	-7.3970E+05	4.2119E-05
1.300E+03	1.1633E+00	1.3112E-02	8.6336E+03	-5.2554E+05	4.2924E-05
1.325E+03	1.1631E+00	1.2971E-02	8.7074E+03	-3.0869E+05	4.3714E-05
1.350E+03	1.1624E+00	1.2836E-02	8.7669E+03	-9.0283E+04	4.4478E-05
1.375E+03	1.1608E+00	1.2706E-02	8.8600E+03	1.2994E+05	4.5205E-05
1.400E+03	1.1583E+00	1.2580E-02	9.0239E+03	3.5331E+05	4.5887E-05
1.425E+03	1.1548E+00	1.2459E-02	9.2883E+03	5.8198E+05	4.6514E-05
1.450E+03	1.1506E+00	1.2341E-02	9.6744E+03	8.1874E+05	4.7078E-05
1.475E+03	1.1460E+00	1.2223E-02	1.0190E+04	1.0668E+06	4.7570E-05
1.500E+03	1.1415E+00	1.2103E-02	1.0822E+04	1.3292E+06	4.7986E-05
1.525E+03	1.1377E+00	1.1982E-02	1.1516E+04	1.6084E+06	4.8323E-05
1.550E+03	1.1352E+00	1.1857E-02	1.2154E+04	1.9046E+06	4.8588E-05
1.575E+03	1.1349E+00	1.1732E-02	1.2531E+04	2.2140E+06	4.8798E-05
1.600E+03	1.1377E+00	1.1609E-02	1.2377E+04	2.5267E+06	4.8985E-05
1.625E+03	1.1444E+00	1.1495E-02	1.1514E+04	2.8268E+06	4.9195E-05
1.650E+03	1.1555E+00	1.1397E-02	1.0101E+04	3.0977E+06	4.9464E-05
1.675E+03	1.1698E+00	1.1317E-02	8.5903E+03	3.3310E+06	4.9807E-05
1.700E+03	1.1849E+00	1.1255E-02	7.3383E+03	3.5294E+06	5.0212E-05
1.725E+03	1.1986E+00	1.1207E-02	6.4221E+03	3.7008E+06	5.0656E-05
1.750E+03	1.2102E+00	1.1169E-02	5.7743E+03	3.8528E+06	5.1123E-05

Continued on next page

$T$ (K)	$\gamma$	$Mw$ (kg/mol)	$c_p$ (J/kg/K)	$h_g$ (J/kg)	$\mu$ (Pa s)
1.775E+03	1.2195E+00	1.1139E-02	5.3118E+03	3.9910E+06	5.1602E-05
1.800E+03	1.2270E+00	1.1115E-02	4.9742E+03	4.1194E+06	5.2087E-05
1.825E+03	1.2329E+00	1.1096E-02	4.7227E+03	4.2405E+06	5.2575E-05
1.850E+03	1.2375E+00	1.1080E-02	4.5331E+03	4.3560E+06	5.3063E-05
1.875E+03	1.2410E+00	1.1066E-02	4.3894E+03	4.4675E+06	5.3552E-05
1.900E+03	1.2435E+00	1.1055E-02	4.2810E+03	4.5758E+06	5.4040E-05
1.925E+03	1.2453E+00	1.1046E-02	4.2004E+03	4.6818E+06	5.4528E-05
1.950E+03	1.2463E+00	1.1038E-02	4.1422E+03	4.7860E+06	5.5015E-05
1.975E+03	1.2468E+00	1.1031E-02	4.1025E+03	4.8890E+06	5.5501E-05
2.000E+03	1.2467E+00	1.1024E-02	4.0783E+03	4.9913E+06	5.5986E-05
2.025E+03	1.2462E+00	1.1019E-02	4.0675E+03	5.0931E+06	5.6471E-05
2.050E+03	1.2452E+00	1.1013E-02	4.0684E+03	5.1947E+06	5.6955E-05
2.075E+03	1.2439E+00	1.1009E-02	4.0797E+03	5.2966E+06	5.7437E-05
2.100E+03	1.2423E+00	1.1004E-02	4.1005E+03	5.3988E+06	5.7920E-05
2.125E+03	1.2404E+00	1.0999E-02	4.1304E+03	5.5017E+06	5.8401E-05
2.150E+03	1.2382E+00	1.0995E-02	4.1687E+03	5.6054E+06	5.8882E-05
2.175E+03	1.2358E+00	1.0990E-02	4.2154E+03	5.7102E+06	5.9363E-05
2.200E+03	1.2332E+00	1.0986E-02	4.2703E+03	5.8162E+06	5.9843E-05
2.225E+03	1.2305E+00	1.0981E-02	4.3333E+03	5.9238E+06	6.0323E-05
2.250E+03	1.2276E+00	1.0975E-02	4.4046E+03	6.0330E+06	6.0802E-05
2.275E+03	1.2245E+00	1.0970E-02	4.4843E+03	6.1441E+06	6.1281E-05
2.300E+03	1.2214E+00	1.0963E-02	4.5727E+03	6.2573E+06	6.1761E-05
2.325E+03	1.2181E+00	1.0957E-02	4.6701E+03	6.3728E+06	6.2240E-05
2.350E+03	1.2148E+00	1.0950E-02	4.7768E+03	6.4908E+06	6.2719E-05
2.375E+03	1.2114E+00	1.0942E-02	4.8932E+03	6.6117E+06	6.3198E-05

Continued on next page

$T$ (K)	$\gamma$	$Mw$ (kg/mol)	$c_p$ (J/kg/K)	$h_g$ (J/kg)	$\mu$ (Pa s)
2.400E+03	1.2080E+00	1.0934E-02	5.0197E+03	6.7356E+06	6.3678E-05
2.425E+03	1.2046E+00	1.0924E-02	5.1568E+03	6.8628E+06	6.4158E-05
2.450E+03	1.2012E+00	1.0914E-02	5.3049E+03	6.9935E+06	6.4638E-05
2.475E+03	1.1978E+00	1.0903E-02	5.4645E+03	7.1281E+06	6.5120E-05
2.500E+03	1.1944E+00	1.0891E-02	5.6362E+03	7.2669E+06	6.5602E-05
2.525E+03	1.1911E+00	1.0878E-02	5.8205E+03	7.4100E+06	6.6085E-05
2.550E+03	1.1878E+00	1.0864E-02	6.0179E+03	7.5580E+06	6.6569E-05
2.575E+03	1.1846E+00	1.0849E-02	6.2291E+03	7.7110E+06	6.7054E-05
2.600E+03	1.1815E+00	1.0832E-02	6.4546E+03	7.8696E+06	6.7541E-05
2.625E+03	1.1785E+00	1.0814E-02	6.6951E+03	8.0339E+06	6.8029E-05
2.650E+03	1.1755E+00	1.0795E-02	6.9512E+03	8.2044E+06	6.8519E-05
2.675E+03	1.1727E+00	1.0774E-02	7.2236E+03	8.3816E+06	6.9011E-05
2.700E+03	1.1700E+00	1.0752E-02	7.5128E+03	8.5658E+06	6.9505E-05
2.725E+03	1.1675E+00	1.0727E-02	7.8198E+03	8.7574E+06	7.0001E-05
2.750E+03	1.1650E+00	1.0701E-02	8.1450E+03	8.9569E+06	7.0500E-05
2.775E+03	1.1627E+00	1.0674E-02	8.4893E+03	9.1648E+06	7.1002E-05
2.800E+03	1.1604E+00	1.0644E-02	8.8535E+03	9.3815E+06	7.1506E-05
2.825E+03	1.1584E+00	1.0612E-02	9.2382E+03	9.6076E+06	7.2013E-05
2.850E+03	1.1564E+00	1.0578E-02	9.6443E+03	9.8436E+06	7.2524E-05
2.875E+03	1.1546E+00	1.0542E-02	1.0073E+04	1.0090E+07	7.3039E-05
2.900E+03	1.1528E+00	1.0503E-02	1.0524E+04	1.0347E+07	7.3557E-05
2.925E+03	1.1512E+00	1.0463E-02	1.0999E+04	1.0616E+07	7.4079E-05
2.950E+03	1.1497E+00	1.0419E-02	1.1498E+04	1.0898E+07	7.4606E-05
2.975E+03	1.1484E+00	1.0374E-02	1.2023E+04	1.1192E+07	7.5137E-05
3.000E+03	1.1471E+00	1.0325E-02	1.2573E+04	1.1499E+07	7.5672E-05

Continued on next page

$T$ (K)	$\gamma$	$Mw$ (kg/mol)	$c_p$ (J/kg/K)	$h_g$ (J/kg)	$\mu$ (Pa s)
3.025E+03	1.1460E+00	1.0274E-02	1.3151E+04	1.1820E+07	7.6213E-05
3.050E+03	1.1449E+00	1.0221E-02	1.3755E+04	1.2157E+07	7.6759E-05
3.075E+03	1.1440E+00	1.0164E-02	1.4387E+04	1.2508E+07	7.7310E-05
3.100E+03	1.1432E+00	1.0105E-02	1.5047E+04	1.2876E+07	7.7867E-05
3.125E+03	1.1424E+00	1.0043E-02	1.5734E+04	1.3261E+07	7.8429E-05
3.150E+03	1.1418E+00	9.9779E-03	1.6449E+04	1.3663E+07	7.8998E-05
3.175E+03	1.1413E+00	9.9101E-03	1.7190E+04	1.4084E+07	7.9572E-05
3.200E+03	1.1408E+00	9.8394E-03	1.7957E+04	1.4523E+07	8.0152E-05
3.225E+03	1.1405E+00	9.7658E-03	1.8747E+04	1.4982E+07	8.0738E-05
3.250E+03	1.1402E+00	9.6894E-03	1.9558E+04	1.5460E+07	8.1329E-05
3.275E+03	1.1401E+00	9.6103E-03	2.0388E+04	1.5960E+07	8.1926E-05
3.300E+03	1.1400E+00	9.5285E-03	2.1232E+04	1.6480E+07	8.2528E-05
3.325E+03	1.1400E+00	9.4442E-03	2.2086E+04	1.7021E+07	8.3134E-05
3.350E+03	1.1401E+00	9.3574E-03	2.2944E+04	1.7584E+07	8.3743E-05
3.375E+03	1.1403E+00	9.2684E-03	2.3802E+04	1.8169E+07	8.4356E-05
3.400E+03	1.1406E+00	9.1774E-03	2.4653E+04	1.8774E+07	8.4969E-05
3.425E+03	1.1409E+00	9.0845E-03	2.5489E+04	1.9401E+07	8.5583E-05
3.450E+03	1.1414E+00	8.9899E-03	2.6305E+04	2.0049E+07	8.6195E-05
3.475E+03	1.1419E+00	8.8941E-03	2.7093E+04	2.0716E+07	8.6804E-05
3.500E+03	1.1425E+00	8.7971E-03	2.7845E+04	2.1403E+07	8.7408E-05
3.525E+03	1.1432E+00	8.6994E-03	2.8557E+04	2.2108E+07	8.8005E-05
3.550E+03	1.1439E+00	8.6012E-03	2.9220E+04	2.2830E+07	8.8593E-05
3.575E+03	1.1447E+00	8.5028E-03	2.9831E+04	2.3569E+07	8.9171E-05
3.600E+03	1.1456E+00	8.4046E-03	3.0385E+04	2.4322E+07	8.9735E-05
3.625E+03	1.1465E+00	8.3067E-03	3.0877E+04	2.5087E+07	9.0285E-05

Continued on next page

$T$ (K)	$\gamma$	$Mw$ (kg/mol)	$c_p$ (J/kg/K)	$h_g$ (J/kg)	$\mu$ (Pa s)
3.650E+03	1.1474E+00	8.2095E-03	3.1305E+04	2.5865E+07	9.0818E-05
3.675E+03	1.1484E+00	8.1133E-03	3.1667E+04	2.6652E+07	9.1332E-05
3.700E+03	1.1495E+00	8.0183E-03	3.1961E+04	2.7448E+07	9.1828E-05
3.725E+03	1.1506E+00	7.9248E-03	3.2188E+04	2.8250E+07	9.2303E-05
3.750E+03	1.1517E+00	7.8329E-03	3.2347E+04	2.9056E+07	9.2756E-05
3.775E+03	1.1529E+00	7.7428E-03	3.2441E+04	2.9866E+07	9.3187E-05
3.800E+03	1.1541E+00	7.6547E-03	3.2470E+04	3.0678E+07	9.3597E-05
3.825E+03	1.1553E+00	7.5687E-03	3.2437E+04	3.1489E+07	9.3984E-05
3.850E+03	1.1565E+00	7.4850E-03	3.2346E+04	3.2299E+07	9.4349E-05
3.875E+03	1.1578E+00	7.4036E-03	3.2198E+04	3.3106E+07	9.4693E-05
3.900E+03	1.1591E+00	7.3246E-03	3.1998E+04	3.3909E+07	9.5016E-05
3.925E+03	1.1604E+00	7.2480E-03	3.1750E+04	3.4706E+07	9.5320E-05
3.950E+03	1.1617E+00	7.1740E-03	3.1458E+04	3.5496E+07	9.5606E-05
3.975E+03	1.1630E+00	7.1025E-03	3.1126E+04	3.6278E+07	9.5874E-05

The decomposition model for TACOT is the phenomenological three-components model discussed in Section 5.2. The coefficients for the model are given in Table ??.

Table D.4: TACOT three-components decomposition coefficients

	$\rho_{i,v}$ (kg/m <sup>3</sup> )	$\rho_{i,c}$ (kg/m <sup>3</sup> )	$A_i$ (s <sup>-1</sup> )	$E_i/R$ (K)	$\psi$	$T_{reac}$ (K)
1	3.000E+02	0.000E+00	1.200E+04	8.556E+03	3.000E+00	3.333E+02
2	9.000E+02	6.000E+02	4.480E+09	2.044E+04	3.000E+00	5.556E+02
3	1.600E+03	1.600E+03	0.000E+00	0.000E+00	0.000E+00	5.556E+03



The transport properties are given as (suggested):

virgin porosity,  $\phi_v = 0.8$ ,

char porosity,  $\phi_c = 0.85$ ,

virgin permeability,  $K_v = 1.6 \times 10^{-11} \text{ m}^2$ ,

char permeability,  $K_c = 2.0 \times 10^{-11} \text{ m}^2$ .

The thermochemistry data table for TACOT is omitted for this document due to its length. The data file can be found in Ref. [110].

## Bibliography

- [1] Jet Propulsion Laboratory, “Mars Science Laboratory/Curiosity,” NASA Facts 400-1537, National Aeronautics and Space Administration, Pasadena, California, 2013.
- [2] “<http://mars.nasa.gov/mer/gallery/artwork/hires/entry.jpg>,” , 2004.
- [3] Amar, A. J., *Modeling of One-Dimensional Ablation with Porous Flow Using Finite Control Volume Procedure*, Master thesis, North Carolina State University, 2006.
- [4] Trumble, K. A., Cozmuta, I., Sepka, S., Jenniskens, P., and Winter, M., “Post-flight Aerothermal Analysis of the Stardust Sample Return Capsule,” *Journal of Spacecraft and Rockets*, Vol. 47, No. 5, 2010, pp. 765–774, doi:10.2514/1.41514.
- [5] Olynick, D., Chen, Y.-K., and Tauber, M. E., “Aerothermodynamics of the Stardust Sample Return Capsule,” *Journal of Spacecraft and Rockets*, Vol. 36, No. 3, 1999, pp. 442–462, doi:10.2514/2.3466.
- [6] Bose, D., Olson, M., Laub, B., White, T., Feldman, J., Santos, J., Mahzari, M., MacLean, M., Dufrene, A., and Holden, M., “Initial Assessment of Mars Science Laboratory Heatshield Instrumentation and Flight Data,” in “51st AIAA Aerospace Sciences Meeting,” AIAA Paper 2013-908, Grapevine, TX, 2013, doi:10.2514/6.2013-908.
- [7] Tran, H. K., Johnson, C. E., Rasky, D. J., Hui, F. C. L., Hsu, M.-T., Chen, T., Chen, Y. K., Paragas, D., and Kobayashi, L., “Phenolic impregnated car-

- bon ablators (PICA) as thermal protection systems for discovery missions,” Technical Report 110440, NASA Technical Memorandum, 1997.
- [8] Ahn, H.-K., Park, C., and Sawada, K., “Response of Heatshield Material at Stagnation Point of Pioneer-Venus Probes,” *Journal of Thermophysics and Heat Transfer*, Vol. 16, No. 3, doi:10.2514/2.6697.
- [9] “[http://www.nasa.gov/centers/ames/research/mssl\\_heatshield.html](http://www.nasa.gov/centers/ames/research/mssl_heatshield.html),” , 2012.
- [10] “[http://www.nasa.gov/mission\\_pages/stardust/multimedia/capsule-1.html](http://www.nasa.gov/mission_pages/stardust/multimedia/capsule-1.html),” .
- [11] Lawson, J. W., Stackpoole, M. M., and Shklover, V., “Examination of Scanning Electron Microscope and Computed Tomography Images of PICA,” , 2011.
- [12] Lachaud, J., Mansour, N. N., Ceballos, A., Pejaković, D., Zhang, L., and Marschall, J., “Validation of a volume-averaged fiber-scale model for the oxidation of a carbon-fiber preform,” in “42nd AIAA Thermophysics Conference,” AIAA, Honolulu, Hawaii, 2011, doi:10.2514/6.2011-3640.
- [13] Houtz, R., ““Orlon” Acrylic Fiber: Chemistry and Properties,” *Textile Research Journal*, Vol. 20, No. 11, 1950, pp. 786–801, doi:10.1177/004051755002001107.
- [14] Moyer, C. B. and Rindal, R. A., “AN ANALYSIS OF THE COUPLED CHEMICALLY REACTING BOUNDARY LAYER AND CHARRING ABLATOR PART II,” Contractor Report CR-1060, NASA, 1968.
- [15] Goldstein, H. E., “Kinetics of Nylon and Phenolic Pyrolysis,” Tech. rep., Lockheed Missiles and Space Company Technical Report, Sunnyvale, California, 1965.

- [16] Hurwicz, H., Fifer, S., and Kelly, M., “Multidimensional Ablation and Heat Flow During Re-Entry,” *Journal of Spacecraft and Rockets*, Vol. 1, No. 3, 1964, pp. 235–242,  
doi:10.2514/3.27643.
- [17] FRIEDMAN, H. A. and MCFARLAND, B. L., “Two-dimensional transient ablation and heat conduction analysis for multimaterial thrust chamber walls.” *Journal of Spacecraft and Rockets*, Vol. 5, No. 7, 1968, pp. 753–761,  
doi:10.2514/3.29353.
- [18] April, G. C., Pike, R. W., and Del Valle, E. G., “Nonequilibrium Flow and the Kinetics of Chemical Reactions in the Char Zone,” *Journal of Macromolecular Science: Part A - Chemistry*, Vol. 3, No. 4, 1969, pp. 685–704,  
doi:10.1080/10601326908053836.
- [19] April, G. C., Pike, R. W., and del Valle, E. G., “Modeling Reacting Gas FLOW in the Char Layer of an Ablator,” *AIAA Journal*, Vol. 9, No. 6, 1971, pp. 1113–1119,  
doi:10.2514/3.6330.
- [20] Pike, R. W., April, G. C., and del Valle, E. G., “EVALUATION OF THE ENERGY TRANSFER IN THE CHAR ZONE DURING ABLATION PART I: Theoretical and Experimental Results for Heat Shield Surface Temperatures up to 3000 F,” NASA Grant NGR 19-001-016, Department of Chemical Engineering, Baton Rouge, LA, Louisiana state university.
- [21] Blackwell, B. F., “Numerical prediction of one-dimensional ablation using a finite control volume procedure with exponential differencing,” *Numerical Heat Transfer*, Vol. 14, No. 1, 1988, pp. 17–34,  
doi:10.1080/10407788808913631.

- [22] Blackwell, B. F. and Hogan, R. E., “Numerical solution of axisymmetric heat conduction problems using finite control volume technique,” *Journal of Thermophysics and Heat Transfer*, Vol. 7, No. 3, 1993, pp. 462–471, doi:10.2514/3.441.
- [23] Blackwell, B. F. and Hogan, R. E., “One-Dimensional Ablation Using Landau Transformation and Finite Control Volume Procedure,” *Journal of Thermophysics and Heat Transfer*, Vol. 8, No. 2, 1994, pp. 282–287, doi:10.2514/3.535.
- [24] Hogan, R. E., Blackwell, B. F., and Cochran, R. J., “Application of Moving Grid Control Volume Finite Element Method to Ablation Problems,” *Journal of Thermophysics and Heat Transfer*, Vol. 10, No. 2, 1996, pp. 312–319, doi:10.2514/3.789.
- [25] Amar, A. J., Blackwell, B. F., and Edwards, J. R., “One-Dimensional Ablation with Pyrolysis Gas Flow Using a Full Newton’s Method and Finite Control Volume Procedure,” in “39th AIAA Thermophysics Conference,” Miami, FL, AIAA 2007-4535, 2007.
- [26] Amar, A. J., Blackwell, B. F., and Edwards, J. R., “One-Dimensional Ablation Using a Full Newton’s Method and Finite Control Volume Procedure,” *Journal of Thermophysics and Heat Transfer*, Vol. 22, No. 1, 2008, pp. 71–82, doi:10.2514/1.29610.
- [27] Amar, A. J., Blackwell, B. F., and Edwards, J. R., “Development and Verification of a One-Dimensional Ablation Code Including Pyrolysis Gas Flow,” *Journal of Thermophysics and Heat Transfer*, Vol. 23, No. 1, 2009, pp. 59–71, doi:10.2514/1.36882.

- [28] Amar, A. J., Calvert, N. D., and Kirk, B. S., “Development and Verification of the Charring Ablating Thermal Protection Implicit System Solver,” in “49th AIAA Aerospace Sciences Meeting and Exhibit,” Orlando, FL, AIAA paper 2011-144, 2011,  
doi:10.2514/6.2011-144.
- [29] Polehn, R. A., Keyhani, M., and Parang, M., “Transient compressible flow in variable permeability media,” *Journal of Thermophysics and Heat Transfer*, Vol. 8, No. 2, 1994, pp. 378–381,  
doi:10.2514/3.552.
- [30] Keyhani, M. and Polehn, R. A., “Finite Difference Modeling of Anisotropic Flows,” *Journal of Heat Transfer*, Vol. 117, No. 2, 1995, pp. 458–464,  
doi:10.1115/1.2822544.
- [31] Frankel, J. I., Keyhani, M., Elkins, B., and Arimilli, R. V., “New In Situ Method for Estimating Thermal Diffusivity Using Rate-Based Temperature Sensors,” *Journal of Thermophysics and Heat Transfer*, Vol. 24, No. 4, 2010, pp. 811–817,  
doi:10.2514/1.46300.
- [32] Frankel, J. I., Keyhani, M., and Elkins, B. E., “Surface Heat Flux Prediction Through Physics-Based Calibration, Part 1: Theory,” *Journal of Thermophysics and Heat Transfer*, Vol. 27, No. 2, 2013, pp. 189–205,  
doi:10.2514/1.T3917.
- [33] Frankel, J. I. and Keyhani, M., “Nonlinear Inverse Calibration Heat Conduction Through Property Physics,” *Journal of Thermophysics and Heat Transfer*, Vol. 28, No. 2, 2014, pp. 203–217,  
doi:10.2514/1.T4269.

- [34] Chen, Y.-K. and Milos, F. S., “Ablation and Thermal Response Program for Spacecraft Heatshield Analysis,” *Journal of Spacecraft and Rockets*, Vol. 36, No. 3, 1999, pp. 475–483,  
doi:10.2514/2.3469.
- [35] Chen, Y.-K. and Milos, F. S., “Two-Dimensional Implicit Thermal Response and Ablation Program for Charring Materials,” *Journal of Spacecraft and Rockets*, Vol. 38, No. 4, 2001, pp. 473–481,  
doi:10.2514/2.3724.
- [36] Chen, Y.-K. and Milos, F. S., “Loosely Coupled Simulation for Two-Dimensional Ablation and Shape Change,” in “40th Thermophysics Conference,” AIAA Paper 2008-3802, Seattle, Washington, 2008,  
doi:10.2514/6.2008-3802.
- [37] Chen, Y.-K., Milos, F. S., and Gokcen, T., “Loosely Coupled Simulation for Two-Dimensional Ablation and Shape Change,” *Journal of Spacecraft and Rockets*, Vol. 47, No. 5, 2010, pp. 775–785,  
doi:10.2514/1.39667.
- [38] Chen, Y.-K. and Milos, F. S., “Three-Dimensional Ablation and Thermal Response Simulation System,” in “38th Thermophysics Conference,” Toronto, Ontario Canada, AIAA 2005-5064, 2005,  
doi:10.2514/6.2005-5064.
- [39] Chen, Y.-K., Milos, F. S., and Gökçen, T., “Validation of a Three-Dimensional Ablation and Thermal Response Simulation Code,” in “10th AIAA/ASME Joint Thermophysics and Heat Transfer Conference,” AIAA Paper 2010-4645, 2010,  
doi:10.2514/6.2010-4645.

- [40] Chen, Y.-K. and Milos, F., “Multidimensional Effects on Heatshield Thermal Response for the Orion Crew Module,” in “39th AIAA Thermophysics Conference,” Miami, FL, AIAA 2007-4397, 2007, doi:10.2514/6.2007-4397.
- [41] Milos, F. S. and Chen, Y.-K., “Ablation and Thermal Response Property Model Validation for Phenolic Impregnated Carbon Ablator,” *Journal of Spacecraft and Rockets*, Vol. 47, No. 5, 2010, pp. 786–805, doi:10.2514/1.42949.
- [42] Chen, Y.-K. and Milos, F. S., “Effects of Nonequilibrium Chemistry and Darcy—Forchheimer Pyrolysis Flow for Charring Ablator,” *Journal of Spacecraft and Rockets*, Vol. 50, No. 2, 2013, pp. 256–269, doi:10.2514/1.A32289.
- [43] Chen, Y.-K. and Gökçen, T., “Effect of Nonequilibrium Surface Thermochemistry in Simulation of Carbon-Based Ablators,” *Journal of Spacecraft and Rockets*, Vol. 50, No. 5, 2013, pp. 917–926, doi:10.2514/1.A32451.
- [44] Suzuki, T., Sawada, K., Yamada, T., and Inatani, Y., “Gas Permeability of Oblique-Layered Carbon-Cloth Ablator,” *Journal of Thermophysics and Heat Transfer*, Vol. 18, No. 4, 2004, pp. 548–550, doi:10.2514/1.6242.
- [45] Suzuki, T., Sawada, K., Yamada, T., and Inatani, Y., “Thermal Response of Ablative Test Piece in Arc-Heated Wind Tunnel,” in “42nd AIAA Aerospace Sciences Meeting and Exhibit,” Reno, Nevada, AIAA 2004-341, 2004, doi:10.2514/6.2004-341.



- [46] Suzuki, T., Sawada, K., Yamada, T., and Inatani, Y., “Experimental and Numerical Study of Pyrolysis Gas Pressure in Ablating Test Piece,” *Journal of Thermophysics and Heat Transfer*, Vol. 19, No. 3, 2005, p. 266,  
doi:10.2514/1.12211.
- [47] Wakefield, R. M. and Pitts, W. C., “Analysis of the Heat-Shield Experiment on the Pioneer-Venus Entry Probes,” in “15th Thermophysics Conference,” Snowmass, CO, AIAA 1980-1494, 1980,  
doi:10.2514/6.1980-1494.
- [48] Sutton, K., “An Experimental Study of a carbon-Phenolic Ablation Material,” NASA Technical Note D-5930, NASA Langley Research Center, Hampton, VA 23365, 1970.
- [49] Suzuki, T., Furudate, M., and Sawada, K., “Unified Calculation of Hypersonic Flowfield for a Reentry Vehicle,” *Journal of Thermophysics and Heat Transfer*, Vol. 16, No. 1, 2002, pp. 94–100,  
doi:10.2514/2.6656.
- [50] Suzuki, T., Yamamoto, Y., Yamada, T., and Sakai, T., “Coupled Analysis of Flowfield and Thermal Response of Ablative Test Piece Under Arc-Heated Flow Conditions,” in “44th AIAA Aerospace Sciences Meeting and Exhibit,” Reno, Nevada, AIAA 2006-778, 2006,  
doi:10.2514/6.2006-778.
- [51] Suzuki, T., Sakai, T., and Yamada, T., “Calculation of Thermal Response of Ablator Under Arcjet Flow Condition,” *Journal of Thermophysics and Heat Transfer*, Vol. 21, No. 2, 2007, p. 257,  
doi:10.2514/1.25499.

- [52] Suzuki, T., Fujita, K., Ando, K., and Sakai, T., “Experimental Study of Graphite Ablation in Nitrogen Flow,” *Journal of Thermophysics and Heat Transfer*, Vol. 22, No. 3, 2008, pp. 382–390, doi:10.2514/1.35082.
- [53] Suzuki, T., Fujita, K., and Sakai, T., “Experimental Study of Graphite Ablation in Nitrogen Flow, Part II: Further Numerical Analysis,” *Journal of Thermophysics and Heat Transfer*, Vol. 24, No. 3, 2010, pp. 589–598, doi:10.2514/1.43264.
- [54] Suzuki, T., Fujita, K., Sakai, T., Ichi Okuyama, K., Kato, S., and Nishio, S., “Prediction Accuracy of Thermal Response of Ablator Under Arcjet Flow Conditions,” in “48th AIAA Aerospace Sciences Meeting Including the New Horizons Forum and Aerospace Exposition,” AIAA 2010-1174, 2010, doi:10.2514/6.2010-1174.
- [55] Suzuki, T., Fujita, K., Yamada, T., Inatani, Y., and Ishii, N., “Postflight Thermal Protection System Analysis of Hayabusa Reentry Capsule,” *Journal of Spacecraft and Rockets*, Vol. 51, No. 1, 2014, pp. 96–105, doi:10.2514/1.A32549.
- [56] Hirata, N., Nozawa, S., Takahashi, Y., Kihara, H., and Ichi Abe, K., “Numerical study of pyrolysis gas flow and heat transfer inside an ablator,” *Computational Thermal Sciences*, Vol. 4, No. 3, 2012, pp. 225–242, doi:10.1615/ComputThermalScien.2012004762.
- [57] Kihara, H., Hirata, N., and Ichi Abe, K., “A Study of Thermal Response and Flow Field Coupling Simulation around Hayabusa Capsule Loaded with Light-Weight Ablator,” *Open Journal of Fluid Dynamics*, Vol. 3, 2013, pp. 100–107, doi:10.4236/ojfd.2013.32A016.

- [58] Lachaud, J., *Physico-chemical modeling of carbon-based composite ablation. Modélisation physico-chimique de l'ablation de matériaux composites en carbone.*, Ph.D. thesis, Bordeaux University, France, 2006.
- [59] Lachaud, J., Bertrand, N., Vignoles, G. L., Bourget, G., Rebillat, F., and Weisbecker, P., “A theoretical/experimental approach to the intrinsic oxidation reactivities of C/C composites and of their components,” *Carbon*, Vol. 45, No. 14, 2007, pp. 2768–2776,  
doi:10.1016/j.carbon.2007.09.034.
- [60] Lachaud, J., Aspa, Y., and Vignoles, G. L., “Analytical modeling of the steady state ablation of a 3D C/C composite,” *International Journal of Heat and Mass Transfer*, Vol. 51, No. 9-10, 2008, pp. 2618–2627,  
doi:10.1016/j.ijheatmasstransfer.2008.01.008.
- [61] Lachaud, J., Mansour, N. N., White, S., Laub, B., and Bouilly, J.-M., “Modeling of the pyrolysis of a composite material Modeling of the pyrolysis of a composite material made of randomly distributed short fibers,” in “Congrès Français de Thermique,” Toulouse, France, 2008.
- [62] Lachaud, J. and Vignoles, G. L., “A Brownian Motion technique to simulate gasification and its application to C/C composite ablation,” *Computational Materials Science*, Vol. 44, No. 4, 2009, pp. 1034–1041,  
doi:10.1016/j.commatsci.2008.07.015.
- [63] Vignoles, G. L., Lachaud, J., Aspa, Y., and Goyhénèche, J.-M., “Ablation of carbon-based materials: multiscale roughness modelling,” *Composites Science and Technology*, Vol. 69, No. 9, 2009, pp. 1470–1477,  
doi:10.1016/j.compscitech.2008.09.019.

- [64] Lachaud, J. and Mansour, N., “Microscopic Scale Simulation of the Ablation of Fibrous Materials,” in “48th AIAA Aerospace Sciences Meeting Including the New Horizons Forum and Aerospace Exposition,” Orlando, Florida, AIAA 2010-984, 2010,  
doi:10.2514/6.2010-984.
- [65] Lachaud, J. and Mansour, N. N., “A pyrolysis and ablation toolbox based on OpenFOAM - with application to material response under high-enthalpy environments,” in “5th OpenFOAM Workshop,” Chalmers University, Gothenburg, Sweden, 2010.
- [66] Lachaud, J., Cozmuta, I., and Mansour, N. N., “Multiscale approach to ablation modeling of phenolic impregnated carbon ablators,” *Journal of Spacecraft and Rockets*, Vol. 47, No. 6, 2010, pp. 910–921,  
doi:10.2514/1.42681.
- [67] Mansour, N., Lachaud, J., Magin, T., de Mûelenaere, J., and Chen, Y.-K., “High-Fidelity Charring Ablator Thermal Response Model,” in “42nd AIAA Thermophysics Conference,” Honolulu, Hawaii, AIAA 2011-3124, 2011,  
doi:10.2514/6.2011-3124.
- [68] Lachaud, J. and Mansour, N., “Porous-material Analysis Toolbox based on OpenFOAM-extend and Applications,” in “44th AIAA Thermophysics Conference,” San Diego, CA, AIAA 2013-2767, 2013,  
doi:10.2514/6.2013-2767.
- [69] Mansour, N. N., Panerai, F., Martin, A., Parkinson, D. Y., MacDowell, A. A., Haboub, A., Sandstrom, T. A., Fast, T., Vignoles, G. L., and Lachaud, J., “A New Approach To Light-Weight Ablators Analysis: From Micro-Tomography Measurements to Statistical Analysis and Modeling,” in “44th AIAA Thermo-

- physics Conference,” AIAA, San Diego, CA, 2013,  
doi:10.2514/6.2013-2768.
- [70] Panerai, F., Martin, A., Mansour, N. N., Sepka, S. A., and Lachaud, J., “Flow-Tube Oxidation Experiments on the Carbon Preform of a Phenolic-Impregnated Carbon Ablator,” *Journal of Thermophysics and Heat Transfer*, Vol. 28, No. 2, 2014, pp. 181–190,  
doi:10.2514/1.T4265.
- [71] Sozer, E., “freeCFD, <https://code.google.com/p/freecfd/>,” .
- [72] Weng, H., Zhang, H., Khan, O. U., and Martin, A., “Multi-dimensional modeling of charring ablators,” in “43rd AIAA Thermophysics Conference,” New Orleans, LA, AIAA Paper 2012-2748, 2012,  
doi:10.2514/6.2012-2748.
- [73] Weng, H. and Martin, A., “Multidimensional Modeling of Pyrolysis Gas Transport Inside Charring Ablative Materials,” *Journal of Thermophysics and Heat Transfer*, Vol. 28, No. 4, 2014, pp. 583–597,  
doi:10.2514/1.T4434.
- [74] Martin, A. and Boyd, I. D., “Simulation of pyrolysis gas within a thermal protection system,” in “40th Thermophysics Conference,” Seattle, WA, AIAA Paper 2008-3805, 2008,  
doi:10.2514/6.2008-3805.
- [75] Zhang, H., Weng, H., and Martin, A., “Simulation of Flow-tube Oxidation on the Carbon Preform of PICA,” in “52nd AIAA Aerospace Sciences Meeting,” National Harbor, MD, AIAA 2014-1209, 2014,  
doi:10.2514/6.2014-1209.

- [76] Zhang, H., Martin, A., and McDonough, J. M., “Parallel Efficiency of the FreeCFD Code for Hypersonic Flows with Chemistry,” in “24th International Conference on Parallel Computational Fluid Dynamics,” Atlanta, GA, 2012.
- [77] Davuluri, R. and Martin, A., “Numerical study of spallation phenomenon in an arc-jet environment,” in “11th AIAA/ASME Joint Thermophysics and Heat Transfer Conference,” American Institute of Aeronautics and Astronautics, 2014,  
doi:10.2514/6.2014-2249.
- [78] Martin, A., Boyd, I., Cozmuta, I., and Wright, M., “Chemistry Model for Ablating Carbon-Phenolic Material During Atmospheric Re-Entry,” in “48th AIAA Aerospace Sciences Meeting Including the New Horizons Forum and Aerospace Exposition,” Orlando, Florida, AIAA 2010-1175, 2010,  
doi:10.2514/6.2010-1175.
- [79] Martin, A. and Boyd, I., “Modeling of heat transfer attenuation by ablative gases during the Stardust re-entry,” in “50th AIAA Aerospace Sciences Meeting including the New Horizons Forum and Aerospace Exposition,” Nashville, Tennessee, AIAA 2012-0814, 2012,  
doi:10.2514/6.2012-814.
- [80] Martin, A., “Modeling of chemical nonequilibrium effects in a charring ablator,” in “51st AIAA Aerospace Sciences Meeting including the New Horizons Forum and Aerospace Exposition,” Grapevine, TX, AIAA 2013-0301, 2013,  
doi:10.2514/6.2013-301.
- [81] Martin, A., “Volume averaged modeling of the oxidation of porous carbon fiber material,” in “44th AIAA Thermophysics Conference,” American Institute of

Aeronautics and Astronautics, San Diego, CA, AIAA 2013-2636, 2013,  
doi:10.2514/6.2013-2636.

- [82] Balay, S., Brown, J., Buschelman, K., Gropp, W.-D., Kaushik, D., Knep-  
ley, M.-G., McInnes, L.-C., Smith, B.-F., and Zhang, H., “PETSc Web page  
<http://www.mcs.anl.gov/petsc>,” , 2013.
- [83] Liou, M.-S., “A sequel to AUSM, Part II: AUSM+-up for all speeds,” *Journal  
of Computational Physics*, Vol. 214, No. 1, 2006, pp. 137 – 170,  
doi:10.1016/j.jcp.2005.09.020.
- [84] Schloegel, K., Karypis, G., and Kumar, V., “Parallel Multilevel Algorithms for  
Multi-Constraint Graph Partitioning,” in “Euro-Par,” LNCS 1900, 2000, pp.  
296–310,  
doi:10.1007/3-540-44520-X\_39.
- [85] Cohen, C. B. and Reshotko, E., “Similar Solutions for the Compressible Lam-  
inar Boundary Layer with Heat Transfer and Pressure Gradient,” Tech. Rep.  
1293, NACA, 1955.
- [86] Eckert, E. R. G. and Drake, J., R. M., *Analysis of Heat and Mass Transfer*,  
McGraw-Hill, New York, NY, 1972.
- [87] Kays, W. M., Crawford, M. E., and Weigand, B., *Convective Heat and Mass  
Transfer*, McGraw-Hill, 4th ed., 2005.
- [88] Milos, F. S. and Rasky, D., “Review of numerical procedures for computational  
surface thermochemistry,” *Journal of Thermophysics and Heat Transfer*, Vol. 8,  
No. 1, 1994, pp. 24–34.
- [89] Alkandry, H., Boyd, I. D., and Martin, A., “Coupled Flow Field Simulations  
of Charring Ablators with Nonequilibrium Surface Chemistry,” in “44th AIAA

- Thermophysics Conference,” AIAA 2013-2634, San Diego, California, 2013,  
doi:10.2514/6.2013-2634.
- [90] Blackwell, B. and Howard, M., “An Element Potential Based Chemical Equilibrium Solver for Gas/Surface Thermochemistry,” in “50th AIAA Aerospace Sciences Meeting,” Nashville, Tennessee, AIAA Paper 2012-0815, 2012.
- [91] Marschall, J. and Cox, M. E., “Gas Permeability of Lightweight Ceramic Ablators,” *Journal of Thermophysics and Heat Transfer*, Vol. 13, No. 3, 1999, pp. 383–386,  
doi:10.2514/2.6451.
- [92] Marschall, J. and Milos, F. S., “Gas permeability of rigid fibrous refractory insulations,” *Journal of Thermophysics and Heat Transfer*, Vol. 12, No. 4, 1998, pp. 528–535,  
doi:10.2514/2.6451.
- [93] Martin, A. and Boyd, I. D., “Non-Darcian Behavior of Pyrolysis Gas in a Thermal Protection System,” *Journal of Thermophysics and Heat Transfer*, Vol. 24, No. 1, 2010, pp. 60–68,  
doi:10.2514/1.44103.
- [94] Darcy, H., “Les Fontaines Publiques de la Ville de Dijon,” Dalmont, Paris, France, 1856.
- [95] Douglas, J., Paes-Leme, P. J., and Giorgi, T., “Generalized Forchheimer flow in porous media,” Technical Report 205, Purdue University, West Lafayette, IN, 1993.
- [96] Gosse, R., “Pyrolysis Gas Modeling of TPS Material Using Finite-Volume Method and Issues with Validation,” in “42nd AIAA Thermophysics Confer-



- ence,” AIAA 2011-3641, 2011,  
doi:10.2514/6.2011-3641.
- [97] Arpaci, V. S., *Conduction Heat Transfer*, Addison-Wesley, MA, 1966.
- [98] Beck, J. V., Blackwell, B. F., and St. Clair, C. R., *Inverse Heat Conduction Problems*, Wiley-Interscience, New York, NY, 1985.
- [99] Lachaud, J., Martin, A., Cozmuta, I., and Laub, B., “Ablation test-case series #1,” in “4th AFOSR/SNL/NASA Ablation Workshop,” Albuquerque, NM, 2010.
- [100] Polehn, R. A., *Thermal Response of an Axisymmetric, Charring-Decomposing Polymer*, Ph.D. thesis, University of Tennessee at Knoxville, Knoxville, TN, 1994.
- [101] van Eekelen, T., Martin, A., Lachaud, J., and Bianchi, D., “Ablation test-case series #3: Numerical simulation of ablative-material response: code and model comparisons,” in “6th Ablation Workshop,” Urbana Champaign, IL, 2014.
- [102] Gökçen, T., Chen, Y.-K., Skokova, K. A., and Milos, F. S., “Computational Analysis of Arc-Jet Stagnation Tests Including Ablation and Shape Change,” *Journal of Thermophysics and Heat Transfer*, Vol. 24, No. 4, 2010, pp. 694–718, doi:10.2514/1.46199.
- [103] Covington, M. A., Heinemann, J. M., Goldstein, H. E., Chen, Y.-K., Terrazas-Salinas, I., Balboni, J. A., Olejniczak, J., and Martinez, E. R., “Performance of a Low Density Ablative Heat Shield Material,” *Journal of Spacecraft and Rockets*, Vol. 45, No. 4, 2008, pp. 854–864, doi:10.2514/1.38249.
- [104] Agrawal, P., Ellerby, D. T., Switzer, M. R., and Squire, T. H., “Multidimensional Tests of Thermal Protection Materials in the Arcjet Test Facility,”

- in “10th AIAA/ASME Joint Thermophysics and Heat Transfer Conference,”  
Chicago, IL, AIAA Paper 2010-4664, 2010,  
doi:10.2514/6.2010-4664.
- [105] Uhl, J., Owens, W. P., Meyers, J. M., and Fletcher, D. G., “Pyrolysis Simulation in an ICP Torch Facility,” in “42nd AIAA Thermophysics Conference,” Honolulu, HI, AIAA Paper 2011-3618, 2011,  
doi:10.2514/6.2011-3618.
- [106] Meyers, J. M., Owens, W. P., Uhl, J., and Fletcher, D. G., “Near Surface CO<sub>2</sub> Detection in an Inductively Coupled Plasma Facility Using Diode Laser Absorption,” in “42nd AIAA Thermophysics Conference,” Honolulu, HI, AIAA Paper 2011-3788, 2011,  
doi:10.2514/6.2011-3788.
- [107] Johnston, C. O., Gnoffo, P. A., and Mazaheri, A., “Study of Ablation-Flowfield Coupling Relevant to the Orion Heatshield,” *Journal of Thermophysics and Heat Transfer*, Vol. 26, No. 2, 2012, pp. 213–221,  
doi:10.2514/1.T3769.
- [108] Tran, H., Johnson, C., Rasky, D., Hui, F., and Hsu, M.-T., “Silicone impregnated reusable ceramic ablators for Mars follow-on missions,” in “31st Thermophysics Conference,” AIAA Paper 1996-1819, 1996,  
doi:10.2514/6.1996-1819.
- [109] Milos, F. S. and Chen, Y.-K., “Two-Dimensional Ablation, Thermal Response, and Sizing Program for Pyrolyzing Ablators,” *Journal of Spacecraft and Rockets*, Vol. 46, No. 6, 2009, pp. 1089–1099,  
doi:10.2514/1.36575.

- [110] van Eekelen, T., Martin, A., Lachaud, J., and Bianchi, D., “Ablation test-case series #3,” in “6th Ablation Workshop,” Urbana Champaign, IL, 2014.

## Vita

### Haoyue Weng

#### Education

- University of Kentucky, Lexington, KY  
Pursuing Ph.D. in Mechanical Engineering, 2009-present  
Dissertation topic: Multidimensional modeling of pyrolysis gas transport inside orthotropic charring ablators
- Beijing University of Posts and Telecommunications, Beijing, China  
Bachelor of Science in Electrical Engineering, 2005-2009  
Major: VLSI design, signal processing

#### Academic Experience

- 08/2013 – 05/2014  
Teaching assistant at University of Kentucky, Lexington, KY  
Assisted courses: Introduction to Fluid Mechanics, Introduction to Mechanical Engineering
- 08/2009 – 05/2010  
Research assistant at University of Kentucky, Lexington, KY  
Research focus: development of the material response module in KATS, expanding capabilities and models
- 08/2010 – 05/2011

Teaching assistant at University of Kentucky, Lexington, KY

Assisted course: Intro to Mechanical Systems

- 08/2009 – 05/2010

Research assistant at University of Kentucky, Lexington, KY

Research focus: implementation of inviscid flux schemes as part of a hypersonic CFD solver

### **Publications in Referred Journals**

- Weng, H., Bailey, S. C. C., and Martin, A., “Numerical study of geometrical effects on charring ablative arc-jet samples,” *International Journal of Heat and Mass Transfer*, vol. 80, pp. 570-596, 2015.  
doi: 10.1016/j.ijheatmasstransfer.2014.09.040.
- Weng, H. and Martin, A., “Multidimensional modeling of pyrolysis gas transport inside charring ablative materials,” *Journal of Thermophysics and Heat Transfer*, vol. 28, no. 4, pp. 583-597, 2014.  
doi: 10.2514/1.T4434.
- Weng, H. and Martin, A., “Numerical investigation of pyrolysis gas blowing pattern and thermal response using orthotropic charring ablative material,” *Journal of Thermophysics and Heat Transfer*, 2015, In Press (Control ID 2014-09-T4576).  
doi: 10.2514/1.T4576.

### **In Preparation**

- Weng, H., Bailey, S. C. C., and Martin, A., “Three-dimensional correction factor for 1D ablative numerical model,” *International Journal of Heat and*

Mass Transfer, 2015, In preparation (Jan. 2015 Estimated).

- Weng, H. and Martin, A., “Numerical investigation of geometric effects of Stardust return capsule heat shield,” *Journal of Thermophysics and Heat Transfer*, 2015, In preparation (Feb. 2015 Estimated).

### **Full Length Articles in Refereed Conference Proceedings**

- Weng, H. and Martin, A., “Numerical investigation of geometric effects of star-dust return capsule heat shield,” in 53rd AIAA Aerospace Sciences Meeting, Accepted (Control ID: 2026425), Kissimmee, FL, 2015.
- Weng, H. and Martin, A., “Numerical investigation of pyrolysis gas blowing pattern and thermal response using orthotropic charring ablative material,” in 11th AIAA/ASME Joint Thermophysics and Heat Transfer Conference, AIAA Paper 2014-2121, Atlanta, GA, 2014.  
doi: 10.2514/6.2014-2121.
- Zhang, H., Weng, H., and Martin, A., “Simulation of flow-tube oxidation on the carbon preform of PICA,” in 52nd AIAA Aerospace Sciences Meeting, AIAA Paper 2014-1209, National Harbor, MD, 2014.  
doi: 10.2514/6.2014-1209.
- Weng, H. and Martin, A., “Multi-dimensional modeling pyrolysis gas flow inside charring ablaters,” in 44th AIAA Thermophysics Conference, AIAA Paper 2013-2635, San Diego, CA, 2013.  
doi: 10.2514/6.2013-2635.
- Weng, H., Zhang, H., Khan, O. U., and Martin, A., “Multi-dimensional modeling of charring ablaters,” 43rd AIAA Thermophysics Conference, AIAA Paper 2012-2748, New Orleans, LA, June 25-28 2012.

doi: 10.2514/6.2012-2748.

### **Abstracts in Refereed Conference Proceedings**

- Weng, H. and Martin, A., “Three-dimensional modeling of pyrolysis gas in charring ablative materials,” in 39th Dayton-Cincinnati Aerospace Sciences Symposium, Dayton, OH, 2014.
- Weng, H. and Martin, A., “Three-dimensional modeling of charring ablative materials,” in 38th Dayton-Cincinnati Aerospace Sciences Symposium, Dayton, OH, 2013.
- Weng, H. and Martin, A., “Development of a three-dimensional charring ablator solver,” in 37th Dayton-Cincinnati Aerospace Sciences Symposium, Dayton, OH, 2012.